



N°d'ordre NNT : 2022LYO1145

**THESE de DOCTORAT DE L'UNIVERSITE DE LYON**  
opérée au sein de  
**L'Université Claude Bernard Lyon 1**

**Ecole Doctorale N° ED-160**  
**Electrotechnique Electronique Automatique**

**LabEx PRIMES**

**Discipline** : Ingénierie pour le vivant

Soutenue publiquement le 08/12/2022, par :

**Arthur GAUTHERON**

---

**Towards quantitative multispectral excitation fluorescence spectroscopy for intraoperative assistance in glioma resection in neurosurgery**

---

Devant le jury composé de :

<b>ABI HAIDAR Darine</b>	Rapporteure
<i>Maître de conférences, Université Paris Diderot</i>	
<b>DA SILVA Anabela</b>	Rapporteure
<i>Directrice de Recherche, CNRS Marseille</i>	
<b>VALDES Pablo A.</b>	Examinateur
<i>Assistant Professor, University of Texas Medical Branch</i>	
<b>PILLONNET Anne</b>	Examinaterice
<i>Professeure des Universités, Université Claude Bernard Lyon 1</i>	
<b>CARMINATI Rémi</b>	Examinateur
<i>Professeur des Universités, ESPCI Paris, Université PSL</i>	
<b>CLERC Raphaël</b>	Examinateur
<i>Professeur des Universités, Université Jean Monnet</i>	
<b>MONTCEL Bruno</b>	Directeur de Thèse
<i>Maître de conférences, Université Claude Bernard Lyon 1</i>	
<b>HEBERT Mathieu</b>	Co-directeur de thèse
<i>Maître de conférences, Université Jean Monnet</i>	
<b>GUYOTAT Jacques</b>	Invité
<i>Praticien Hospitalier, Hospices Civils de Lyon</i>	
<b>SDIKA Michaël</b>	Invité
<i>Ingénieur de Recherche, CNRS Lyon</i>	



# **Université Claude Bernard - Lyon 1**

Président de l'Université  
Président du Conseil Académique  
Vice-Président du Conseil d'Administration  
Vice-Président du Conseil des Études et de la  
Vie Universitaire  
Vice-Président de la Commission de Recherche  
Directeur Général des Services

M. Frédéric FLEURY  
M. Hamda BEN HADID  
M. Didier REVEL  
M. Philippe CHEVALIER  
M. Jean-François MORNEX  
M. Pierre ROLLAND

## **Composantes Santé**

Département de Formation et Centre de  
Recherche en Biologie Humaine  
Faculté d'Odontologie  
Faculté de Médecine et Maïeutique Lyon Sud-  
Charles Mérieux  
Faculté de Médecine Lyon-Est  
Institut des Sciences et Techniques de la  
Réadaptation (ISTR)  
Institut des Sciences Pharmaceutiques et Bi-  
ologiques (ISBP)

Directrice : Mme Anne-Marie SCHOTT  
Doyenne : Mme Dominique SEUX  
Doyenne : Mme Carole BURILLON  
Doyen : M. Gilles RODE  
Directeur : M. Xavier PERROT  
Directrice : Mme Christine VINCIGUERRA

## **Composantes & Départements de Sciences & Technologie**

Département Génie Électrique et des Procédés  
(GEP)  
Département Informatique  
Département Mécanique  
École Supérieure de Chimie, Physique, Élec-  
tronique (CPE Lyon)  
Institut de Science Financière et d'Assurances  
(ISFA)  
Institut National du Professorat et de  
l'Éducation  
Institut Universitaire de Technologie de Lyon  
1  
Observatoire de Lyon  
Polytech Lyon  
UFR Biosciences  
UFR des Sciences et Techniques des Activités  
Physiques et Sportives (STAPS)  
UFR Faculté des Sciences

Directrice : Mme Rosaria FERRIGNO  
Directeur : M. Behzad SHARIAT  
Directeur M. Marc BUFFAT  
Directeur : Gérard PIGNAULT  
Directeur : M. Nicolas LEBOISNE  
Administrateur Provisoire : M. Pierre CHAREYRON  
Directeur : M. Christophe VITON  
Directrice : Mme Isabelle DANIEL  
Directeur : Emmanuel PERRIN  
Administratrice provisoire : Mme Kathrin GIESELER  
Directeur : M. Yannick VANPOULLE  
Directeur : M. Bruno ANDRIOLETTI



# Funding

This work was supported by the LABEX PRIMES (ANR-11-LABX-0063) of Université de Lyon, within the program "Investissements d'Avenir" (ANR-11-IDEX-0007) operated by the French National Research Agency (ANR).







*La leçon d'anatomie du docteur Tulp*, Rembrandt, 1632



# Acknowledgements

Seule une personne reçoit le titre de Docteur à la fin d'une thèse, et pourtant, la réussite des travaux que je vous expose ici fut uniquement possible grâce à un travail d'équipe et un soutien incroyable pendant ces 3 ans. Je veux donc maintenant prendre le temps de remercier tous ceux qui m'ont aidé dans cette aventure et j'espère que chacun de vous, collègues, amis et famille, saura se reconnaître quelque part dans les lignes qui suivent.

Je souhaite commencer cette liste de remerciements en m'adressant à mes encadrants de thèse, grâce à qui j'ai pu mener à bien ce travail.

**Mathieu**, merci de m'avoir encouragé à postuler à cette thèse. Merci aussi pour ton regard bienveillant et efficace, notamment en tant que relecteur d'écrits et de présentations. Merci aussi d'avoir accepté de porter le projet de post-doc qui arrive.

**Bruno**, merci de m'avoir choisi pour mener ces travaux de thèse et de les avoir dirigés ! Ta rigueur et ton exigence scientifique m'ont obligé à creuser toujours plus les différents points bloquants; à être exact et précis dans les résultats que je te présentais.

**Raphaël**, tu n'étais pas officiellement dans l'encadrement, mais un immense merci pour le travail fournit officieusement, et pour ton aide précieuse, ta grande disponibilité dans les périodes houleuses de la thèse et pour ton exigence aussi.

**Jacques**, merci de m'avoir fait découvrir le monde de la neurochirurgie. J'ai vraiment apprécié mon sujet de thèse et je peux même dire qu'il m'a passionné! Et même si la pandémie de COVID ne nous a pas permis de faire autant de mesures au bloc opératoire qu'espéré, j'espère que l'avenir soit plus clément. Merci aussi à **Thiébaud** ainsi qu'aux membres des HCL (anesthésistes, Ibodes, ...) pour les différentes manip' au bloc !

Merci aux membres du jury qui ont lu et évalué ce manuscrit ainsi que ma présentation orale.

Merci à Mesdames da Silva et Abi Haidar pour vos rapports sur mon manuscrit ainsi que vos questions et retours.

Merci aussi à Madame Pillonnet, Monsieur Valdès et Monsieur Carminati pour vos questions.

Merci aux permanents de l'équipe MAGICS et à ceux de la plateforme. Merci Olivier de m'avoir accepté au sein du laboratoire **CREATIS** et merci Hélène de m'avoir accueilli dans l'équipe. Merci Kevin, pour ton écoute et ton sens du service. Merci aux doctorants : Pilar, Charly, Paul, Benoît, Jiqing et aux plus jeunes Antoine, Laura, Antoine. Merci pour vos coups de pouces, merci à toutes les petites mains qui m'ont aidé, au labo ou au bloc, merci pour votre amitié en somme.

Merci aussi aux doctorants d'autres laboratoires : Vincent, Fanny et Alice pour nos discussions scientifiques et la journée "Modèles Optiques".

Merci aux collègues d'enseignement, avec une mention particulière pour toi Kévin pour

le temps passé à m'expliquer, me réexpliquer certains TD. Merci à vous, compagnons et amis du quotidien au laboratoire, de m'avoir permis d'apprendre tant de choses, tant sur le plan scientifique que sur le plan humain !

Merci au **LabEx PRIMES** pour le financement de ces travaux, avec un merci spécial à Jean-Baptiste et Béatrice pour votre aide efficace et sympa ! Merci à toutes celles et ceux qui travaillent dans l'ombre pour m'offrir des conditions matérielles idéales pour réaliser ma thèse. Le travail de l'ombre n'est pas toujours souligné mais vous avez tous contribué à la réussite de ce projet. Ces quelques mots ne représentent pas grand-chose pour résumer toute cette aventure, mais du fond du cœur, MERCI !

Je n'allais pas conclure ses remerciements sans avoir une pensée pour tous ceux qui ont participé à rendre ces dernières années plus agréables.

Merci aux amis de ma plus tendre enfance, de SupOp, aux Scouts, à la Team Bretagne, aux Bibis, et aux gens qu'on aime bien. Merci d'avoir fait le déplacement pour la soutenance et pour votre oreille attentive durant ces trois années, même si ma réalité vous était parfois peu compréhensible.

Merci au soutien familial : mes parents bien sûr, pour les conseils durant la thèse mais surtout pour tout ce que vous m'avez transmis. On ne le dit pas souvent, alors MERCI. Merci aussi à mes frères et sœurs, beaux-frères et belles-sœurs, beaux-parents, grand-parents ainsi qu'aux cousins de vous être intéressés à mon sujet de thèse et à son déroulement.

Merci Marie d'avoir mis au monde le plus beau des bébés au cours de la thèse. **Samuel**, j'espère que tu n'auras pas été traumatisé par tes premiers mois de vie passés avec un papa thésard. Je te remercie finalement pour le bonheur que tu m'apportes quotidiennement et ton regard émerveillé sur le monde qui t'entoure.

Et enfin, merci à toi **Marie**. Merci une fois, merci mille fois ! Notre couple est un roc sur lequel je peux bâtir mes engagements et mes rêves, et c'est une chance incroyable. Merci d'avoir indirectement accepté cette aventure éprouvante qu'a été la thèse ! Merci pour ta patience, ton écoute, et tes encouragements face à mon stress fluctuant tout au long de la thèse.

Bref, merci à vous, famille et amis pour votre présence et pour tout ce que vous m'apportez, je suis gâté et je vous en suis reconnaissant !

Enfin, à toi cher lecteur, chère lectrice, qui ouvre ce manuscrit résumant 3 ans et demi de travail toujours passionnant mais parfois compliqué, j'espère que tu y trouveras tout ce que tu cherches.

# Doctor's Oath

En présence de mes pairs.

Parvenu à l'issue de mon doctorat en ingénierie du vivant, et ayant ainsi pratiqué, dans ma quête du savoir, l'exercice d'une recherche scientifique exigeante, en cultivant la rigueur intellectuelle, la réflexivité éthique et dans le respect des principes de l'intégrité scientifique, je m'engage, pour ce qui dépendra de moi, dans la suite de ma carrière professionnelle quel qu'en soit le secteur ou le domaine d'activité, à maintenir une conduite intègre dans mon rapport au savoir, mes méthodes et mes résultats.

\*\*\*\*\*

*In the presence of my peers.*

*With the completion of my doctorate in life sciences engineering, in my quest for knowledge, I have carried out demanding research, demonstrated intellectual rigour, ethical reflection, and respect for the principles of research integrity. As I pursue my professional career, whatever my chosen field, I pledge, to the greatest of my ability, to continue to maintain integrity in my relationship to knowledge, in my methods and in my results*



# Abstract

Glioma is the most common primary brain tumor and the most aggressive in terms of malignancy and progression. The primary treatment is surgery to completely remove the tumor.

Currently, a problem persists in the accuracy of lesion delineation, particularly because healthy tissue and the tumor margin can look the same during surgery and due to the lack of preoperative imaging modalities specific to infiltration. The 5-ALA-induced protoporphyrin IX (PpIX) fluorescence microscopy technique is now the most effective clinical standard but still suffers from a lack of sensitivity and specificity. At the beginning of this PhD, it had been shown that the spectral complexity of the intraoperative fluorescence emission of PpIX is relevant to identify tumor tissue and in particular the infiltrated component. A first clinical trial on 10 patients was also performed with a prototype of intraoperative fluorescence spectroscopy validated by the ANSM. This study demonstrated the relevance of the two PpIX forms as new biomarkers proposed to identify the tumor margin and its border with healthy tissue. However, several obstacles remained related to the understanding and quantification of these biomarkers.

The present work aims to overcome some of these obstacles through several approaches. On the first hand, because the quantification aspect relies on more or less complex optical models, it looked necessary to verify that some of the assumptions made for relevant optical models are compatible with the studied case. We have highlighted the importance of the value of the internal reflectance of the air-tissue interface in simplistic optical models widely used. Compared to the commonly used internal reflectance values, whose error on the prediction of reflectance and transmittance is about 10%, we have shown that considering an accurate internal reflectance value in simple optical models leads to a reduction of the reflectance and transmittance prediction error to less than 1.0% for translucent media. On the other hand, we proposed a new method to estimate the relative concentration of PpIX fluorescence-related biomarkers. Existing methods suffer from crosstalk on the estimation of PpIX fluorescence-related biomarkers. This crosstalk can be due to the omission or the wrong spectral shape of one or more endogenous fluorophore present in the measured signal. It occurs when the spectrum of the omitted endogenous fluorophore(s) is spectrally close to the PpIX emission spectral range and leads to an overestimation of the PpIX and thus to a "tumor" classification of healthy samples. The method we propose seeks to be free from *a priori* on the endogenous fluorophores present in the measured signal and their respective spectral shape. For this, several fluorescence excitation wavelengths are necessary to transfer the *a priori* in the fluorescence quantum yield of PpIX fluorescence-related biomarkers and to estimate the part of the signal related to endogenous fluorophores, called baseline. Since a closed form solution was found, the computation time was greatly reduced. Finally, this new method is as efficient as the existing models for previously solved cases, but it keeps a specificity equal to 100% compared to the ground truth in cases where the one of existing models drops to 0%.

Finally, we have realized a new intraoperative prototype allowing multi-wavelength excitation and extracting optical properties of biological tissues from spectral diffuse reflectance measurements. Measurements with this new prototype can be corrected from scattering and absorption of biological tissues.



# Résumé

Le gliome est la tumeur cérébrale primaire la plus courante et la plus agressive en termes de malignité et de progression. L'exérèse chirurgicale est le traitement principal pour le retrait de la tumeur. Actuellement, un problème persiste dans la précision de la délimitation des lésions, notamment parce que le tissu sain et la marge tumorale peuvent avoir la même apparence pendant l'opération et en raison du manque de modalités d'imagerie préopératoire spécifiques à l'infiltration tumorale. La microscopie à fluorescence de la protoporphyrine IX (PpIX) induite par le 5-ALA est aujourd'hui la technique clinique la plus efficace, mais elle souffre d'un manque de sensibilité et de spécificité.

Au démarrage de cette thèse, il avait déjà été démontré que la complexité spectrale de l'émission de fluorescence peropératoire de PpIX est pertinente pour identifier le tissu tumoral et en particulier la composante infiltrée. Egalement, un premier essai clinique avait été réalisé sur 10 patients avec un prototype de spectroscopie de fluorescence peropératoire validé par l'ANSM. Cette étude a démontré la pertinence des deux formes de la PpIX comme nouveaux biomarqueurs proposés pour identifier la marge tumorale et sa frontière avec le tissu sain. Cependant, ce travail se heurte à plusieurs obstacles liés à la compréhension et à la quantification des biomarqueurs. Le travail présenté ici vise à surmonter certains de ces obstacles à travers deux approches.

D'une part, la quantification reposant sur des modèles optiques plus ou moins complexes, il semblait pertinent de vérifier que certaines des hypothèses faites dans les modèles simples sont compatibles avec le cas étudié. Nous nous sommes intéressé à l'une d'entre-elles qui concerne la forme de la distribution angulaire de la lumière. Cette hypothèse influe directement sur la valeur d'un paramètre appelé la réflectance interne, c'est-à-dire la réflectance de l'interface air-tissu du côté des tissus. Par rapport aux valeurs de réflectance interne couramment utilisées qui dépendent uniquement de l'indice optique du milieu, et qui peuvent induire une erreur sur la prédiction de la réflectance et de la transmittance d'environ 10 %, nous avons montré que la prise en compte d'une valeur précise de la réflectance interne de l'interface tissu-air, fonction de l'épaisseur du matériau et de ses propriétés optiques, dans les modèles optiques simples conduit à une réduction de l'erreur de prédiction de la réflectance et de la transmittance à moins de 1.0 % pour les milieux translucides.

D'autre part, nous avons proposé une nouvelle méthode pour estimer la contribution des biomarqueurs liés à la fluorescence de la PpIX. En effet, les méthodes actuelles souffrent d'interférences lors de l'estimation des biomarqueurs liés à la fluorescence PpIX. Elles peuvent être dues à l'omission ou à la mauvaise forme spectrale d'un ou plusieurs fluorophores endogènes présents dans le signal mesuré. Ces interférences se produisent lorsque le spectre des fluorophores endogènes omis est spectralement proche de la gamme spectrale d'émission de PpIX et conduit à une surestimation de PpIX et donc à une classification comme "tumeur" des tissus sains. La méthode que nous proposons cherche à s'affranchir des *a priori* sur les fluorophores endogènes présents dans le signal mesuré et leurs formes spectrales respectives. Pour cela, plusieurs longueurs d'onde d'excitation de fluorescence sont nécessaires pour transférer les *a priori* dans le rendement quantique de fluorescence des biomarqueurs liés à la fluorescence de la PpIX et pour estimer la partie du signal liée aux fluorophores endogènes, appelée ligne de base. Comme une solution mathématique explicite a été trouvée, le temps de calcul a été considérablement réduit. Finalement, cette nouvelle méthode est aussi efficace que les modèles existants pour les cas déjà résolus, mais elle conserve une spécificité égale à 100 % par rapport à la vérité terrain dans les cas où celle des modèles existants tombe à 0 %.

Enfin, nous avons réalisé un nouveau prototype peropératoire utilisant une excitation multi-longueurs d'onde et permettant l'extraction des propriétés optiques des tissus biologiques à partir de mesures de réflectance spectrale diffuse. Les mesures effectuées avec ce nouveau prototype peuvent être corrigées de la diffusion et de l'absorption des tissus biologiques.

# Contents

<b>Fundings</b>	v
<b>Doctor's Oath</b>	xi
<b>Abstract</b>	xiii
<b>Contents</b>	xxi
<b>List of Symbols</b>	xxiii
<b>Medical Glossary</b>	xxv
<b>I Introduction</b>	1
<b>1 General Introduction</b>	3
<b>2 Background and issues</b>	7
2.1 The healthy brain and glioma . . . . .	7
2.1.1 Morphology of the healthy brain . . . . .	7
2.1.2 Scale of cell structures (Ultrastructure scale) . . . . .	9
2.1.3 Gliomas . . . . .	9
2.1.4 Description of the Glioma Resection Neurosurgery . . . . .	10
2.1.5 Clinical Issue . . . . .	12
2.2 Basics of light-matter interaction in biological tissues . . . . .	14
2.2.1 Absorption . . . . .	14
2.2.2 Scattering . . . . .	16
2.2.3 Principle of Fluorescence . . . . .	17
2.2.4 Fluorescence of the protoporphyrin IX (PpIX) . . . . .	18
2.2.5 Fluorescence of other endogenous molecules . . . . .	19
2.2.6 Exogenous fluorophores used in neurosurgery: Indocyanine green and fluorescein . . . . .	21
2.2.7 Current techniques of intraoperative assistance for identification of tumor margins and their limitations . . . . .	22
2.3 PpIX fluorescence spectroscopy : one assistive technique under development for use in the operating theater . . . . .	25
2.3.1 Semi-quantitative approach . . . . .	26
2.3.2 Quantitative approach: Theory-based attenuation correction techniques . . . . .	31
2.3.3 Experimental Setups to determine optical properties of tissues . . . . .	35

2.3.4	Example of a diffuse reflectance spectroscopy probe . . . . .	36
2.4	Conclusions . . . . .	38
<b>II</b>	<b>Spectral estimation method of PpIX contributions without <i>a priori</i> on other components by multispectral excitation</b>	<b>41</b>
<b>3</b>	<b>Multi-wavelength models &amp; analytical resolution of the Estimated Baseline model</b>	<b>45</b>
3.1	Physical Model . . . . .	45
3.2	Estimation Model . . . . .	46
3.2.1	Estimated Baseline Model (EB) . . . . .	46
3.2.2	Analytic Resolution of Estimated Baseline Model . . . . .	46
3.2.3	Analytical estimation of the parameters . . . . .	48
3.2.4	Residual calculation and $\gamma$ estimation . . . . .	48
3.3	Conclusion . . . . .	50
<b>4</b>	<b>Performance evaluation of the Estimated Baseline model</b>	<b>51</b>
4.1	Multiple-excitation models for comparison purpose . . . . .	52
4.1.1	Baseline Free Model (BF) . . . . .	52
4.1.2	Gaussian Baseline Model (GB) . . . . .	52
4.2	Digital phantom of fluorescence . . . . .	52
4.3	Sets of Baseline parameters . . . . .	53
4.4	Classification method . . . . .	54
4.5	Errors Measurement . . . . .	56
4.5.1	Estimation Error on $\alpha$ . . . . .	56
4.5.2	Impact of $\alpha^*$ on classification . . . . .	58
4.5.3	Clinical Practice performance on synthesized glioma image . . . . .	62
4.6	Conclusions . . . . .	64
<b>III</b>	<b>Advances in quantitative methods</b>	<b>65</b>
<b>5</b>	<b>Resolution of Radiative Transfer with discrete ordinate method</b>	<b>69</b>
5.1	Introduction . . . . .	69
5.2	Physical quantities in transport theory . . . . .	70
5.2.1	Radiance . . . . .	71
5.2.2	Irradiance, Exitance . . . . .	72
5.2.3	Fresnel angular reflectance and transmittance . . . . .	72
5.2.4	Plane-Parallel geometry . . . . .	73
5.3	Equation of transfer in radiative transport theory . . . . .	74
5.3.1	Derivation of the radiative transfer equation . . . . .	74
5.3.2	Incident radiance and diffuse radiance . . . . .	79
5.4	Solution of the radiative transfer equation by the discrete ordinates method . . . . .	80
5.4.1	Discretization of the radiative transfer equation by the discrete ordinates method . . . . .	81
5.4.2	Boundary conditions for the slab geometry with index-matching interfaces . . . . .	82
5.4.3	Boundary conditions for the semi-infinite plane geometry with index-matching interface . . . . .	84

5.4.4	Boundary conditions for the slab geometry without index-matching interfaces (Fresnel reflections) . . . . .	84
5.4.5	Boundary conditions for the semi-infinite plane geometry without index-matching interface (Fresnel reflections) . . . . .	87
5.4.6	Fluorescent Medium . . . . .	88
5.5	Conclusion . . . . .	92
<b>6</b>	<b>Validation of the RTE solver by comparison with MC and literature</b>	<b>93</b>
6.1	Monte Carlo Method . . . . .	93
6.1.1	Correspondences between Monte-Carlo & radiative transfer equation	94
6.1.2	Media . . . . .	94
6.2	Validation . . . . .	95
6.2.1	Validation metrics . . . . .	95
6.2.2	Non-fluorescent isotropic scattering medium with index-matching interfaces . . . . .	96
6.2.3	Non-fluorescent anisotropic scattering medium with index-matching interfaces . . . . .	97
6.2.4	Non-fluorescent isotropic scattering medium without index-matching interfaces . . . . .	98
6.2.5	Non-fluorescent anisotropic scattering medium without index-matching interfaces . . . . .	99
6.2.6	Literature reference configurations . . . . .	100
6.2.7	Fluorescent media . . . . .	102
6.2.8	Conclusion . . . . .	103
6.3	Comparative study between angular discretization methods . . . . .	104
6.3.1	Isotropic scattering medium with index-matching interfaces . . . . .	104
6.3.2	Anisotropic scattering medium with index-matching interfaces . . . . .	104
6.3.3	Isotropic scattering medium without index-matching interfaces . . . . .	106
6.3.4	Anisotropic scattering medium without index-matching interfaces . . . . .	106
6.3.5	Conclusion . . . . .	107
<b>7</b>	<b>Internal reflectance of the air-medium interfaces</b>	<b>109</b>
7.1	Introduction . . . . .	109
7.2	Reminders about the Kubelka-Munk model . . . . .	110
7.2.1	Description of the object of study . . . . .	111
7.3	Semi-infinite layer: Results and discussion . . . . .	112
7.4	Finite thickness layer (slab): Results and Discussion . . . . .	115
7.4.1	Radiance angular variations and internal reflectances in the case of an isotropic scattering phase function . . . . .	116
7.4.2	Radiance angular variations and internal reflectances in the case of an anisotropic scattering phase function . . . . .	118
7.5	Validity of the 2- and 4-flux models with and without internal reflectances calculated by the Radiative Transfer Equation . . . . .	120
7.6	Conclusion . . . . .	124
<b>IV</b>	<b>Experimental Setup</b>	<b>127</b>
<b>8</b>	<b>A new acquisition system</b>	<b>131</b>
8.1	Specifications of the Experimental System . . . . .	131

8.2	Hardware of block 2 . . . . .	133
8.2.1	Detection system . . . . .	133
8.2.2	Electronic Shutters . . . . .	134
8.2.3	Excitation System . . . . .	135
8.2.4	Microcontroller Board . . . . .	137
8.2.5	Home Made Electronic Shield . . . . .	139
8.3	Optical Probe (block 3) . . . . .	142
8.4	Study of the validity of the probe for brain samples measurements . . . . .	143
8.5	Conclusion . . . . .	144
<b>9</b>	<b>Calibration of the experimental setup</b>	<b>145</b>
9.1	Theoretical ground . . . . .	145
9.2	Experimental Calibration . . . . .	147
9.2.1	Performing diffuse reflectance measurements . . . . .	147
9.2.2	Realization of phantoms . . . . .	148
9.2.3	Calibration Results . . . . .	148
9.3	Discussion and Conclusions . . . . .	150
<b>10</b>	<b>Acquisition software</b>	<b>151</b>
10.1	User Interface Description . . . . .	151
10.2	Software Engineering . . . . .	153
10.3	Acquisition Process & Post-Processing . . . . .	155
10.4	Software Acquisition Parameters File . . . . .	156
10.5	Conclusion . . . . .	158
<b>V</b>	<b>Perspectives and Conclusion</b>	<b>159</b>
<b>11</b>	<b>Perspectives initiated during the PhD</b>	<b>161</b>
11.1	Direct continuation of the PHD . . . . .	161
11.2	Application to Focal Cortical Dysplasia . . . . .	161
11.3	Contribution to the Scan'n'Treat european project : Characterization of the fluorescence dose-effect response of X-PDT nanoparticles . . . . .	162
<b>12</b>	<b>Conclusion</b>	<b>171</b>
<b>Appendix</b>		<b>175</b>
<b>A</b>	<b>Résumé en français</b>	<b>175</b>
A.1	Introduction . . . . .	175
A.2	Méthode d'estimation des concentrations relatives de PpIX par analyse spectrale sous excitation multispectrale sans <i>a priori</i> sur les autres composantes . . . . .	177
A.3	Avancées dans les méthodes quantitatives . . . . .	179
A.4	Système expérimental . . . . .	182
A.5	Perspectives . . . . .	184
A.5.1	Poursuite directe . . . . .	184
A.5.2	Application à la dysplasie corticale focale . . . . .	184

A.6 Contribution au projet européen Scan'n'Treat : Caractérisation de la réponse dose-effet de fluorescence des nanoparticules X-PDT . . . . .	185
A.7 Conclusion . . . . .	187
<b>B Publications and communications</b>	<b>189</b>
<b>Bibliography</b>	<b>220</b>



# List of Symbols and abbreviations

## Abbreviations

5-ALA	5-Aminolevulinic acid
BBB	Blood Brain Barrier
CCD	Charge Coupled Device
CpIII	CoProporphyrin III
DMSO	Dimethyl sulfoxide
DRS	Diffuse Reflectance Spectroscopy
EOR	Extent Of Resection
FGS	Fluorescence Guided Surgery
FIFO	First In First Out
FLAIR	FLuid-Attenuated Inversion Recovery is an MRI sequence described in [ <a href="#">De Coene et al. (1992)</a> ]
FS	Fluorescence Spectroscopy
GBM	Glioblastoma multiform
HGG	High Grade Glioma
ICG	Indo Cyanine Green
I/O	Input/Output
KM	Kubelka-Munk
LGG	Low Grade Glioma
MC	Monte Carlo
MRI	Magnetic Resonance Imaging
MTF	Modulation Transfert Function
NA	Numerical Aperture
NADH	Nicotinamide adenine dinucleotide
NADPH	Nicotinamide adenine dinucleotide phosphate
NaOH	Sodium hydroxide
PiLoT	Plateforme d'Imagerie Multimodale sur LyonTech
PBS	Phosphate Buffered Saline
PCB	Printed Circuit Board
PpIX	Protoporphyrin IX
PSF	Point Spread Function
PWM	Pulse Width Modulation
RTE	Radiative Transfer Equation
SFDI	Spatial Frequency Domain Imaging
SMA	SubMiniature version A
SSOP	Single Snapshot Optical Properties
TTL	Transistor-Transistor Logic
WHO	World Health Organisation



# Medical Glossary

Medical terms followed by an asterisk in this thesis are defined here from the Larousse dictionary.

Anaplastic	Refers to certain neoplasms whose lack of histological differentiation makes it difficult to diagnose the origin. Anaplastic tumors thus present tumor cells that are very different from the initial healthy cells.
Cortex	The outer part that forms the envelope of an organ
Cytonucleic	Relating to the morphological characteristics of the nuclei
Encephalon	Part of the central nervous system and its envelopes contained in the cranium of vertebrates
Endogenous	Qualifies everything that is generated by the organism itself without any external contribution, as opposed to exogenous.
Endothelial	Relating to the endothelium
Endothelium	Thin layer of cells lining the inner surface of blood and lymphatic vessels
Exeresis	Operation consisting in removing an organ, a set of tissues or a foreign body by surgical means
Exogenous	Qualifies everything that is generated by the organism itself with an external contribution, as opposed to endogenous.
Girus	Brain circumvolution
Homeostasis	Process of regulation by which the organism maintains the various constants of the internal environment between the limits of the normal values.
Metabolism	All the complex and unceasing processes of transformation of matter and energy by the cell or the organism.
Mitotic	Relating to mitosis
Mitosis	General mode, rather complex, of division of the cell, characterized by the duplication of all its elements and by their equal distribution in the two daughter cells
Necrosis	Transformation of physico-chemical and chemical order that the living matter is affected by and which leads to its death.
Pericytes	Cells surrounding the small blood vessels of the brain, which play an essential role in the regulation of cerebral blood flow. They also stabilize the vascular network and modulate the inflammatory response.
Resection	Operation consisting in removing an organ, a set of tissues or a foreign body or a foreign body by surgical means
Peroxidase technique	Immunological technique for revealing antigens
Gliosis	Proliferation of glial cells, often to form an astrocytic scar.
Dessication	Action of drying out



# I Introduction

---



# Chapter 1

---

## General Introduction

---

Cancer kills 13% of the world's population and this percentage is constantly increasing [[WHO \(2022\)](#)]. Brain tumors represent only a small proportion of cancers (1% in France) but one third of them are malignant. Gliomas represent half of all brain tumors and are a major public health issue with 308,102 new cases in 2020 according to [[Sung et al. \(2021\)](#)]. They are infiltrating tumors, which makes them difficult to cure. The majority of gliomas are glioblastomas (GBM), a tumor whose patients' life expectancy is barely more than one year [[Yu et al. \(2022\)](#)]. In addition to the malignant nature of some gliomas, their presence can involve various symptoms such as headaches, nausea, but also seizures, personality changes, muscle weakness, and even semi-paralysis or complete paralysis of the patient. Whenever possible, patients with glioma undergo surgery to remove as many tumor cells as possible to reduce the effects of the tumor and prevent its progression. However, in more than 85% of glioblastoma cases, operated patients have a recurrence in the cavity of the previous operation [[Petrecca et al. \(2013\)](#)]. This high risk of recurrence is explained by the infiltrative nature of gliomas and the difficulty of separating tumor infiltrates from healthy tissue in real time during surgery. Moreover, these tumors appear in the glial tissue, which is a supporting tissue of the neurons. Gliomas can therefore be located next to or even in a functional brain area, which complicates removal due to the severe postoperative deficits that resection of these areas can cause.

In the presence of a glioma, the neurosurgeon is confronted with a double challenge: on one hand, they must identify the tumor infiltrations in order to remove a maximum of tumor to increase life expectancy, and on the other hand, they must identify the cerebral functionality in order to limit postoperative damage and thus preserve quality of life. This double identification must be done in real time, once the brain is exposed, because

preoperative imaging techniques do not provide maps that are sufficiently faithful to what the surgeon observes during the operation. Indeed, the opening of the cranium implies a change in pressure and a collapse of the brain, a phenomenon called "brain shift", which generates a shift of up to 3 cm between the arrangement of the brain tissue on the pre-craniectomy image and the one in the operating field [Nabavi *et al.* (2009)].

Various intraoperative techniques already exist to guide the neurosurgeon and have increased the average life expectancy by a few months while improving quality of life. However, those techniques have a number of limitations that need to be overcome today. The emergence of optical techniques has great potential as they are non-invasive, non-ionizing, compatible with real-time analysis and economical [Valdés *et al.* (2016)]. In order to identify tumor infiltration in real time, the exploitation of fluorescence properties of tissues has notably been proven over the last 20 years and protoporphyrin IX (PpIX) fluorescence microscopy is now used in clinical routine [Stummer *et al.* (2000)]. However, fluorescence microscopy does not allow a correct delineation of the glioma, especially because it is an infiltrating tumor. Thus, the method and tools to enable the neurosurgeon to perform a complete resection of the glioma is still an open problem.

A multitude of possibilities are being explored to solve this open issue, including fluorescence spectroscopy. The latter uses spectral information of fluorescent optical biomarkers, also called dyes, and has demonstrated a real interest for the extension of glioma resection [Stummer *et al.* (1998), Sanai *et al.* (2011)b, Lacroix and Toms (2014), Corns *et al.* (2015)]. A real scientific emulation has appeared since, in order to remove this lock that obsesses the biomedical optics community: improving the sensitivity of fluorescence-guided surgery (FGS) to allow a complete resection, which directly implies to be able to distinguish healthy tissues from surrounding infiltrated tissues which often resemble normal tissues. Two of the major approaches of the scientific community are the quantification of biomarkers [Valdés *et al.* (2011), Saager *et al.* (2011), Valdés *et al.* (2012), Valdés *et al.* (2014), Valdés *et al.* (2015), Valdés *et al.* (2016), Sibai *et al.* (2017), Angelo *et al.* (2019)] and the analysis of the spectral shape of the emitted fluorescence [Haidar *et al.* (2015), Montcel *et al.* (2013)b, Montcel *et al.* (2013)a, Alston *et al.* (2018), Alston *et al.* (2019), Black *et al.* (2021)]. Each approach requires a specific acquisition probe, and also specific models to correctly quantify dyes, *resp.* estimate dyes contributions according to their spectral shape.

The work reported in this thesis manuscript is part of this approach, following two distinct approaches that are in line with the approaches described above. The first approach attempts to better estimate the contributions of fluorophores useful for the delineation of the tumor infiltrating zone by an analysis of fluorescence spectra. The other one, more exploratory, aims at modeling the light propagation in tissues, from the source to the detector, in order to eventually obtain robust methods for fluorophore quantification.

This thesis manuscript is structured in such a way as to first recall the general scientific and clinical problems of intraoperative imaging in neurosurgery for total glioma resection

---

(Chapter 2), then to present the main contributions of this thesis in this field through original models for the estimation of fluorophore contributions by multi-spectral analysis of fluorescence (Part II), and advances on quantitative methods (Part III) in particular through the implementation of a radiative transfer model where the internal reflectance of the tissue-air interface is more rigorously analyzed than in many previous studies. Part IV is devoted to the description of the experimental system that has been designed in order to be able to carry out measurements combining quantitative and semi-quantitative methods. The research perspectives that are foreseen for the next years and our contribution to the European Scan'n'treat project are described in Part V, before proposing a more personal conclusion and some thoughts for the future. Finally, I thought it would be useful to summarize my scientific communications in the appendix B.



# Chapter 2

---

## Background and issues

---

In this chapter, we present the context of this work to improve the identification of tumor infiltrations in real time, in the operating room, by quantifying the fluorescence emitted by *protoporphyrin IX* (PpIX) after ingestion of the molecule *5-aminolevulinic acid* (5-ALA) by the patient. Thus, we will start by describing the biological tissues of study, both the healthy brain and the gliomas. Then, we will state the physical basis of interactions between light and biological tissues, especially fluorescence. Finally, we will focus on PpIX fluorescence spectroscopy, one assistance technique under development for use in the operating room.

### 2.1 The healthy brain and glioma

In this section, we describe the two types of tissues analyzed during this work and the clinical problematic which results from it. Concerning the presentation of the tissues, we will only focus on the elements and properties of interest for the thesis.

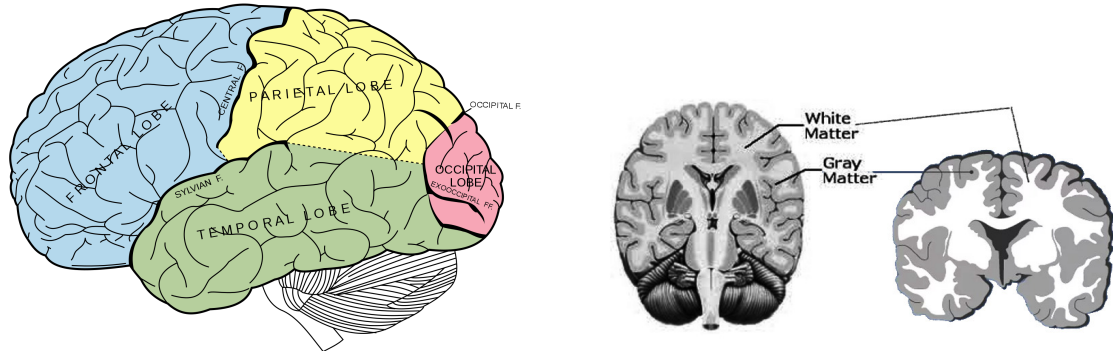
#### 2.1.1 Morphology of the healthy brain

This section contains the structure and properties of the healthy tissue. The brain is schematically separated into two hemispheres, right and left. Each is further subdivided into 4 lobes and gyri<sup>\*1</sup> individualized by grooves, visible in Figure 2.1a. A functional cartography based on an organization into areas dedicated to specific functions was sketched by Gall and confirmed by Broca in the 19<sup>th</sup> century [[Saban \(2002\)](#)]. This structuration

---

<sup>1</sup>Words followed by an asterisk are defined in the medical glossary on page xxv.

is currently being questioned and a network organization is now being suggested [Duffau (2018)]. The functional cartography requires awake patient surgery to avoid permanent neurological damage and increase return-to-work capacities [Duffau (2022)].



(a) Principal fissures and lobes of the cerebrum viewed laterally.(Extracted from Gray's Anatomy [Gray (1878)])

(b) Cross-section of the brain.(Extracted from Neuranaatomy [Mercadante and Tadi (2022)])

Figure 2.1

Represented in Figure 2.2, the brain is surrounded by various tissues. First, we observe protective envelopes, the meninges, composed of 3 layers: the dura mater (adhering to the endocranum\*), the arachnoid and the pia mater (adhering to the cortex). Between the arachnoid and the pia mater is the cerebrospinal fluid, a liquid composed of 99% water which plays a role in maintaining the stability of the intracranial pressures and the cellular homeostasis\* of the brain. Surrounding these envelopes are the cranium (bone and periosteum), the temporal and occipital muscles (not shown in Figure 2.2) and the skin.

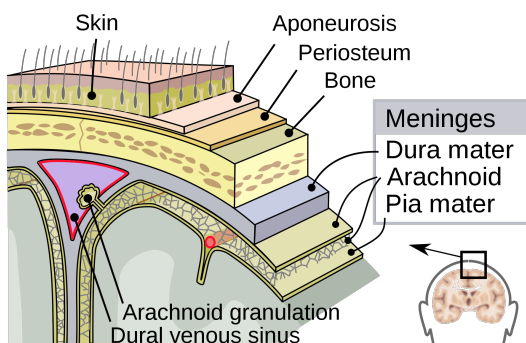


Figure 2.2: Protective envelopes of the brain (image from the SEER Development Team of National Institute of Health).

During surgery, these tissues are incised to access the brain. The opening of the meningeal cavity leads to a decrease in intracranial pressure due to the leakage of cerebrospinal fluid, and therefore to a displacement of the brain tissue. This phenomenon, called "brain shift", causes a shift between the location of anatomical structures or the

limits of a tumor visualized intraoperatively and their location on preoperative imaging. This shift can be up to 3 centimeters [[Nabavi et al. \(2001\)](#)].

### 2.1.2 Scale of cell structures (Ultrastructure scale)

The brain contains several hundred billion cells, divided into two categories: *neurons* and *glial cells*. These cells are located in the peripheral *grey matter*, also called the cerebral cortex, and in the subcortical *white matter*. The white and grey matters are shown in Figure 2.1b. Neurons are composed of a cell body located in the cortex, where information is processed, and an axon located in the white matter, which transmits nerve impulses between the cortex and various structures of the brain\*. Nerve impulses are propagated within neurons by changes in electrical potential. At the synapses at the end of the axons, each neuron communicates with an average of 10,000 others via physico-chemical processes. Glial cells form the support tissue of neurons, ensuring in particular the cerebral metabolism\*. They are mixed with neurons and are five to ten times more numerous than neurons in the cortex [[Azevedo et al. \(2009\)](#)]. This interconnection explains the complexity of removing the associated tumors, e.g., gliomas. These glial cells can be divided into two groups: *microglia* and *macrogliia*. Microglia is composed of cells involved in the immune defense of the brain (macrophage and other inflammatory cells); macrogliia is composed of oligodendrocytes and astrocytes. Oligodendrocytes are responsible for the formation of the myelin sheath that surrounds the axons, which increases the speed and frequency of nerve impulses. The associated tumors are oligodendrogiomas. Astrocytes provide nutrition to neurons and regulate the extracellular environment (being located between neurons and the vascular system). The tumor associated with these cells is the astrocytoma.

Astrocytes, together with pericytes\* and endothelial cells, form the *Blood Brain Barrier* (BBB). This barrier is a selective physiological filter that protects the brain from attack by external elements. This filter allows only the nutrients necessary for brain function to pass through and the elimination of waste products [[Janzer \(1993\)](#)]. Many active molecules cannot cross this BBB, and it would seem that the 5-ALA molecule has difficulty crossing it in healthy tissue. However, the presence of a high-grade glioma implies a rupture of this barrier, which allows the passive passage of some molecules that are normally blocked, such as gadolinium (a marker used in MRI to identify these tumors), chemotherapy molecules, 5-ALA at higher doses [[Novotny and Stummer \(2003\)](#)] or fluorescein. For information, the use of focused ultrasound sonication (FUS) combined with intravascular microbubbles allows bypassing the BBB and improving drug delivery in the CNS [[Dasgupta et al. \(2016\)](#)].

### 2.1.3 Gliomas

Gliomas represent 50% of primary brain tumors. Their degree of malignancy, and thereby their consequences for the patient, varies a lot. The origin of these tumors is unknown, although searches for genetic mutations are ongoing [[Chen et al. \(2020\)](#), [Louis](#)

*et al.* (2016), Marumoto and Saya (2012)] and some environmental factors have been claimed. In 2007, the World Health Organization (WHO) proposed a classification of brain tumors based on histological criteria [Louis *et al.* (2007)] and then improved this classification in 2016 by considering molecular criteria in addition to histology [Louis *et al.* (2016)]. The purpose of this classification is to better predict the prognosis of these tumors and thus improve the therapeutic management of patients by offering an adapted protocol. This classification divides gliomas into four grades, according to their malignancy level: grade I is well circumscribed and curable by surgery, grade II (benign glioma) is a diffuse tumor originating from astrocytes or oligodendrocytes, grade III is derived from the same cells that have acquired malignant properties, and grade IV or *glioblastoma multiforme* (GBM) is derived from an undifferentiated cell (primary glioblastoma) or from the malignant degeneration of a grade II or grade III glioma (secondary glioblastoma) [Louis *et al.* (2016)]. However, in our study as in many other ones, we will separate gliomas into two classes: on the one hand, *High Grade Gliomas* (HGG) of grade IV (GBM) or grade III and on the other hand, *Low Grade Gliomas* (LGG) of grades I and II.

Grade II gliomas are considered to be histologically benign but can be described as pre-cancerous. They appear in younger patients (around 40 years old versus 60 years old for GBM) and are intensively monitored since they almost always transform into malignant gliomas after 5 to 10 years [Gilbert and Lang (2007)]. Moreover, they are very diffuse tumors whose boundaries are difficult to specify by current imaging techniques [Fouke *et al.* (2015), Pouratian and Schiff (2010), Prabhu *et al.* (2010), Sanai *et al.* (2011)a].

GBMs are the most common brain tumors, representing 80% of gliomas. They are also the most malignant: the life expectancy of a patient with a GBM does not exceed 1.5 years, with a 5-year survival rate of less than 10%. These tumors occur at any age but preferentially in the elderly, which raises the question of the risk of surgery. In view of their high incidence and low survival rate, many studies are particularly interested in these tumors, as evidenced, by the substantial number of recent literature studies [Acerbi *et al.* (2014), Kubben *et al.* (2011), Leroy *et al.* (2015), Li *et al.* (2014), Su *et al.* (2014)] and the increasing number of publications related to this topic (refer Fig. 2.3).

In addition to the already stated BBB disruption, the presence of this tumor alters other properties of the tissue, such as its pH [Estrella *et al.* (2013)], vascularization [Khalfaoui-Bendriss (2010)], cell appearance and density, or the light absorption and emission properties of the tissue. The different assistance techniques therefore use changes of one of these different properties to try to discriminate healthy tissue from tumor.

#### 2.1.4 Description of the Glioma Resection Neurosurgery

Surgery is the key component, whether in the context of resection or biopsy (EANO recommendations [Weller *et al.* (2014)]). Neurosurgery specializes in surgery of the central and peripheral nervous system. The neurosurgeon opens a part of the skull to see the

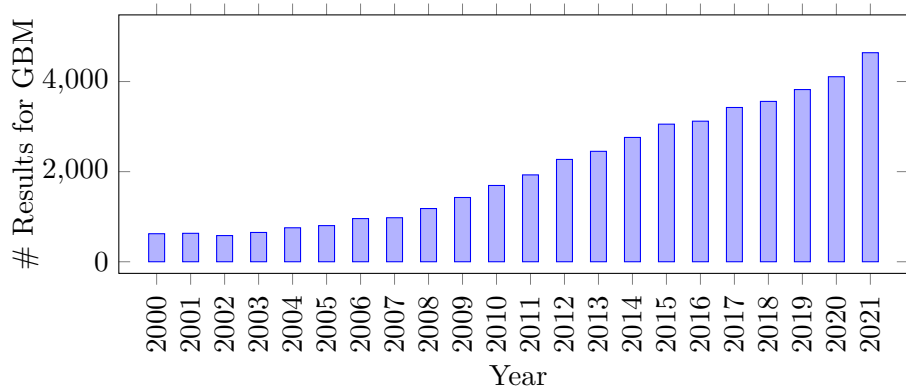


Figure 2.3: Number of publications related to GBM depending on the year from 2000 to 2021. (data taken from PubMed)

brain. In case of resection neurosurgery, special tools are used to cut through the tumor and remove it. After surgery, the skull is sewn or stapled back into place, along with the skin. The scheme in Figure 2.4 describes the interventional context. This figure shows the

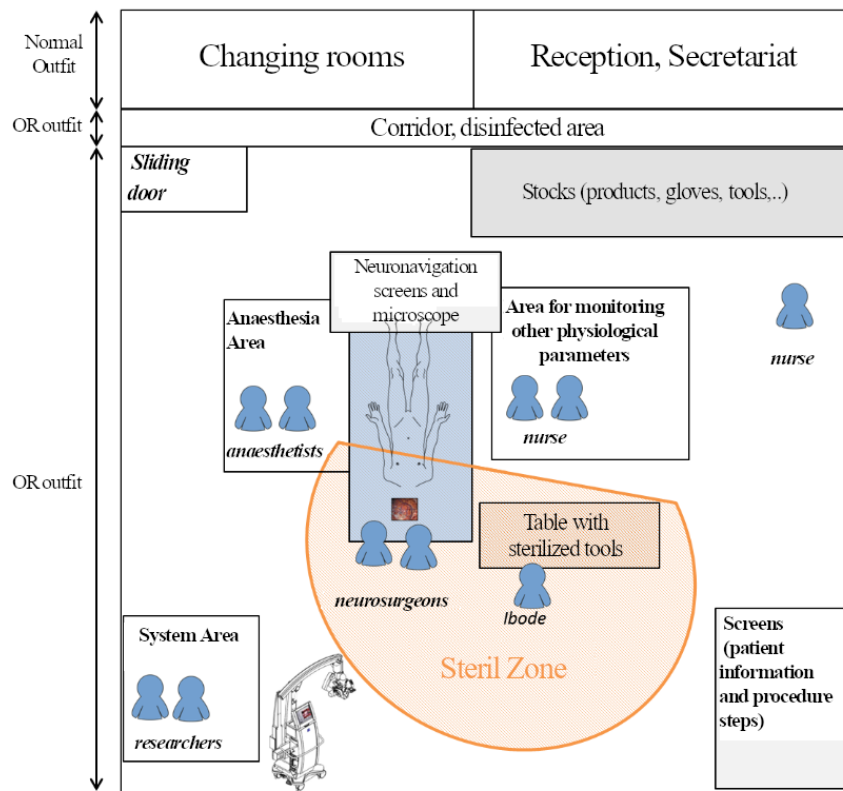


Figure 2.4: Schematic of the operating room. In orange, the sterile area, in blue the people present and in grey the areas occupied by tools (operating microscope, screens, neuronavigation system, stocks...) The space dedicated to the prototype is in the disinfected area. (adapted from [Alston (2017)])

sterile area (hatched in orange), in which the different actors (neurosurgeons, OR-nurses,

patient, ...) of the surgery take place. We cannot access the latter because it is mandatory to wear a sterilized outfit, thus we have to stay in the disinfected area. The rest of the diagram describes the layout of the room and the disinfected area. As the disposable area for our research is small, we notice the important need for a compact and transportable device. In addition, it is common for the patient to be under hypnosis for the surgery. Therefore, it is also important that our system is as quiet as possible so as not to influence the patient's hypnosis.

### 2.1.5 Clinical Issue

The particularity of gliomas is their infiltrating characteristic. This makes them difficult to resect using a microscope because part of the infiltration is invisible by current imaging techniques and therefore by the neurosurgeon. Figure 2.5 presents the concentration of tumor cells according to the distance to the visible area on MRI for high grade astrocytomas (Grade III). We observe in this figure the presence of tumor cells more than 4 cm from the MRI contrast. Real-time identification of these cells in the operating room is therefore essential to improve excision and prevent recurrence.

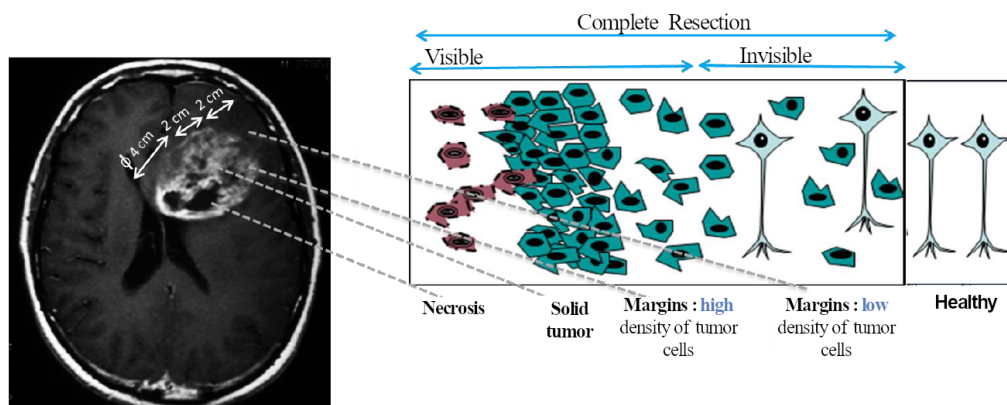


Figure 2.5: Modeling infiltrations of high-grade gliomas (translated from [[Alston \(2017\)](#)])

The goal of this thesis is to improve PpIX fluorescence spectroscopy which is a technique to assist in the visualization of tumor cells in low-density tissues in order to maximize glioma resection while preserving as much as possible the healthy functional tissues around. The underlying assumption is that maximizing resection will increase the life expectancy and quality of life of the patient. It is relevant to ask whether maximizing the *extent of resection* (EOR) actually increases survival. This question was controversial in the 1990s [[Kreth et al. \(1999\)](#), [Nitta and Sato \(1995\)](#), [Quigley and Maroon \(1991\)](#)], because of the absence of a prospective randomized study, which is difficult to design for obvious ethical reasons. However, in 2003, a research team did [[Vuorinen et al. \(2003\)](#)] a randomized study with a small number of patients comparing biopsy to surgical resection in patients over 65 years of age, the median survival was 171 days in the resection group, compared with 85 days in the biopsy group ( $p=0.035$ ). These results are consistent with two other randomized

studies for which this was not the primary objective [Stummer *et al.* (2008), Stupp *et al.* (2005)] and many other non-randomized studies, e.g. [Sanai and Berger (2008)].

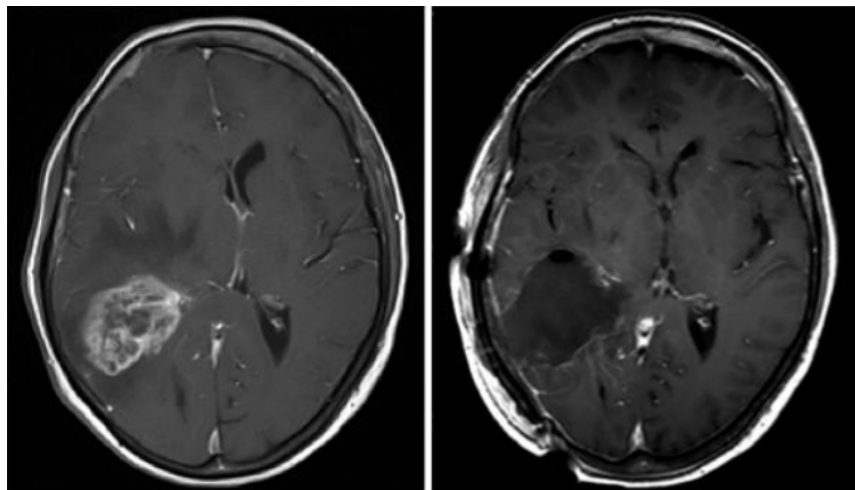


Figure 2.6: Pre-operative MRI showing a high-grade glioma located in associative areas and ventricular crossroad. On the right, early post-operative control (<72h) with no more contrast enhancing tumor (taken from [Dupont *et al.* (2016)]).

On the other hand, the oncological interest of a complete excision is still debated, particularly as it is currently defined by the absence of residual contrast on immediate postoperative MRI, which must be performed within 48 to 72 hours after surgery (Fig. 2.6). Indeed, the surgeon's subjective impression is not reliable enough [Menei *et al.* (2005)], but it is also illusory to resect all the tumor cells according to this criterion because the tumor infiltration extends beyond the MRI contrast.

Thus, in the literature, the term "complete" is contrasted with "subtotal" (98% of contrast) and "partial" (< 98% of resected contrast) resection. Concluding on the "threshold" value of maximizing excision at which there is an oncological benefit (98% for [Lacroix *et al.* (2001)], 78% for [Sanai *et al.* (2011)b], 95% for [Chaichana *et al.* (2014)]) is difficult in particular due to the amount of criteria correlated with EOR that also influence survival rate, such as the age of the patient, the location of the tumor or the degree of necrosis. The arguments against excision are the cost, the risk of postoperative damage and the stress induced to the patient. This controversy was resolved starting in the 2000s, when the value of surgery was demonstrated, both to remove as much tumor as possible and to favor adjuvant therapy thereafter in grades III and IV [Chaichana *et al.* (2014), Lacroix and Toms (2014), Lacroix *et al.* (2001), Sanai *et al.* (2011)b, Stupp *et al.* (2005)]. Recently, Li's study of 1229 patients with GBM proved the value of resection beyond tumor contrast on MRI [Li *et al.* (2016)]. Nowadays, all studies agree to maximize resection when possible, i.e., when brain functionality is not threatened. Moreover, recent studies like [Skardelly *et al.* (2021)], demonstrated the correlation between the overall survival of patient and the residual tumor volume after surgery; the lower the residual tumor volume the better

the overall survival for the patient.

Nonetheless, a standard treatment protocol is clearly established for GBM since 2005: the Stupp protocol. This protocol involves surgery when possible, followed, always if possible, by radio- and/or chemotherapy [[Stupp et al. \(2005\)](#)]. When surgery is not possible or not desired, a biopsy can be performed to identify the grade of the tumor in order to classify it according to the WHO grades and adapt the treatment. If necessary, a brain function identification is performed during the operation in order to preserve functional areas. For an in-depth presentation of optical methods for the identification of brain functionality, the interested reader can for example go to the PhD dissertation of Charly Caredda [[Caredda \(2020\)](#)]. This section contains only glioma properties that are relevant for our work. The curious reader can get a presentation of other brain tumors and extended description of glioma properties in the first chapter of Leh's PhD dissertation [[Leh \(2011\)](#)].

## 2.2 Basics of light-matter interaction in biological tissues

Since the resection must be as complete as possible, but remain extremely limited, the delineation of the infiltrating zone is very important and yet delicate. We will see later that optical techniques offer advantages for this task. But to understand them, it is important to introduce some notions about the properties of biological tissues in relation to light.

We will present the basics of light-matter interaction of biological tissues. We will begin by presenting the *absorption* and *scattering* of light, phenomena that occur regardless of the light source and the tissue. We will then present the phenomenon of *fluorescence*, which occurs only when photons arrive on certain atoms or molecules so called *fluorophores*.

### 2.2.1 Absorption

Light absorption occurs when the energy of an incident photon matches an electronic transition of a chromophore, which, in medical biology, is a molecule capable of absorbing radiation. This energy is then mainly dissipated in the tissues as heat. Each chromophore can be modeled by a sphere of a size proportional to its absorbance to which an effective absorption cross-section  $\sigma_a$  is associated. The absorption coefficient  $\mu_a$  of a pure compound is expressed from the absorbing properties of each of the absorbing centers, which are characterized by an effective absorption cross section  $\sigma_a$ , in  $\text{mm}^2$ . With  $\rho$  the density of absorbing centers in  $\text{mm}^{-3}$ , we thus have:

$$\mu_a = \rho\sigma_a. \quad [\text{mm}^{-1}] \quad (2.1)$$

As described in [[Duncan \(1940\)](#)], if the non-diffusing medium is composed of  $N$  different absorbers, the absorption coefficient of the mixture,  $\mu_a$ , is the sum of the absorption

coefficient of each pure component  $\mu_{a,i}$ , weighted by their respective volumic fraction  $\rho_i$ :

$$\mu_a = \sum_{i=1}^N \rho_i \mu_{a,i}, \text{ with } \sum_{i=1}^N \rho_i = 1. \quad (2.2)$$

When light propagates in a homogeneous absorbing non-scattering medium, it is attenuated exponentially as a function of the traveled distance and a spectral absorption coefficient  $\mu_a(\lambda)$ . This phenomenon is known as *Bouguer's law*, named after the same French scientist Pierre Bouguer [[Simonot and Boulenguez \(2019\)](#)].

By studying colored liquids in 1852 [[Beer \(1852\)](#)], the German scientist August Beer (1825-1863) concluded that by changing the concentration of a dye, the absorption coefficient is changed in the same proportion. This is the Beer's law, Lambert's law or *Beer-Lambert's law*, which links the flux  $F$  at the depth  $z$  with the incident flux  $F_0$  as follows:

$$F(z) = F_0 e^{-\mu_a z}. \quad [W] \quad (2.3)$$

The *transmittance* of a layer of thickness  $h$  is therefore:

$$t = e^{-\mu_a h} = \frac{F(h)}{F_0} \quad (2.4)$$

Note that a change of  $\mu_a$  or a change of the layer thickness to the same extent have the same consequence of the layer's transmittance. Without scattering, the product  $\mu_a \cdot h$  is sometimes considered as one parameter, called *optical thickness*. Thus, a change in dye concentration has a similar effect to a change in layer thickness.

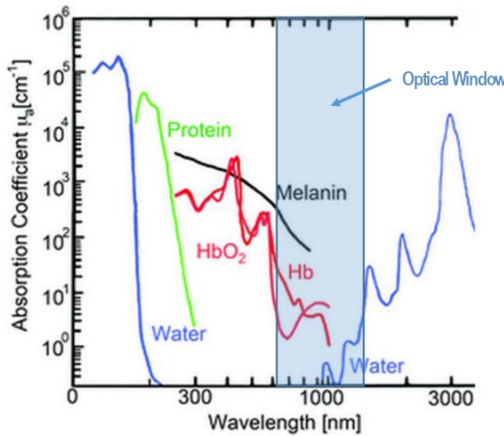


Figure 2.7: Absorption spectra of the main components of biological tissues: water, melanin, protein, hemoglobin (Hb), oxyhemoglobin ( $\text{HbO}_2$ ). The quantity given as a function of wavelength is the absorption coefficient  $\mu_a$ . Extracted and translated from [[Ogien \(2017\)](#)]

Coming back to the biological tissues, the main absorbers are presented in Figure 2.7. We observe on this Figure 2.7 that the 600-1000 nm spectral domain is where the

absorbance of tissues is the weakest, with notably a very limited absorbance by water. This domain is called the "optical window" or "therapeutic window" and is the working area of many techniques referred to as near-infrared techniques [[Scholkmann et al. \(2014\)](#)].

In the case of working with PpIX, the latter having absorption properties towards 405 nm and emission of fluorescence in the spectral band 600-800 nm, we will focus on these spectral bands hereinafter.

### 2.2.2 Scattering

The scattering of light is due to changes or fluctuations of the refractive index of media. The refractive index of a medium is defined as the ratio between the speed of light in a vacuum and the speed of light in the medium it passes through. Please note that, as for absorption, we define the *scattering coefficient*  $\mu_s$  for a tissue as a linear combination of the product of the density of scatterers and their respective scattering cross-sections. The inverse of this coefficient represents the distance that a photon can travel on average while having a probability  $1/e$  to be scattered. In the case where the medium is slightly scattering, the attenuation of a directional light beam follows a similar exponential attenuation as the one described by the Beer-Lambert law:

$$F(z) = F_0 e^{-\mu_e z}. \quad [W] \quad (2.5)$$

where  $\mu_e = \mu_a + \mu_s$  is the *extinction coefficient*, sum of the absorption and scattering coefficients. The notion of optical thickness stands also for absorbing and scattering media. Because the measured attenuation of light depends a lot on the detector and transmitter geometry, and the scattering and absorption properties of tissues, Delpy *et al.* in [[Delpy et al. \(1988\)](#)] suggested to use the *modified Beer-Lambert law* defined as :

$$\ln \left( \frac{F}{F_0} \right) = \mu_a L + G \quad (2.6)$$

with  $F$  the detected light flux and  $F_0$  the incident flux.  $G$  is a coefficient that depends on the geometry of the tissue and the system and  $L$  (in mm) is the length of the average optical path traveled by the photons in the medium. The optical path depends on the tissue probed, it can be calculated or estimated.  $\mu_a$  is the absorption coefficient of the tissue.

Light scattering means that the propagation direction of light is modified. Different models, called *phase function*, translate this phenomenon of elastic scattering, depending on the size of the scattering particles (Mie scattering, Rayleigh scattering). Scattering is said "isotropic" when light goes equivalently in every direction. But scattering is generally not isotropic. An anisotropy factor  $g$  is introduced, which varies from -1 for predominantly backward scattering, to 1 for predominantly forward scattering, through 0 for isotropic

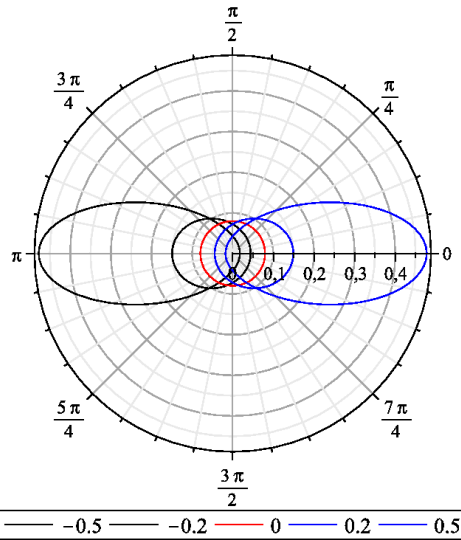


Figure 2.8: Henyey-Greenstein phase function [Henyey and Greenstein (1941)] for various values of the anisotropy parameter  $g$ . The incident radiation arrives from the left. (Wikimedia)

scattering, i.e., uniform over all directions. Defining  $\Theta$  as the angle between the incident- and the scattered direction of a photon, the anisotropy factor is:

$$g = \frac{1}{4\pi} \int_{4\pi} p(\Theta) \cos(\Theta) d\Theta \quad (2.7)$$

where  $p$  is the scattering phase function. In this thesis, we will use the Henyey-Greenstein scattering phase function, plotted for various values of  $g$  in Figure 2.8, inside our model; a detailed presentation of this is made in Chapter 5. The product  $\mu'_s = \mu_s(1 - g)$  is called *reduced scattering coefficient*.

### 2.2.3 Principle of Fluorescence

Fluorescence is one of the properties of the electronic cloud of certain molecules which, absorbing an incident photon, pass from the energetic rest state to an excited state. In order to return to the rest state, different phenomena are possible, including fluorescence. Figure 2.9 shows the Jablonski diagram, illustrating the different phenomena of return to the fundamental state after absorption of an incident photon, by linear processes. The fluorescent molecule absorbs the energy of an incident photon, which makes its electrons pass from the rest state  $S_0$  to an excited state  $S_1$  or  $S_2$  for example. After a step of internal reconversion of the captured energy, the return to the equilibrium of the electrons of the molecule is carried out either by a non radiative release of energy, or by an emission of less energetic photons, thus of wavelength larger than the initially absorbed photon. This phenomenon of light re-emission is called *fluorescence* if the excited molecule was in a

singlet state, or *phosphorescence* if the excited molecule was in a triplet state. The singlet or triplet state depends on the spins of the electrons of the molecule. The fluorescence emission is faster than the phosphorescence emission. The energy required to excite a molecule depends on its energy levels. The absorption of a photon at the frequency  $\nu$  by a molecule is governed by the relationship  $E = h\nu$  where  $E$  is the energy required,  $h$  the Planck constant and  $\nu$  the frequency of the incident photon. An absorption spectrum allows to identify the optimal wavelengths to excite a molecule. For some fluorescent molecules, including porphyrins, the Soret band is defined as the UV wavelength where the absorption is at its maximum.

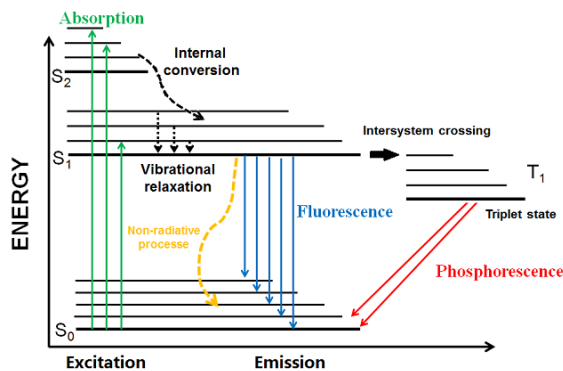


Figure 2.9: Jablonski diagram illustrating the phenomena of fluorescence and phosphorescence

Different fluorescence properties characterize a fluorophore. The quantum yield  $\eta$  of a fluorescent molecule is defined as the number of photons emitted over the number of photons absorbed. The extinction coefficient reveals the probability of absorption of photons by a molecule per unit distance. The *fluorescence spectrum* emitted by a molecule represents the number of photons emitted as a function of their wavelength and its shape is often independent of the excitation source. In order to determine the presence of a molecule in a sample, several parameters can be studied. In the Part II we will use results of a previous study which characterize the fluorescence of PpIX under two-photon excitation [[Jonin et al. \(2020\)](#)]. This spectrum is specific to a molecule and the fluorescence spectrum of a tissue can be considered as the sum of the fluorescence spectra of each of its components, weighted by their properties (quantum yield, extinction coefficient, concentration, absorption...). The study of the fluorescence spectra of biological tissues allows us to identify their properties [[Patterson and Pogue \(1994\)](#)], as we will present later.

## 2.2.4 Fluorescence of the protoporphyrin IX (PpIX)

The fluorophore of interest in this thesis is PpIX. PpIX is a member of the porphyrin family which are precursors of the *heme molecule*. The heme biosynthetic cycle is presented in Figure 2.10 and we observe that PpIX is the last element of the cycle before heme. We also observe that the 5-ALA molecule is a natural precursor of PpIX, present at the

beginning of the cycle. In this cycle, the transformation from one element to the other is done by a succession of enzymatic actions, sometimes in the mitochondria, sometimes in the cytoplasm of the cell. For more readability, the enzymes are not presented on the graph, except the ferrochelatase, which allows the transformation of PpIX into heme. Note further that a deficiency in any of these steps causes a disease called porphyria, and various works use porphyrin fluorescence to diagnose these diseases [Lang *et al.* (2015)].

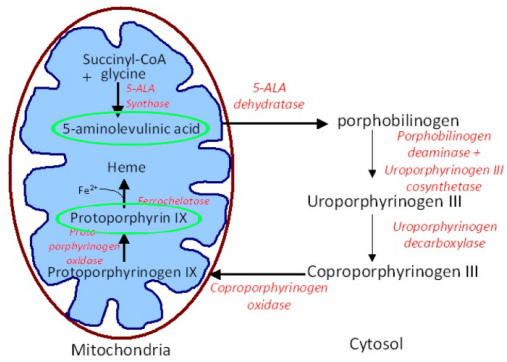


Figure 2.10: Cycle of heme biosynthesis in a human cell from 5-ALA. Enzymes are written in red and products are black. Circled in green, the two molecules of interest in the thesis. (adapted from [Olivo *et al.* (2011)])

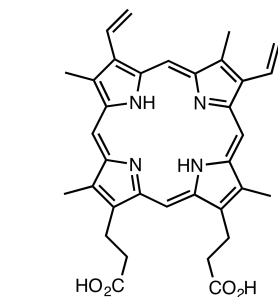


Figure 2.11: Chemical structure of PpIX

Figure 2.11 shows the structure of PpIX. We observe the presence of a ring in the middle of which atoms such as Fe, Zn or Mn can be linked. The association with these atoms creates metallo-porphyrins and modifies the properties of PpIX such as its fluorescence emission spectrum. [Corwin *et al.* (1968), Richter and Rienits (1980)].

PpIX has the particularity of accumulating in the cells of various tumors, notably glioblastomas, when it is brought in excess by exogenous way. This makes it possible to visualize them by various imaging techniques. The cause of this accumulation of PpIX in HGG tumor cells is not yet well established [Collaud *et al.* (2004)] but the two main hypotheses are the rupture of the BBB allowing 5-ALA to enter the tumor tissues and to be synthesized into PpIX and an enzymatic deficiency preventing the transformation of PpIX into heme [Dailey and Smith (1984)]. The deficient enzyme is ferrochelatase, noted in Figure 2.10. Thus, from a practical standpoint, the patient ingests 5-ALA (not PpIX) a few hours before surgery. The latter crosses the BBB and is then transformed into PpIX, which accumulates in the tumor cells.

## 2.2.5 Fluorescence of other endogenous molecules

Many other endogenous molecules can fluoresce, especially in biological tissues. Figure 2.12 adapted from [Leh (2011)] shows the absorption (top) and emission (bottom) spectra of these molecules. To excite PpIX, Figure 2.12 shows us that, like all porphyrins, excitation around 405 nm in the blue part of the visible spectrum at the edge of the ultraviolet range is optimal. This is confirmed by various studies cited in this manuscript.

Furthermore, the detection of the spectrum emitted by PpIX is performed in the 600-800 nm spectral band approximately.

According to Figure 2.12, other endogenous fluorophores also excited in the blue at the UV limit are NADH (reduced Nicotinamide Adenine Dinucleotide), flavins, lipopigments and other porphyrins. Elastin is also excited at 380-400 nm but this protein is not very present in the brain [[Neuman and Logan \(1950\)](#)], so we will not present it here.

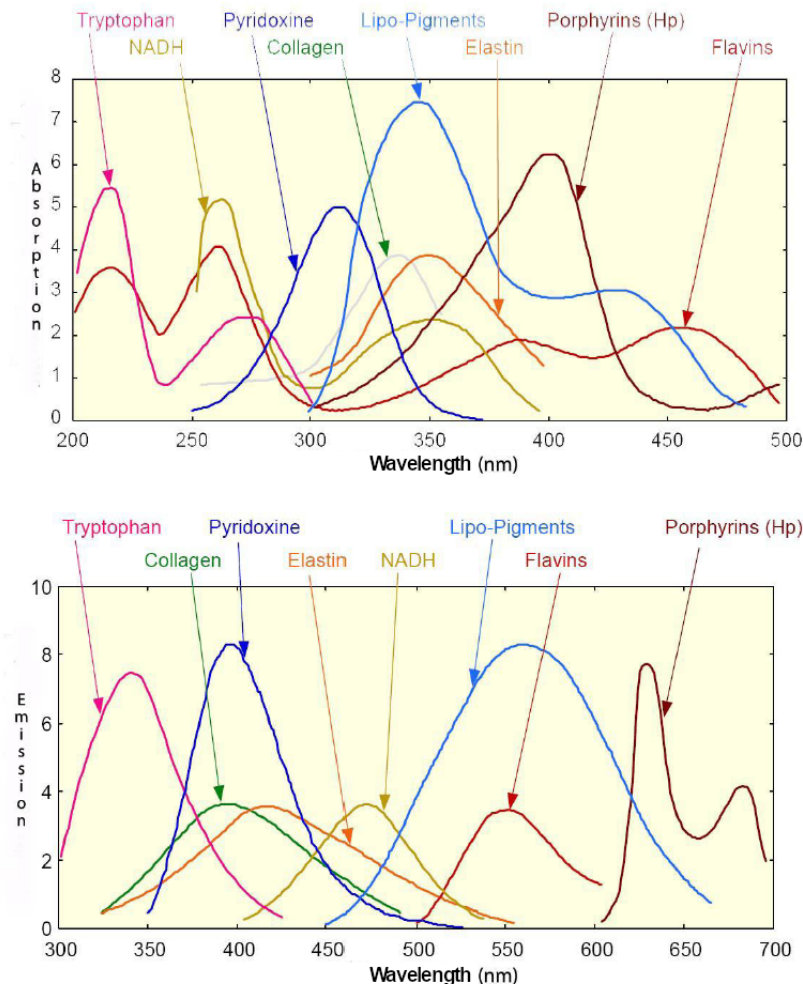


Figure 2.12: Absorption (top) and emission (bottom) spectra of different endogenous fluorophores. Adapted from [[Leh \(2011\)](#)].

NADH and flavins are proteins involved in cellular energy production. The amount of NADH is decreased in tumor cells because energy production is altered. Thus, the detection of its fluorescence intensity is an indication of the presence or absence of tumor cells, with a decrease in intensity of up to 25% [[Croce et al. \(2003\)](#)]. According to Figure 2.12, NADH can be excited around 260 nm but also around 340 nm and the emitted fluorescence is in the spectral band that we detect, after 450 nm. Similarly for flavins which are globally excited in a wide range of wavelengths, with however a peak of absorption a little

below 400 nm. These proteins emit in the 500-750 nm spectral band, thus overlapping with the spectrum emitted by PpIX.

Lipopigments are a group of lipid derivatives, consisting of an autofluorescent pigment and a lipid component. The amount of lipopigments increases with age [[Porta \(2002\)](#), [Jolly et al. \(2002\)](#)], so its relative contribution in the total fluorescence signal is correlated with the age of the patient. From Figure 2.12, the fluorescence properties of lipopigments are close to those of PpIX (with strong absorption around 400 nm and emission centered around 570 nm).

Among the porphyrins, besides PpIX, we also consider uroporphyrin III (UpIII) and coproporphyrin III (CpIII). These fluorescent molecules are precursors of PpIX visible on the heme biosynthesis cycle in Figure 2.10. Their concentration in brain tissue is therefore likely increased during excision as the patient ingests 5-ALA. However, studies mainly suggest an accumulation of PpIX, with a 50 times higher ratio of accumulation in HGG compared to healthy tissue [[Collaud et al. \(2004\)](#), [Johansson et al. \(2010\)](#)]. In contrast to PpIX, both porphyrins are hydrophilic [[Dietel et al. \(2007\)](#)]. Their absorption spectrum is centered around the 380-400 nm spectral band and their emission spectrum looks like the spectrum name Hp in Figure 2.12, i.e. a double hump over the 600-750 nm spectral band, with a main peak around 620 nm and a secondary hump around 680 nm [[Dietel et al. \(2007\)](#)].

The study of endogenous fluorescence, also called "autofluorescence", is a tool to discriminate tumor tissues from healthy tissues, as shown by Croce, Toms or Butte in their in vivo studies [[Butte et al. \(2011\)](#), [Croce et al. \(2003\)](#), [Toms et al. \(2005\)](#)] and as studied by many teams ex vivo [[Pascu et al. \(2009\)](#), [Yong et al. \(2006\)](#), [Zanello et al. \(2017\)](#)]. In our work, we study tissue fluorescence after 5-ALA ingestion, thus in a configuration where the relative concentration of PpIX, also called *contribution of PpIX* in fluorescence, is dominant in gliomas and increased in healthy tissue.

Moreover, the fluorescence of 5-ALA derivatives is also used in photodynamic therapy (PDT), and PpIX is also widely used here. This technique is based on the accumulation of a photosensitizer (here a 5-ALA derivative) in cancer cells. The tissue is irradiated at a wavelength suitable for the photosensitizer, which causes a reaction between oxygen, light and tissue and kills the cell [[Krammer and Plaetzer \(2008\)](#)]. A pilot study was proposed in 2007 in neurosurgery [[Beck et al. \(2007\)](#)], but this technique is mostly used in dermatology.

## 2.2.6 Exogenous fluorophores used in neurosurgery: Indocyanine green and fluorescein

In addition to 5-ALA-induced PpIX fluorescence, other fluorophores are available and being studied to guide the neurosurgeon. The literature review done by Belykh and Senders identifies the various ongoing studies using fluorescent markers in neurosurgery [[Belykh et al. \(2016\)](#), [Senders et al. \(2017\)](#)]. According to these studies, three contrast agents are

commonly used in neurosurgery: PpIX, Indo Cyanine Green (ICG), and fluorescein. ICG is a light and hydrophilic molecule, with broadband absorption, resp. emission, spectra including a maximum absorbance at 805 nm, resp. a maximum emission around 830 nm. ICG binds to plasma and thus forms a marker of vascularization. As discussed in section 2.1.3, the presence of a glioma may imply a phenomenon of neo-angiogenesis visible by ICG [[Ferroli et al. \(2011\)](#)]. However, this fluorescence is not tumor-specific and has a too short lifetime, making it difficult to use ICG to discriminate gliomas [[Belykh et al. \(2016\)](#)].

Fluorescein is another marker excited between 460-490 nm and emitting light around 510-530 nm. According to Diaz's study [[Diaz et al. \(2015\)](#)], fluorescein crosses the BBB whose permeability is altered and is therefore a marker for high-grade gliomas. In addition, Diaz *et al.* point out that fluorescein reaches tumor cells through the cerebral vasculature. There is indeed no fluorescent response from the necrotic part of the tumor because of the absence of cerebral vasculature. The first use of fluorescein in neurosurgery was in 1948 where Moore and his team gave a predictive value of 96% for localizing brain tumors [[Moore et al. \(1948\)](#)]. However, the use of this fluorescence will not be compared to the one of PpIX in the rest of this chapter.

### **2.2.7 Current techniques of intraoperative assistance for identification of tumor margins and their limitations**

In order to identify the tumor tissue, the neurosurgeon first uses his senses (his sight, his touch) and his experience, the tumor tissue having characteristics (transparency, elasticity) different from those of healthy tissue. In addition to the experience of the neurosurgeon, two non-optical techniques (MRI or ultrasound) and one optical technique (fluorescence microscopy) are commonly used.

Preoperative MRI provides an image of the brain on which the tumor is visible. For high-grade gliomas, the contrast on the preoperative T1 gadolinium sequences represents the limits of the tumor to be resected in terms of macroscopically complete resection. This contrast is explained by the passage of the contrast agent in the tumor cells due to the rupture of the BBB [[Wu et al. \(2006\)](#)]. On the contrary, in low-grade gliomas, there is no tumor contrast because the BBB is not disrupted. Nevertheless, the T2-weighted FLAIR sequence reflects tumor infiltration in LGGs [[Li et al. \(2016\)](#), [Sanai et al. \(2011\)a](#)]. Correlation of this preoperative image with neuronavigation (intraoperatively) allows the neurosurgeon to localize his or her tools in the surgical field in relation to the preoperative image. The limitations of this technique are mainly the limits of sensitivity of MRI to detect margins of low density of tumor cells and the phenomenon of brain shift, which can induce a significant mismatch between the preoperative localization of the tumor and the one observed intraoperatively. To overcome the brain shift problem, the use of intraoperative MRI has been proposed. While this technique has demonstrated its potential to maximize excision [[Kubben et al. \(2011\)](#), [Senft et al. \(2011\)](#)], this significantly increases the duration of the operation and often requires a change of room. This also increases

costs, complicates patient setup, and requires the use of non-magnetic surgical tools when operating in the MRI [Kubben *et al.* (2011), Senft *et al.* (2011)]. In addition, there are still few interventional MRIs in France.

Intraoperative ultrasound is another technique which can be used to guide the neurosurgeon, because it is non-ionizing, portable, real-time and much less expensive than intraoperative MRI. This technique avoids the brain shift phenomenon and identifies the center of the tumor. However, the ability to discriminate healthy tissue from tumor tissue is limited [Mahboob *et al.* (2016), Mursch *et al.* (2017), Van Velthoven and Auer (1990), Chan *et al.* (2021)]. Mahboob's literature review further shows that as one moves further away from the tumor core, the sensitivity and specificity of ultrasound decreases, limiting its value for identifying tumor margins. Thus, if ultrasound allows the visualization of relatively dense margins and thus guides the neurosurgeon, it does not seem to allow the identification of sparse infiltrations and thus maximizes excision [Unsgaard *et al.* (2002)].

The contribution of optical techniques emerged in the mid-twentieth century with the use of fluorescein [Moore *et al.* (1948)]. Intraoperative assistance using optical techniques has developed considerably over the last twenty years with the use of 5-ALA and the development of specific filters included in operating microscopes. Today, the use of fluorescence to guide surgery has already proved its worth, as shown in recent literature reviews [Belykh *et al.* (2016), Senders *et al.* (2017)]. The interest of these techniques relies in their non-invasive, non-ionizing, real-time and inexpensive aspects [Valdés *et al.* (2016)]. Thus, fluorescence microscopy has been commonly used to guide the neurosurgeon since the early 2000s, using adapted modules added to the surgical microscope. Numerous literature studies highlight the importance of these techniques in maximizing high-grade glioma resection [Behbahaninia *et al.* (2013), Ewelt *et al.* (2015), Hefti (2013), Leroy *et al.* (2015)].

Let us now present the clinical use of fluorescein and PpIX.

As presented in Section 2.2.6, fluorescein is a fluorophore that accumulates in brain cells when the BBB is disrupted, making it an attractive marker to guide resection of high-grade gliomas [Acerbi *et al.* (2014), Murray (1982)]. This has been implemented in the surgical microscope via the Yellow560 module [Kuroiwa *et al.* (1998)], allowing direct visualization of fluorescence at a very low cost [Acerbi *et al.* (2013), Hamamcioglu *et al.* (2016), Koc *et al.* (2008), Schebesch *et al.* (2013), Zhang *et al.* (2017), Zhang *et al.* (2018)]. For example, Koc's study shows that fluorescein increases from 55% total resection to 83% using this marker for HGG. While these numbers seem higher than the study by Stummer and his team for the value of 5-ALA [Stummer *et al.* (2006)], the methodologies differ and Koc's team concludes that their results are comparable to Stummer's. The Acerbi team performed a Phase III study to conclude on the benefit of fluorescein for HGGs but does not propose its use for LGGs.

The advantage of fluorescein versus 5-ALA is its cost. 5-ALA costs €600 per gram whereas fluorescein costs €5 per gram [Bongetta *et al.* (2016)]. However, fluorescein fluorescence-based techniques are limited in identifying HGG margins as well as LGGs, for the same reasons as the limitations of gadolinium contrast uptake. Finally, Diaz's team recently proved that fluorescein is not a specific marker of tumorality but only of BBB deficiency, limiting its use to the hearts of HGGs [Diaz *et al.* (2015)]. In HGG cases, the patient ingests 5-ALA three hours before surgery at a dose of 20 mg/kg. The latter is biosynthesized into PpIX which itself accumulates in the tumor cells and allows them to be visualized in real time using a surgical microscope equipped with specific filters. The principle of this technique was presented by Stummer in 1998 [Stummer *et al.* (1998)]. When necessary, the neurosurgeon illuminates the tissue with a source integrated into the microscope exciting the tissue in the 400-410 nm spectral band. The tumor cells appear in pink, as shown in Figure 2.13.

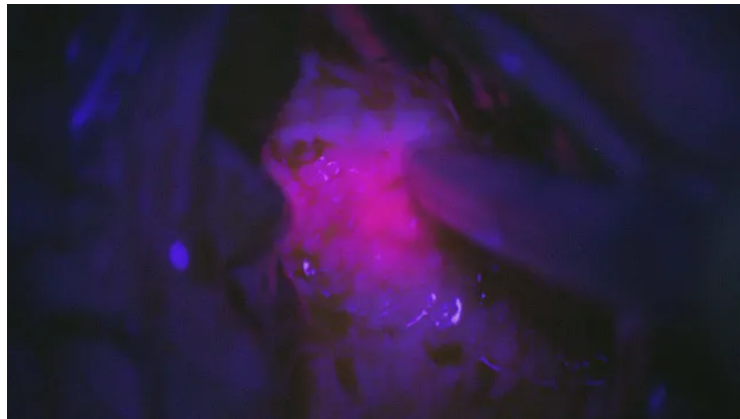


Figure 2.13: Cerebral cortex with a tumor, under excitation at 405 nm. (image taken from Zeiss' website)

According to the instructions of the Zeiss microscope (Opmi Pentero – Blue 400) available to the neurosurgeon at the time of our work, the fluorescent signal is filtered on the 620-710 nm spectral band, collecting mainly the fluorescence emitted by PpIX but also that of the various endogenous fluorophores presented in section 2.2.4. This technique is a full-field technique, allowing the neurosurgeon to see in real time an image, not only a given point. However, this measurement is subjective and qualitative. It can also be biased by the fluorescence of other components, and by the optical properties of the tissues (absorption and scattering) which distort the signal collected by the microscope.

This technique has been successful in improving HGG ablation because it has doubled the number of "maximal" resections, going from 25% to 65%, and increased the survival rate by six months [Stummer *et al.* (2006)]. However, it cannot be used for low-grade gliomas due to a sensitivity issue: the BBB is not disrupted and these tumors do not show visible fluorescence under excitation at 405 nm. Furthermore, all studies agree to show

the limitations of the technique to identify minimally infiltrated margins of high-grade tumors [Bravo *et al.* (2017), Hadjipanayis *et al.* (2015), Stummer *et al.* (2006), Toms *et al.* (2005)]. In order to overcome these sensitivity limitations, different projects are under development, that we will present in the next section.

Different studies have reviewed the diversity of assistance techniques, their advantages and disadvantages, all agreeing on the difficulty of identifying low infiltration margins of HGG and LGG [Krivosheya *et al.* (2016), Liu *et al.* (2014), Valdés *et al.* (2016), Vasefi *et al.* (2017)]. A recent study [Coburger *et al.* (2014)] has shown the value of fluorescence microscopy with 5-ALA in front of intraoperative MRI to identify tumor margins and concluded in [Coburger *et al.* (2015)] that the combination of the two may be even more beneficial than using either technique alone. Authors from [Stummer *et al.* (2014)] conclude that fluorescence microscopy is more sensitive than MRI.

## 2.3 PpIX fluorescence spectroscopy : one assistive technique under development for use in the operating theater

The list of optical techniques under development is very long, and the interested reader can approach the various recent literature reviews to further investigate these studies [Valdés *et al.* (2016), Ewelt *et al.* (2015), Leroy *et al.* (2015), Liu *et al.* (2014), Hefti (2013), Toms *et al.* (2006)]. Hereafter, we focus on fluorescence spectroscopy as a way to overcome the limitations of fluorescence microscopy.

The use of PpIX fluorescence spectroscopy was proposed in the late 2000s, initially in the form of "optical pointers". These "optical pointers" are spectroscopic probes deposited by the neurosurgeon on the brain tissue. Different approaches exist, some of them will be presented hereafter with their limitations. It should be pointed out that all approaches are relevant because they are intermediary steps toward the final aim of PpIX fluorescence measurements, which is the classification of measurements into relevant pathological status. Historically, quantification of PpIX concentration has been proposed with combined measurements of fluorescence spectroscopy and diffuse reflectance spectroscopy. This enables to correct distortions of the spectral signal [Kim *et al.* (2010)a, Valdés *et al.* (2011)]. Other methods estimate the *contributions*, also called relative concentrations, of PpIX fluorescence-related biomarkers in fluorescence spectroscopy measurements [Zanello *et al.* (2017), Dietel *et al.* (1997), Ando *et al.* (2011), Montcel *et al.* (2013)b, Montcel *et al.* (2013)a, Hope and Higham (2016), Alston *et al.* (2018), Alston *et al.* (2019), Black *et al.* (2021)]. More recently, machine learning approaches have emerged to address the clinical problem [Leclerc *et al.* (2020)], but the small amount of available data remains the main limiting factor.

### 2.3.1 Semi-quantitative approach

At the early 2000s, works of Stummer [[Stummer et al. \(1998\)](#), [Stummer et al. \(2000\)](#)] and Utsuki [[Utsuki et al. \(2006\)](#)] highlight the interest of fluorescence spectroscopy in tissues where gadolinium contrast has not taken place and where there is no visible fluorescence.

Utsuki's study includes six patients. Three of them show weak visible fluorescence and three do not. The system developed by Utsuki *et al.* excites the tissue with a 405 nm laser and looks for fluorescence at 636 nm. The main difference of this study compared to those of the next section is that measurements are not corrected from optical effects. Their method offers 100% specificity to identify tumor tissue without visible fluorescence. However, histopathological analysis of 16 samples without a 636 nm peak indicates the presence of tumor cells in at least seven of them, resulting in a 59% sensitivity. The sensitivity of this method can therefore be further increased. This team then seems to have turned its attention to the study of PpIX in metastasized brain tumors [[Utsuki et al. \(2007\)a](#), [Utsuki et al. \(2007\)b](#)]. Moreover, their 2008 work improves the 2006 work by suggesting to consider the ratio between the intensity at 636 nm and the one at 632 nm. They also improved their system by adding a hearable alert when this ratio exceeds 500 [[Utsuki et al. \(2008\)](#)].

Similarly, the work by Haj-Hosseini *et al.* [[Haj-Hosseini et al. \(2010\)](#), [Richter et al. \(2011\)](#)] shows the interest of an optical pointer using a laser source at 405 nm and analysing the fluorescence spectrum. Tissue discrimination is achieved by a ratio of the intensity at 635 nm after autofluorescence removal to the maximum autofluorescence value.

Existing studies demonstrated more complex links between the shape of fluorescence spectra and the PpIX concentration. Using fluorescence spectroscopy and light scattering in aqueous solutions, Melo's team [[Melø and Reisaeter \(1986\)](#)] studied the structure of PpIX as a function of pH. They assume that PpIX can be in monomeric, dimeric or micellar form. Thus, its fluorescence properties, hydrodynamic radius and molecular mass are different. This work concludes that in a basic medium, PpIX forms large micella and emits a spectrum with a maximum around 620 nm whereas in acid medium, the fluorescence emission is maximum around 634 nm. This work allows us to introduce the presence of various forms of PpIX since the variations of fluorescence emission are correlated to variations of hydrodynamic radius and molecular mass, thus to the configuration of PpIX. This effect of pH on PpIX in solution is also studied by other teams, such as [[Fuchs et al. \(1997\)](#), [Tian et al. \(2006\)](#)] or more recently [[Lu et al. \(2020\)](#)].

In 1990, a study varying the microenvironment of PpIX in beakers confirms the variability of the spectrum emitted by PpIX as a function of the presence of proteinoids or human albumin [[Lozovaya et al. \(1990\)](#)]. Taken from the publication, Figure 2.14b, resp. Figure 2.14a, shows the absorption, resp. the emission, spectra of PpIX as a function of its environment.

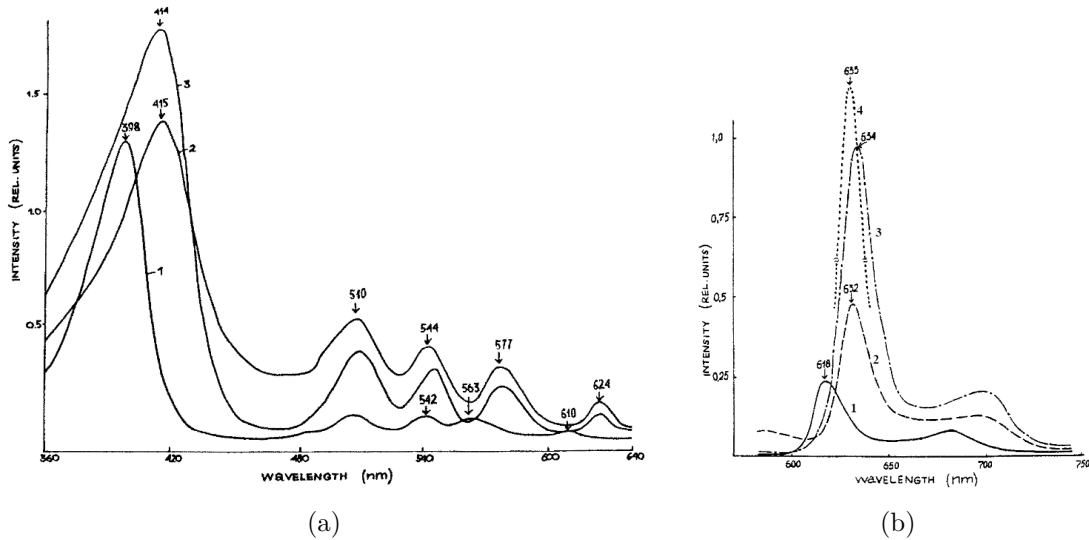


Figure 2.14: Absorption (a) and emission (b) spectra of PpIX according to the microenvironment. 1) pH 7; 2) pH 7 and addition of proteinoids; 3) pH 7 and addition of human albumin; 4) dissolution of PpIX in methanol. Taken from [[Lozovaya et al. \(1990\)](#)]

Curves (1) correspond to PpIX dissolved in hydrochloric acid and diluted in PBS to reach a pH of 7, without any other additive. The curves (2) correspond to the same solution in which were added proteinoids and the curves (3) correspond to the solution at pH 7 to which were added albumin contained in human serum. Finally, curve (4) of the figure 2.14b presents the emission spectrum of PpIX dissolved in methanol. It can be seen from these two graphs that the emission and absorption spectra of PpIX differ according to its micro environment. The curves (1) of the two graphs highlight an emission spectrum with a main peak at 618 nm and an absorption spectrum with a main band around 398 nm. These spectra are obtained in a beaker at pH 7, without any other component. The other emission spectra, Fig. 2.14b, show a peak at 633 nm and are obtained by modifying the aqueous environment of PpIX (by adding albumin from human serum or proteinoids, or by dissolving PpIX in methanol). In the figure 2.14a, one can observe a 14 nm shift between the absorption maximum of the solution emitting a spectrum with a maximum at 620 nm and those emitting a spectrum with a maximum around 633 nm. These phantom experiments support that the properties of PpIX depend on its environment and corroborate the experiments with pH variation of Melo's team [[Melo and Reisaeter \(1986\)](#)]. This study further shows that the quantum yield of these different PpIX forms varies, ranging from 0.011 for the spectrum with a maximum at 618 nm to 0.155 for the spectrum with a maximum at 633 nm. There is thus a ratio 15 between the two quantum yields.

The two previous studies are performed using dissolved PpIX. In the following, we present the variation of the spectrum emitted by cultures of bacteria or human cells with ingestion of 5-ALA.

The work of Dietel and his team [[Dietel et al. \(1997\)](#), [Dietel et al. \(2007\)](#)] focuses on the spectra emitted by different porphyrins in a murine tumor model [[Dietel et al. \(1997\)](#)]

and in 31 varieties of bacteria extracted from the human oral cavity and gastrointestinal tract after exposure to the 5-ALA molecule [Dietel *et al.* (2007)]. These studies suggest that fluorescence at 620 nm is due to hydrophilic porphyrins (uro- and co-proporphyrin) while fluorescence at 634 nm is due to PpIX. This work also raises the question of the hydrophobicity of PpIX, as opposed to the hydrophilicity of its precursors, which can therefore be removed by abundant "rinsing". Moreover, the 2007 study shows that with time, the same bacterium can emit first a spectrum centered at 635 nm and then a spectrum centered at 618 nm. These studies also raise the complexity of the photoproducts created by oxidation and irradiation of porphyrins. Carried out this time in a living environment, they show the complexity of the study of the fluorescence emitted by porphyrins, and the difficulty of associating a spectrum to the emitting porphyrin. This does not contradict the hypothesis of a fluorescence at 620 nm induced by PpIX but underlines the complex influence of the study environment. Similarly, the work of Barron and his team [Barron *et al.* (2013)] shows that for the same amount of 5-ALA added in four human cell lines, the amount and profile of the spectrum emitted by PpIX differs according to the sites and the microenvironment. This team also highlights a main peak at 635 nm and a secondary peak around 620 nm, again illustrating the complexity of the microenvironment.

In addition, PpIX fluorescence is used for visualization of caries. For example, Hope and his team studied the influence of pH on porphyrins in bacteria, with the goal of correlating their results and the study of dental plaques [Hope and Higham (2016)]. The selected bacteria contained 83% PpIX and 17% CoProporphyrin III (CpIII). The results of the study, shown in Figure 2.15, first show a shoulder at 620 nm when the pH is basic (8.63). The presence of this shoulder may be due to CpIII since the latter emits around 620 nm. However, the authors argue that there is no reason why the change in pH should imply a shift from PpIX to CpIII. Thus, this work concludes that the spectrum emitted by PpIX depends on the pH and that the latter, under certain conditions, presents an emission spectrum with a main peak at 620 nm. This Figure 2.15 suggests two other interesting phenomena: the first one is that a variation in the excitation wavelength varies the shape of the spectrum. The second one is that the total fluorescence emitted varies with the pH. Note that the variation of the emitted spectrum with the excitation source supports the hypothesis of the presence of two forms and has been confirmed by the two-photon excited fluorescence study of PpIX made by [Jonin *et al.* (2020)].

This work [Hope and Higham (2016)] thus raises the question of the monomeric form of PpIX as a function of the microenvironment: it would be in monomeric form emitting with a peak at 634 nm (PpIX634) and in dimeric or highly aggregated form when emitting at 620 nm (PpIX620). Results of [Hope and Higham (2016)] concerning the variation of the emitted spectrum with pH is in agreement with the study of Melo who performed a ph-metric titration of PpIX solutions [Melø and Reisaeter (1986)].

A recent study proposes to standardize PpIX phantoms for characterization of systems subsequently used in the operating room [Marois *et al.* (2016)]. Marois' study considers only one PpIX form but a more recent study, described in [Alston *et al.* (2019)] and the

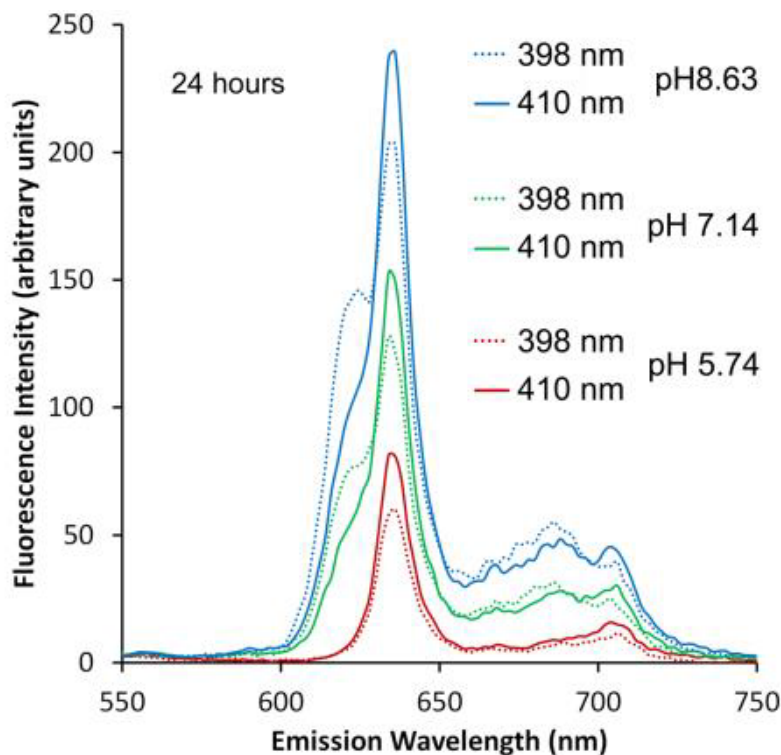
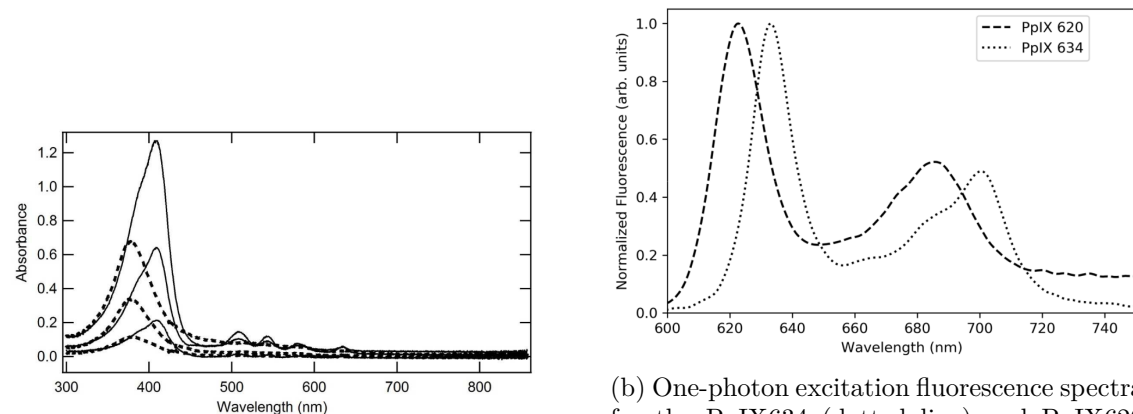


Figure 2.15: Emission spectra of *P. intermedia* suspensions (bacteria containing mainly PpIX) under excitation at 398 nm and 410 nm. In red, acidic pH. In green, neutral pH and in blue, basic pH. From [Hope and Higham (2016)]

Chapter 3 of [Alston (2017)], extends results to phantoms where both forms contribute to the total fluorescence. Thus, the fluorescence of PpIX depends on its microenvironment and reflects a change in aggregation.

According to the study of [Jonin *et al.* (2020)], the configuration that emits a fluorescence spectrum with a high quantum yield shows a peak around 634 nm. Reversely, the fluorescence quantum yield associated to the PpIX form which peaks around 620 nm is then lower. The study of [Jonin *et al.* (2020)] confirms the absorption and emission spectrum of each PpIX suggested in [Alston (2017)].

In a clinical context, the authors of [Ando *et al.* (2011)] made a study on biopsies from 5 patients, which suggests a wavelength shift of the peak intensity of the emitted spectrum in a tumor and healthy regions. Another study on biopsies realized by the authors of [Montcel *et al.* (2013)a] raised the presence of two forms of PpIX with different fluorescence spectra, peaking at 634 nm and also at 620 nm, in HGG as well as in LGG. In a 10 patient clinical study described in [Alston *et al.* (2019)], the contribution of a second form of PpIX (named PpIX620) is added to the well-known and commonly used reference spectra of PpIX (named PpIX634) to analyze fluorescence spectra of glioma. Results highlight that the contribution of PpIX634 dominates in HGG and their high density margins. In addition, they reveal that the contribution of PpIX620 is higher than the one of PpIX634 in low density margins of HGG and in LGG. Blue shift of the central



(a) UV-Visible absorption spectra for PpIX634 (full lines) and PpIX620 (dashed lines) aqueous solutions. The solution concentrations are  $2.23 \times 10^{-5}$  mol.L<sup>-1</sup>,  $1.15 \times 10^{-5}$  mol.L<sup>-1</sup> and  $3.35 \times 10^{-6}$  mol.L<sup>-1</sup> respectively.(Extracted from [Jonin *et al.* (2020)])

(b) One-photon excitation fluorescence spectra for the PpIX634 (dotted line) and PpIX620 (dashed line) in aqueous solutions. The excitation wavelength is tuned at 405 nm for PpIX634 and 385 nm for PpIX620 respectively in order to match the absorption maxima. The maxima of each spectrum are normalized to unity.(Extracted from [Jonin *et al.* (2020)])

Figure 2.16

wavelength when the density of tumor cells decreases confirms the weight of PpIX620 in low density margins. Those results could explain the lack of sensitivity of current techniques, which looks at PpIX634 even when PpIX620 dominates.

Despite all, the sensitivity of Fluorescence Spectroscopy (FS) remains limited by the presence of other non 5-ALA induced fluorophores such as NADH, FAD, flavins or lipopigments. The variability of the spectral emission by these other fluorophores depends a lot on the patient [Alston *et al.* (2019), Haidar *et al.* (2015), Black *et al.* (2021)], his/her age [Dolman *et al.* (1981)] and pathology [Ando *et al.* (2011)], but it also varies between two samples from the same patient [Dietel *et al.* (2007), Montcel *et al.* (2013)a, Montcel *et al.* (2013)b, Zanello *et al.* (2017), Alston *et al.* (2019), Black *et al.* (2021)]. These fluorophores and their high variability can lead to important *crosstalk* with PpIX [Black *et al.* (2021)]. Omitting a fluorophore, poorly modeling it, or using an incorrect base spectrum affects the detection of the specific fluorescence signal due to PpIX, yielding generally an overestimation of PpIX's amplitude, and thereby these crosstalk events are responsible for an overestimation of the PpIX fluorescence biomarkers contributions. This leads to a drop in specificity when biomarker contributions are used in a classification pipeline [Alston *et al.* (2019), Black *et al.* (2021)] because healthy samples are classified as tumoral.

To eliminate crosstalk, the overall approach described in the literature is to model the baseline with everything that is not due to 5-ALA-induced PpIX. Existing approaches are effective when the emission spectral band of the baseline is far from the one of the PpIX [Montcel *et al.* (2013)a, Haidar *et al.* (2015), Black *et al.* (2021)]. In these cases, the analytical or empirical *a priori* on the baseline can be a weighted sum of NADH, FAD and flavins spectra [Haidar *et al.* (2015), Black *et al.* (2021)] or an exponential decay function if the wavelength range starts at 500 nm [Ando *et al.* (2011), Montcel *et al.* (2013)a, Montcel

*et al.* (2013)b]. When the emission spectral band of the baseline is close to or within the one of the PpIX, as it is the case with lipopigments, the existing methods remain limited and very often expert dependent [Alston *et al.* (2019), Black *et al.* (2021)]. The baseline is modeled by a Gaussian function [Alston *et al.* (2019)], or an expert-dependent weighted sum, which contains a finite number of fluorophores whose fluorescence spectral shape is assumed to be known [Haidar *et al.* (2015), Black *et al.* (2021)]. However, fluorophores whose spectral emission band overlaps the one of PpIX spectral emission band are difficult to consider by these methods. Such issues arise with water-soluble porphyrins [Dietel *et al.* (1997)] with emission spectrum in the 615-625 nm region. Photoproducts could also be produced in 5-ALA induced condition, with an emission spectrum in the 620-680 nm region [Dietel *et al.* (1997), Dysart and Patterson (2006), Montcel *et al.* (2013)a]. Moreover, some works propose a larger emission spectrum for lipofuscin [Black *et al.* (2021)] up to the 620-700 nm region. These high levels of crosstalk largely impair specificity. The Part II of this manuscript is dedicated to a novel solution we suggest to reduce specificity impairs using an estimated baseline approach relying on multiple wavelength excitation. The next section will focus on the main complementary approach which aims at quantifying fluorophores as a mean to distinguish healthy from tumoral tissues.

### 2.3.2 Quantitative approach: Theory-based attenuation correction techniques

A recent article from [Valdes *et al.* (2019)] describes clearly fundamental concepts in quantitative fluorescence, including autofluorescence correction, tissue optical absorption and scattering correction and the way they affect the fluorescence measurements. In addition of providing an overview of the major implementations of quantitative fluorescence in neurosurgery, this study suggests some *fluorescence attenuation correction techniques* like the ones exposed in [Richards-Kortum and Sevick-Muraca (1996)] or [Durkin *et al.* (1994)]. But a lot of other attenuation correction techniques exists depending on the light propagation assumptions that are considered. Let us underline that the methods presented here for attenuation correction techniques are also used in many other fields such as diffuse optical tomography (DOT) or diffuse fluorescence optical tomography (FDOT) for example. An overview of all these techniques is given by [Da Silva (2013)]. Nevertheless, it seems relevant to describe them briefly before focusing on more practical elements such as the various experimental techniques which exists to determine optical properties. Finally, a special attention will be paid to the method suggested in [Kim *et al.* (2010)b].

#### 2.3.2.1 Theory based attenuation correction techniques

The present section discusses only theoretical studies, but the interested reader can get elements of empirical techniques in the following reviews of attenuation correction techniques [Mycek and Pogue (2003), Bradley and Thorniley (2006), Tuchin (2015), Boas *et al.* (2016)]. In cases where the wave nature of light has no significant effect such as

diffraction or interferences, which is true for most random media illuminated with a large and broad spectrum light source, the *radiative transfer equation* (RTE) can be used to describe the scattering of light within the medium. The non approximated RTE is an integro-differential equation whose difficulty of solution lies mainly in the evaluation of the integral term. The radiative transfer approach has been extensively investigated since the 50's. Following the pioneering work of Chandrasekhar [[Chandrasekhar \(1960\)a](#)] for the study of the atmosphere, the book [[Ishimaru \(1978\)](#)] suggests to extend the radiative transfer theory to the propagation of multiple wave types like optical, acoustic, and microwave but also to apply it in broader fields such as scattering in atmospheres, oceans, and biological media. Despite this, there are multiple methods for solving the radiative transfer equation, which can nevertheless be grouped into distinct categories:

- The methods of discretization of space (Finite Element Method (FEM), Finite Volume Method (FVM)) and/or angles (Discrete Order Method (DOM or  $S_N$  approximation),  $P_N$  approximation,  $SP_N$  approximation...) are widely used and efficient for simple geometries. They offer the advantage of leading to semi-analytical expressions of the specific intensity. However, they remain limited to simple geometries, otherwise the computation times become exorbitant, and the accuracy itself depends on the discretization. Since the contribution of Klose *et al.* [[Klose and Hielscher \(2002\)](#), [Klose et al. \(2002\)](#)], this type of resolution has been applied in so-called "thin" media where the diffusion approximation is not valid. This is for example the case of biological tissues [[Klose and Larsen \(2006\)](#), [Klose \(2009\)](#), [Klose \(2010\)](#)].
- Analytical expressions for the Diffusion Approximation (also called the  $P_1$  approximation or the discrete dipole approximation) are easy to obtain and then implement. However, they are reserved only for simple geometries and very particular scattering systems. Nevertheless, the Diffusion Approximation framework has been widely used for biological tissues [[Patterson et al. \(1989\)](#), [Boas et al. \(1997\)](#), [Chen et al. \(1998\)](#), [Chance et al. \(1998\)](#)].
- Stochastic methods (such as Random Walk or Monte Carlo simulations) are easy to implement, but expensive in computation time when the geometry of the problem becomes complex. The Monte Carlo method, which "simulates" the light propagation like that of a set of classical particles, remains the leading method in this category.

All these ways to solve the RTE in addition of the modified Beer–Lambert law, explained in 2.2.1, and the Kubelka–Munk theory, explained in the next paragraph, have been employed as a basis for describing light propagation in biological tissues [[Wilson and Mycek \(2011\)](#)] and thus offer a number of correction techniques. The modified Beer–Lambert law can be used when changes in light transmission (in any geometry) can be related to differential changes in tissue absorption; ie the scattering loss is assumed to be constant. As brain tissues are highly diffuse, the modified Beer-Lambert law assumptions are not satisfied for estimating absorption and scattering properties, thus we will not consider this method

hereafter, but the interested reader can refer to one of the reviews cited at the beginning of the section. When scattering strongly dominates absorption, the Kubelka–Munk (KM) theory and diffusion approximation are suitable for use. In both cases, light can thus be considered to be effectively isotropically scattered [[Cheong et al. \(1990\)](#),[Richards-Kortum and Sevick-Muraca \(1996\)](#),[Hoffmann et al. \(1998\)](#)].

In 1931, Paul Kubelka and Franz Munk published the famous eponymous Kubelka–Munk model [[Kubelka \(1931\)](#)], which describes the propagation of forward and backward Lambertian fluxes, i.e. with an isotropic radiance distribution, in a homogeneous scattering medium and gives analytical formulas for the reflectance and transmittance of a layer of this medium of any thickness, possibly deposited on a scattering background. The original Kubelka–Munk theory is not applicable when the incident radiation is collimated or when the scattering medium has an optical index different from the one of the surrounding medium. But this *two-flux approach* includes the extension proposed by Saunderson in 1942 to take into account the Fresnel reflections and refractions of light at the interfaces bordering the layers [[Saunderson \(1942\)](#)], as well as the extension proposed by Kubelka in 1954 for stacks of different diffusing layers. From the observation geometry, illumination geometry and shift of refractive index between the layer and its surrounding medium, the Saunderson equation corrects the reflectance/transmittance calculated by the Kubelka–Munk model. In addition, [[Maheu et al. \(1984\)](#)] proposed a *4-flux model*, as an extension of the 2-flux model that can consider collimated fluxes in addition to diffuse fluxes. Finally, an attenuation correction technique using the original Kubelka–Munk (two-flux) model has been introduced by [[Durkin et al. \(1994\)](#)].

The diffusion approximation is an approximated solution of the radiative transfer equation, valid in highly scattering media. This approximation has been extensively used to model light scattering in extremely diffusing medium such as living tissues or paper [[Farrell et al. \(1992\)](#),[Patterson and Pogue \(1994\)](#),[Jacques \(1998\)](#),[Rogers \(1998\)](#),[Kienle et al. \(1998\)](#)]. Contrary to the exact RTE, it offers closed-form solutions even when describing the diffusion with two or three dimensions, and also time-dependent solution. The major difficulty in using the diffusion approximation relies on the application of boundary conditions, which are for example discussed in [[Kim \(2011\)](#)]. Moreover, it is important to remember that the diffusion approximation may not be valid in the first steps of the light scattering process ( $d \ll \frac{1}{\mu_s}$ ), and should be used only when the scattering medium is thick enough to ensure many scattering events between the source and the optical detector [[Star et al. \(1988\)](#)]. More recently, an analytical model of photon migration has been developed [[Wu et al. \(1993\)](#)]. Nevertheless, a correction technique based on a diffusion approximation model depending only on the depth has been suggested in [[Zhadin and Alfano \(1998\)](#)]. This correction technique assumes that illumination is provided by an infinitely wide beam, falling at a given angle on the tissue surface. The correction of fluorescence emission or excitation spectra is achieved by dividing the measured spectra by a wavelength dependent correction factor, which is calculated from the diffuse reflectance spectrum.

When neither the strong absorption nor the strong scattering approximation can be assumed, another possibility to determine the intrinsic fluorescence properties relies on Monte Carlo (MC) modeling of light propagation. Monte Carlo simulation was applied for the first time for biological tissues by [Wilson and Adam (1983)].

In addition to being highly adaptable to different tissue organizations (including layered structures), probe geometry, MC is valid for arbitrary optical properties and wavelengths. MC is used as a gold standard for checking the accuracy of other models, in particular analytical models. The computationally intensive aspect of the MC method is however the main disadvantage of this technique. To achieve statistical significance, paths of millions or more photons must indeed be calculated and recorded. Thus, MC techniques are limited in their ability to provide intrinsic spectra in near real time. As explained in [Boas *et al.* (2016)], Palmer *et al.* recently developed a MC model to extract intrinsic fluorescence and applied it to fluorescence spectroscopy (FS) measurements of the breast [Palmer and Ramanujam (2006), Palmer and Ramanujam (2008), Zhu *et al.* (2008)]. Their model assumed a single layer with homogenous optical properties. First, the reflectance of Monte Carlo model is used to obtain scattering and absorption coefficients ( $\mu_a, \mu'_s$ ) from measured broadband diffuse reflectance measurements. Then, these extracted coefficients are used as inputs to their fluorescence MC model. This model was applied to FS measurements of excised breast tissue from patients with carcinoma and fibrous or benign conditions. Their assumption is that NADH, retinol, and collagen are the contributing fluorophores. By using the extracted fluorophore results, they were able to classify malignant from benign tissue with a sensitivity of 82.6% and a specificity of 75.7% in a validation set. More complex MC model have also been developed, like the two-layer MC model in [Drezek *et al.* (2001)] to describe fluorescence in the cervix, or the five-layer one in [Pavlova *et al.* (2008)] to describe fluorescence in oral tissue.

## Conclusion

All the theory-based attenuation correction techniques described previously differ from each other by their domain of validity or by the approximations on which they depend. Other approximations, which may be employed, include considering the tissue to be of infinite width and depth, and/or to have a refractive index of the tissue equal to the one of the surrounding medium. Thus, all these techniques are compared with eachothers in the table 2.1.

More generally, these quantification techniques rely on the common assumption that the concentration of PpIX is proportional to the emitted PpIX fluorescence intensity. This is supported by the link between the fluorescence emitted intensity and the tumor cellular density [Johansson *et al.* (2010), Yoneda *et al.* (2018), Kröger *et al.* (2018)].

All techniques assume that the optical properties of the medium are known. Thus, the next section focuses on the experimental setups that exists to determine optical properties.

	Discrete Ordinates	Diffusion Approximation (when $\mu_s \gg \mu_a$ )	2-flux	4-flux	Monte-Carlo	Beer-Lambert	Beer-Lambert Modified
Scattering	✓	✓	✓	✓	✓	✗	~
Anisotropy	✓	~	✗	~	✓	✗	~
Analytical (for simple geometries)	✗	✓	✓	✓	✗	✓	✓
Directional lighting	✓	✓	✗	✓	✓	✓	✓
Complex geometries	✓	✓	✗	✗	✓	✗	✗
Including fluorescence	✓	✓	✓	✓	✓	✗	✗
Highly translucent media	✓	✗	✗	✗	✓	✗	✗

~ Partially taken into account.

Table 2.1: Comparison of methods for solving the radiative transfer equation with other light propagation models.

### 2.3.3 Experimental Setups to determine optical properties of tissues

As the final step of fluorescence quantification process needs the attenuation correction of fluorescence measurements, which requires the use of empirical or theory based techniques, it is important to underline that the estimation of optical properties is only one step in the fluorescence quantification process. The aim of this section is to describe existing experimental setups that have been used in the neurosurgery's operating room to determine optical properties. The common point of all of them is that they are spatially resolved. They can be classified into two major categories, experimental setups that samples the *Point Spread Function* (PSF) of a material and those which samples the *Modulation Transfert Function* (MTF) of the material. Diffuse reflectance spectroscopy (DRS) samples the PSF of a material (here biological tissues) by illuminating it punctually, collecting the backscattered light and measuring the optical signal with a spectrometer. While this method was proved useful for a number of applications, DRS systems are often handheld spectroscopic probes that are put into direct contact with the tissue [Koenig *et al.* (2015)], which risks altering its optical properties depending on the pressure applied. This limitation has been overcome by the development of contactless systems relying on imaging. Yet, DRS only provides an average measurement over a small area, which provides much less information than imaging methods for the study of heterogeneous materials such as skin.

A contactless and wide-field method, called Spatial Frequency Domain Imaging (SF DI), was developed in the early 2000s [Dögnitz and Wagnières (1998), Cuccia *et al.* (2005),

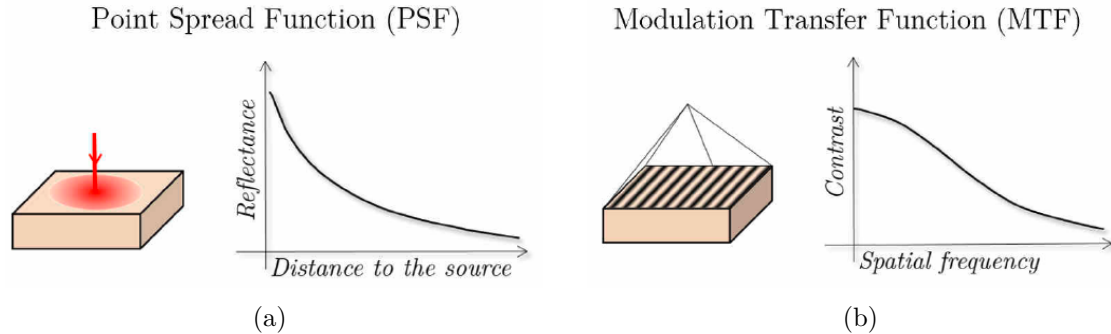


Figure 2.17: (a) Point spread function (PSF), which can be measured using DRS, and (b) modulation transfer function (MTF), which can be measured using SFDI. (Taken from [Gevaux (2019)])

Cuccia *et al.* (2009)] to estimate the optical properties of a material by sampling of the modulation transfer function. MTF describes the loss of contrast of a sinusoidal fringe light pattern projected onto the material in function of the spatial frequency of the fringes. While PSF measurement requires punctual illumination (Figure 2.17a), MTF is generally measured by projecting sinusoidal fringes on the surface (Figure 2.17b). SFDI offers a powerful way to acquire the tissue reflectance properties simultaneously for every pixel of an image. However, standard SFDI processing requires typically 6 images to generate tissue property maps [Cuccia *et al.* (2009)], slowing down acquisition rate possible for acquiring the fluorescence correction factor [Sibai *et al.* (2017), Saager *et al.* (2011)].

In [Vervandier and Gioux (2013)] is presented a technique using single snapshot imaging of optical properties (SSOP) to image the tissue optical properties in real time. SSOP is based on SFDI, but in contrast with standard SFDI it offers the possibility to get video-rate wide-field acquisition of tissue optical properties, including sample profile acquisition and correction [Giessen *et al.* (2015)]. The literature dealing with SFDI methods and its potential for medical applications has steadily increased in recent years [Gioux *et al.* (2019), Aguénounon *et al.* (2020)]. As example in [Valdes *et al.* (2017)], quantitative fluorescence Single Snapshot of Optical Properties (qF-SSOP) imaging relies on the adaptation of an SSOP imaging system to perform acquisition of the tissue fluorescence to derive optical property corrected maps of fluorescence.

Nevertheless, as the setup built by [Alston (2017)] was a single-point optical probe, it is relevant to describe precisely the original DRS system implemented by [Kim *et al.* (2010)b] which is a single-point optical probe used both to measure fluorescence and to determine the optical properties.

### 2.3.4 Example of a diffuse reflectance spectroscopy probe

The team from Dartmouth has initially developed a probe that collected both the fluorescence spectrum emitted by the tissue and the diffuse reflectance spectrum in order to correct the fluorescence spectrum from distortions using a light transport model

based on the diffusion approximation of the radiative transfer equation (RTE) [Kim *et al.* (2010)b, Kim *et al.* (2010)a, Valdés *et al.* (2011), Valdés *et al.* (2011)b]. The goal of their work is to trace the PpIX concentration in order to have a quantitative and objective measure, as opposed to the measurement, which is subjective and biased by the propagation of the fluorescence in the tissue before reaching the sensor.

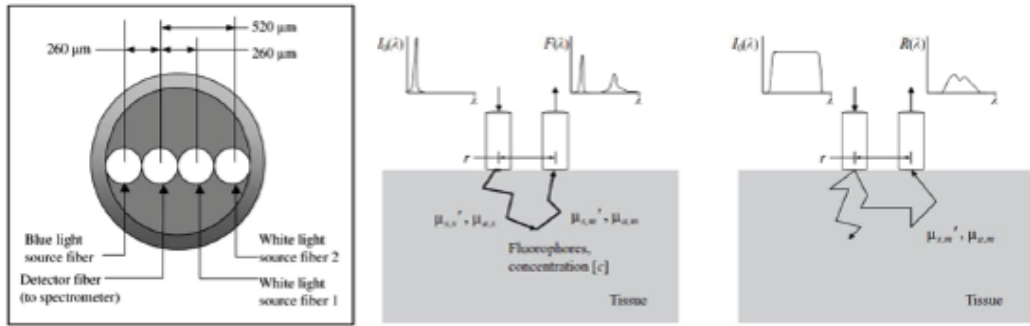


Figure 2.18: Optical probe measuring both fluorescence and scattering reflectance to correct the fluorescence measurement from effects of absorption and scattering induced by the tissue. (Taken from [Kim *et al.* (2010)b])

In their work, reflectance measurements are made at different distances from the source, in order to obtain the optical properties of the tissue ( $\mu_a, \mu'_s$ ), which allows correcting distortions of the fluorescence spectrum collected successively. Figure 2.18 briefly shows the instrumental probe developed to apply this algorithm to the problem of PpIX quantification [Kim *et al.* (2010)a]. A blue excitation channel exists to obtain the fluorescence spectrum and two white excitation sources to measure the diffused reflectance spectrum. The tissue properties are obtained under the assumption that light transport can be described in tissues by the diffusion equation solved with the boundary conditions of a semi-infinite, homogeneous and optically turbid medium, with moreover several source-detector distances to increase the range where the algorithm is valid [Kim *et al.* (2010)b]. The application of this algorithm to the quantification of PpIX also assumes that the mean-free-path of photons emitted by fluorescence is the same as the one of photons collected by diffuse reflectance at the same wavelength and that there is therefore a proportional relationship between the measured fluorescence spectrum and the diffuse reflectance measured on the same sample. The measured fluorescence spectrum is then corrected according to the absorption and scattering properties of the tissue obtained from the reflectance measurement and the light transport model. This corrected spectrum is then adjusted using a linear combination of the different fluorophores present in the brain tissue, using for PpIX a fixed and unique reference spectrum obtained in vitro. This adjustment allows them to retrieve to the PpIX concentration and thus to obtain a more appropriate diagnosis of the probed tissue.

This technique was first applied on 14 patients with brain tumors [Valdés *et al.* (2011)]. During surgery, the probe is deposited on the studied tissue, a 0.5-second measurement

is performed, and the PpIX concentration is returned within 2 seconds. A biopsy of the tissue is then taken for histopathological analysis and the visible fluorescence is qualitatively evaluated by the neurosurgeon in parallel. Biopsies are classified as LGG, HGG, meningioma, healthy tissue or metastasis. The results of this study propose a significant increase in PpIX concentration in the different tumor tissues compared to healthy tissue, with a threshold value of 100 ng/ml for which 40% of tumor biopsies do not fluoresce. The relevance of the obtained concentration was compared to the parameters proposed in the uncorrected fluorescence spectrum studies, and the concentration is the best classification metric. Authors from [Valdés *et al.* (2011)] show a comparison between the raw fluorescence measurement, the measured and adjusted spectrum, and the histological section for healthy tissue, LGG, and HGG. They observe a significant increase in PpIX concentration between healthy tissue and HGG through LGG.

Developed according to a point sampling system, this technique has been proposed for full-field imaging for glioblastoma, using a variable filter positioned in front of a CCD (Charge Coupled Device) camera [Valdés *et al.* (2012)]. This study is the first to propose quantitative full-field fluorescence and thus provides the neurosurgeon with global information comparable to that given by the microscope, but with much greater sensitivity. This full-field imaging is easier to use for the neurosurgeon than point techniques. The *in vivo* results of the first full field use of this model confirm that the corrected fluorescence is more sensitive than the raw one, with a factor of 10, and this method proposes a positive predictive value higher than 90% for a PpIX threshold around 100 ng/ml. This threshold is consistent with their previous measurements [Valdés *et al.* (2011a)], and with the concentrations obtained by Johansson [Johansson *et al.* (2010)]. Furthermore, this study proposes a hyperspectral image, which is suitable for the tracking of multiple fluorophores at the same time.

## 2.4 Conclusions

In this chapter, we described the background needed to understand the rest of the manuscript. We first described the brain tissues studied, both healthy tissue and gliomas. We then presented the clinical issue related to this manuscript, namely the difficulty of identifying tumor infiltrations, in real time, in the operating room and therefore the need for assistance. Before presenting in detail the assistance techniques, we presented the basic of the light-matter interaction useful for the understanding of chapters that will follow, in particular the phenomenon of fluorescence. Then, we presented the techniques currently used to guide the neurosurgeon in the resection of gliomas and their limitations, and the different research works already tested *in vivo* to overcome these limitations.

PpIX fluorescence has identified as a promising biomarker to discriminate tumor cells from healthy cells. Thus, we focused on one promising technique, named fluorescence spectroscopy.

We described two approaches, the first one tries to quantify the PpIX via its intrinsic

fluorescence. The assumptions of the optic models and their related simplifications used to recover the intrinsic fluorescence are often oversimplified, especially concerning the assumption of index-matching or lambertian radiance distributions. We will describe it more rigorously and precisely in the Part III.

The second approach, considered as semi-quantitative, analyses the components of the fluorescence emission spectrum to get information of the associated pathological status. This second method highlighted the existence of two forms of PpIX whose emitting spectra are respectively centered around 620 nm and 634 nm and with very different fluorescence properties. The two forms will be called "PpIX620" and "PpIX634" in the rest of the manuscript, even if their maximum emission can be slightly shifted according to the measurements. In addition, it has previously been highlighted that considering these two forms improves the discrimination of tumor cells, especially because decrease in fluorescence observed in the tumor margins is not a decrease of the PpIX concentration but a change of form involving the presence of PpIX620. However, the method suggested by the literature [Alston (2017)] suffers from crosstalk, which drops the specificity. Part II will focus on a proposal to solve the crosstalk issue by using multi-spectral excitation of fluorescence and its associated post-processing model.

Finally, it is important to underline that the frontier between quantitative and semi-quantitative approaches is porous. Indeed, one notices that the work of the Dartmouth team for the quantification approach considers only the PpIX634 form [Kim *et al.* (2010)a, Valdés *et al.* (2011)a, Valdés *et al.* (2011), Valdés *et al.* (2012), Valdés *et al.* (2015)]. But it proposed to adjust the spectra measured in the operating room using PpIX photoproducts emitting with a maximum around 620 nm [Bravo *et al.* (2017)]. So they do not explicitly consider the presence of two forms, they simply mention the need to consider a second fluorescence spectrum of PpIX centered around 620 nm in addition of the PpIX634.



## II Spectral estimation method of PpIX contributions without *a priori* on other components by multispectral excitation

---



---

In this section, we propose a method to estimate the relative concentration of PpIX fluorescence-related biomarkers, also called *contribution*. As mentionned in the introduction of this manuscript, existing approaches for the estimation of the contributions of PpIX are limited by the omission or the wrong spectral shape of some endogenous fluorophores present in the measured signal, hereafter called *crosstalk*. It largely impairs specificity in the classification of tissues according to their pathological status.

This crosstalk occurs when the spectrum of the omitted endogenous fluorophore(s) is spectrally close to the PpIX emission. This leads to an overestimation of the PpIX contribution and thus to a wrong classification of healthy tissues into a tumoral category.

The problem is that the endogenous products able to emit a fluorescence signal are numerous and strongly varying from one individual to one another. Usually, the spectral shape of their fluorescence signal is approximately modeled with strong *a priori* assumptions. Here, we propose a method where no *a priori* on these endogenous products and the respective spectral shape is needed. For this, several fluorescence excitation wavelengths are necessary to transfer the *a priori* in the fluorescence quantum yield of fluorophores of interest and to estimate the part of the signal related to endogenous fluorophores, in the *baseline*. The new method nevertheless makes the assumption that the spectral shape of the baseline is unchanged between signals of different excitation wavelengths. This assumption makes sense because we are only interested in fluorophores whose emission is spectrally close to that of the PpIX. Additionally, we were able to derive an analytical solution for all the variables of our nonlinear estimation problem. This makes our method computationally efficient, free from parameter tuning and from cumbersome iterative estimation procedure.

Thus, Chapter 3 describes our new method and its analytical resolution, then Chapter 4 focuses on the comparison with state-of-the-art methods and the related discussion.



# Chapter 3

---

## Multi-wavelength models & analytical resolution of the Estimated Baseline model

---

In this chapter is described the model for estimating the relative concentration of PpIX, hereafter called *contribution of PpIX*, to the fluorescence signal. This new model is based on the analysis of fluorescence emission spectra obtained under multiple excitation wavelengths. The explanation and the mathematical description of the physical model are given first. Then, the analytical solution for all the variables of our nonlinear estimation problem that we were able to derive is describe.

### 3.1 Physical Model

The fluorescence emission spectrum of fluorescing substances always depends on the excitation wavelength. Thus, because we consider multiple excitation wavelengths, the fluorescence spectrum  $m$  can be written as:

$$\mathbf{m}(\lambda_e) = \sum_{i=1}^n \alpha_i \eta_i(\lambda_e) \mathbf{S}_i + \gamma(\lambda_e) \mathbf{b}, \quad (3.1)$$

where  $\lambda_e$  is the fluorescence excitation wavelength,  $\mathbf{S}_i \in \mathbb{R}^{p \times 1}$  is the unitary energy emission spectrum of the  $i^{th}$  fluorophore,  $\eta_i(\lambda_e) \in \mathbb{R}^1$  the quantum yield of the same fluorophore at excitation wavelength  $\lambda_e \in \mathbb{R}^1$ ,  $\alpha_i \in \mathbb{R}^1$  its contribution.  $\mathbf{b} \in \mathbb{R}^{p \times 1}$ , the baseline, represents other endogenous fluorophore emission spectra whose amplitude with respect to the excitation wavelength is modeled by  $\gamma(\lambda_e) \in \mathbb{R}^1$ . Please note that in the presence of

$k$  distinct excitation wavelengths, the condition  $n + k - 1 \leq (k - 1)p$  is required for the problem to be either overdetermined or perfectly determined. For the sake of concreteness, we consider only the case of two excitations wavelengths, and  $n = 2$  fluorophores of interest, PpIX634 and PpIX620. Thus we consider here that  $p \leq 2$ , Eq. 3.1 becomes:

$$\begin{aligned}\mathbf{m} &= \alpha_1 \eta_1 \mathbf{S}_1 + \alpha_2 \eta_2 \mathbf{S}_2 + \mathbf{b} \\ \mathbf{m}' &= \alpha_1 \eta'_1 \mathbf{S}_1 + \alpha_2 \eta'_2 \mathbf{S}_2 + \gamma \mathbf{b}.\end{aligned}\tag{3.2}$$

Defining a contribution vector  $\boldsymbol{\alpha} = (\alpha_1, \alpha_2)^T$  and a measurements vector  $\tilde{\mathbf{m}} = (\mathbf{m}, \mathbf{m}')^T$ , equation 3.2 can be written in a matrix form as

$$\begin{aligned}\tilde{\mathbf{m}} &= \begin{pmatrix} \mathbf{S} & \mathbf{I} \\ \mathbf{SE} & \gamma \mathbf{I} \end{pmatrix} \begin{pmatrix} \boldsymbol{\alpha} \\ \mathbf{b} \end{pmatrix} \\ &= \mathbf{M} \begin{pmatrix} \boldsymbol{\alpha} \\ \mathbf{b} \end{pmatrix}\end{aligned}\tag{3.3}$$

where  $\mathbf{S} = \begin{pmatrix} \eta_1 \mathbf{S}_1 & \eta_2 \mathbf{S}_2 \end{pmatrix} \in \mathbb{R}^{p \times 2}$ ,  $\mathbf{E} = \text{diag}(\rho_1, \rho_2) \in \mathbb{R}^{2 \times 2}$  with  $\rho_i = \frac{\eta'_i}{\eta_i}$ , and  $\mathbf{I} \in \mathbb{R}^{p \times p}$  is the identity matrix.

## 3.2 Estimation Model

### 3.2.1 Estimated Baseline Model (EB)

Our estimator of the fluorophore contributions is the least square solution of the equations 3.3 :

$$\boldsymbol{\alpha} = \underset{\boldsymbol{\alpha}, \mathbf{b}}{\operatorname{argmin}} \left\| \tilde{\mathbf{m}} - \mathbf{M} \begin{pmatrix} \boldsymbol{\alpha} \\ \mathbf{b} \end{pmatrix} \right\|_2^2.\tag{3.4}$$

In this optimization problem,  $\boldsymbol{\alpha}$ ,  $\mathbf{b}$  and  $\gamma$  are the variables to estimate and all other parameters are given. We stress that, as opposed to the state of the art, no assumption is made on the spectral shape of the baseline emission: the baseline is estimated directly from the data.

### 3.2.2 Analytic Resolution of Estimated Baseline Model

The interaction between  $\gamma$  and  $\mathbf{b}$  makes the Estimated Baseline Model non-linear. However we will show in this section that it is still possible to find a closed-form expression for  $\boldsymbol{\alpha}$ .

The problem is treated in two steps:

$$\min_{\alpha, \gamma, b} \left\| \tilde{\mathbf{m}} - \mathbf{M} \begin{pmatrix} \alpha \\ b \end{pmatrix} \right\|^2 = \min_{\gamma} \min_{\alpha, b} \left\| \tilde{\mathbf{m}} - \mathbf{M} \begin{pmatrix} \alpha \\ b \end{pmatrix} \right\|^2 \quad (3.5)$$

the least-square solution  $(\alpha_\gamma, b_\gamma)$  for a given  $\gamma$  is first derived and then the optimal  $\gamma$  is found:

$$\begin{aligned} \min_{\alpha, \gamma, b} \left\| \tilde{\mathbf{m}} - \mathbf{M} \begin{pmatrix} \alpha \\ b \end{pmatrix} \right\|^2 &= \min_{\gamma} \min_{\alpha, b} \left\| \tilde{\mathbf{m}} - \mathbf{M} \begin{pmatrix} \alpha \\ b \end{pmatrix} \right\|^2 \\ &= \min_{\gamma} \left\| \tilde{\mathbf{m}} - \mathbf{M} \begin{pmatrix} \alpha_\gamma \\ b_\gamma \end{pmatrix} \right\|^2. \end{aligned} \quad (3.6)$$

For a fixed  $\gamma$ , matrix  $\mathbf{M}$  is constant and the problem is linear. The optimal  $(\alpha, b)$  is given by  $(\alpha_\gamma, b_\gamma)^T = \mathbf{M}^+ \tilde{\mathbf{m}} = (\mathbf{M}^T \mathbf{M})^{-1} \mathbf{M}^T \tilde{\mathbf{m}}$  where  $\mathbf{M}^+$  is the Moore Penrose pseudo inverse of  $\mathbf{M}$ . An expression for  $\mathbf{M}^+$  can be obtained using a formula for the inverse of block matrices, equation 2.3 of [Lu and Shiou (2002)].  $\mathbf{M}^T \mathbf{M}$  is given by:

$$\mathbf{M}^T \mathbf{M} = \begin{pmatrix} \mathbf{S}^T \mathbf{S} + (\mathbf{SE})^T \mathbf{SE} & (\mathbf{I} + \gamma \mathbf{E}) \mathbf{S}^T \\ \mathbf{S} (\mathbf{I} + \gamma \mathbf{E}) & (1 + \gamma^2) \mathbf{I} \end{pmatrix} \quad (3.7)$$

and if  $\mathbf{E}_g = \gamma \mathbf{I} - \mathbf{E}$  and  $\bar{\mathbf{S}} = (\mathbf{S}^T \mathbf{S})^{-1}$ , the Schur complement  $\mathbf{S}_u$  of  $\mathbf{M}^T \mathbf{M}$  is:

$$\begin{aligned} \mathbf{S}_u &= \bar{\mathbf{S}}^{-1} + \mathbf{E}^T \bar{\mathbf{S}}^{-1} \mathbf{E} - (\mathbf{I} + \gamma \mathbf{E}) \mathbf{S}^T \frac{\mathbf{I}}{1 + \gamma^2} \mathbf{S} (\mathbf{I} + \gamma \mathbf{E}) \\ &= \frac{\mathbf{E}_g \bar{\mathbf{S}}^{-1} \mathbf{E}_g}{1 + \gamma^2}. \end{aligned} \quad (3.8)$$

The inversion of  $\mathbf{M}^T \mathbf{M}$  is possible as soon as  $(1 + \gamma^2) \mathbf{I}$  and its Schur complement (eq. 3.8) are invertible:

**The invertibility is conditioned by  $\gamma \notin \{\rho_1, \rho_2\}$ .**

These two conditions are in agreement with the physics of the problem:  $\mathbf{S}$  is full rank when the fluorophores of interest are not correlated, invertibility of  $\mathbf{E}_g$  means that the baseline and the fluorophores of interest are not correlated. The two excitation wavelengths should be chosen to insure that  $\gamma$  at these wavelengths is different from the ratios of the fluorophores of interest. From a signal processing point of view, this condition creates specific hot points for  $\gamma$  values at which  $\alpha$  cannot be estimated. Noises in the measurements  $\mathbf{m}$  and  $\mathbf{m}'$  enlarges these hot points into instability regions. It is assumed hereinafter that these conditions are satisfied. Defining  $\mathbf{E}_{gg} = (\mathbf{I} + \gamma \mathbf{E}) \mathbf{E}_g^{-1}$  and  $\bar{\mathbf{S}} = (\mathbf{S}^T \mathbf{S})^{-1}$ ,

$(\mathbf{M}^T \mathbf{M})^{-1}$  has the following expression:

$$(\mathbf{M}^T \mathbf{M})^{-1} = \begin{pmatrix} (1 + \gamma^2) \mathbf{E}_g^{-1} \bar{\mathbf{S}} \mathbf{E}_g^{-1} & -\mathbf{E}_g^{-1} \bar{\mathbf{S}} \mathbf{E}_{gg} \mathbf{S}^T \\ -\mathbf{S} \mathbf{E}_{gg} \bar{\mathbf{S}} \mathbf{E}_g^{-1} & \frac{(\mathbf{I} + \mathbf{S} \mathbf{E}_{gg} \bar{\mathbf{S}} \mathbf{E}_{gg} \mathbf{S}^T)}{1 + \gamma^2} \end{pmatrix} \quad (3.9)$$

and finally, the pseudo inverse  $\mathbf{M}^+$  is given by:

$$\begin{aligned} \mathbf{M}^+ &= \begin{pmatrix} \frac{\gamma^2 + \gamma \mathbf{E} + 2}{1 + \gamma^2} \mathbf{S}_u^{-1} \mathbf{S}^T & \mathbf{E}_g^{-1} (\mathbf{S}^T \mathbf{S})^{-1} (\mathbf{E}_g^{-1} \mathbf{E} + \gamma^2 \mathbf{E}_g^{-1} \mathbf{E} - \gamma \mathbf{E}_{gg}) \cdot \mathbf{S}^T \\ \frac{1}{1 + \gamma^2} - \mathbf{S} \cdot \frac{\gamma^3 \mathbf{E} + \gamma^2 \mathbf{I} + \gamma \mathbf{E}}{1 + \gamma^2} \cdot \frac{\mathbf{S}_u^{-1}}{1 + \gamma^2} \mathbf{S}^T & \frac{\gamma}{1 + \gamma^2} \mathbf{I} + \mathbf{S} \cdot \mathbf{E}_{gg} (\mathbf{S}^T \mathbf{S})^{-1} (\mathbf{E}_{gg} \frac{\gamma}{1 + \gamma^2} - \mathbf{E}_g^{-1} \mathbf{E}) \mathbf{S}^T \end{pmatrix} \\ &= \begin{pmatrix} \gamma \cdot \mathbf{E}_g^{-1} \mathbf{S}^+ & -\mathbf{E}_g^{-1} \mathbf{S}^+ \\ \frac{1}{1 + \gamma^2} (\mathbf{I} - \gamma \mathbf{S} \mathbf{E}_{gg} \mathbf{S}^+) & \frac{1}{1 + \gamma^2} (\gamma \mathbf{I} + \mathbf{S} \cdot \mathbf{E}_{gg} \mathbf{S}^+) \end{pmatrix} \end{aligned} \quad (3.10)$$

where  $\mathbf{S}^+ = \bar{\mathbf{S}} \mathbf{S}^T = (\mathbf{S}^T \mathbf{S})^{-1} \mathbf{S}^T$ .

### 3.2.3 Analytical estimation of the parameters

Using expression 3.10 for  $\mathbf{M}^+$ , the least-square solution for  $\boldsymbol{\alpha}$  and  $\mathbf{b}$  for a given  $\gamma$  are given by:

$$\boldsymbol{\alpha}_\gamma = \mathbf{E}_g^{-1} \mathbf{S}^+ \cdot (\gamma \mathbf{m} - \mathbf{m}') \quad (3.11)$$

$$\begin{aligned} \mathbf{b}_\gamma &= \frac{\mathbf{m} + \gamma \mathbf{m}'}{1 + \gamma^2} + \frac{\mathbf{S} \mathbf{E}_{gg} \mathbf{S}^+}{1 + \gamma^2} (\mathbf{m}' - \gamma \mathbf{m}) \\ &= \frac{1}{1 + \gamma^2} [\mathbf{m} + \gamma \mathbf{m}' - (\boldsymbol{\alpha}_{\gamma,1} (1 + \gamma \rho_1) \mathbf{S}_1 + \boldsymbol{\alpha}_{\gamma,2} (1 + \gamma \rho_2) \mathbf{S}_2)] \\ &= \frac{1}{1 + \gamma^2} [\mathbf{m} + \gamma \mathbf{m}' - \mathbf{S} \mathbf{E}_{gg} \mathbf{E}_g \boldsymbol{\alpha}_\gamma] \end{aligned} \quad (3.12)$$

### 3.2.4 Residual calculation and $\gamma$ estimation

With  $\phi(\gamma) = \left\| \mathbf{M} \begin{pmatrix} \boldsymbol{\alpha}_\gamma \\ \mathbf{b}_\gamma \end{pmatrix} - \tilde{\mathbf{m}} \right\|^2$ , equation 3.6 can now be written:

$$\min_\gamma \phi(\gamma) = \left\| \mathbf{r} \right\|^2 + \left\| \mathbf{r}' \right\|^2 \quad (3.13)$$

where  $\begin{pmatrix} \mathbf{r} \\ \mathbf{r}' \end{pmatrix} = \mathbf{M} \begin{pmatrix} \boldsymbol{\alpha}_\gamma \\ \mathbf{b}_\gamma \end{pmatrix} - \begin{pmatrix} \mathbf{m} \\ \mathbf{m}' \end{pmatrix} = \begin{pmatrix} \mathbf{S} \boldsymbol{\alpha}_\gamma + \mathbf{b}_\gamma - \mathbf{m} \\ \mathbf{S} \mathbf{E} \boldsymbol{\alpha}_\gamma + \gamma \mathbf{b}_\gamma - \mathbf{m}' \end{pmatrix}$ .

Using equations 3.11 and 3.12, one obtains:

$$\begin{aligned}
(1 + \gamma^2)\mathbf{r} &= (1 + \gamma^2)\mathbf{S}\boldsymbol{\alpha}_\gamma + \mathbf{m} + \gamma\mathbf{m}' - \mathbf{S}(\mathbf{I} + \gamma\mathbf{E})\boldsymbol{\alpha}_\gamma - (1 + \gamma^2)\mathbf{m} \\
&= \gamma\mathbf{SE}_g\boldsymbol{\alpha}_\gamma - \gamma(\gamma\mathbf{m} - \mathbf{m}') \\
&= \gamma\mathbf{SE}_g\mathbf{E}_g^{-1}\mathbf{S}^+(\gamma\mathbf{m} - \mathbf{m}') - \gamma(\gamma\mathbf{m} - \mathbf{m}') \\
&= \gamma(\mathbf{SS}^+ - \mathbf{I})(\gamma\mathbf{m} - \mathbf{m}'),
\end{aligned} \tag{3.14}$$

and

$$\begin{aligned}
(1 + \gamma^2)\mathbf{r}' &= (1 + \gamma^2)\mathbf{SE}\boldsymbol{\alpha} + \gamma\mathbf{m} + \gamma^2\mathbf{m}' - \gamma\mathbf{S}(\mathbf{I} + \gamma\mathbf{E})\boldsymbol{\alpha} - (1 + \gamma^2)\mathbf{m}' \\
&= \mathbf{SE}\boldsymbol{\alpha} - \gamma\mathbf{S}\boldsymbol{\alpha} + (\gamma\mathbf{m} - \mathbf{m}') \\
&= -\mathbf{SE}_g\boldsymbol{\alpha} + (\gamma\mathbf{m} - \mathbf{m}') \\
&= -\mathbf{SE}_g\mathbf{E}_g^{-1}\mathbf{S}^+(\gamma\mathbf{m} - \mathbf{m}') + (\gamma\mathbf{m} - \mathbf{m}') \\
&= (\mathbf{I} - \mathbf{SS}^+)(\gamma\mathbf{m} - \mathbf{m}') \\
-\gamma(1 + \gamma^2)\mathbf{r}' &= (1 + \gamma^2)\mathbf{r},
\end{aligned} \tag{3.15}$$

from which the following expression of  $\phi$  can be deduced:

$$\phi(\gamma) = \frac{\|(\mathbf{SS}^+ - \mathbf{I})(\gamma\mathbf{m} - \mathbf{m}')\|^2}{(1 + \gamma^2)} = \frac{\|(\gamma\mathbf{q} - \mathbf{q}')\|^2}{(1 + \gamma^2)} = \frac{\gamma^2\|\mathbf{q}\|^2 - 2\gamma\mathbf{q}^T\mathbf{q}' + \|\mathbf{q}'\|^2}{1 + \gamma^2}$$

where  $\mathbf{q} = (\mathbf{I} - \mathbf{SS}^+)\mathbf{m}$  and  $\mathbf{q}' = (\mathbf{I} - \mathbf{SS}^+)\mathbf{m}'$ .

As  $\phi$  is a rational function with no real pole and goes to  $+\infty$  when  $\gamma$  approaches  $\pm\infty$ , the optimal  $\gamma$  is a zero of:

$$\begin{aligned}
\frac{d\phi}{d\gamma} &= 2 \frac{(\gamma\mathbf{q}^T\mathbf{q} - \mathbf{q}^T\mathbf{q}')(1 + \gamma^2) - \gamma(\gamma^2\mathbf{q}^T\mathbf{q} - \gamma\mathbf{q}^T\mathbf{q}' + \mathbf{q}'^T\mathbf{q}')}{(1 + \gamma^2)^2} \\
&= \frac{2}{(1 + \gamma^2)^2} (\gamma(\mathbf{q}^T\mathbf{q} - \mathbf{q}'^T\mathbf{q}') + \gamma^2\mathbf{q}^T\mathbf{q}' - \mathbf{q}^T\mathbf{q}').
\end{aligned} \tag{3.16}$$

As the discriminant of the numerator

$$\Delta = (\mathbf{q}^T\mathbf{q} - \mathbf{q}'^T\mathbf{q}')^2 + 4(\mathbf{q}^T\mathbf{q}')^2 \geq 0 \tag{3.17}$$

is positive, there are two distinct roots:

$$\gamma_\epsilon = \frac{\mathbf{q}'^T\mathbf{q}' - \mathbf{q}^T\mathbf{q} + \epsilon\sqrt{\Delta}}{2\mathbf{q}^T\mathbf{q}'} \quad \text{with } \epsilon \in \{-1, 1\} \tag{3.18}$$

such as  $\frac{d\phi}{d\gamma}(\gamma_\epsilon) = 0$ .

The second derivative of  $\phi$  must be positive for the optimal  $\gamma$  and:

$$\begin{aligned}\frac{d^2\Phi}{d\gamma^2} &= \frac{d}{d\gamma} \left( \frac{2\mathbf{q}^T \mathbf{q}'}{(1+\gamma^2)^2} (\gamma - \gamma_{opt}^+)(\gamma - \gamma_{opt}^-) \right) \\ &= \frac{2\mathbf{q}^T \mathbf{q}'}{(1+\gamma^2)^4} \left[ (2\gamma - \gamma_{opt}^+ - \gamma_{opt}^-)(1+\gamma^2)^2 - (\gamma - \gamma_{opt}^+)(\gamma - \gamma_{opt}^-)4\gamma(1+\gamma^2) \right] \quad (3.19)\end{aligned}$$

and consequently

$$\frac{d^2\phi}{d\gamma^2}(\gamma_\epsilon) = \frac{\epsilon 2\sqrt{\Delta}}{(1+(\gamma_{-1})^2)^2} > 0 \Rightarrow \epsilon = 1 \quad (3.20)$$

and we conclude that  $\gamma^+$  is the optimal  $\gamma$ .

### 3.3 Conclusion

In this Chapter, we have described the model for estimating the contributions of PpIX to the fluorescence signal. This model is based on the analysis of fluorescence emission spectra obtained under multiple excitation wavelengths. We were able to derive an analytical solution for all the variables of our non linear estimation problem when there are two different excitation wavelengths. All the calculations carried out in this chapter made it possible to obtain the expressions of  $\gamma$  and then  $\alpha, b$  solving the estimation problem. In the next Chapter, we will compare this model with models from the state of the art.

## Chapter 4

---

# Performance evaluation of the Estimated Baseline model

---

The new Estimated Baseline model described in the previous chapter is now compared to state-of-the-art models. We consider the practical case of the estimation of contributions of PpIX in a fluorescence signal adapted from real clinical data. We consider the two different forms of PpIX described in [Montcel *et al.* (2013)b]. Besides the well-known PpIX fluorescence emission appearing with a maximum at 634 nm under excitation at 405 nm, another fluorescence band can be observed with a maximum at 620 nm under specific conditions [Montcel *et al.* (2013)b]. These two bands, hereinafter labeled PpIX620 and PpIX634, can be interpreted as bands corresponding to two different forms of PpIX [Montcel *et al.* (2013)b, Alston *et al.* (2018), Alston *et al.* (2019)], both ones having some interest. Parameters with subscript 1 denote quantities related to PpIX620 and parameters with subscript 2 denote quantities related to PpIX634.

We define a digital phantom calibrated on real High Grade Gliomas (HGG) and Low Grade Gliomas (LGG) data to get a realistic simulation environment. We now distinguish LGG with two pathological status, LGG and Healthy, from HGG with four pathological status : Solid Part, Dense Margins, Sparse Density Margins, and Healthy.

The baseline is defined as the non-5-ALA induced fluorescence, meaning the fluorescence that would be emitted in the same tissue without prior administration of 5-ALA to the patient. The performance of the EB model is estimated for various conditions of baseline fluorophores whose emission spectrum overlaps the one of PpIX. Performance metrics that we consider are the error of estimated PpIX contributions and the accuracy,

sensitivity and specificity of classification in the pathological status. Finally, the clinical diagnostic performance is assessed using glioma images synthesized by an experimentally calibrated digital phantom.

## 4.1 Multiple-excitation models for comparison purpose

Using the same notations as in Chapter 3, Section 3.2, we now describe multiple excitation models extrapolated from those of the literature.

### 4.1.1 Baseline Free Model (BF)

In this model, the baseline contribution is discarded. In the existing literature [[Montcel et al. \(2013\)b](#),[Ando et al. \(2011\)](#)] after having subtracted an exponential decay function, a least-square regression is used to estimate the fluorescence contributions of PpIX into the fluorescence signal from the model  $\mathbf{m} = \mathbf{S}\boldsymbol{\alpha}$ . Extrapolated to two excitation wavelengths, it can be written in matrix form as follows:

$$\tilde{\mathbf{m}} = \begin{pmatrix} \mathbf{S} \\ \mathbf{SE} \end{pmatrix} \boldsymbol{\alpha} \quad (4.1)$$

and parameters are estimated using a linear least square regression.

### 4.1.2 Gaussian Baseline Model (GB)

In this model from [[Alston et al. \(2019\)](#)], the contribution of the baseline into the fluorescence signal is a Gaussian function and a least-square method is used to estimate PpIX contributions  $\alpha_1, \alpha_2$  from the model defined in equation 4.2. Extrapolated to two excitation wavelengths, it can be written as follows :

$$\mathbf{m} = \alpha_1 \mathbf{S}_1 + \alpha_2 \mathbf{S}_2 + A \cdot \mathcal{G}(\mu, \sigma) \quad (4.2)$$

$$\mathbf{m}' = \alpha_1 \eta'_1 \mathbf{S}_1 + \alpha_2 \eta'_2 \mathbf{S}_2 + A' \cdot \mathcal{G}(\mu, \sigma) \quad (4.3)$$

where  $\alpha_1, \alpha_2, A, A', \mu, \sigma$  are estimated by a bounded least squares curve fitting method with  $\alpha_1 \in [0, 10^6]$ ,  $\alpha_2 \in [0, 10^6]$ ,  $A \in [0, 10^6]$ ,  $A' \in [0, 10^6]$ ,  $\mu \in [580, 605]$ ,  $\sigma \in [5, 100]$ . Bounds have been defined from [[Alston et al. \(2019\)](#)].

## 4.2 Digital phantom of fluorescence

In order to make a fair comparison of the new Estimated Baseline model (EB) with existing ones, we use a digital phantom of fluorescence that is not spatially resolved. This phantom includes PpIX as well as additive fluorophores which compose the baseline. The digital phantom is parameterized from *in vivo* data [[Alston et al. \(2019\)](#)] and experimental data obtained on liquid PpIX phantom made as in [[Alston et al. \(2018\)](#)],[Melø and Reisaeter](#)

(1986)].

We consider two excitation wavelengths  $\lambda_e = 405$  nm and  $\lambda'_e = 385$  nm which are the respective maxima of absorption spectrum of the two forms of PpIX considered here; the quantum yield ratio for PpIX620 is  $\eta'_1/\eta_1 = 1.62$ ; for PpIX634, it is  $\eta'_2/\eta_2 = 0.76$ , referring to [Jonin *et al.* (2020)]. The baseline is modeled as a Lorentzian function with various parameters: the quantum yield  $\gamma(\lambda_e) \in \mathbb{R}^1$ , central emission wavelength  $\lambda_{para} \in \mathbb{R}^1$ , standard deviation  $\sigma_{para} \in \mathbb{R}^1$ , and amplitude  $A \in \mathbb{R}^1$ .

A two-part noise calibrated on experimental data is included in the fluorescence simulation phantom: a Poisson noise  $\mathcal{P}$  mimics photon noise and an additive Gaussian white noise  $\mathcal{N}$  mimics electronic noise. This leads to the following function representing the generated spectrum:

$$\mathbf{m} = \mathcal{P} [\alpha_1 \eta_1 \mathbf{S}_1 + \alpha_2 \eta_2 \mathbf{S}_2 + \mathbf{b}(\lambda_e)] + \mathcal{N}, \quad (4.4)$$

where

$$\mathbf{b}(\lambda_e) = \gamma(\lambda_e) \cdot A \cdot \frac{2}{\pi \sigma_{para}} \frac{1}{1 + \left( \frac{\lambda - \lambda_{para}}{\frac{\sigma_{para}}{2}} \right)^2}.$$

All results given in this work have been computed over  $10^5$   $\alpha$  random draws equally split in 100x100 bins to map the region  $\alpha \in [0, 2] \times [0, 2]$ . Each region of the  $\alpha$  plane is associated with a pathological status (cf. Fig. 4.2). We focus on the boundary between healthy and tumoral tissues, which corresponds to an area of this plane. All random draws were performed with Gaussian distributions linked with pathological status, whose parameters are extracted from previous *in vivo* works [Alston *et al.* (2019)].

### 4.3 Sets of Baseline parameters

Seven baseline datasets have been simulated. These datasets correspond to different scenarii for the application of our method in clinical practice. An example of fluorescence spectrum for some of the baseline sets are plotted in Fig. 4.1. The simulation parameters are given in Table 4.1 where  $\mathcal{U}(a, b)$  is a uniform distribution between  $a$  and  $b$ , and  $\Gamma(k, \beta)$  is a gamma distribution with shape factor  $k$  and scale factor  $\beta$ .

The first three sets of parameters are defined to study the robustness regarding the amplitude or width parameters of the fluorescence spectrum attached to the baseline. The Outside and Inside sets allow studying the influence of the position of the baseline central wavelength regarding the spectral emission band of PpIX. The Inner and Across sets are defined to study the impact of the baseline fluorescence quantum yield. This parameter is particularly critical regarding the instability areas of EB (see 3.2.2). The Inner set models baseline quantum yields ranging out of the PpIX instability spots, whereas the Across set models intersection of baseline and PpIX quantum yields ranges.

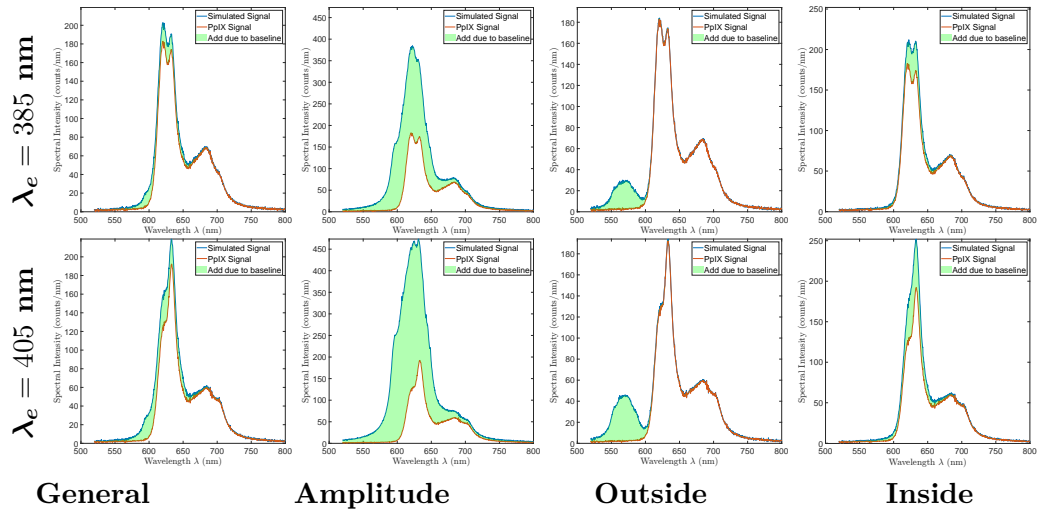


Figure 4.1: Measurement signal (in blue) and PpIX signal (in orange) for each baseline dataset in row and for each excitation wavelength in column. The green area corresponds to the signal addition due to the baseline.

#### 4.4 Classification method

In order to reach the final aim of pathological status prediction, we evaluated the ability to classify tissues from the estimated contributions of PpIX to the fluorescence spectrum. The same simulated measurements  $\tilde{m}$  have been independently processed by each estimation model, and estimated PpIX contributions  $\alpha^*$  have been classified with a naive Bayesian classifier [Cheeseman *et al.* (1988)].

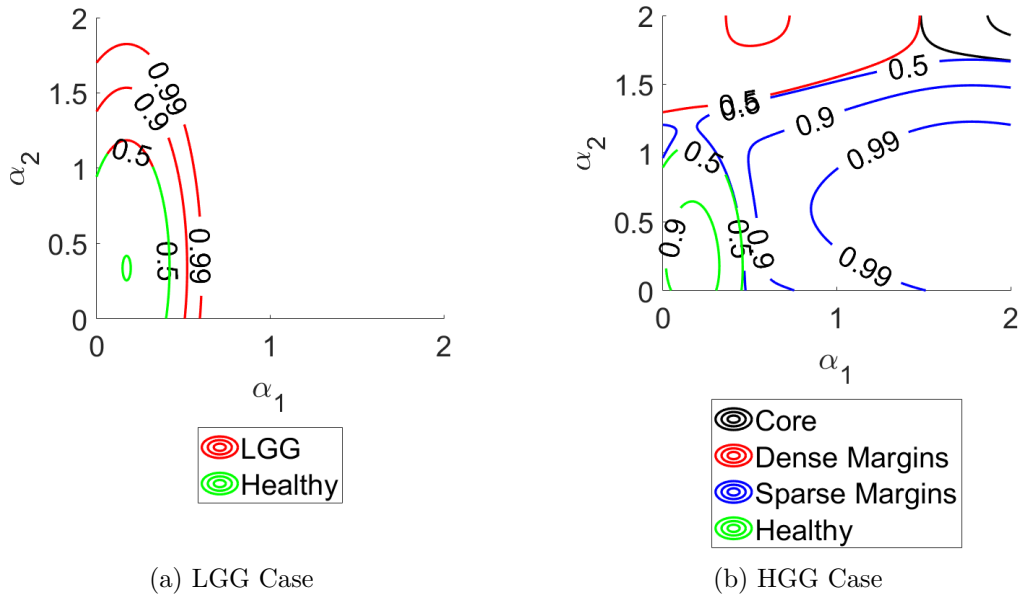


Figure 4.2: Probability Maps with categories identified.

The *a priori* knowledge of categories given in [Alston *et al.* (2019)] has been used to define

Name of the dataset	Parameters	Description
General	$A = \Gamma(4.102, 82.6840)$ u.a. $\lambda_{para} = \mathcal{U}(590, 650)$ nm $\sigma_{para} = \mathcal{U}(0, 25)$ nm $\gamma = \mathcal{U}(0.1, 1.125)$	General case with all the existing problems due to an endogenous fluorophore of low amplitude compared to PpIX
Amplitude	$A = \Gamma(4.102, 826.684)$ u.a.	Study of the influence of endogenous fluorophore's ** amplitude. For example, the amplitude of the lipopigments fluorescence signal increases with aging [Porta (2002), Jolly <i>et al.</i> (2002)].
Width	$\sigma_{para} = \mathcal{U}(0, 50)$ nm	Study of the influence of the spectral width of the endogenous fluorophore **. For example the spectral width of the lipofuscin classically extends on 80 nm [Croce <i>et al.</i> (2017)] but in certain studies it is extended well beyond [Black <i>et al.</i> (2021)].
Outside	$\lambda_{para} = \mathcal{U}(550, 590)$ nm $\gamma = \mathcal{U}(0.1, 3.00)$	Study of the influence of the central wavelength of the endogenous fluorophore ** located in the emission range of the PpIX. For example, water-soluble porphyrins have an emission maximum near the PpIX emission range [Dietel <i>et al.</i> (1997), Dysart and Patterson (2006), Montcel <i>et al.</i> (2013)a, Bravo <i>et al.</i> (2017)].
Inside	$\lambda_{para} = \mathcal{U}(620, 640)$ nm $\gamma = \mathcal{U}(0.1, 3.00)$	
Inner	$\gamma = \mathcal{U}(1, 1.2)$	Study of the influence of the quantum yield of the endogenous fluorophore **. For example, endogenous fluorophores such as water-soluble porphyrins may have quantum yields close to those of PpIX620 and PpIX634.
Across	$\gamma = \mathcal{U}(0.6, 0.8)$	

Table 4.1: Parameters used for the simulation of the seven baseline datasets. Only differences from "General" are specified for the following six datasets. \*\*: In this Table, endogenous fluorophore corresponds to non 5-ALA-induced fluorophore.

*a priori* probability laws associated to each category. Ground truth PpIX contributions  $\alpha$  used in the phantom have also been classified to serve as reference for classification performance. For each bin, we compute the accuracy  $acc$  by using the formula 4.5 below where  $c$  is a category,  $c^*$  an estimated category,  $C$  the set of classes,  $s$  a sample,  $S_c$  the set of samples in class  $c$ ,  $c_s^*$  the estimated category for the sample  $s$ ,  $N$  the total number

of samples in a bin, and  $N_c$  the number of samples of the bin that belong to the class  $c$ .

$$acc = \sum_{c \in C} \left( \frac{\sum_{s \in S_c} (c_s^* = c)}{N_c} \frac{N_c}{N} \right) = \sum_{c \in C} p(c^* = c) \cdot p(c) \quad (4.5)$$

$p(c)$  follows a gaussian probability law whose parameters are defined in [Alston *et al.* (2019)]. The accuracy is computed in LGG or HGG cases.

By referring to Fig. 4.2, we computed the probability map of categories of the HGG case, resp. LGG, in the  $(\alpha_1, \alpha_2)$  plane to help interpret the accuracy maps. For each bin of any map hereafter, the color is related to the accuracy value, the greener the higher accuracy. This allows to associate a most probable category to each region of the  $(\alpha_1, \alpha_2)$  plane. The region in the bottom-left corner of each map corresponds to the healthy tissue region (refer to Fig. 4.2). One can notice that the probability 0.5 represents the border between two different categories of the  $(\alpha_1, \alpha_2)$  plane region.

## 4.5 Errors Measurement

As a reminder, fluorescence signal by non-5-ALA-induced fluorophores varies a lot, which leads to important crosstalks with PpIX. Each set of baseline parameters represents one example among all possible spectra. We now look at the estimation error on the parameters of interest provided by each model and for all these sets.

### 4.5.1 Estimation Error on $\alpha$

In Fig. 4.3, one can see the map of  $\alpha$  estimation error by each model for all the baseline parameters sets. Each column corresponds to an estimation model and each row to a set of baseline parameters. At first sight, one can notice that the Estimated Baseline model (EB) has a small error for each baseline set except Across. Considering Amplitude, Width and Inside datasets, one can see that EB has the lowest error compared to other models. It highlights the robustness to the baseline's variability of EB compared to state-of-the-art (Baseline Free (BF<sub>1</sub>), Gaussian Baseline (GB<sub>1</sub>)) models even extrapolated at two excitation wavelengths (BF<sub>2</sub>, GB<sub>2</sub>). Looking at the Outside dataset, one notice that EB yields a greater error than the other models, but this dataset refers to a clinical case which is already solved. Comparing Inner with Across datasets, we notice that the error yielded by state-of-the-art models remains constant while the one yielded by EB increases a lot. This is due to the EB instability when  $\gamma$  is close to  $\rho_1$  or  $\rho_2$ .

In Fig. 4.4 are presented the mean value and the standard deviation of the absolute estimation error between the ground truth  $\alpha$  used to generate spectra with the numerical phantom and  $\alpha^*$  estimated using a given method on a specific baseline set of parameters (see Table 4.1). In agreement with Fig. 4.4, one can notice that concerning General, Amplitude and Width datasets, existing models are all quite insensitive to Width but very sensitive to Amplitude and that EB<sub>2</sub> remains insensitive to Width while solving the

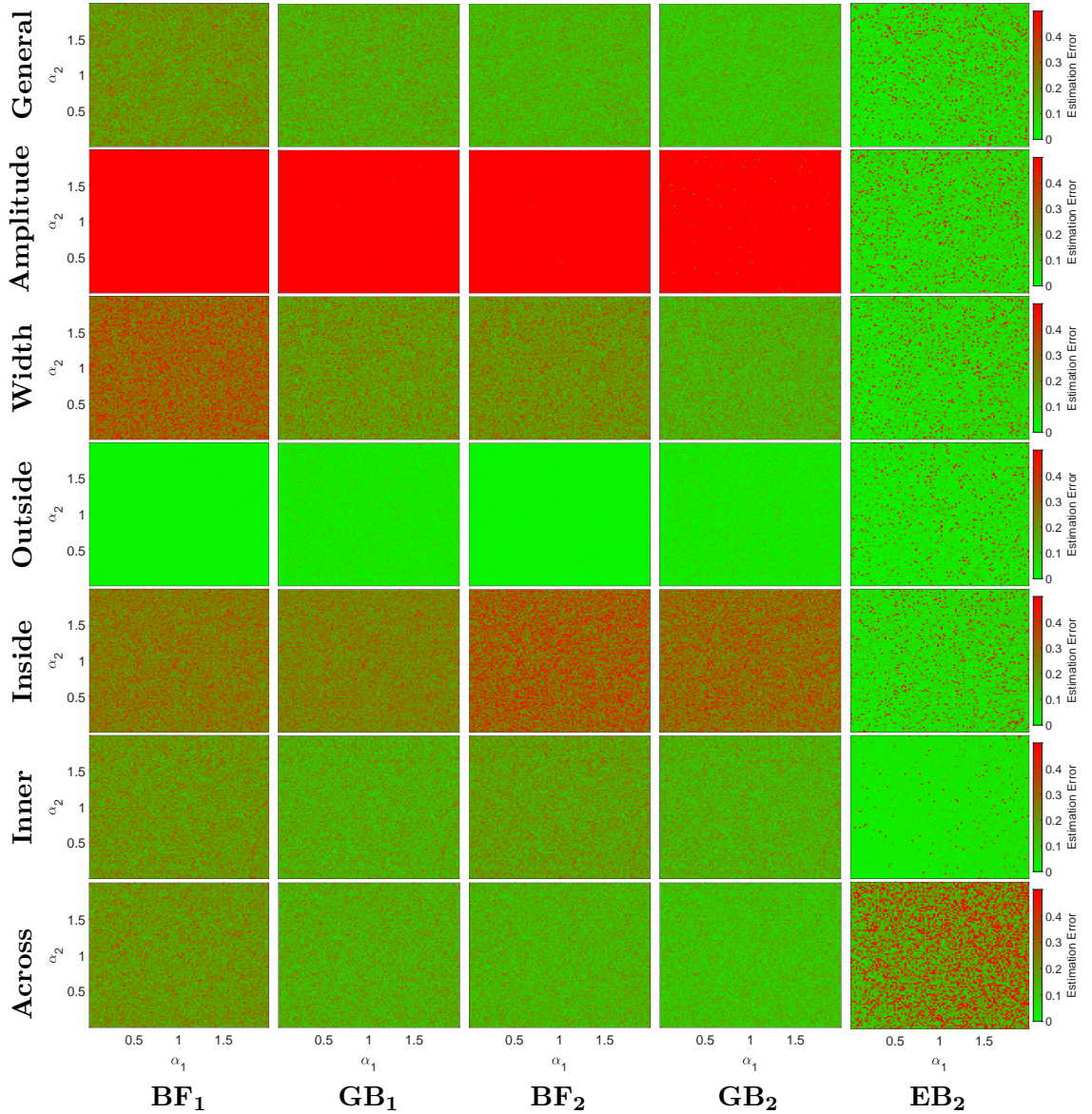


Figure 4.3: Map of  $(\alpha_1, \alpha_2)$  absolute estimation Error for each estimation method in row : Baseline Free (BF), Gaussian Baseline (GB), and Estimated Baseline (EB). Each column represent the same baseline dataset defined in Table 4.1. Each map has been computed by 100000 drawings equally split in 100x100 bins. The more red is the color, the greater the absolute error of estimation and the greener the color, the lower the absolute error of estimation.

Amplitude issue.

Considering the Outside dataset, existing models work well because the emission band of the baseline is far from the PpIX emission spectrum: crosstalk is low, the contributions of PpIX are not impacted by the presence of the baseline. Comparing the Inside dataset with the Outside dataset, we notice that the error made by the state-of-the-art models is multiplied in average by at least a factor 5. In the same time, EB model varies very little: the error is in average increased by a factor 1.24. EB is not very sensitive to Inside/Outside

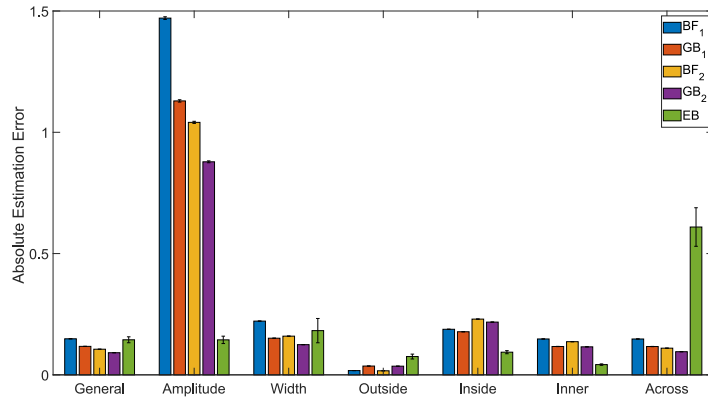


Figure 4.4: Mean and standard error of Absolute estimation Error of  $\alpha$ . Each color bar corresponds to an estimation method, and each group corresponds to a set of baseline parameters (refer Table 4.1). BF<sub>1</sub>, GB<sub>1</sub>, BF<sub>2</sub>, GB<sub>2</sub> refer to state-of-the-art methods and EB is our proposed method.

datasets since it has no *a priori* on the spectrum of the baseline, while existing methods are very sensitive to the baseline emission band.

For Inner dataset, EB has the lowest error and, at the same time, other models are not better than the General case. The Inner dataset is chosen to be favorable for EB since the baseline quantum yield  $\gamma$  is decorrelated from those of PpIX. Because existing models do not consider it, they are insensitive to changes of  $\gamma$ . In opposition, Across dataset is chosen to be unfavorable for EB. One can notice the significant increase of EB's error when the quantum yield of the baseline approaches those of PpIX. This is a direct consequence of specific hot areas explained in previous chapter, Section 3.2.2. It seems important to point out that the case modeled by the Across dataset is not very plausible physically because it considers a fluorophore with a quantum yield  $\gamma$  close to PpIX without the spectral shape corresponding to the one of PpIX. Moreover, if this case happens, one solution to tackle this issue can be to change  $\lambda_e$ , so the hotpoints will be outside the area of interest.

EB is not always the model that has the lowest error, especially when the *a priori* are in favor of existing models (see for example the Outside dataset). In any case, it maintains a low error even when the amplitude increases. The Across case is not very plausible physically. A merge of Across and Inside datasets would be more physically plausible where fluorophores are very close to PpIX. We assume that all the models would become bad because the case is very difficult for all models, even EB would not solve this difficulty.

#### 4.5.2 Impact of $\alpha^*$ on classification

In Fig. 4.6, one can see with both LGG and HGG that with the Amplitude dataset, EB is the only model able to correctly classify Healthy samples when the baseline ampli-

tude increases. Comparing single- and two- excitation wavelength models for Amplitude dataset, one can notice that two excitation wavelength models ( $GB_2$ ,  $BF_2$ ) improve a little the correct classification of Healthy class samples located in the center of the region. It is confirmed by an increase of  $BF_2$ , resp.  $GB_2$ , accuracy compared to  $BF_1$ , resp.  $GB_1$ , in Fig. 4.5. Thus, we assume that the success of EB is rather due to the estimated baseline than the multiple excitation wavelengths. Still looking at Fig. 4.6 in the case of HGG, the border between Low Density Margins, High Density Margins and Core is thicker for  $GB_1$ ,  $GB_2$  and  $BF_1$ ,  $BF_2$  models than for EB which is a direct consequence of the estimation error by these models (refer to Fig. 4.3). In addition, the shading effect reveals a loss in classification precision for Core and Margins categories. In the case of LGG, the ability to classify is lost because there are only two categories. For the Width dataset, we notice that EB is the only model whose accuracy remains constant with both LGG and HGG. Thus, EB seems to be the most relevant model if the baseline amplitude or width has an important variability.

We now study the impact of the baseline central wavelength on accuracy (see Fig. 4.5).

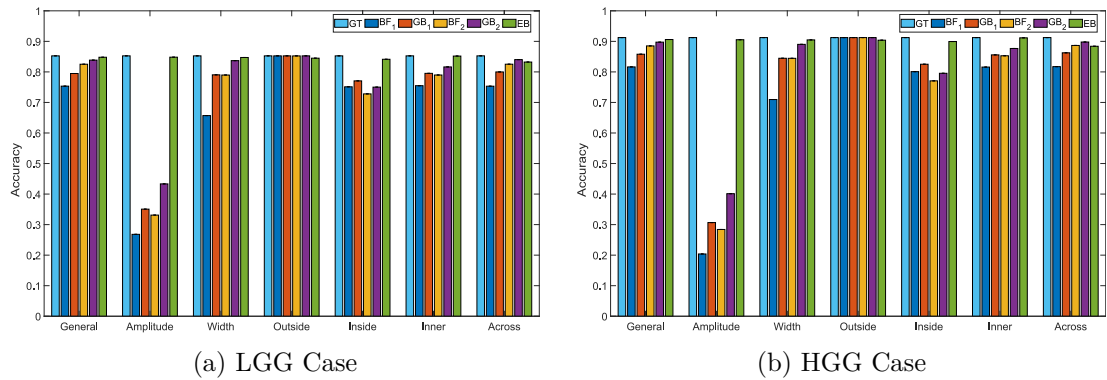


Figure 4.5: Mean Accuracy of the ROI ( $0 \leq \alpha_1 \leq 0.25$ ,  $0 \leq \alpha_2 \leq 0.75$ ). Each color corresponds to the same model and each group to a specific set of baseline parameters. GT refers to Ground Truth,  $BF_1$ ,  $GB_1$ ,  $BF_2$ ,  $GB_2$  refer to state of the art methods and  $EB_2$  is our proposed method.

Considering Outside dataset, all models have similar performances. One can notice for Inside dataset that EB is the only model whose accuracy overpasses 75%. Despite the estimation error being higher with EB than with existing models, the classification performance is equivalent in the Outside dataset where there is no crosstalk between baseline and PpIX fluorescence spectra. We can thus consider using EB even when there is no crosstalk issue since it is as good as models from the state of the art. This result is striking because EB was not particularly expected to perform in this case. This result reveals the strength of EB compared to other models: it is less sensitive to the emission band of the baseline.

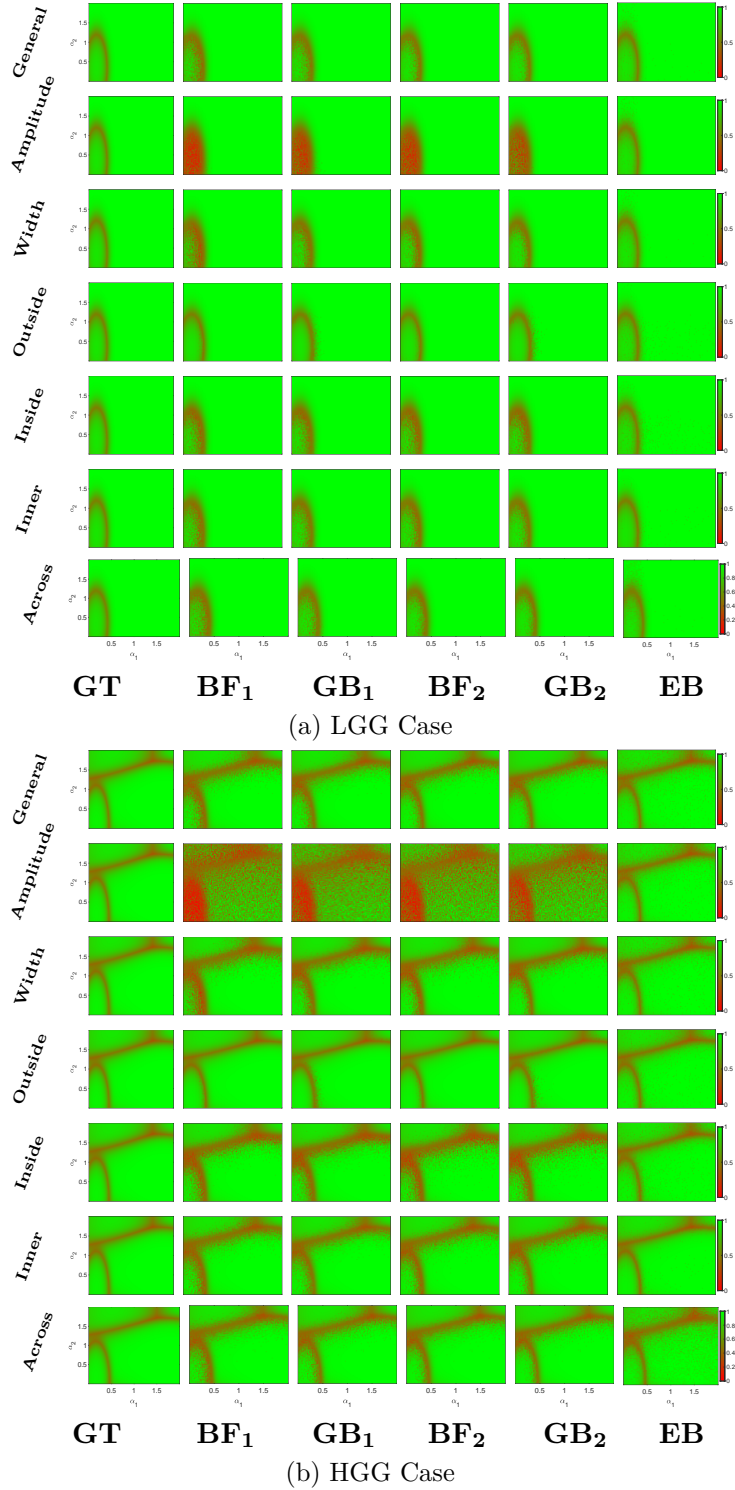


Figure 4.6: Accuracy Map for each estimation method in column : BF<sub>1</sub>, GB<sub>1</sub>, BF<sub>2</sub>, GB<sub>1</sub> refer to state-of-the-art methods and EB is our proposed method. We classify on one side Low Grade Glioma (a) and on the other side High Grade Glioma (b). Rows give the set name defined in Table 4.1.

Let us assess the impact of baseline fluorescence quantum yield on accuracy. For the Inner dataset, the accuracy is the same as in the General dataset for all models. Thus, the drop of error with EB in this case has no effect on the classification. Indeed, EB has a better accuracy than the existing models when the baseline amplitude increases, and it keeps an accuracy equivalent to those of existing models in the unfavorable case of Across dataset where the baseline quantum yield  $\gamma$  is close to those of the PpIX. One can imagine using EB all the time even in the cases modeled by the Across dataset, since at worst it will be equivalent to state of the art performances.

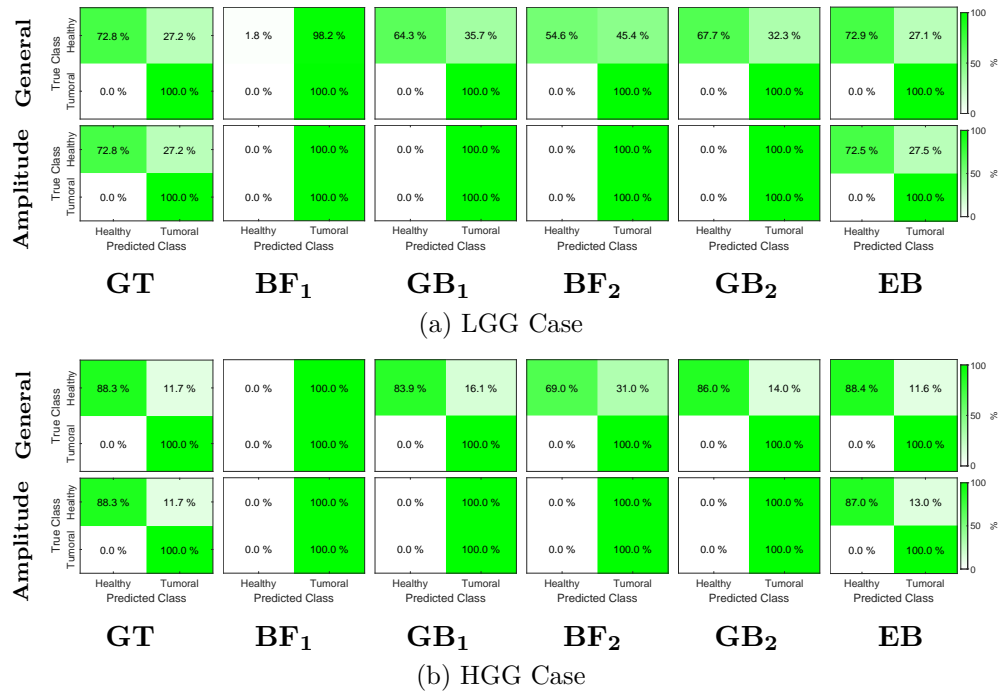


Figure 4.7: Confusion matrices of healthy/tumoral classification on images of simulated glioma accounting for the spatial point spread function of the probe. In the case of LGG and HGG, each row corresponds to a specific baseline dataset referring to Table 4.1 and each column to an estimation model. Each confusion matrix is row normalized. Inside each confusion matrix, each row corresponds to the true class while each column to the predicted class.

Because the final aim is to determine the boundary between healthy tissues and margins, we simplify the classification task into two categories: tumoral and healthy.

In Fig. 4.7, one can see confusion matrices in LGG and HGG for General and Amplitude datasets accounting for the measurement probe. In each confusion matrix, the bottom-right corner corresponds to the correctly predicted tumoral category and the top-left corner to the correctly predicted healthy category. One can notice that the classification task is an ill-posed problem because anti-diagonal terms of the confusion matrix associated to Ground Truth (GT) are not zero. In LGG and HGG, for both baseline parameters sets, all models are as performant as the GT for predicting truly tumoral samples. In the Gen-

eral dataset,  $\text{BF}_1$  is unable to correctly predict truly healthy samples, and  $\text{EB}$  has the closest percentage value to GT. Considering Amplitude dataset in both LGG and HGG, only  $\text{EB}$  is able to correctly predict truly healthy samples. In HGG, only 13%, resp. 11.7%, of healthy samples are predicted as tumoral with  $\text{EB}$ , resp. with GT, while it is 100% with other models. The classification error of  $\text{EB}$  may be caused by its instability when  $\gamma$  is close to  $\rho_1$  or  $\rho_2$ . The classification error of other models highlights the lack of robustness to the baseline's variability of models with an analytic *a priori* on the baseline.

To conclude, this work proposed an estimated baseline model whose robustness to the baseline variability has been demonstrated in terms of parameters estimation error and healthy/tumoral classification.

#### 4.5.3 Clinical Practice performance on synthesized glioma image

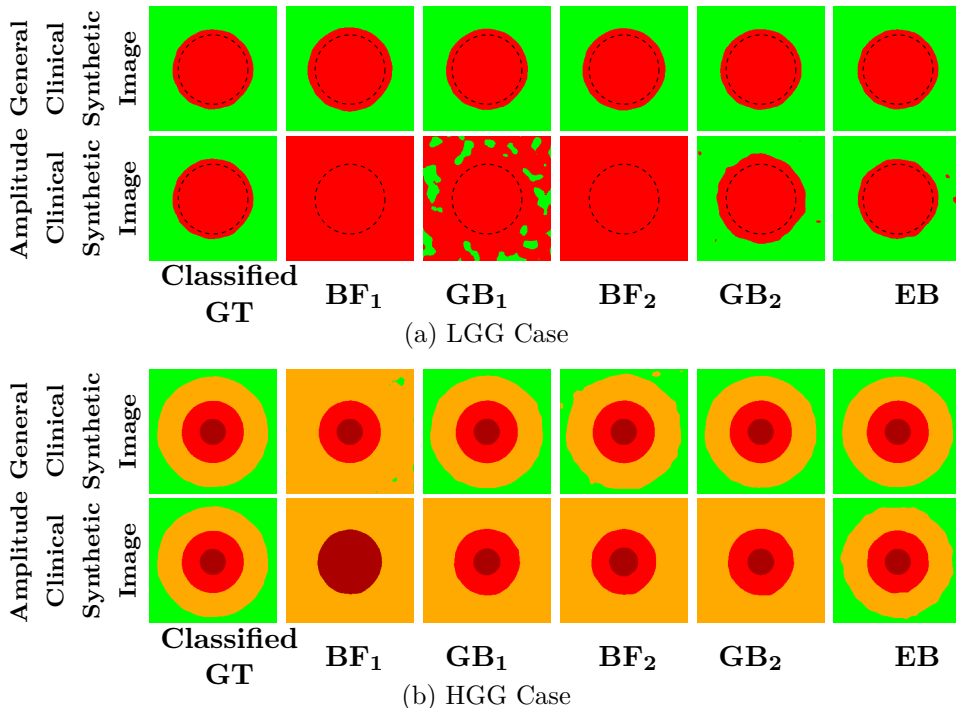


Figure 4.8: Results on a 300x300 clinical synthetic images of Low Grade Glioma (a) and High Grade Glioma (b). Row name corresponds to an estimation models : GT refers to Ground Truth,  $\text{BF}_1$ ,  $\text{GB}_1$ ,  $\text{BF}_2$ ,  $\text{GB}_2$  refer to state of the art methods and  $\text{EB}_2$ . Columns gives the set name defined in Table 4.1 : the baseline's amplitude increased when going from General to Amplitude dataset. Red color refers to tumor area while green color refers to healthy area. In HGG Case (b), orange color refers to sparse tumor margins.

In order to measure the final impact of this study on the clinical practice, we applied the "estimation + classification" pipeline to an image of glioma considering a real experimental system. Each glioma is either LGG (Fig. 4.8a) or HGG (Fig. 4.8b). Clinically, the average size of the glioma is 3 cm. We set its size to 75% of image size, the pixelsize corresponds to 130  $\mu\text{m}$ , a typical scale at the tissue level. A single spectrum is generated in each

pixel according to the pixel's ground truth category. The size of a measurement probe is 4 mm (30 pixels in the image) which corresponds to typical size of spectroscopic probe or hyperspectral imaging system in the litterature [Alston *et al.* (2019), Widhalm *et al.* (2019), Bravo *et al.* (2017), Valdés *et al.* (2011), Kim *et al.* (2010)a, Haj-Hosseini *et al.* (2010), Ishihara *et al.* (2007), Utsuki *et al.* (2006), Stummer *et al.* (2000)]. Images of Fig. 4.8 account for the spatial point spread function of the probe: results are convolved with a Gaussian kernel of size 30x30 pixels. To numerically estimate the classification, we simplify the problem into two classes, healthy or tumoral. For all parameters sets, we thus calculate the *sensitivity*, also called *true positive rate* (TPR), and *specificity*, also called *true negative rate* (TNR), of each classification. These metrics are relevant because sensitivity refers to the model's ability to correctly detect tumor tissues, while specificity relates to the model's ability to correctly detect healthy tissues. Case General 1 px of Table 4.2 is equivalent to what is described in Section 4.5.2 because the convolution effect of the probe is not considered. Let us notice that the classification task is an ill-posed problem because the sensitivity and specificity of ground truth is unable to reach 1.

We first focus on the Amplitude and General datasets. Corresponding sensitivity (TPR) and specificity (TNR) values are given in Tables 4.2a, 4.2b. We notice a strong impact of the measurement probe's convolution on the classification sensitivity (TPR) which goes from approximately 80% to 100% with a degradation of spatial resolution. In the same way, the specificity (TNR) increases from 59% to 73 % at best. This is relevant in terms of clinical practice since the neurosurgeon removes millimeter-sized pieces that therefore give very high sensitivity. Moreover, previous results are confirmed on simulated glioma: only EB is able to correctly distinguish healthy tissues from tumoral ones when the amplitude of baseline increases.

Model	General 1px		General CSI		Amplitude CSI		Outside CSI		Inside CSI		Inner CSI		Across CSI	
	TNR	TPR	TNR	TPR	TNR		TNR		TNR		TNR		TNR	
Ground Truth	0.58	0.79	0.88	1.00	0.88		0.88		0.88		0.88		0.88	
BF <sub>1</sub>	0.41	0.86	0.00	1.00	0.00		0.00		0.00		0.00		0.00	
GB <sub>1</sub>	0.46	0.84	0.84	1.00	0.00		0.84		0.00		0.84		0.84	
BF <sub>2</sub>	0.48	0.83	0.69	1.00	0.00		0.69		0.00		0.03		0.56	
GB <sub>2</sub>	0.51	0.82	0.86	1.00	0.00		0.86		0.00		0.84		0.86	
EB	<b>0.58</b>	0.79	<b>0.88</b>	<b>1.00</b>	<b>0.87</b>		<b>0.88</b>		<b>0.87</b>		<b>0.88</b>		<b>0.88</b>	

(a) LGG Case

Model	General 1px		General CSI		Amplitude CSI		Outside CSI		Inside CSI		Inner CSI		Across CSI	
	TNR	TPR	TNR	TPR	TNR		TNR		TNR		TNR		TNR	
Ground Truth	0.60	0.89	0.73	1.00	0.73		0.73		0.73		0.73		0.73	
BF <sub>1</sub>	0.43	0.93	0.02	1.00	0.00		0.69		0.00		0.02		0.02	
GB <sub>1</sub>	0.48	0.92	0.64	1.00	0.00		0.78		0.15		0.64		0.64	
BF <sub>2</sub>	0.49	0.91	0.55	1.00	0.00		0.71		0.44		0.25		0.51	
GB <sub>2</sub>	0.52	0.91	0.68	1.00	0.00		0.75		0.55		0.65		0.67	
EB	<b>0.59</b>	<b>0.89</b>	<b>0.73</b>	<b>1.00</b>	<b>0.73</b>		<b>0.73</b>		<b>0.73</b>		<b>0.73</b>		<b>0.73</b>	

(b) HGG Case

Table 4.2: Sensitivity (TPR) and Specificity (TNR) values. For all clinical synthetic images (CSI) datasets, each model's sensitivity is equal to 1.

One can see a loss of specificity when comparing Inside with Outside dataset for all models except EB. This goes along with previous results. Specificities of the Outside

dataset are higher than in the General dataset. This is due to the difference of baseline positions between the two datasets. In the HGG case, we notice that specificity of  $\text{GB}_1$  and  $\text{GB}_2$  is better than the one of Ground Truth. This bias of the method has no physical meaning and is due to the fact that the Lorentzian function is narrower than the Gaussian function. Thus, when the Lorentzian function is positioned where the Gaussian function of the GB models can be (i.e., the Outside dataset), then the Gaussian function modeling the baseline of GB models have higher values than the Lorentzian function at the level of the PpIX peaks. As a result,  $\alpha$  is systematically underestimated and we have this effect of a fall in the number of true healthy identified as tumoral, thereby an increase in specificity.

Looking at Inner and Across datasets, we notice that the specificity of each model is not impacted by any change related to these datasets. EB has the best specificity in the unfavorable case of Across dataset where the baseline quantum yield  $\gamma$  is close to those of the PpIX.

## 4.6 Conclusions

We proposed a novel method using several excitation wavelengths to estimate the PpIX fluorescence-related biomarkers contributions which make our method free from any *a priori* on the fluorescence emission spectrum of the baseline. We derived analytical expressions for the least square estimator of the proposed model. This allows our method to be computationally efficient and free from the use of iterative non linear estimation procedure.

We have shown that the EB method better estimates the pathological status of the measured tissue when baseline amplitude increases: it keeps a specificity almost equal to the one of the ground truth when the one of existing models drops to 0. In addition, this new model is as accurate as existing models in unfavorable cases, e.g., when baseline quantum yield is near PpIX ones. This new model reveals the potential of multiple excitation wavelengths to increase the classification sensitivity of fluorescence measurements.

Future work may focus on hot spot management, extending this study to more than two excitation wavelengths, and extending the comparison of EB with state-of-the-art methods on clinical data acquired by [Alston (2017)].

### III Advances in quantitative methods

---



---

The previous section attempted to identify the relative concentration, also called contributions, of the two forms of PpIX. The following part aims to go a step further by trying to quantify the absolute concentration of each of these substances. The methods to be used are no longer the same: if, to determine the relative concentration of each, an analysis of the shape of measured spectra is sufficient, in this new approach it is necessary to exploit the signal in an absolute way, i.e. by considering the effects of the propagation medium on the signal in addition to its amplitude and its spectral shape. It is therefore necessary to be able to estimate the effects of the medium and then the quantity of fluorophores having generated the signal. To summarize, it is necessary to be able to model rigorously the light trajectories throughout the process, from the light source to the optical sensor. For this, chapter 5 describes first how the radiative transfer equation is established in a general way. In a second time, the emphasis is put on the method of resolution by discrete ordinates in the case of plane-parallel geometry with an exhaustive description of boundary conditions. Finally, the fluorescent case is also described mathematically. Chapter 6 is dedicated to the validation of the discrete ordinates solver we have implemented. As said in Chapter 2, some optical models such as the Kubelka-Munk model or the diffusion approximation (also called P1 approximation) result from simplifying assumptions in the resolution of the radiative transfer equation (RTE) that allow in particular to fix the value of some parameters. Thus, Chapter 7 focuses on the study of one of these fixed parameters, the internal reflectance, for the Kubelka-Munk model and its direct application on a case related to the subject of the thesis.



# Chapter 5

---

## Resolution of Radiative Transfer with discrete ordinate method

---

### 5.1 Introduction

The transport theory of light diffusion (also called radiative transfer formalism) is a powerful method to model light scattering through a turbid medium. It takes into account absorption and multiple scattering (possibly anisotropic), but neglects any type of wave effect (diffraction and interference effects) except polarization. The specific intensity (in the vocabulary of the radiative transference theory) or spectral luminance (in the vocabulary of radiometry) can be calculated with this approach, allowing to investigate in detail angular dependent effects.

The radiative transfer approach has been extensively investigated since the 50's, following the pioneering work of Chandrasekhar (Nobel Prize in 1983 for his theoretical studies of the physical processes of importance to the structure and evolution of the stars). It has many applications in the field of tissue optics, marine biology, paper optics, virtual reality (BRDF modeling) and the propagation of radiant energy in the atmosphere of planets, stars and galaxies.

This chapter is largely inspired by the book [[Ishimaru \(1978\)](#)]. Details about the boundary conditions have been more clearly specified in this chapter, in particular Fresnel reflection which are neglected in scattering media such as gas or the atmosphere, but is crucial in scattering materials such as biological tissues.

## 5.2 Physical quantities in transport theory

Before looking specifically at the physical quantities of the theory of radiative transfer, it seemed important to recall some basic radiometric elements. Thus, Fig. 5.1 reminds the definition of the polar angle  $\theta$  and the azimuthal angle  $\phi$  in spherical coordinates.

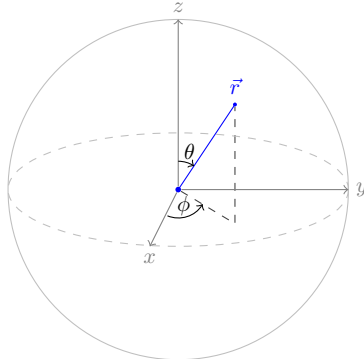


Figure 5.1: Definition of angles  $\theta$  and  $\phi$  in a system of spherical coordinates

In addition, we briefly remind the geometric concepts of *solid angle* and *geometrical extent*, which are extensively described in the book [Hébert (2022)].

The infinitesimally small solid angle  $d^2\Omega(\theta, \phi)$  is defined as the angle which, seen from the center of a sphere, includes an infinitesimal piece of the sphere's surface. Its numerical value is equal to ratio of the size of the infinitesimal area over to the square of the sphere's radius. The elementary solid angle denoting a given direction  $(\theta, \phi)$  of the sphere expressed in spherical coordinates is:

$$d^2\Omega(\theta, \phi) = \sin(\theta)d\theta d\phi \quad (5.1)$$

The geometrical extent is a second geometrical concept which aims at characterizing the size of light beams.

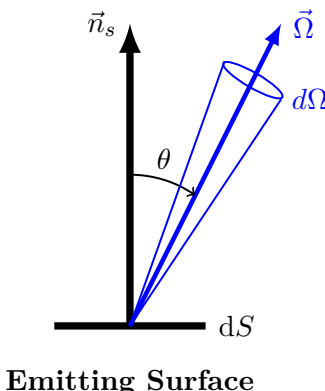


Figure 5.2: Geometrical extent  $d^3G$  describing a large pencil of light based on a infinitesimal area  $dS$  on a surface and a solid angle  $d^2\Omega$  in the spatial direction  $\vec{\Omega}$ .

As in Fig. 5.2, let us consider an infinitesimal surface element,  $dS$ , with a normal  $\vec{n}_s$  on which the light density is uniform and an infinitesimal solid angle  $d^2\Omega$  along a direction  $\vec{\Omega}$  which makes an angle  $\theta$  with the normal  $\vec{n}_s$ . The geometrical extent is then:

$$d^3G = dS \cos(\theta) d^2\Omega \quad (5.2)$$

Thus, in a system of spherical coordinates, the geometrical extent  $dG$  of this light crossing  $dS$  is defined as:

$$d^3G = dS \cos(\theta) \sin(\theta) d\theta d\phi \quad (5.3)$$

### 5.2.1 Radiance

The physical quantities used in radiative transfer are the same as in radiometry. The most important quantity is the *radiance*  $I$ , also sometimes called brightness, *luminance* in French. Radiance is defined as the density of power per unit geometrical extent, i.e., the power flowing within a solid angle  $d\Omega$  around a direction  $\vec{\Omega}$  through a surface  $dS$  located around a point  $A$  is (see Fig.5.3):

$$d^3\Phi = I(A, \vec{\Omega}, \nu) \cos(\theta) dS d^2\Omega \quad (5.4)$$

with  $\cos(\theta) = \vec{n} \cdot \vec{\Omega}$ . The unit of radiance  $I$  is  $\text{Wm}^{-2}\text{sr}^{-1}$  and the unit of the directional radiative power  $\Phi$  is watts (W). Radiance can be defined over any spectral band, large

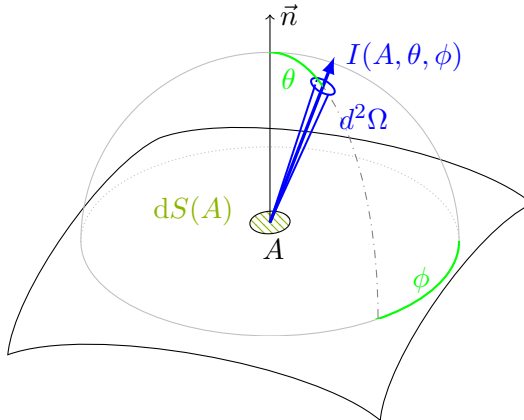


Figure 5.3: Radiance  $I(A, \theta, \phi)$  emitted by a small area  $dS$  around point  $A$  on a curved surface. Angles are defined in the hemisphere based on the plane containing  $dS$ . (*adapted from [Hébert (2022)]*)

or small. The distribution of radiance over the different wavelengths is specified by the *spectral radiance*,

$$I_\lambda = \frac{dI}{d\lambda} \quad (5.5)$$

in  $\text{Wm}^{-2}\text{sr}^{-1}\text{nm}^{-1}$ .

Usually, the frequency or wavelength dependency of  $I$  is not explicitly specified, as in

most case, there is no exchange of energy between each frequency or each wavelength. Thus the *radiative transfer equation* (RTE) can be solved for each wavelength independently.

### 5.2.2 Irradiance, Exitance

The irradiance in  $\text{W/m}^2$ , also called flux according to the vocabulary of the radiative transfer theory, is the power density received per unit area  $d\Phi/dS$ . If the radiance  $I$  from each direction is known, then we can deduce the elementary flux  $d\Phi$  associated with each direction lighting a small area  $dS$  on the surface, refer eq. 5.4. Then, by integration, the total flux  $dF$  that illuminates  $dS$  is deduced. The irradiance  $dF/dS$  is then:

$$\frac{dF}{dS} = \int_{2\pi} I(dS, \vec{\Omega}) \cos(\theta) d\Omega . \quad (5.6)$$

The exitance, also in  $\text{W/m}^2$ , is defined in exactly the same way, for a flux that leaves out of the surface.

### 5.2.3 Fresnel angular reflectance and transmittance

Light propagates at the speed  $c = 2.998 \cdot 10^8 \text{ m.s}^{-1}$  in vacuum and more slowly at speed  $v$  when the propagation medium is not the vacuum. The ratio  $n = c/v$  is called *refractive index* and characterizes the optical properties of the medium. When light propagating in a medium A with a given refractive index  $n_A$  reaches the interface with a medium B with a different refractive index  $n_B$ , a part of the incident light is reflected and the rest is refracted. The fraction of light that is reflected by the interface between media A and B is called *angular reflectance*. It is given by Fresnel's formulae, established by writing the transition equation of electromagnetic waves at the interface [Born *et al.* (1999)]. It depends on the angle of incidence  $\theta_A$ , the polarization of the incident light, as well as the relative refractive index of the interface  $n = n_B/n_A$ . This latter is greater than 1 if medium B is the most refracting, i.e.,  $n_B > n_A$ , and lower than 1 otherwise.

Because we consider unpolarized incident light hereinafter, the Fresnel reflectance formulae for a light ray coming from medium A with angle of incidence  $\theta_A$  is:

$$R_{AB}(\theta_A) = \frac{1}{2} \left( \left| \frac{n^2 \cos(\theta_A) - \sqrt{n^2 - \sin^2(\theta_A)}}{n^2 \cos(\theta_A) + \sqrt{n^2 - \sin^2(\theta_A)}} \right|^2 + \left| \frac{\cos(\theta_A) - \sqrt{n^2 - \sin^2(\theta_A)}}{\cos(\theta_A) + \sqrt{n^2 - \sin^2(\theta_A)}} \right|^2 \right) \quad (5.7)$$

Remind that if medium A is the most refracting ( $n < 1$ ), light is totally reflected beyond the critical angle

$$\theta_c = \arcsin \left( \frac{n_A}{n_B} \right) = \arcsin \left( \frac{1}{n} \right) .$$

In this case, the term  $n^2 - \sin^2(\theta_A)$  is negative and the square root gives a complex number. However, formula 5.7 remain valid thanks to the modulus operator, and we obtain the

expected values  $R_{AB} = 1$ .

Regarding the refracted component, since no light is absorbed at the interface, the angular transmittance is:

$$T_{AB}(\theta_A) = 1 - R_{AB}(\theta_A) \quad (5.8)$$

When light comes from medium B, the angular reflectance, denoted by  $R_{BA}(\theta_B)$ , is still given by Eq. 5.7 by considering the relative refractive index  $n = \frac{n_A}{n_B}$ . The angular reflectance or transmittance is the same if light comes from medium A at the angle  $\theta_A$  or comes from medium B at the regular angle  $\theta_B = \arcsin(n \cdot \sin(\theta_A))$ :  $R_{AB}(\theta_A) = R_{BA}(\theta_B)$  and  $T_{AB}(\theta_A) = T_{BA}(\theta_B)$ .

This equality means that for a given path of light, the angular transmittance does not depend whether light transits from medium A to medium B or from medium B to medium A. In case of total reflection, the angular transmittance is zero.

#### 5.2.4 Plane-Parallel geometry

Hereinafter, only the case of the plane parallel geometry, also called "slab", is considered (see Fig. 5.4). For simplicity, the incident flux is assumed to be specular, normal to the surface, and thus we can assume an azimuthal symmetry (no dependency on azimuthal angle  $\phi$  defined in Fig. 5.1). It would not be the case for oblique incidence (not considered here). Physical quantities only depend in this case on  $z$  and  $\theta$ . Note that the incident flux is uniform on the incident surface, i.e. no  $(x,y)$  dependency.

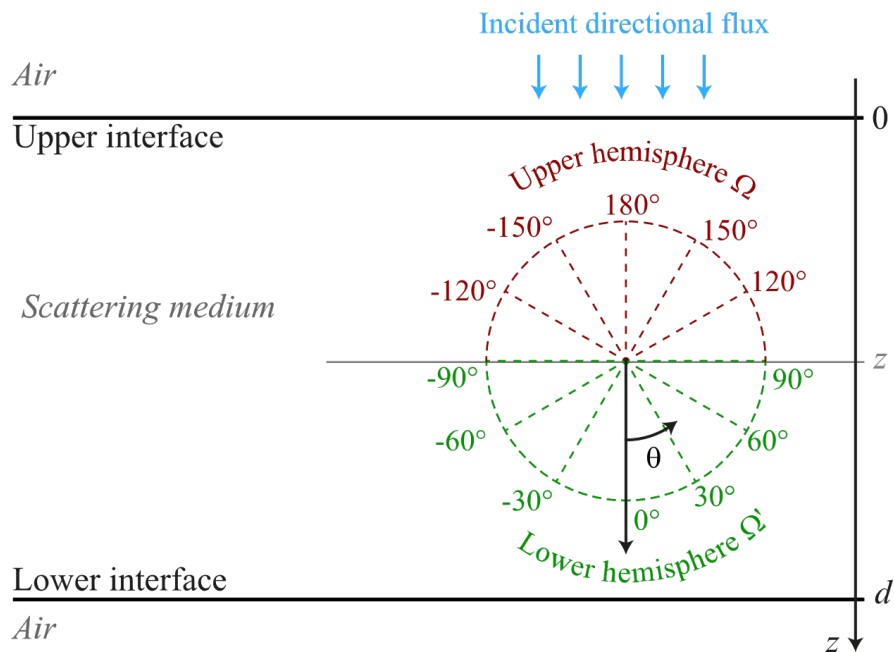


Figure 5.4: The plane parallel geometry. The axis  $z$  and angle  $\theta$  are defined.

The previous assumptions, i.e. azimuthal symmetry and uniform incident flux over the entire surface, and their related consequences, i.e. the physical quantities depend only in  $z$  and  $\theta$ , define what we call hereafter the *1D model*. The semi-infinite medium  $d \rightarrow \infty$

is a particular case of this problem. In this latter case, in absence of absorption, it is sometimes considered that the light is coming from the deep inside ( $d \rightarrow \infty$ ).

Thus, the emittance  $F_+$  ( $\text{W/m}^2$ ) is given by:

$$F_+(z) = \int_0^{2\pi} I(z, \theta) \cos(\theta) d\Omega = 2\pi \int_0^{\frac{\pi}{2}} I(z, \theta) \cos(\theta) \sin(\theta) d\theta \quad (5.9)$$

Introducing  $\mu = \cos(\theta)$  and advising the reader to note that  $\theta = 0$  is obtained for  $\mu = 1$ , emittance is then expressed:

$$F_+(z) = 2\pi \int_0^1 I(z, \mu) \mu d\mu . \quad (5.10)$$

Similarly, irradiance is expressed:

$$F_-(z) = 2\pi \int_{-1}^0 I(z, \mu) \mu d\mu . \quad (5.11)$$

The total flux  $F$  is then:

$$F(z) = 2\pi \int_{-1}^1 I(z, \mu) \mu d\mu = F_+(z) - F_-(z) . \quad (5.12)$$

## 5.3 Equation of transfer in radiative transport theory

### 5.3.1 Derivation of the radiative transfer equation

In this section, the balance equation governing the evolution of the radiance is derived (see Fig. 5.5). Let us consider a cylindrical elementary volume with a cross-section  $dS$  and a length  $dl$ . This cylinder is designed around one light direction  $\vec{\Omega}$  of solid angle  $d\Omega$ .

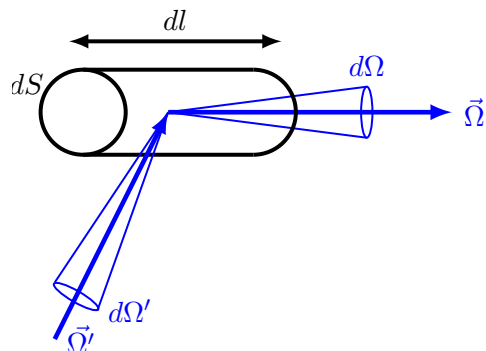


Figure 5.5: Energy balance in an elementary volume designed around the light direction  $\vec{\Omega}$

There is a certain difference between the radiance at the entrance of the cylinder, and the

one at the exit. This variation of radiance for the solid angle  $d\Omega$  is written:

$$(I(s + dl, \vec{\Omega}) - I(s, \vec{\Omega})) dS d\Omega = \frac{dI}{dl} dldS d\Omega \quad (5.13)$$

This variation may result from several mechanisms:

- (a) light absorption,
- (b) light scattered out of the solid angle  $d\Omega$ ,
- (c) light scattered in the solid angle  $d\Omega$  coming from other directions  $\vec{\Omega}'$ ,
- (d) potentially light emission within the volume (e.g. fluorescence).

Introducing the absorption, resp. scattering, coefficient  $\mu_a$ , resp.  $\mu_s$ , (in  $\text{m}^{-1}$ ), the fraction of incident power absorbed or scattered out (mechanisms (a) and (b)) of the elementary volume of length  $dl$  is given by:

$$-(\mu_a + \mu_s)I(s, \vec{\Omega})dldS d\Omega \quad (5.14)$$

These coefficients are related to the particle cross-section:  $\mu_a = \rho\sigma_a$  and  $\mu_s = \rho\sigma_s$ , where  $\rho$  is the particles' concentration (unit  $\text{m}^{-3}$ ), and  $\sigma_a$  is the absorption cross-section (unit  $\text{m}^2$ ),  $\sigma_s$  is the scattering cross-section if particles are all the same and scattering events independent. Cross-sections can be calculated using electromagnetic theory, such as the Mie theory for spherical particles, for instance. In most cases, however,  $\mu_a$  and  $\mu_s$  are extracted from experiments for each wavelength.

In order to describe the anisotropic character of scattering by one or many particles, a directional cross section, called the *differential scattering cross section*, denoted  $\frac{d\sigma_s}{d\Omega}$ , needs to be introduced. We have of course:

$$\sigma_s = \int_{4\pi} \frac{d\sigma_s}{d\Omega} d\Omega \quad (5.15)$$

The differential scattering cross section describes the angular scattering pattern. We will see in Chapter 7 that the angular distribution of the scattered radiance matters especially when we are interested in the multiple scattering of light by a large number of particles. When describing the propagation of light in a scattering medium, we usually define the *phase function*, denoted  $p(\vec{\Omega}, \vec{\Omega}')$ , which gives the fraction of spectral intensity scattered in the  $\vec{\Omega}$  direction over the total spectral flux arriving with a  $\vec{\Omega}'$  direction. The phase function is none other than the normalized differential scattering cross section. Assuming that we are interested in a medium of identical particles, the phase function is defined as:

$$p(\vec{\Omega}, \vec{\Omega}') = \frac{4\pi}{\sigma_s} \frac{d\sigma_s}{d\Omega} . \quad (5.16)$$

With this definition, the phase function is usually normalized by:

$$\int 4\pi p(\vec{\Omega}, \vec{\Omega}') d\Omega = 4\pi . \quad (5.17)$$

Nevertheless, in these chapter, for practical reasons, we use the following normalization equation:

$$\frac{1}{4\pi} \int_{4\pi} p(\vec{\Omega}, \vec{\Omega}') d\vec{\Omega}' = \omega_0 = \frac{\mu_s}{\mu_a + \mu_s} \quad (5.18)$$

where  $\omega_0$  is the albedo of the considered medium.  $\omega_0 = 1$  means that there is no absorption, i.e. conservative transport. The normalization condition becomes in spherical coordinates:

$$\frac{1}{4\pi} \int_{4\pi} p(\vec{\Omega}, \vec{\Omega}') d\vec{\Omega}' = \frac{1}{4\pi} \int_0^{2\pi} d\Phi \int_0^\pi p(\Theta) \sin(\Theta) d\Theta = \omega_0 \quad (5.19)$$

This normalization condition has the advantage of simplifying the writing of the radiative transfer equation as we will see later.

The degree of anisotropy of the scattering is usually measured by the *anisotropy parameter*, denoted  $g$ , which is the average of the cosine of the scattering angle  $\Theta$  between the vectors  $\vec{\Omega}'$  and  $\vec{\Omega}$ . It is thus defined as:

$$g = \frac{1}{4\pi} \int_{4\pi} p(\vec{\Omega}, \vec{\Omega}') \vec{\Omega}' \cdot \vec{\Omega} d\Omega \quad (5.20)$$

For particles small compared to the wavelength, for which the scattering pattern is quasi-isotropic, we have  $g \approx 0$ . For particles scattering essentially forward (e.g. large spherical particles), we have  $g > 0$  and often  $g \approx 1$ . Note that we can even have  $g < 0$  for backward scattering particles.

The parameter  $g$  has a practical interest when the phase function itself is a function of  $\cos(\Theta) = \vec{\Omega}' \cdot \vec{\Omega}$  (e.g. Mie scattering phase function); otherwise  $g$  depends on the direction of incidence  $\vec{\Omega}'$ . A consequence of having an homogenous medium with the phase function which only depends from  $\cos(\Theta) = \vec{\Omega} \cdot \vec{\Omega}'$  is that  $p(\vec{\Omega}, \vec{\Omega}') = p(\vec{\Omega}', \vec{\Omega})$ . For the plane-parallel geometry, we have:

$$\cos(\Theta) = \cos(\theta') \cos(\theta) + \sin(\theta') \sin(\theta) \cos(\phi - \phi') = \mu' \mu + \sqrt{1 - \mu'^2} \sqrt{1 - \mu^2} \cos(\phi - \phi') \quad (5.21)$$

Indeed, in spherical coordinates, we can express  $\vec{\Omega}$  and  $\vec{\Omega}'$  as:

$$\vec{\Omega} = \begin{pmatrix} \sin(\theta) \cos(\phi) \\ \sin(\theta) \sin(\phi) \\ \cos(\theta) \end{pmatrix} \text{ and } \vec{\Omega}' = \begin{pmatrix} \sin(\theta') \cos(\phi') \\ \sin(\theta') \sin(\phi') \\ \cos(\theta') \end{pmatrix} .$$

Thus, we finally obtain:

$$\begin{aligned}\vec{\Omega} \cdot \vec{\Omega}' &= \sin(\theta) \cos(\phi) \sin(\theta') \cos(\phi') + \sin(\theta) \sin(\phi) \sin(\theta') \sin(\phi') + \cos(\theta) \cos(\theta') \\ &= \cos(\theta) \cos(\theta') + \sin(\theta) \sin(\theta') [\cos(\phi) \cos(\phi') + \sin(\phi) \sin(\phi')] \\ &= \cos(\theta') \cos(\theta) + \sin(\theta') \sin(\theta) \cos(\phi - \phi') .\end{aligned}\quad (5.22)$$

The commonly used phase functions are:

- Uniform phase function (isotropic scattering)
- Rayleigh phase function (for particles smaller than the wavelength):  
 $p(\cos \Theta) \propto 1 + \cos \Theta$
- The Mie phase function (for spherical metallic or dielectric particles of any size), computed by solving Maxwell equations,
- Henyey-Greenstein phase function, which is an empirical phase function:  
 $p(\cos \Theta) \propto \frac{1-g^2}{(1+g^2-2g \cos \Theta)^{3/2}}$

There is a rigorous theory of electromagnetic scattering by a homogeneous spherical particle, called Mie's theory (thanks to Gustav Mie who developed it in 1908). Given the complex refractive index and the radius of the particle, as well as the wavelength, this theory provides the scattered fields (and thus the cross sections and the phase function) with series developments that can be calculated numerically. [Bohren and Huffman (1983)]

Although ready-to-use Mie theory calculation routines are available on internet as a standard tool for light scattering, the Henyey-Greenstein phase function has proven useful and widely used in various fields. This function was introduced for practical reasons, as its form gives realistic behaviors to approximate the angular scattering dependence of single scattering events in many fields. Thus, with the parameters  $\Theta = \vec{\Omega}' \cdot \vec{\Omega}$  and the anisotropy factor  $g$ , the Henyey-Greenstein function allows to represent any regular distribution with a forward ( $g > 0$ ) or backward ( $g < 0$ ) dominance. The value  $g = 0$  corresponds to an isotropic distribution. Because biological tissues strongly scatter photons in the forward direction [Cheong *et al.* (1990)], Henyey and Greenstein have devised a useful phase function. However, the Henyey-Greenstein phase function lacks to correctly describe backscattering [Mourant *et al.* (1998)]. Indeed, one of the main drawbacks of the historical Henyey-Greenstein phase function, also called single-term phase function, is that at the time of the study of atmospheric effects, it cannot produce rainbows whereas they are almost always present in realistic phase functions calculated from Mie theory. This is of major importance when calculating synthetic spectra in planetary atmospheres. To produce the rainbow phenomenon, one must use a superposition of two Henyey-Greenstein phase functions, which is proposed by Irvine in [Irvine (1965)]. This two-term Henyey-Greenstein phase function was then applied to biological tissue by [Jacques *et al.* (1987)]. Other phase functions inspired from the original Henyey-Greenstein one has been suggested, like the one of Cornette-Shanks in [Cornette and Shanks (1992)]. Nevertheless, as

biological tissues are strongly forward scattering, the majority of the literature considers the original Henyey-Greenstein phase function [Jacques (2013)b, Yaroslavsky *et al.* (2002)].

Using the phase function concept, the contribution to the power variation of light scattered in the solid angle  $d\Omega$  coming from other directions  $\vec{\Omega}'$  with solid angles  $d\Omega'$  is:

$$\frac{\mu_a + \mu_s}{4\pi} dS d\Omega dl \int_{4\pi} p(\vec{\Omega}, \vec{\Omega}') I(s, \vec{\Omega}') d\Omega' \quad (5.23)$$

We thus have:

$$\frac{dI}{dl} = -(\mu_a + \mu_s) I(s, \vec{\Omega}) + \frac{\mu_a + \mu_s}{4\pi} \int_{4\pi} p(\vec{\Omega}, \vec{\Omega}') I(s, \vec{\Omega}') d\Omega' \quad (5.24)$$

The variable  $s$  depends on the light direction  $\vec{\Omega}$  which is considered.

We can detail this derivative in cartesian coordinate:

$$dI = \frac{\partial I}{\partial x} dx + \frac{\partial I}{\partial y} dy + \frac{\partial I}{\partial z} dz = \vec{\nabla} I \cdot d\vec{r}$$

$$dl = \vec{\Omega} \cdot d\vec{r} = \Omega_x dx + \Omega_y dy + \Omega_z dz$$

Thus,

$$\frac{dI}{dl} = \vec{\nabla} \cdot (I \vec{\Omega}) = \vec{\Omega} \cdot \vec{\nabla} I = \text{div}(I \vec{\Omega}) \quad (5.25)$$

The equation 5.24 can be simplified in the case of the plane parallel problem.

Indeed, first of all, for specular incidence at normal incidence or for diffuse lighting, we have an azimuthal symmetry (the radiance or luminance does not depend on  $\phi$ ). Moreover, let us notice that  $s = \frac{z}{\mu}$  (Fig. 5.4). Finally, we have

$$\begin{aligned} \int_{4\pi} p(\vec{\Omega}, \vec{\Omega}') I(s, \vec{\Omega}') d\Omega' &= \frac{1}{4\pi} \int_0^{2\pi} d\phi' \int_0^\pi p(\theta, \phi, \theta', \phi') I(z, \theta', \phi') \sin(\theta') d\theta' \\ \int_{4\pi} p(\vec{\Omega}, \vec{\Omega}') I(s, \vec{\Omega}') d\Omega' &= \frac{1}{4\pi} \int_0^{2\pi} d\phi' \int_{-1}^1 p(\mu, \phi, \mu', \phi') I(z, \mu', \phi') d\mu'. \end{aligned} \quad (5.26)$$

To eliminate the dependence in  $\phi$  of the equation 5.26, we integrate the previous equation with respect to  $\phi$  over the full  $2\pi$  range. The equation 5.24 thus reduces to:

$$\mu \frac{dI}{dz} = (\mu_a + \mu_s) \left[ -I + \frac{1}{2} \int_{-1}^1 p_0(\mu, \mu') I(z, \mu') d\mu' \right] \quad (5.27)$$

with

$$p_0(\mu, \mu') = \frac{1}{2\pi} \int_0^{2\pi} d\phi' \int_0^{2\pi} p(\mu, \phi, \mu', \phi') d\phi. \quad (5.28)$$

The normalization condition of the phase function previously described becomes:

$$p_0(\mu, \mu') = \frac{1}{2} \int_0^\pi p_0(\Theta) \sin(\Theta) d\Theta = \omega_0. \quad (5.29)$$

This new phase function can be simplified using an expansion in term of Legendre poly-

nomials [Thomas and Stamnes (2002), Chandrasekhar (1960b)]. In the following, for simplification, we will note  $p$  the phase function  $p_0$ . Introducing the optical distance  $\tau = (\mu_a + \mu_s) z$ , we obtain:

$$\mu \frac{dI}{d\tau} = -I + \frac{1}{2} \int_{-1}^1 p(\mu, \mu') I(\tau, \mu') d\mu' \quad (5.30)$$

Solutions of this equation will be discussed in Section 5.4.

### 5.3.2 Incident radiance and diffuse radiance

The radiance  $I$  can be split into incident radiance  $I_r$  and diffuse radiance  $I_d$ .

#### Incident radiance

The incident radiance relates to light from the initial incident beam that retains its original collimated wave form and has neither been absorbed nor scattered. It therefore obeys the following "easy to solve" differential equation, comparable to Beer's law.

$$\frac{dI_r}{dl} = -(\mu_a + \mu_s) I_r \quad (5.31)$$

In the plane parallel problem, the collimated incident flux can be written as:

$$I_r(z = 0, \vec{\Omega}) = F_0 \delta_\Omega(\vec{\Omega}) \quad (5.32)$$

where  $\delta_\Omega(\vec{\Omega})$  denotes a Dirac delta function in the positive  $z$  direction ( $\theta = 0$ ), defined in standard physicist notation, with the well known properties:

$$\begin{aligned} \int_\Omega \delta_\Omega(\vec{\Omega}) d\Omega &= 1 \\ \int_\Omega \delta_\Omega(\vec{\Omega}) g(\vec{\Omega}) d\Omega &= g(\theta = 0, \phi) \end{aligned}$$

where  $g$  is an arbitrary function of  $\vec{\Omega}$  continuous at  $\theta = 0$ . The Dirac delta function on the  $\vec{\Omega}$  direction satisfies:

$$\int_\Omega \delta_\Omega(\vec{\Omega}) d\Omega = 1 \quad \int_\Omega 2\pi \sin(\theta) \delta_\Omega(\vec{\Omega}) d\theta = \int_\Omega 2\pi \delta_\Omega(\vec{\Omega}) d\mu = 1 \quad (5.33)$$

Other Dirac delta functions can be introduced:

$$\int_0^\pi \delta_\theta(\vec{\theta}) d\theta = 1 \quad \int_{-1}^1 \delta_\mu(\mu - 1) d\mu = 1 \quad (5.34)$$

We thus have:

$$I_r(z = 0, \vec{\Omega}) = F_0 \delta_\Omega(\vec{\Omega}) = \frac{F_0}{2\pi} \frac{\delta_\theta(\vec{\theta})}{\sin(\theta)} = \frac{F_0}{2\pi} \delta_\mu(\mu - 1) \quad (5.35)$$

The solution of the reduced radiance equation  $\mu \frac{dI_r}{d\tau} = -I_r$  is:

$$I_r(\tau, \theta) = \frac{F_0}{2\pi} e^{-\frac{\tau}{\mu}} \frac{\delta_\theta(\vec{\theta})}{\sin(\theta)} = \frac{F_0}{2\pi} e^{-\frac{\tau}{\mu}} \delta_\mu(\mu - 1) \quad (5.36)$$

## Diffuse radiance

The diffuse radiance is solution of:

$$\frac{dI_d}{dl} = -(\mu_a + \mu_s) I_d + \frac{\mu_a + \mu_s}{4\pi} \int_{4\pi} p(\vec{\Omega}, \vec{\Omega}') I_d(s, \vec{\Omega}') d\vec{\Omega}' + \frac{\mu_a + \mu_s}{4\pi} \int_{4\pi} p(\vec{\Omega}, \vec{\Omega}') I_r(s, \vec{\Omega}') d\vec{\Omega}' \quad (5.37)$$

Leading to

$$\begin{aligned} \mu \frac{dI_d}{d\tau} &= -I_d + \frac{1}{2} \int_{-1}^1 p(\mu, \mu') I_d(\tau, \mu') d\mu' + \frac{1}{2} \int_{-1}^1 p(\mu, \mu') \frac{F_0}{2\pi} e^{-\frac{\tau}{\mu'}} \delta(\mu' - 1) d\mu' \\ &= -I_d + \frac{1}{2} \int_{-1}^1 p(\mu, \mu') I_d(\tau, \mu') d\mu' + \frac{F_0}{4\pi} e^{-\tau} p(\mu, 1) \end{aligned} \quad (5.38)$$

In many cases, there is no incident diffuse flux on both side of the layer, which make easier the application of boundary conditions. As an example, in the plane-parallel geometry:

$$I_d(z = 0, \mu > 0) = 0 \quad \text{and} \quad I_d(z = d, \mu < 0) = 0 \quad (\text{Index-matching boundary conditions})$$

We detail all possible boundary conditions in Sections 5.4.2 to 5.4.5.

## 5.4 Solution of the radiative transfer equation by the discrete ordinates method

Several methods exist to solve the radiative transfer equation. Here, we decided to use the discrete ordinates method for several reasons. The first reason is that this method provides a really simple way to include partially reflective boundary conditions. This makes this method very attractive compared to the well-known spherical harmonic method where partially reflective boundary conditions are difficult to implement due to the expansion of the Fresnel reflectance law on the base of spherical harmonics. The second is that the discrete ordinates method still performs well in cases of strong absorption. Finally, the increase in computational time decried by [Kokhanovsky (2009)] compared to the spherical harmonics method has not been found prejudicial in our case: it remains acceptable (less than 5 minutes) with the discrete ordinates method even in complex cases.

### 5.4.1 Discretization of the radiative transfer equation by the discrete ordinates method

We intend to solve the equation

$$\mu \frac{dI_d}{d\tau} = -I_d + \frac{1}{2} \int_{-1}^1 p(\mu, \mu') I_d(\tau, \mu') d\mu' + \frac{F_0}{4\pi} e^{-\tau} p(\mu, 1). \quad (5.39)$$

The principle of the discrete ordinates method consists in expanding  $I_d(\tau, \mu)$  on a discrete set of  $2N \mu_n$  values. The discretization of  $\mu$  was carefully chosen in order to get the best accuracy with a minimum  $N$  values when evaluating the scattering integral. To this aim, the Gauss's quadrature formula is used. This method allows approximating an integral by a sum with a very good approximation:

$$\int_{-1}^1 f(x) dx \approx \sum_{\substack{j=-N \\ j \neq 0}}^N a_j f(x_j).$$

This result is obtained by a Lagrange interpolation formula

$$f(x) \approx \sum_{\substack{j=-N \\ j \neq 0}}^N f(x_j) \frac{P_{2N}(x)}{(x - x_j) P'_{2N}(x_j)}$$

where  $P_{2N}$  is the Legendre polynomial of degree  $2N$  and  $x_j$  its roots which satisfy

$$\frac{P_{2N}(x)}{(x - x_j) P'_{2N}(x_j)} = 1.$$

Coefficients  $a_j$  are the Christoffel number associated with  $P_{2N}$ , given by

$$a_j = \int_{-1}^1 \frac{P_{2N}(x)}{(x - x_j) P'_{2N}(x_j)} dx$$

which, in the case of Legendre polynomials, reduce to:

$$a_j = \frac{2}{((1 - x_j^2) P'_{2N}(x_j))^2}.$$

Introducing the Gauss's quadrature formula into the RTE equation, we obtain:

$$\mu \frac{dI_d}{d\tau} = -I_d + \frac{1}{2} \sum_{\substack{j=-N \\ j \neq 0}}^N a_j p(\mu, \mu_j) I_d(\tau, \mu_j) + \frac{F_0}{4\pi} e^{-\tau} p(\mu, 1) \quad (5.40)$$

where  $\mu_j$  are the roots of the Legendre polynomial of degree  $2N$ , and  $a_j$  the corresponding

Christoffel number. We thus obtain a set of  $2N$  discrete coupled linear equations :

$$\forall i \in \llbracket -N, -1 \rrbracket \cup \llbracket 1, N \rrbracket, \\ \frac{dI_d(\tau, \mu_i)}{d\tau} + \frac{Id(\tau, \mu_i)}{\mu_i} - \sum_{\substack{j=-N \\ j \neq 0}}^N a_j p(\mu_i, \mu_j) \frac{I_d(\tau, \mu_j)}{2\mu_i} = \frac{F_0}{4\pi} e^{-\tau} \frac{p(\mu_i, 1)}{\mu_i} \quad (5.41)$$

which can be written as a compact matrix formula  $\frac{d}{d\tau} I(\tau) + S I(\tau) = B e^{-\tau}$  where  $\mathbf{I}$ ,  $\mathbf{B}$  are  $2N$  sized vectors and  $\mathbf{S}$  a  $2N \times 2N$  symmetrical matrix.

Matrix elements are  $S_{ii} = \frac{1}{\mu_i} - \frac{1}{2\mu_i} a_i p(\mu_i, \mu_i)$ ,  $S_{ij} = -\frac{1}{2\mu_i} a_j p(\mu_i, \mu_j)$  and  $\mathbf{B}_i = \frac{F_0}{4\pi} \frac{p(\mu_i, 1)}{\mu_i}$ . The system of coupled ordinary differential equation is linear, and can be solved by the classical procedure.

First, a particular solution can be found with a trial solution of the shape  $\mathbf{I}_p(\tau) = \mathbf{A} e^{-\tau}$ .  $\mathbf{A}$  is found:  $\mathbf{A} = (\mathbf{S} - \mathbf{I})^{-1} \mathbf{B}$ .

Then, the complementary solution is  $\frac{d}{d\tau} \mathbf{I}_c(\tau) + S \mathbf{I}_c(\tau) = \mathbf{0}$ , where  $\mathbf{0}$  is a  $2N$  sized vector of 0. Assuming that the complementary solution is given by  $\mathbf{I}_c = \mathbf{X} e^{-\lambda \tau}$ , the  $\lambda$  and  $\mathbf{X}$  value must satisfy,  $S \mathbf{X} = \lambda \mathbf{X}$  which means that  $\mathbf{X}$  and  $\lambda$  can be found by solving a matrix eigenvalue problem. The final complementary solution is a linear combination of all the eigenvectors of the  $\mathbf{S}$  matrix:

$$\mathbf{I}_c = \sum_{\substack{n=-N \\ n \neq 0}}^N C_n \mathbf{X}^{<n>} e^{-\lambda_n \tau}.$$

Let us stress out that  $\mathbf{X}^{<n>}$  is a vector, while  $C_n$  and  $\lambda_n$  are scalar sorted in ascending index order. The resulting diffuse luminance  $\mathbf{I}$  is thus:

$$\mathbf{I} = \mathbf{I}_p + \mathbf{I}_c = \mathbf{A} e^{-\tau} + \sum_{\substack{n=-N \\ n \neq 0}}^N C_n \mathbf{X}^{<n>} e^{-\lambda_n \tau}.$$

$C_n$  coefficients are found by using the boundary conditions, as explained after.

#### 5.4.2 Boundary conditions for the slab geometry with index-matching interfaces

We consider the configuration of a slab which has the same optical index as its surrounding media (e.g., gases). As explained in Fig. 5.6, there is no diffuse incident light neither at the top nor at the bottom interface. Assuming that  $\lambda_n$  are sorted in ascending order,  $\lambda_n < 0$  for  $n \in \llbracket -N, -1 \rrbracket$  (resp.  $\lambda_n > 0$  for  $n \in \llbracket 1, N \rrbracket$ ), the boundary conditions

are expressed as follows:

$$\forall i \in \llbracket 1, N \rrbracket, \sum_{\substack{n=-N \\ n \neq 0}}^N \mathbf{C}_n \mathbf{X}_{i,n} + \mathbf{A}_i = 0$$

$$\forall i \in \llbracket -N, -1 \rrbracket, \sum_{\substack{n=-N \\ n \neq 0}}^N \mathbf{C}_n \mathbf{X}_{i,n} e^{-\lambda_n \tau_d} + \mathbf{A}_i e^{-\lambda_n \tau_d} = 0.$$

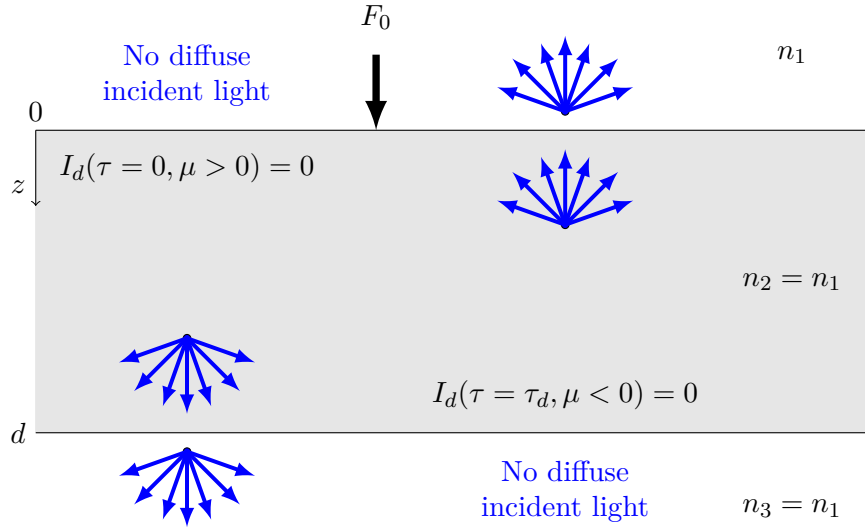


Figure 5.6: Boundaries of an index-matching slab medium

These two conditions can be put in one single matrix inversion (where the  $\mathbf{C}$  vector is the unknown variable).

$$\begin{pmatrix} X_{N,N} & \cdots & X_{N,1} & X_{N,-1} & \cdots & X_{N,-N} \\ \vdots & \ddots & \vdots & \vdots & \ddots & \vdots \\ X_{1,N} & \cdots & X_{1,1} & X_{1,-1} & \cdots & X_{1,-N} \\ X_{-1,N} e^{-\lambda_N \tau_d} & \cdots & X_{-1,1} e^{-\lambda_1 \tau_d} & X_{-1,-1} e^{-\lambda_{-1} \tau_d} & \cdots & X_{-1,-N} e^{-\lambda_{-N} \tau_d} \\ \vdots & \ddots & \vdots & \vdots & \ddots & \vdots \\ X_{-N,N} e^{-\lambda_N \tau_d} & \cdots & X_{-N,1} e^{-\lambda_1 \tau_d} & X_{-N,-1} e^{-\lambda_{-1} \tau_d} & \cdots & X_{-N,-N} e^{-\lambda_{-N} \tau_d} \end{pmatrix} \begin{pmatrix} C_N \\ \vdots \\ C_1 \\ C_{-1} \\ \vdots \\ C_{-N} \end{pmatrix} = - \begin{pmatrix} A_N \\ \vdots \\ A_1 \\ A_{-1} e^{-\tau_d} \\ \vdots \\ A_{-N} e^{-\tau_d} \end{pmatrix}$$

In addition,  $R_{c \rightarrow d}$  is called collimated-to-diffuse reflectance, which can be computed as

$$R_{c \rightarrow d} = \frac{\int_{\mu \leq 0} I_d(\tau = 0, \mu) \mu d\mu}{F_0}.$$

In the same manner, collimated-to-diffuse transmittance  $T_{c \rightarrow d}$  can be computed as

$$T_{c \rightarrow d} = \frac{\int_{\mu \geq 0} I_d(\tau = \tau_d, \mu) \mu d\mu}{F_0}.$$

### 5.4.3 Boundary conditions for the semi-infinite plane geometry with index-matching interface

As described in Fig. 5.7, in a semi-infinite medium, there is only one interface, located at  $\tau = 0$ . Therefore, we need to suppress half of the  $\lambda_n$  eigenvalues: the ones that are negative because they are related to an increase in luminance with depth. We thus need to find only  $N$  scalar values  $\mathbf{C}$ , and not  $2N$  as previously.

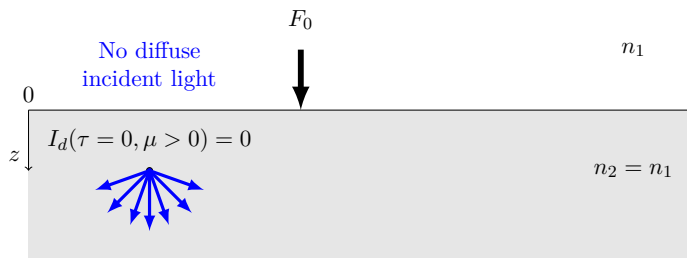


Figure 5.7: Boundary of an index-matching semi-infinite medium

Assuming that  $\lambda_n$  are sorted in ascending order, the boundary condition related to the top interface becomes:

$$\forall i \in \llbracket 1, N \rrbracket, \sum_{\substack{n=1 \\ \lambda_n > 0}}^N \mathbf{C}_n \mathbf{X}_{i,n} + \mathbf{A}_i = 0$$

For these particular  $N$  values, we have:

$$\begin{pmatrix} X_{N,N} & \cdots & X_{N,1} \\ \vdots & \ddots & \vdots \\ X_{1,N} & \cdots & X_{1,1} \end{pmatrix} \begin{pmatrix} C_N \\ \cdots \\ C_1 \end{pmatrix} = - \begin{pmatrix} A_N \\ \cdots \\ A_1 \end{pmatrix}$$

In addition,  $R_{c \rightarrow d}$  is called collimated to diffuse reflectance, which can be computed as

$$R_{c \rightarrow d} = \frac{\int_{\mu \leq 0} I_d(\tau = 0, \mu) \mu d\mu}{F_0}.$$

### 5.4.4 Boundary conditions for the slab geometry without index-matching interfaces (Fresnel reflections)

Usually, the diffusing slab medium (let us label it “2”) does not have the same optical index than the entrance medium at the front (label “1”) and the exit medium on the back

(label “3”). The boundary conditions than become:

$$\begin{aligned} I_d(\tau=0, \mu > 0) &= R_{21}(\mu)I_d(\tau=0, \mu < 0), \\ I_d(\tau=\tau_d, \mu < 0) &= R_{23}(\mu)I_d(\tau=\tau_d, \mu > 0), \end{aligned} \quad (5.42)$$

where  $R_{ij}(\mu)$  is the Fresnel angular reflectance described in Section 5.2.3. Remind that, according to Fresnel formulas,  $R_{21}(\mu) \neq R_{12}(\mu)$  and  $\mu = \cos(\theta) = \cos(-\theta)$ .

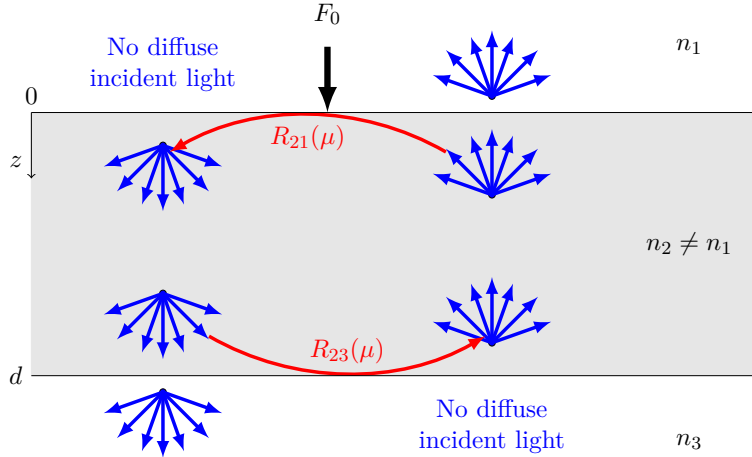


Figure 5.8: Boundaries of a non index-matching slab medium

Moreover, the specular light is also subject to reflection at the back interface. Let's us first detail the application of the boundary condition in the RTE where reflection of the specular light at the back interface are neglected. Consequently, we have  $2N$  equations expressed as:

$$\begin{aligned} \forall i \in \llbracket 1, N \rrbracket, \sum_{\substack{n=-N \\ n \neq 0}}^N \mathbf{C}_n \mathbf{X}_{i,n} + \mathbf{A}_i &= R_{21}(\mu_i) \left( \sum_{\substack{n=-N \\ n \neq 0}}^N \mathbf{C}_n \mathbf{X}_{-i,n} + \mathbf{A}_{-i} \right), \text{ and} \\ \forall i \in \llbracket -N, -1 \rrbracket, \sum_{\substack{n=-N \\ n \neq 0}}^N \mathbf{C}_n \mathbf{X}_{i,n} e^{-\lambda_n \tau_d} + \mathbf{A}_i e^{-\tau_d} &= R_{23}(\mu_i) \left( \sum_{\substack{n=-N \\ n \neq 0}}^N \mathbf{C}_n \mathbf{X}_{-i,n} e^{-\lambda_n \tau_d} + \mathbf{A}_{-i} e^{-\tau_d} \right). \end{aligned}$$

This leads to

$$\begin{aligned} \forall i \in \llbracket 1, N \rrbracket, \sum_{\substack{n=-N \\ n \neq 0}}^N \mathbf{C}_n (\mathbf{X}_{i,n} - R_{21}(\mu_i) \mathbf{X}_{-i,n}) &= R_{21}(\mu_i) \mathbf{A}_{-i} - \mathbf{A}_i, \text{ and} \\ \forall i \in \llbracket -N, -1 \rrbracket, \sum_{\substack{n=-N \\ n \neq 0}}^N \mathbf{C}_n (\mathbf{X}_{i,n} - R_{23}(\mu_i) \mathbf{X}_{-i,n}) e^{-\lambda_n \tau_d} &= (R_{23}(\mu_i) \mathbf{A}_{-i} - \mathbf{A}_i) e^{-\tau_d}, \end{aligned}$$

which is expressible in a matrix form. The  $\mathbf{C}_n$  coefficients are found by inverting the corresponding matrix.

To correctly describe the light propagation in cases where reflection at the back interface are included, the right member of the RTE changes and becomes:

$$\frac{1}{4\pi} p(\mu, 1) T_{12}(\mu = 1) F_0 \frac{e^{-\tau} + R_N e^{-(2\tau_d - \tau)}}{1 - R_N^2 e^{-2\tau_d}} \quad (5.43)$$

where  $R_N$  is the Fresnel reflectance at  $\mu = 1$  (normal incidence).

This impacts the matrix expression of the differential equation:

$$\frac{d}{d\tau} I(\tau) + S I(\tau) = B e^{-\tau} + B' e^\tau, \quad (5.44)$$

$$\text{with } B_i = \frac{1}{4\pi} T_{12}(\mu = 1) F_0 \frac{p(\mu_i, 1)}{\mu_i} \frac{1}{1 - R_N^2 e^{-2\tau_d}},$$

$$\text{and } B'_i = \frac{1}{4\pi} T_{12}(\mu = 1) F_0 \frac{p(\mu_i, 1)}{\mu_i} \frac{R_N e^{-(2\tau_d)}}{1 - R_N^2 e^{-2\tau_d}}.$$

As the right member of the equation 5.44 is the sum of two source terms, it implies to find two particular solutions:

$$\mathbf{I}_p(\tau) = \mathbf{A} e^{-\tau}, \text{ and } \mathbf{I}'_p(\tau) = \mathbf{A}' e^\tau.$$

By linearity, we have:

$$\mathbf{A} = (\mathbf{S} - \mathbf{I})^{-1} \mathbf{B}, \text{ and } \mathbf{A}' = (\mathbf{S} + \mathbf{I})^{-1} \mathbf{B}'.$$

Finally, the application of the boundary conditions is also impacted by the change of the right member of the RTE in Eq. 5.43 in the following way:

$$\forall i \in \llbracket 1, N \rrbracket, \sum_{\substack{n=-N \\ n \neq 0}}^N \mathbf{C}_n \mathbf{X}_{i,n} + \mathbf{A}_i + \mathbf{A}'_i = R_{21}(\mu_i) \left( \sum_{\substack{n=-N \\ n \neq 0}}^N \mathbf{C}_n \mathbf{X}_{-i,n} + \mathbf{A}_{-i} + \mathbf{A}'_{-i} \right)$$

$$\forall i \in \llbracket -N, -1 \rrbracket, \sum_{\substack{n=-N \\ n \neq 0}}^N \mathbf{C}_n \mathbf{X}_{i,n} e^{-\lambda_n \tau_d} + \mathbf{A}_i e^{-\tau_d} + \mathbf{A}'_i e^{\tau_d} = R_{23}(\mu_i) \left( \sum_{\substack{n=-N \\ n \neq 0}}^N \mathbf{C}_n \mathbf{X}_{-i,n} e^{-\lambda_n \tau_d} + \mathbf{A}_{-i} e^{-\tau_d} + \mathbf{A}'_{-i} e^{\tau_d} \right).$$

This leads to

$$\begin{aligned} \forall i \in \llbracket 1, N \rrbracket, \sum_{\substack{n=-N \\ n \neq 0}}^N \mathbf{C}_n (\mathbf{X}_{i,n} - R_{21}(\mu_i) \mathbf{X}_{-i,n}) &= R_{21}(\mu_i) \mathbf{A}_{-i} - \mathbf{A}_i + R_{21}(\mu_i) \mathbf{A}'_{-i} - \mathbf{A}'_i, \text{ and} \\ \forall i \in \llbracket -N, -1 \rrbracket, \sum_{\substack{n=-N \\ n \neq 0}}^N \mathbf{C}_n (\mathbf{X}_{i,n} - R_{23}(\mu_i) \mathbf{X}_{-i,n}) e^{-\lambda_n \tau_d} &= (R_{23}(\mu_i) \mathbf{A}_{-i} - \mathbf{A}_i) e^{-\tau_d} + (R_{23}(\mu_i) \mathbf{A}'_{-i} - \mathbf{A}'_i) e^{\tau_d}, \end{aligned}$$

which is once again expressible in a matrix form. Again, the  $\mathbf{C}_n$  coefficients are found by inverting the corresponding matrix. In addition,  $R_{c \rightarrow d}$  is called collimated to diffuse reflectance, which can be computed as

$$R_{c \rightarrow d} = \frac{\int_{\mu \leq 0} T_{21}(\mu) \mu I_d(\tau = 0, \mu) d\mu}{F_0}.$$

In the same manner, collimated to diffuse transmittance  $T_{c \rightarrow d}$  can be computed as

$$T_{c \rightarrow d} = \frac{\int_{\mu \geq 0} T_{23}(\mu) \mu I_d(\tau = \tau_d, \mu) d\mu}{F_0}.$$

#### 5.4.5 Boundary conditions for the semi-infinite plane geometry without index-matching interface (Fresnel reflections)

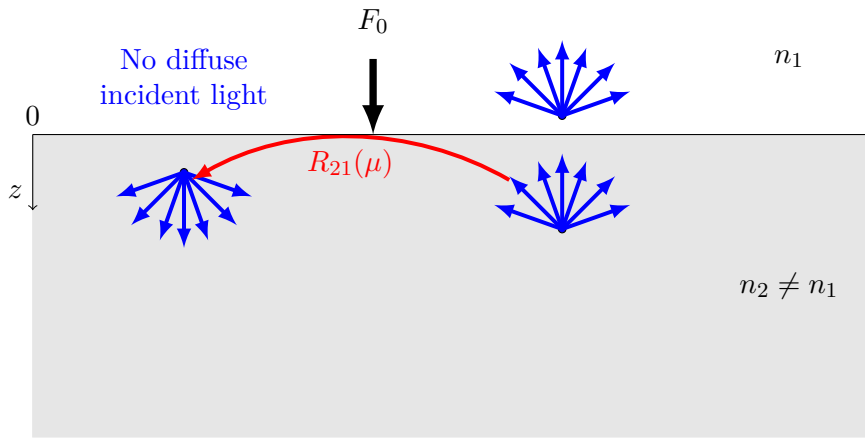


Figure 5.9: Boundaries of a non index-matching semi-infinite medium

The diffusing semi-infinite medium (label “2”) does not have the same optical index than the surrounding medium (label “1”). The boundary conditions expressed in Eq. 5.42 become:

$$I_d(\tau=0, \mu > 0) = R_{21}(\mu) I_d(\tau=0, \mu < 0),$$

where  $R_{ij}(\mu)$  is the Fresnel angular reflectance described in Section 5.2.3. Consequently,

we have  $N$  equations given by:

$$\forall i \in \llbracket 1, N \rrbracket, \sum_{\substack{n=1 \\ \lambda_n > 0}}^N \mathbf{C}_n \mathbf{X}_{i,n} + \mathbf{A}_i = R_{21}(\mu_i) \left( \sum_{\substack{n=1 \\ \lambda_n > 0}}^N \mathbf{C}_n \mathbf{X}_{-i,n} + \mathbf{A}_{-i} \right).$$

This leads to

$$\forall i \in \llbracket 1, N \rrbracket, \sum_{\substack{n=1 \\ \lambda_n > 0}}^N \mathbf{C}_n (\mathbf{X}_{i,n} - R_{21}(\mu_i) \mathbf{X}_{-i,n}) = R_{21}(\mu_i) \mathbf{A}_{-i} - \mathbf{A}_i,$$

which is as before expressible in a matrix form. The  $\mathbf{C}_n$  coefficients are found by inverting the corresponding matrix. As previously, collimated to diffuse reflectance  $R_{c \rightarrow d}$  can be computed with the same formula as previously.

#### 5.4.6 Fluorescent Medium

When the medium is fluorescent, it is mandatory to distinguish the light that propagates until absorption (excitation of the fluorophores) and the light that propagates after emission by fluorescence. Thus, all variables indexed  $x$ , resp.  $m$ , define quantities at excitation wavelength, resp. emission wavelength. We call  $I_{d,x}$  the diffuse luminance and  $I_{s,x}$  the specular luminance at the excitation wavelength. In the same way, we define the transport free-mean-path at the excitation wavelength  $l_x^* = 1/\mu_{t,x} = 1/(\mu_{a,x} + \mu_{s,x})$  and at the emission wavelength  $l_m^* = 1/\mu_{t,m}$ . As in [Mycek and Pogue (2003)], we define the parameters  $\mu_{a,x \rightarrow m}$ , which corresponds to the part of absorption reemitted and  $\mu_{a,x,0}$  which corresponds to the part of absorption not reemitted. The total absorbance at the excitation wavelength is  $\mu_{a,x} = \mu_{a,x \rightarrow m} + \mu_{a,x,0}$ . In addition, the parameter  $\eta$  refers to the quantum yield of the fluorophore. We also introduce the optical thickness at the excitation wavelength  $\tau_x = (\mu_{a,x} + \mu_{s,x})z$  and the one at the emission wavelength  $\tau_m = (\mu_{a,m} + \mu_{s,m})z$ . Let us now look at the mathematical description of the fluorescence phenomenon. At the excitation wavelength, the radiative transfer is described and the RTE is solved in the same way as before. We simply distinguish the diffuse luminance  $I_{d,x}$  and the specular luminance  $I_{s,x}$ . At the emission wavelength, the only light source results from the re-emission of the excitation light absorbed by the fluorophores, which is expressed as follows:

$$\frac{1}{2} \int_{-1}^1 \frac{\eta \mu_{a,x \rightarrow m}}{\mu_{a,m} + \mu_{s,m}} (I_{d,x}(\tau_x, \mu') + I_{s,x}(\tau_x, \mu')) d\mu'. \quad (5.45)$$

Thus, at the emission wavelength, we intend to solve the following radiative transfer equation:

$$\begin{aligned} \mu \frac{dI_{d,m}}{d\tau_m} = & -I_{d,m} + \frac{1}{2} \int_{-1}^1 p_m(\mu, \mu') I_{d,m}(\tau_m, \mu') d\mu' \\ & + \frac{1}{2} \int_{-1}^1 \frac{\eta \mu_{a,x \rightarrow m}}{\mu_{a,m} + \mu_{s,m}} (I_{d,x}(\tau_x, \mu') + I_{s,x}(\tau_x, \mu')) d\mu' \end{aligned} \quad (5.46)$$

with the following boundary conditions for a slab

$$\begin{aligned} I_{d,m}(\tau_m = 0, \mu > 0) &= R_{21}(\mu) I_{d,m}(\tau_m = 0, \mu < 0) \\ I_{d,m}(\tau_m = \mu_{t,m} d, \mu < 0) &= R_{23}(\mu) I_{d,m}(\tau_m = \mu_{t,m} d, \mu > 0) \end{aligned} \quad (5.47)$$

where  $R_{ij}(\mu)$  is the Fresnel angular reflectance described in Section 5.2.3. Note that light emission by fluorescence is always considered as isotropic, i.e., light is emitted uniformly over the sphere without preferred direction. However, once the emitted light starts to propagate within the medium, it is subject to scattering, and a phase function  $p_m(\mu, \mu')$  characterizes the scattering properties of the medium. Introducing the Gauss's quadrature formula into the RTE equation 5.46 gives:

$$\begin{aligned} \mu \frac{dI_{d,m}}{d\tau_m} = & -I_{d,m} + \frac{1}{2} \sum_{\substack{j=-N \\ j \neq 0}}^N a_j p_m(\mu, \mu_j) I_{d,m}(\tau_m, \mu_j) \\ & + \frac{\eta \mu_{a,x \rightarrow m}}{\mu_{t,m}} \left( \frac{F_0}{4\pi} e^{-\tau_x} + \frac{1}{2} \sum_{\substack{j=-N \\ j \neq 0}}^N a_j I_{d,x}(\tau_x, \mu_j) \right) \end{aligned} \quad (5.48)$$

where  $\mu_j$  are the roots of the Legendre polynomial of degree  $2N$ , and  $a_j$  the corresponding Christoffel number. As we solve a differential equation depending on  $\tau_m$ , we can rewrite  $\tau_x$  as  $\frac{\mu_{t,x}}{\mu_{t,m}} \tau_m$ . Thus, we obtain a set of  $2N$  coupled linear discrete equations:

$$\begin{aligned} \frac{dI_{d,m}(\tau_m, \mu_i)}{d\tau_m} + \frac{I_{d,m}}{\mu_i} - \sum_{\substack{j=-N \\ j \neq 0}}^N a_j p_m(\mu_i, \mu_j) \frac{I_{d,m}(\tau_m, \mu_j)}{2\mu_i} = & \frac{\eta \mu_{a,x \rightarrow m}}{\mu_{t,m}} \frac{1}{\mu_i} \left( \frac{F_0}{4\pi} e^{-\frac{\mu_{t,x}}{\mu_{t,m}} \tau_m} \right. \\ & \left. + \frac{1}{2} \sum_{\substack{j=-N \\ j \neq 0}}^N a_j I_{d,x} \left( \frac{\mu_{t,x}}{\mu_{t,m}} \tau_m, \mu_j \right) \right) \end{aligned} \quad (5.49)$$

with

$$I_{d,x} \left( \frac{\mu_{t,x}}{\mu_{t,m}} \tau_m, \mu_j \right) = \sum_{\substack{n=-N \\ n \neq 0}}^N \mathbf{G}_n \mathbf{W}^{<:,n>} e^{-\omega_n \frac{\mu_{t,x}}{\mu_{t,m}} \tau_m} + \mathbf{A} e^{-\frac{\mu_{t,x}}{\mu_{t,m}} \tau_m} + \mathbf{A}' e^{\frac{\mu_{t,x}}{\mu_{t,m}} \tau_m}$$

where  $\mathbf{W}$  and  $\omega$  can be found by solving the RTE for excitation only. The following notation  $\langle i,j \rangle$  refers to the  $i^{th}$  row and  $j^{th}$  column of a matrix.

Thus, Equation 5.49 becomes:

$$\begin{aligned} \frac{dI_{d,m}(\tau_m, \mu_i)}{d\tau_m} + \frac{I_{d,m}(\tau_m, \mu_i)}{\mu_i} - \sum_{\substack{j=-N \\ j \neq 0}}^N a_j p_m(\mu_i, \mu_j) \frac{I_{d,m}(\tau_m, \mu_j)}{2\mu_i} = \\ \frac{\eta \mu_{a,x \rightarrow m}}{\mu_{t,m}} \frac{1}{\mu_i} \left[ \frac{1}{2} \sum_{\substack{j=-N \\ j \neq 0}}^N a_j A'^{<j,:>} e_x^\tau + \left( \frac{1}{4\pi} F_0 + \frac{1}{2} \sum_{\substack{j=-N \\ j \neq 0}}^N a_j A^{<j,:>} \right) e^{-\tau_x} \right. \\ \left. + \frac{1}{2} \sum_{\substack{j=-N \\ j \neq 0}}^N a_j \sum_{\substack{n=-N \\ n \neq 0}}^N (G_n W^{<:,n>})^{<j,:>} e^{-\omega_n \tau_x} \right] \end{aligned}$$

which is equivalent to:

$$\begin{aligned} \frac{dI_{d,m}(\tau_m, \mu_i)}{d\tau_m} + \frac{I_{d,m}(\tau_m, \mu_i)}{\mu_i} - \sum_{\substack{j=-N \\ j \neq 0}}^N a_j p_m(\mu_i, \mu_j) \frac{I_{d,m}(\tau_m, \mu_j)}{2\mu_i} = \\ \frac{\eta \mu_{a,x \rightarrow m}}{\mu_{t,m}} \frac{1}{\mu_i} \left[ \frac{1}{2} \sum_{\substack{j=-N \\ j \neq 0}}^N a_j A'^{<j,:>} e^{\frac{\mu_{t,x}}{\mu_{t,m}} \tau_m} + \left( \frac{1}{4\pi} F_0 + \frac{1}{2} \sum_{\substack{j=-N \\ j \neq 0}}^N a_j A^{<j,:>} \right) e^{-\frac{\mu_{t,x}}{\mu_{t,m}} \tau_m} \right. \\ \left. + \frac{1}{2} \sum_{\substack{n=-N \\ n \neq 0}}^N e^{-\omega_n \frac{\mu_{t,x}}{\mu_{t,m}} \tau_m} \sum_{\substack{j=-N \\ j \neq 0}}^N a_j (G_n W^{<:,n>})^{<j,:>} \right]. \quad (5.50) \end{aligned}$$

Please notice that

$$\frac{1}{2} \sum_{\substack{n=-N \\ n \neq 0}}^N e^{-\omega_n \frac{\mu_{t,x}}{\mu_{t,m}} \tau_m} \sum_{\substack{j=-N \\ j \neq 0}}^N a_j (G_n W^{<:,n>})^{<j,:>}$$

can be expressed as

$$\sum_{\substack{n=-N \\ n \neq 0}}^N \mathbf{f}_n e^{-\omega_n \frac{\mu_{t,x}}{\mu_{t,m}} \tau_m}$$

with

$$\mathbf{f}_n = \sum_{\substack{j=-N \\ j \neq 0}}^N \frac{1}{2} a_j (G_n \mathbf{W}^{<:,n>})^{<j,:>}$$

Thus, equation 5.50 can be written as a compact matrix formula:

$$\frac{d}{d\tau_m} \mathbf{I}(\tau_m) + \mathbf{S}\mathbf{I}(\tau_m) = \mathbf{B} e^{-\frac{\mu_{t,x}}{\mu_{t,m}} \tau_m} + \mathbf{B}' e^{\frac{\mu_{t,x}}{\mu_{t,m}} \tau_m} + \sum_{\substack{n=-N \\ n \neq 0}}^N \mathbf{f}_n e^{-\omega_n \frac{\mu_{t,x}}{\mu_{t,m}} \tau_m}$$

where  $\mathbf{I}, \mathbf{B}$  are  $2N$  sized vectors and  $\mathbf{S}$  a  $2N \times 2N$  symmetrical matrix. Matrix elements are:

$$\begin{aligned}\mathbf{S}_{i,i} &= \frac{1}{\mu_i} - \frac{1}{2\mu_i} a_i p_m(\mu_i, \mu_i), \\ \mathbf{S}_{i,j} &= -\frac{1}{2\mu_i} a_j p_m(\mu_i, \mu_j), \\ \mathbf{B}_i &= \frac{\eta \mu_{a,x \mapsto m}}{\mu_{t,m}} \frac{1}{2\mu_i} \left( \frac{F_0}{2\pi} + \sum_{\substack{j=-N \\ j \neq 0}}^N a_j \mathbf{A}^{<j,:>} \right), \\ \mathbf{B}'_i &= \frac{\eta \mu_{a,x \mapsto m}}{\mu_{t,m}} \frac{1}{2\mu_i} \sum_{\substack{j=-N \\ j \neq 0}}^N a_j \mathbf{A}'^{<j,:>}\end{aligned}$$

The system of coupled ordinary differential equation is linear, and can be solved by the classical procedure briefly described hereafter.

First, a particular solution is obtained:

$$\mathbf{I}_p(\tau_m) = \mathbf{Y} e^{-\frac{\mu_{t,x}}{\mu_{t,m}} \tau_m} + \mathbf{Y}' e^{\frac{\mu_{t,x}}{\mu_{t,m}} \tau_m} + \sum_{\substack{n=-N \\ n \neq 0}}^N \mathbf{Z}_n e^{-\omega_n \frac{\mu_{t,x}}{\mu_{t,m}} \tau_m} \quad (5.51)$$

where

$$\mathbf{Y} = (\mathbf{S} - \frac{\mu_{t,x}}{\mu_{t,m}} \mathbf{I})^{-1} \mathbf{B}, \quad \mathbf{Y}' = (\mathbf{S} + \frac{\mu_{t,x}}{\mu_{t,m}} \mathbf{I})^{-1} \mathbf{B}'$$

and

$$\forall k \in [-N, N], \quad \mathbf{Z}_k = (\mathbf{S} - \frac{\mu_{t,x}}{\mu_{t,m}} \omega_k \mathbf{I})^{-1} \mathbf{f}_k$$

with

$$\mathbf{f}_k = \sum_{\substack{j=-N \\ j \neq 0}}^N \frac{1}{2} a_j (\mathbf{G}_k \mathbf{W}^{<:,k>})^{<j,:>}.$$

Then, the complementary solution is:

$$\frac{dI_c(\tau_m)}{d\tau_m} + S I_c(\tau_m) = 0 \quad (5.52)$$

Assuming that the complementary solution is given by  $\mathbf{I}_c = \mathbf{X} e^{-\lambda \tau}$ , the  $\lambda$  and  $\mathbf{X}$  value must satisfy  $\mathbf{S} \mathbf{X} = \lambda \mathbf{X}$  which means that  $\mathbf{X}$  and  $\lambda$  can be found by solving a matrix eigenvalue problem. The final complementary solution is a linear combination of all the eigenvectors of the  $\mathbf{S}$  matrix:

$$\mathbf{I}_c = \sum_{\substack{n=-N \\ n \neq 0}}^N \mathbf{C}_n \mathbf{X}^{<n>} e^{-\lambda_n \tau_m} \quad (5.53)$$

Let us stress out that  $\mathbf{X}^{<n>}$  is a vector, while  $\mathbf{C}_n$  and  $\lambda_n$  are scalar. The resulting diffuse

radiance  $\mathbf{I}$  is thus:

$$\mathbf{I} = \mathbf{I}_c + \mathbf{I}_p = \sum_{\substack{n=-N \\ n \neq 0}}^N C_n \mathbf{X}^{<n>} e^{-\lambda_n \tau_m} + \mathbf{Y}' e^{\tau_x} + \mathbf{Y} e^{-\tau_x} + \sum_{\substack{n=-N \\ n \neq 0}}^N \mathbf{Z}_n e^{-\omega_n \tau_x} \quad (5.54)$$

The  $C_n$  coefficients are found by using the boundary conditions (eq. 5.47), as explained for solving the excitation part.

The resolution of the fluorescent case is here described considering a single fluorophore. Nevertheless, if multiple fluorophores are considered, it is necessary to change

$$\eta \mu_{a,x \rightarrow m}$$

by  $\sum_{i=1}^{N_F} \eta^i \mu_{a,x \rightarrow m}^i$  with  $N_F$  the number of fluorophores. Then the resolution remains identical as previously.

## 5.5 Conclusion

In this chapter, we have first described the physical quantities related to the radiative transfer theory. Then, we have reconstructed the radiative transfer equation. Then, we presented the discrete ordinates method to solve the RTE in the case of a plane-parallel geometry. We then took the time to explain extensively the boundary conditions in cases with and without index-matching interfaces. Finally, we have also treated the case of fluorescence which introduces a system of two coupled radiative transfer equations. The next chapter focuses on the validation of our RTE resolution tool by comparison with Monte Carlo simulations.

# Chapter 6

---

## Validation of the RTE solver by comparison with MC and literature

---

This chapter aims at explaining how we have benchmarked our implementation of the radiative transfer equation Solver based on Discrete Ordinates Method explained in Chapter 5. We will explain how simulation setup has been build, then describe results of the validation in various configurations, including configurations comparable to the ones found in the literature [[Giovanelli \(1955\)](#), [Van de Hulst \(1980\)](#), [Prahl \*et al.\* \(1989\)](#), [Leh \(2011\)](#)].

Finally, we discuss on the discretization we have chosen to use and also on the effect of non index-matching interfaces on the polynomial order required to have correct simulation results.

### 6.1 Monte Carlo Method

In this section, we will describe how we performed Monte-Carlo computations using MCX from Q. Fang [[Fang \*et al.\* \(2009\)](#)]. Monte Carlo method simulates the propagation of light as the propagation of a set of particles. The principle of these methods is based on Monte Carlo sampling. Consider a variable  $x$  (optical path of a photon between two diffusion events) with a probability density  $\rho(x)$  normalized to unity over an interval  $[a, b]$  such that  $\int_a^b \rho(x)dx = 1$  (refer to the fourth quadrant of Fig. 6.1). In order to sample  $x$  randomly, a random variable  $rnd$  uniformly distributed between 0 and 1 is generated.  $rnd$  is calculated by a pseudo-random number generator using seeds. We note  $\rho(rnd)$  the probability density of  $rnd$  (refer to the first quadrant of Fig. 6.1) and  $F(rnd)$  represents

the distribution function of  $rnd$  (refer to the second frame of Fig. 6.1). A value of  $x$  is chosen from the selected value of  $F(x)$  (distribution function of  $x$ ) from  $F(rnd)$ .

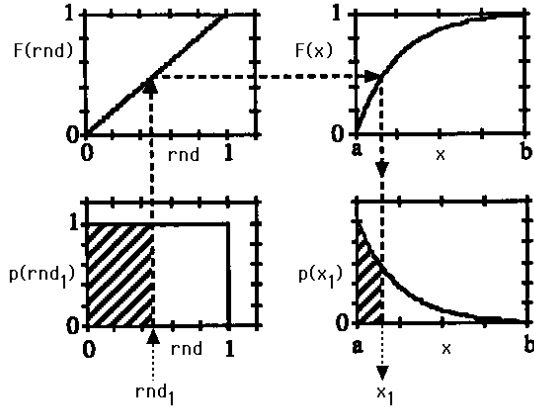


Figure 6.1: Monte Carlo randomization process (taken from [Jacques (1998)])

### 6.1.1 Correspondences between Monte-Carlo & radiative transfer equation

The RTE solver we implemented and the Monte Carlo software MCX [Fang *et al.* (2009)] consider different physical quantities as input. In this section, we provide explanations on how to convert results from one software to be comparable with results from the other one.

$F_0$  defined in the radiative transfer equation model is an irradiance, which is the equivalent of the number of photons  $n$  defined in Monte Carlo (MC) divided by the surface of the incident lightning surface,  $S$ . Hence,

$$F_0 = \frac{n}{S}.$$

MC considers that each photon has a power of 1 W, therefore for  $10^6$  photons launched over a  $25 \text{ mm}^{-2}$  surface, the incident irradiance is  $F_0$  is  $80000 \text{ W.mm}^{-2}$ .

Results of Monte-Carlo simulations are given in Fluence  $\Phi$ , whereas the RTE solver outputs radiance  $L$  or mean irradiance  $U$ . A factor  $\frac{1}{4\pi}$  is needed to convert Fluence into a mean irradiance  $U$ :

$$U(\vec{r}) = \frac{\Phi(\vec{r})}{4\pi} .$$

### 6.1.2 Media

In MCX, we model only finite volumes. However, it is possible to model a semi-infinite medium by considering a very deep volume. Moreover, it is possible to adjust the

parameters at the volume boundaries to describe what happens to the photon that reaches one of them (e.g., refraction or reflection).

In our case, we want to model a semi-infinite medium which is infinite in along the x- and the y-axes and semi-infinite along the z direction. This corresponds to a 1D model as defined in Section 5.2.4. It requires to correctly set the boundary conditions of the MCX volume such that all photons leaving the volume at the +x, resp +y, boundary re-enter the volume at the -x, resp. -y, boundary and vice versa. To be confident with our RTE solver implementation, we decided to validate it with a comparison with MCX in different configurations.

## 6.2 Validation

In order to validate the implementation of the RTE solver explained in the previous chapter, we propose to compare the results provided by our analytical model with Monte-Carlo simulations in various configurations. In this section, we will discuss the results obtained in various typical configurations.

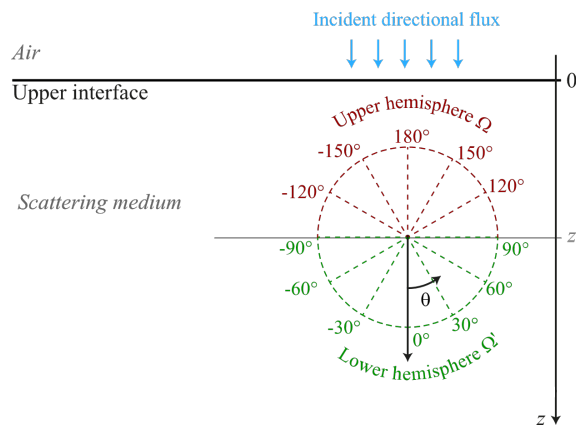


Figure 6.2: Studied configuration where a semi-infinite scattering medium with a refractive index different from the surrounding air is illuminated by directional light at normal incidence. Physical quantities depend on depth  $z$  and angle  $\theta$ .

The direct solving method enables to obtain the diffused radiance distribution at any depth in the medium, therefore at the depth of interest here  $z = 0$ .

In Fig. 6.2, angles  $|\theta| \leq 90^\circ$  (i.e.,  $\mu \geq 0$ ) correspond to the lower hemisphere  $\Omega'$  where radiance values depict the angular distribution of the light going downwards. The other angles correspond to the upper hemisphere  $\Omega$ , where radiance values depict the angular distribution of the light going towards negative values of  $z$  (therefore upwards).

### 6.2.1 Validation metrics

The validity of the simulation in a given configuration is defined by two different metrics: the relative convergence of the solution of the analytic RTE solver and the relative

error between Monte-Carlo and analytic solver diffuse reflectances. The relative convergence is defined as:

$$\forall n \in \{2k \leq N_n, k \in \mathbb{N}^*\}, CV(n) = \sqrt{\sum_i^N \frac{(U_n(z_i) - U_{n-2}(z_i))^2}{N}} \quad (6.1)$$

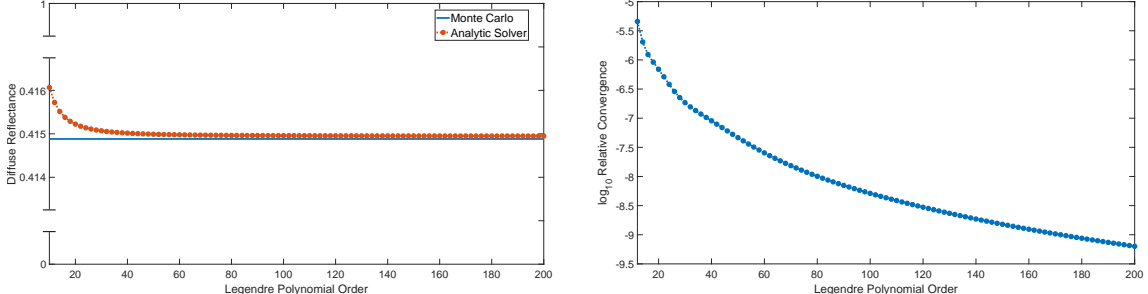
where  $n$  is the Legendre polynomial order,  $U_n$  the average irradiance at a given  $n$ ,  $N$  the last depth for which the average irradiance is computed, and  $N_n$  the maximal order of the Legendre polynomial. We remember that the order of the Legendre polynomial is directly linked with the number of angular discretization points. All validation cases presented below consider a semi-infinite medium. We also validated our implementation of a slab medium, but we decide not to add results to lighten this manuscript. In addition, we consider a Henyey-Greenstein phase function for all cases.

### 6.2.2 Non-fluorescent isotropic scattering medium with index-matching interfaces

Here, we consider an isotropic scattering medium with index-matching interfaces. This is equivalent to consider no preferred direction for scattering and no Fresnel reflection at the air-medium interface. Thus, this configuration verifies the validity of the implementation of particular and complementary solutions.

medium name	$\mu_a$	$\mu_s$	$g$	$n$
air	0	0	1	1
medium	1	9	0	1

Table 6.1: Optical Parameters for isotropic index matching case of a semi-infinite medium



(a) Diffuse Reflectance comparison between the Analytic solver (orange dashed line) and the Monte Carlo Simulation (blue solid line) for the study case. The relative error for  $N_n \geq 150$  is below 0.017 %.

(b)  $\log_{10}$  of the Relative Convergence of the Analytic solver solution for the study case. The relative error for  $N_n \geq 150$  is below  $1.453 \cdot 10^{-9}$ .

Figure 6.3: Plots of Validity Metrics versus the Legendre polynomial order

Results presented in Fig.6.3 are related to the simulation whose parameters given in Table 6.1 corresponds to an absorbing and extremely scattering medium. In Fig. 6.3a, we notice

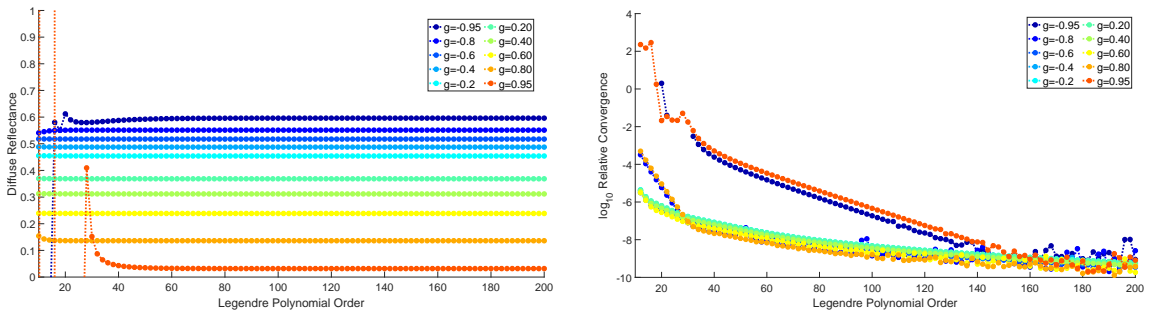
that the diffuse reflectance error becomes minimal ( $\epsilon \leq 0.023\%$ ) for a Legendre polynomial order higher than 60. Fig. 6.3b shows that the relative convergence value decreases as the order of the Legendre polynomial increases, i.e. the number of discretization points increases. Putting the figures 6.3a and 6.3b in perspective, we conclude that in this case of study we must consider a sufficient number of discretization points to obtain the right value of diffuse reflectance. Nevertheless, we want to warn the reader that after a certain point, the increase of the order of Legendre polynomial makes the matrix ill-conditioned, which affects the numerical stability.

### 6.2.3 Non-fluorescent anisotropic scattering medium with index-matching interfaces

Because biological tissues are known to be highly anisotropic [Jacques (2013)a, Jacques (2013)b], it is mandatory to check the validity of the Henyey-Greenstein phase function we implemented. Even if biological tissues have a positive value of the anisotropy factor  $g$ , we decided to extend our validation study to negative values of the anisotropy factor  $g$  because they exist in a part of the optic domain [Frka-Petescic *et al.* (2015)]. This also enables us to highlight the failure of MCX for negative values of  $g$ . Thus curves related to negative values of  $g$  are visible in Figs 6.4a and 6.4b for information purposes.

medium name	$\mu_a$	$\mu_s$	$g$	$n$
air	0	0	1	1
medium	1	9	$\neq 0$	1

Table 6.2: Optical Parameters for isotropic index matching case of a semi-infinite medium



(a) Diffuse reflectance from the Analytic solver depending on the order of the Legendre polynomial, i.e. the number of discretization points. Each plot corresponds to a different value of the anisotropy factor between -0.95 and 0.95. Please refer to the insert for the link between the value and the color of the plot.

(b) Log<sub>10</sub> of the Relative Convergence of the Analytic solver solution for various values of the anisotropy factor  $g$ . Please refer to the legend inset for the link between the anisotropy factor and the color of plots. For each of all the cases, the relative error for  $N_n \geq 150$  is below  $1.10^{-8}$ .

Figure 6.4: Plots of Validity Metrics versus the Legendre polynomial order

Results presented in Fig. 6.4 are related to the simulation whose parameters, described in Table 6.2, corresponds to an absorbing and highly scattering medium with a priviledged

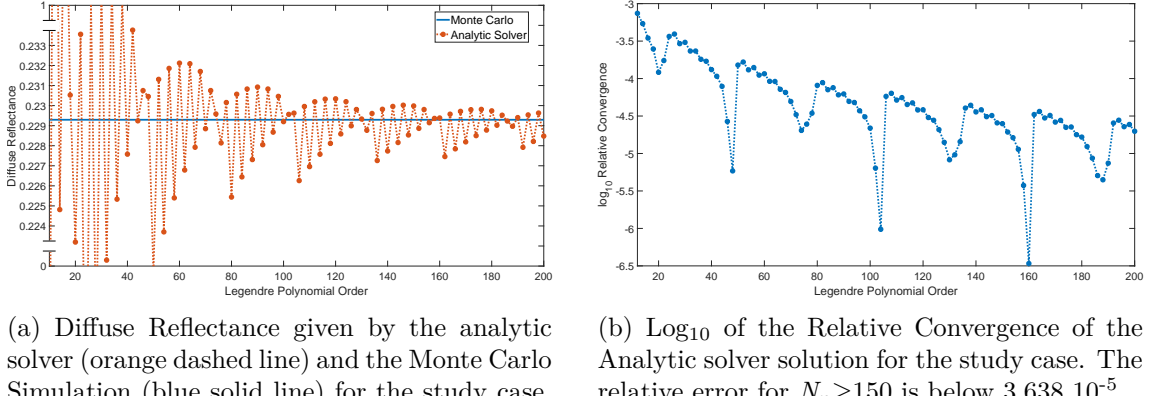
scattering direction due to a non-zero anisotropy factor  $g$ . Looking at Fig. 6.4a, we notice tiny variations of the diffuse reflectance value when the Legendre Polynomial order is higher than 60. Considering Fig. 6.4b, we notice that the relative convergence value decreases slower with large values of  $|g|$ . It is explained by the more and more sharp form of the phase function, which thus requires more and more points to be correctly discretized. However, setting a Legendre polynomial order of 160 sounds correct in terms of diffuse reflectance value and solution stability.

#### 6.2.4 Non-fluorescent isotropic scattering medium without index-matching interfaces

This validation case takes into account a non index-matching interface between the air ( $n = 1$ ) and the medium ( $n = 1.5$ ). We want to verify the correct implementation of the boundary conditions including Fresnel reflectance formulae previously described in Section 5.2.3.

medium name	$\mu_a$	$\mu_s$	$g$	$n$
air	0	0	1	1
medium	1	9	0	1.5

Table 6.3: Optical Parameters for the isotropic medium and air



(a) Diffuse Reflectance given by the analytic solver (orange dashed line) and the Monte Carlo Simulation (blue solid line) for the study case. The relative error for  $N_n \geq 150$  is below 0.8 %.

(b)  $\log_{10}$  of the Relative Convergence of the Analytic solver solution for the study case. The relative error for  $N_n \geq 150$  is below  $3.638 \cdot 10^{-5}$ .

Figure 6.5: Plots of Validity Metrics versus the Legendre polynomial order

The results presented in Fig. 6.5 are related to the simulation whose parameters are described in Table 6.3. Looking at Fig. 6.5a, one notices that the diffuse reflectance value computed by our RTE solver is not converging regularly. This effect is clearly linked with the sawtooth aspect of the relative convergence (Fig. 6.5b). To understand the origin of this effect, it is important to remember that using the Legendre discretization implies the use of specific discretization points (angles' cosines) defined as the roots of a Legendre polynomial with a specific even order.

Moreover, we recall that at each discretization point, the interface Fresnel function

is approximated by a piecewise constant function. The width  $w$  of the  $i^{th}$  piece is defined as  $w^i = (x_{Nn}^{i+1} - x_{Nn}^{i-1})/2$  where  $x_{Nn}^i$  is the  $i^{th}$  root of the Legendre polynomial of order  $N_n$ . Furthermore, the value of the approximated function on the piece considered is the value of the Fresnel function at the root  $x_{Nn}^i$  included in this piece.

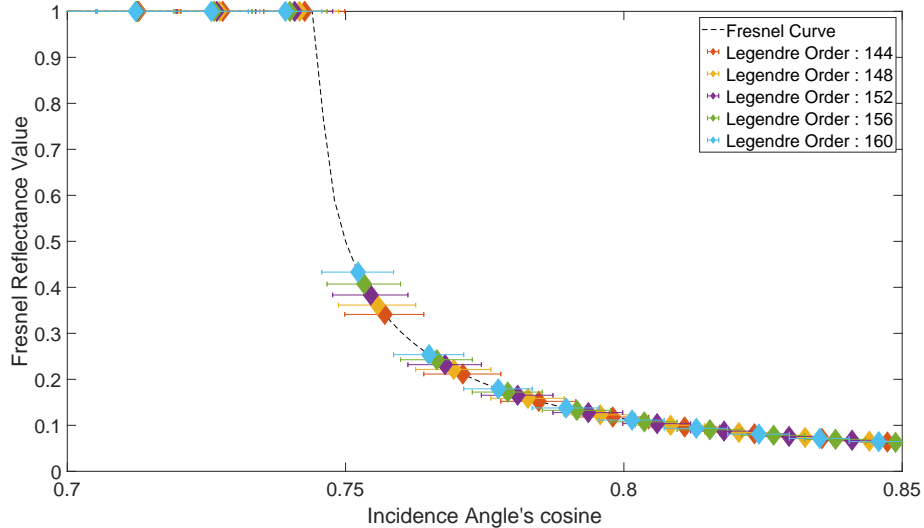


Figure 6.6: Fresnel angular reflectance function (dashed black line) and it piecewise constant discretisation for various Legendre polynomial order (color diamonds).

Thus, on Fig. 6.6, the horizontal bar on both sides of each diamond correspond to the width of the piece. It is then understandable that the discretization of the Fresnel angular reflectance is crucial in the region whose incidence angle's cosine is around 0.75. Especially, the discretization is less approximative for a Legendre order of 160 than 144 in this region as confirmed by the RMS Error in Table 6.4.

Legendre polynomial order	144	148	152	156	160	164
RMS Error ( $\times 10^{-6}$ )	347.7	287.7	217.4	128.5	2.884	406.8

Table 6.4: RMS Error of Fresnel Reflectance Function Discretization with roots of various Legendre polynomial order.

### 6.2.5 Non-fluorescent anisotropic scattering medium without index-matching interfaces

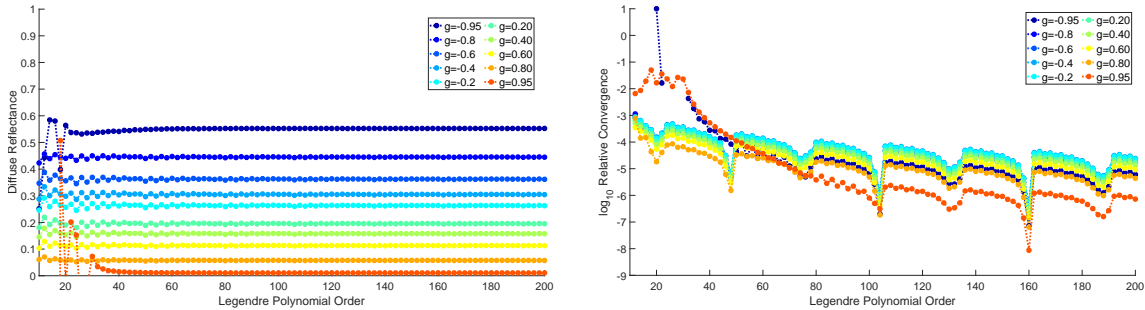
medium name	$\mu_a$	$\mu_s$	$g$	$n$
air	0	0	1	1
medium	1	9	$\neq 0$	1.5

Table 6.5: Optical Parameters for anisotropic semi-infinite medium with an interface with the air

The given configuration combines both effects of the anisotropic phase function and the

Fresnel angular reflectance. Comparing Figs. 6.4b, 6.5b and 6.7b, we notice that the main impact on the relative convergence between the anisotropy and the Fresnel reflectance depends on the order range of the Legendre polynomial under consideration.

Indeed, at low orders ( $N_n < 80$ ), high values of anisotropy factor has a major impact on the convergence while for high orders ( $N_n > 80$ ) the Fresnel Reflectance impacts the convergence with a sawtooth effect on the convergence curves.



(a) Diffuse reflectance from the Analytic solver depending on the order of the Legendre polynomial, i.e. the number of discretization points. Each plot corresponds to a different value of the anisotropy factor between -0.95 and 0.95. Please refer to the insert for the link between the value and the color of the plot.

(b)  $\log_{10}$  of the Relative Convergence of the Analytic solver solution for various values of the anisotropy factor  $g$ . Please refer to the legend inset for the link between the anisotropy factor and the color of plots. For each of all the cases, the relative error for  $N_n \geq 150$  is below  $4.421 \cdot 10^{-5}$ .

Figure 6.7: Plots of Validity Metrics versus the Legendre polynomial order

### 6.2.6 Literature reference configurations

Papers dedicated to the Monte Carlo simulator and RTE resolution uses two reference configurations for validation and comparison with existing results. We suggest comparing these two examples with our implementation of an RTE solver based on Legendre polynomials in cases 1 and 2. Moreover, the angular dependencies of the relative radiance in a slab and a semi-infinite medium with index-matching and with or without absorption have also been benchmarked with van de Hulst *et al.* data, and are reported a third case.

#### Case 1: isotropic semi-infinite medium without index-matching interface (Fresnel Reflectance)

In this case, we compare the reflectance predicted by the RTE and the one given in [Giovanelli (1955)] by using the set of parameters given in Table 6.6. The reflectance values are shown in Table 6.7. We notice that the absolute error on the total reflection

medium name	$\mu_a$	$\mu_s$	$g$	$n$
air	0	0	1	1
medium	1	9	0	1.5

Table 6.6: Optical Parameters extracted from article [Prahl *et al.* (1989)])

value is in the same range as Prahl *et al.*, which let us consider that our RTE solver works for isotropic semi-infinite medium with an interface with air. The error is mainly due to the discretization of the Fresnel angular reflectance function.

	[Giovanelli (1955)]	[Prahl <i>et al.</i> (1989)]	[Leh (2011)]	Discrete Ordinates ( $N_n = 150$ )
Total reflectance	0.2600	0.2608	0.2512	0.2608
Absolute error		0,0008	0,0088	0,0008

Table 6.7: Results comparison between various methods

### Case 2: anisotropic slab medium with index-matching interfaces

In this case, we compare the reflectance predicted by the RTE and the one given in [Van de Hulst (1980)] by using the set of parameters given in Table 6.8. The reflectance values are shown in Table 6.9.

medium name	$\mu_a$	$\mu_s$	$g$	$n$	$d$
air	0	0	1	1	$\infty$
medium	1	9	0.8	1	0.2
air	0	0	1	1	$\infty$

Table 6.8: Optical Parameters extracted from article [Prahl *et al.* (1989)])

	[Van de Hulst (1980)]	[Prahl <i>et al.</i> (1989)]	Discrete Ordinates ( $N_n = 150$ )
Total Reflectance	0.09739	0.0971	0.09739
<i>Absolute Error</i>		0,0003	$< 1e^{-5}$
Total Transmittance	0.66096	0.6616	0.66096
<i>Absolute Error</i>		0,0005	$< 1e^{-5}$

Table 6.9: Results comparison between various methods

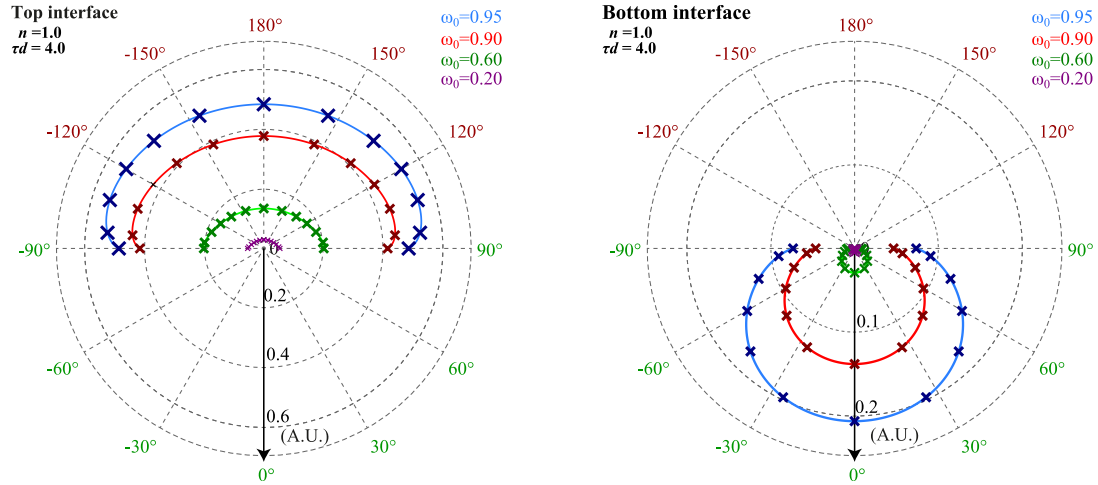
In Table 6.9, the absolute error on the total reflection and transmission values are smaller than the one of Prahl *et al.*. Again, we consider that our RTE solver works for anisotropic scattering slab media with index-matching interfaces.

### Case 3: relative angular radiance near interfaces of a slab medium

The discrete ordinate method as we use it gives access to the radiance according to the depth  $z$  and according to the angle  $\theta$  defined in Fig. 5.4 of the section 5.2.4. It seemed necessary to validate the angular distribution of the radiance with data issued from the literature provided in Table 12 of [Van de Hulst (1980)]. The proposed table is limited to isotropic scattering media with index-matching interfaces for different optical thicknesses

and albedo. This offers only a partial but no less relevant validation of the angular radiance distributions.

Among all the cases listed in the table, various ones have been studied, but we have chosen to present in the Fig. 6.8 only those associated with a single optical thickness for the sake of brevity.



(a) Cut views of the relative angular radiance diagram near the top interface between our solver (solid lines) and values given by Van de Hulst (crosses) for a scattering layer of optical thickness  $\tau_d = 4.00$  and relative refractive index  $n = 1.0$ , with  $g = 0$  with various albedo values  $\omega_0 = 0.95, \omega_0 = 0.9, \omega_0 = 0.6$  and  $\omega_0 = 0.2$ .

(b) Cut views of the relative angular radiance diagram near the bottom interface between our solver (solid lines) and values given by Van de Hulst (crosses) for a scattering layer of optical thickness  $\tau_d = 4.00$  and relative refractive index  $n = 1.0$ , with  $g = 0$  with various albedo values  $\omega_0 = 0.95, \omega_0 = 0.9, \omega_0 = 0.6$  and  $\omega_0 = 0.2$ .

Figure 6.8

As we can notice in Fig. 6.8, angular radiance computed with our RTE solver is consistent with data provided by [Van de Hulst (1980)] at both interfaces and for various albedo.

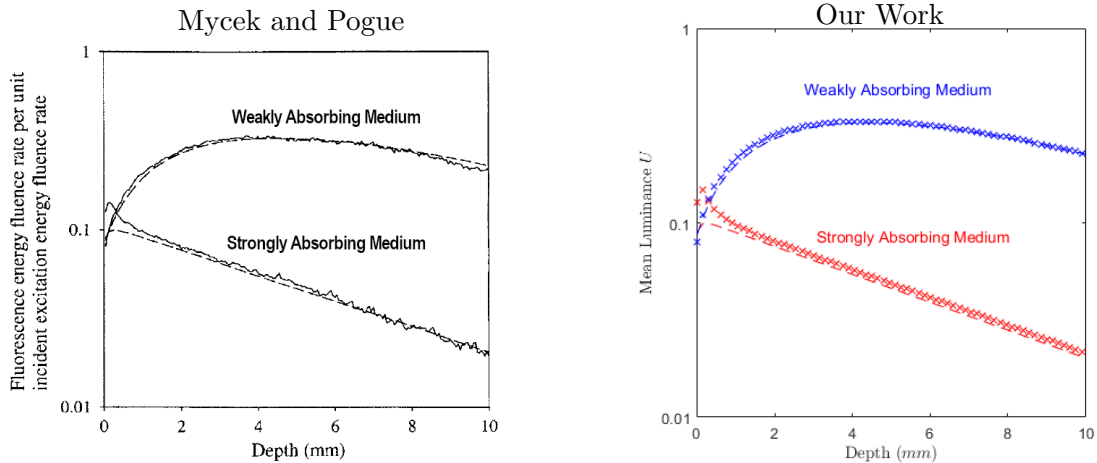
This case concludes the validation of the no fluorescence RTE solver code. In next section, we will now validate the RTE solver code including fluorescence.

### 6.2.7 Fluorescent media

The literature of optical fluorescence models is abundant. Nevertheless, too few papers provide tabulated data useful for validating the implementation of our RTE solver. We thus will rely on the Chapter I-2 of [Mycek and Pogue (2003)], which is to our knowledge the only element of literature providing data consistent with our geometry and assumptions. We want to compare the exitance as a function of depth from our RTE solver with that of the diffusion models presented in the handbook.

However, it is important to underline the description of two distinct diffusion models in the handbook. The first one considers that the excitation flux is described by a Beer-Lambert law (non-scattering or scattering and strongly absorbing media). The second one considers that the diffusion is important (media more scattering than absorbing), so the excitation

flux is a solution of the diffusion equation.



(a) Plot of fluorescence fluence rate as functions of depth for broad-beam steady-state excitation irradiation of a semi-infinite medium. Diffusion theory results are compared with Monte Carlo for the strongly absorbing medium and the weakly absorbing medium. Monte Carlo and Diffusion theory are plotted as solid and dashed lines, respectively. (Adapted from [Mycek and Pogue (2003)])

(b) Plot of fluorescence average irradiance as functions of depth for broad-beam steady-state excitation irradiation of a semi-infinite medium. discrete ordinates results are compared with diffusion theory for the strongly absorbing medium and the weakly absorbing medium. Diffusion theory and discrete ordinates are plotted as dashed lines and crosses, respectively.

Figure 6.9

Since fluorescence is not integrated in MCX and it would have been too long to implement it by ourselves, we only do an empirical visual validation. For this validation, tissue optical properties in  $\text{mm}^{-1}$  are: strongly absorbing  $\mu'_{s,x} = 1.4$ ,  $\mu_{a,x} = 8.5$ ,  $\mu_{a,x,d} = 0.5$ ,  $\mu'_{s,m} = 1.0$ ,  $\mu_{a,m} = 0.009$ ,  $\mu_{a,m,d} = 0.001$ ; weakly absorbing  $\mu'_{s,x} = 1.4$ ,  $\mu_{a,x} = 0.015$ ,  $\mu'_{a,x,d} = 0.005$ ,  $\mu'_{s,m} = 1.0$ ,  $\mu_{a,m} = 0.009$ ,  $\mu_{a,m,d} = 0.001$ . The fluorescence quantum yield is 1.

Visually, the solution proposed by our fluorescence RTE solver code (crosses in Fig.6.9b) matches the solution proposed by the Monte Carlo model of Mycek and Pogue (solid lines in Fig.6.9a), thus our fluorescence RTE solver code is valid.

### 6.2.8 Conclusion

The aim of this part was to validate the implementation of the RTE solver code in various cases, in particular those of the literature (section 6.2.6).

This validation by comparison with MC has highlighted first that the anisotropy impacts the relative convergence: for high anisotropy factor values, the relative convergence is slower than with an anisotropy factor set to 0. Then, it has been shown that the Fresnel angular reflectance impacts a lot the relative convergence especially in media without index-matching interfaces (sawtooth effect on the relative convergence curve). Further-

more, it points out that in the cases studied, there is an order of the Legendre polynomial beyond which the precision of the relative convergence has a small impact on the value of the diffuse reflectance.

Finally, we briefly demonstrate that the model of fluorescent cases is coherent with Monte-Carlo simulations reported in literature.

In the rest of the chapter, we propose to study the impact of the discretization method on the relative convergence.

### 6.3 Comparative study between angular discretization methods

As noticed previously, the discretization of the Fresnel angular reflectance impacts the speed of convergence of the discrete ordinates method using Legendre polynomial roots. In this section, we would like to compare the relative convergence of two distinct discretization methods: one using Legendre polynomial roots and another one with a regular step. We only consider a semi-infinite medium. The parameters for the refractive index and the anisotropy factor are the same as those given in Tables 6.2 to 6.5.

#### 6.3.1 Isotropic scattering medium with index-matching interfaces

An isotropic scattering medium, having the same refractive index as the surrounding medium, is considered as the "easy" case because there is neither anisotropy nor step index. In each case, for each discretization method, the  $\log_{10}$  of the relative convergence is plotted in blue (refer to the left vertical Axis). The  $\log_{10}$  RMS error between the two methods is also plotted in orange line (refer to the right vertical Axis).

By looking at Fig. 6.10, we notice that the Legendre discretization method converges faster than the regular step discretization method.

This can be explained by the fact that the solver we have implemented uses Gauss-Legendre quadrature to simplify integral terms of the radiative transfer equation. Indeed, because we try to integrate functions over the  $[-1,1]$  interval with Gauss-Legendre quadrature, the associated orthogonal polynomials are Legendre polynomials, denoted by  $P_n(x)$ . This explains why the Legendre discretization is the best one in terms of convergence speed.

#### 6.3.2 Anisotropic scattering medium with index-matching interfaces

In this case, we consider an anisotropic scattering medium, characterized by a Henyey-Greenstein scattering phase function with  $g = 0.5$ .

Considering Fig.6.11, we notice that the Legendre discretization method converges faster than the regular step discretization method.

Adding the anisotropy effect on scattering phase function has even more fastened the relative convergence. This can be explained by the location of roots as their number

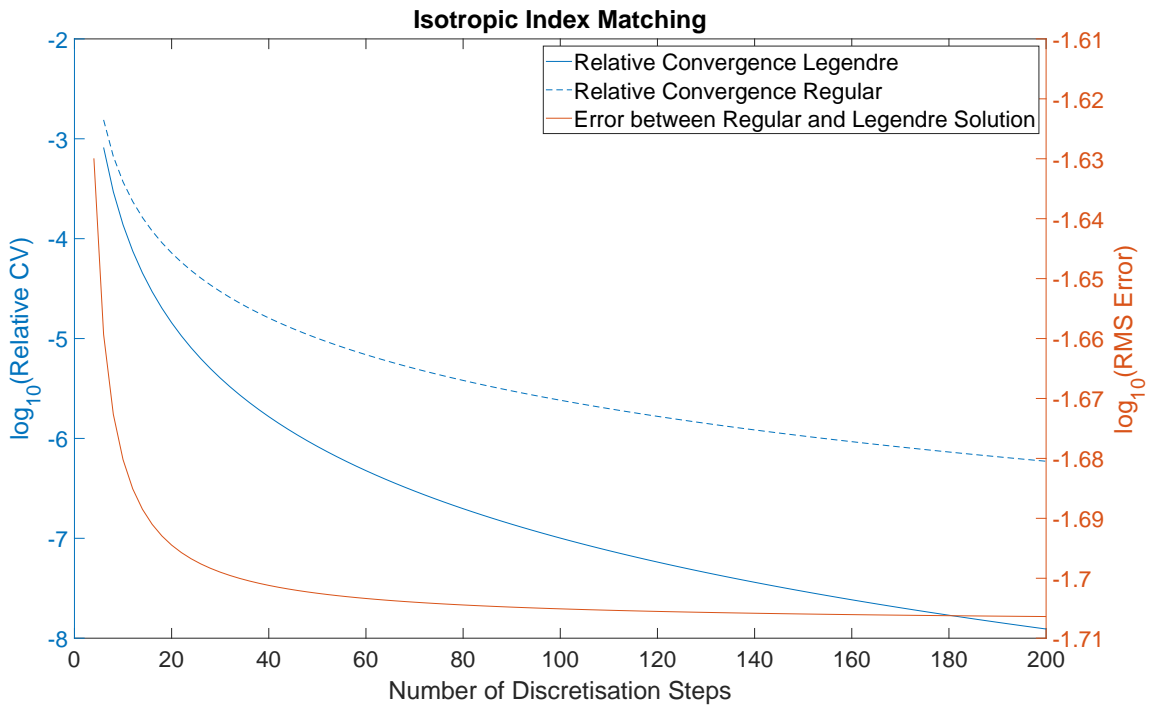


Figure 6.10:  $\log_{10}$  of the Relative Convergence of the Legendre Discretization- (solid line) and Regular Discretization- (dashed line) solver solution for the study case.

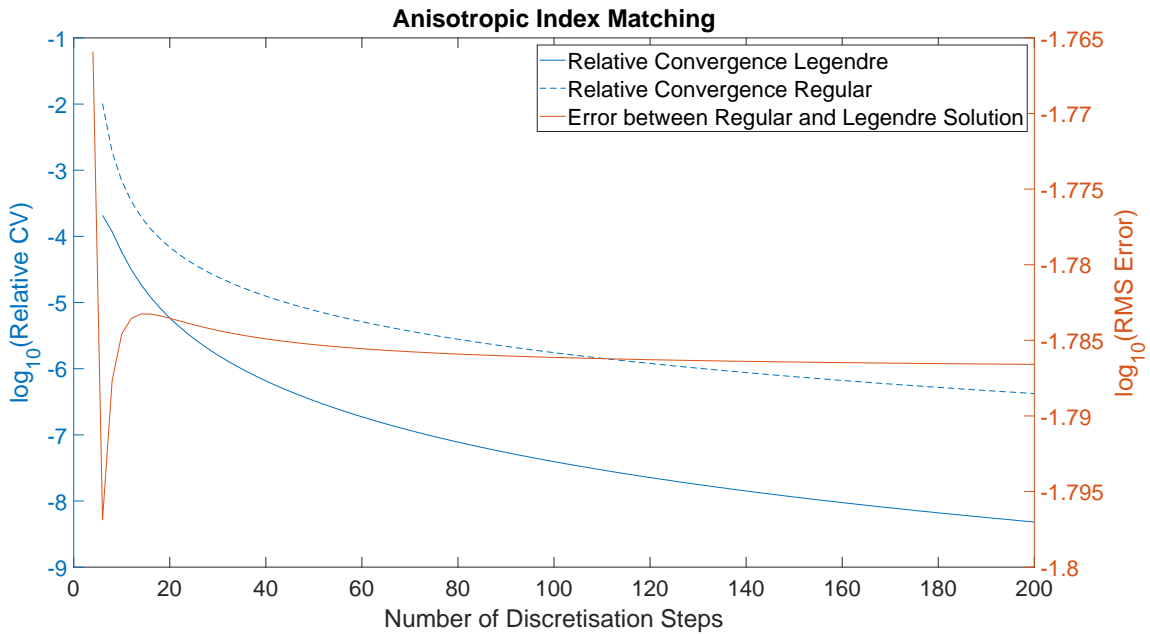


Figure 6.11:  $\log_{10}$  of the Relative Convergence of the Legendre Discretization- (solid line) and Regular Discretization- (dashed line) solver solution for the study case.

increases: Legendre roots are indeed not regularly located in the  $[-1,1]$  interval; there are more roots at the neighborhood of the boundaries (i.e., -1 and 1). This is an advantage because the phase function varies a lot in these regions and it must be finely sampled. This also explains the difference of convergence speed with a regular discretization. However,

this stands for a moderate anisotropy factor ( $g=0.5$ ). With an anisotropy factor approaching 1 or -1, the convergence would be slower.

Let us now study the case which includes non index-matching boundaries between the scattering medium and the surrounding medium.

### 6.3.3 Isotropic scattering medium without index-matching interfaces

When the refractive index of the medium (e.g., glass) differs from the one of the surrounding medium (e.g., air), the Fresnel reflection depends on the orientation of light. This must be taken into account in the solving of the RTE.

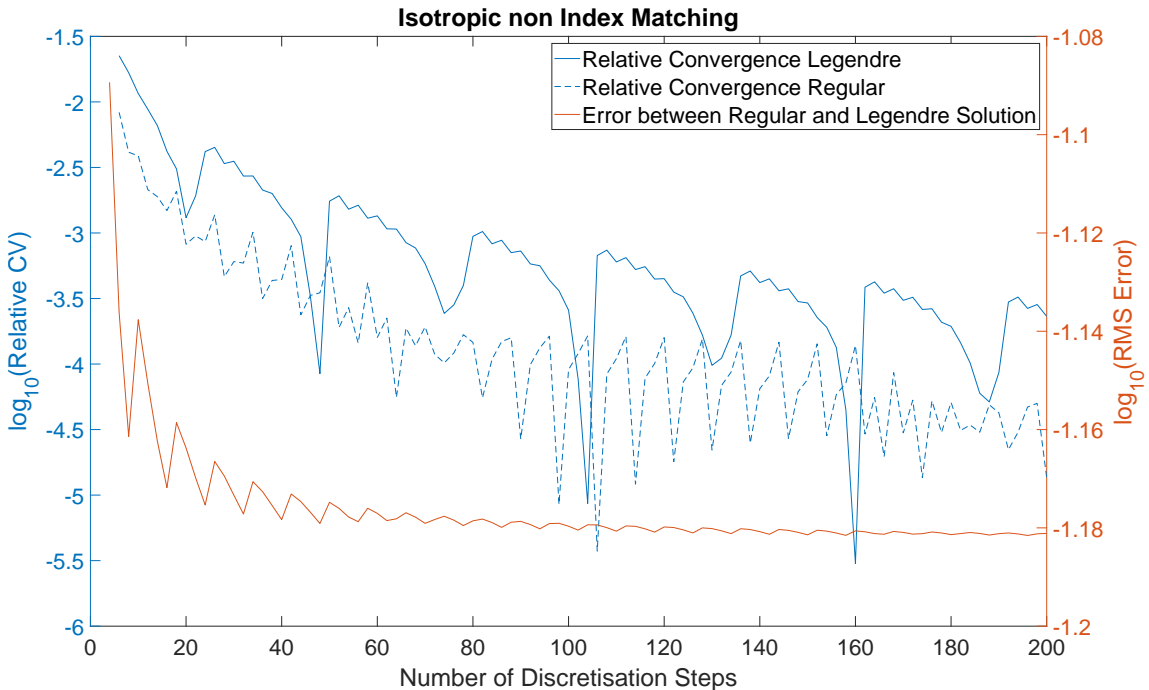


Figure 6.12: Log<sub>10</sub> of the Relative Convergence of the Legendre Discretization- (solid line) and Regular Discretization- (dashed line) solver solution for the study case.

We see in Figure 6.12 that in average the Legendre discretization method converges slower than the regular step one. This has to do with the location of the sampling points and their ability to correctly sample the Fresnel angular reflectance (cf. Section 6.2.4).

In addition, when comparing the log<sub>10</sub> RMS Error with the one of Fig. 6.10, the final value for 200 discretization points is higher without- than with index-matching interfaces, which highlights the effect of the discretization of the Fresnel angular reflectance.

### 6.3.4 Anisotropic scattering medium without index-matching interfaces

In this case, we consider a medium which is the most realistic for biological tissues: a high anisotropy factor and no index-matching interfaces with the surrounding medium. As we have seen previously, the Fresnel angular reflectance presents a very pronounced

discontinuity. To correctly describe this discontinuity, it requires a higher discretization on the basis of Legendre polynomials than for a regular discretization. Moreover, we have also noticed that, with index-matching, the anisotropy has a little effect on the convergence speed of the Legendre discretization compared to the regular discretization.

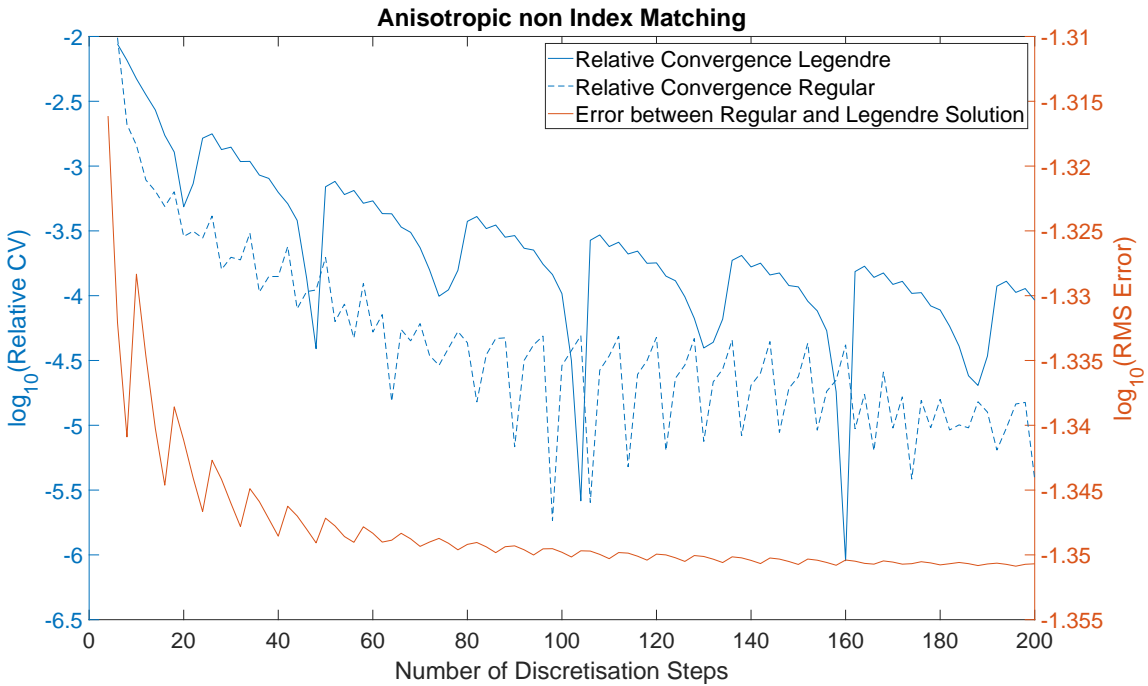


Figure 6.13: Log<sub>10</sub> of the Relative Convergence of the Legendre Discretization- (solid line) and Regular Discretization- (dashed line) solver solution for the study case.

In Figure 6.13, we notice that in average the Legendre discretization method converges slower than the regular step discretization method. Furthermore, when we confront the log<sub>10</sub> RMS Error with the one of Fig. 6.11, the final value with 200 discretization points is higher without- than with index-matching interfaces. This reinforce the previous conclusion : the discretization of the Fresnel angular reflectance function is more difficult with the Legendre polynomials discretization than with a regular discretization.

### 6.3.5 Conclusion

In this last study, we wanted to compare two discretization methods, one relying on Legendre polynomial roots, the other on a regular step. Results of the comparative study are summed up in Table 6.10, which suggests a correct number of discretization steps for the different configurations studied. As expected, we conclude that the Legendre discretization is very efficient according to the relative convergence criterion for isotropic or anisotropic scattering medium with index-matching interfaces. Nevertheless, the discretization of the Fresnel angular reflectance is so difficult that the constant step discretization method seems to be more efficient than Legendre when there is no index matching interfaces. Despite this, we will voluntarily keep the Legendre discretization method for

the other chapters of this manuscript, considering a high order (e.g. 160) to avoid errors due to a too coarse discretization.

As mentioned in the introduction, some optical models such as the Kubelka-Munk model or the diffusion approximation (also called P1 approximation) result from simplifying assumptions in the resolution of the radiative transfer equation (RTE) that allow in particular to fix the value of some parameters. Next chapter focuses on the study of one of these fixed parameters, the internal reflectance, and its direct application on a case related to the subject of the thesis.

Medium	Residual Error ( $\times 10^{-6}$ )	Legendre discretization	Regular step discretization
Isotropic scattering with index matching interfaces	$0.97 \pm 0.04$	48	154
Anisotropic scattering with index-matching interfaces	$2.57 \pm 0.06$	104	106
Isotropic scattering without index-matching interfaces	$3.37 \pm 0.51$	160	106
Anisotropic scattering without index-matching interfaces	$1.37 \pm 0.66$	160	98

Table 6.10: Recommended number of discretization steps for the different configurations studied in this section

# Chapter 7

---

## Internal reflectance of the air-medium interfaces

---

### 7.1 Introduction

In quantification of fluorescence as in many fields of engineering such as computer graphics, dental restorations or 3D printing technologies, it is necessary to characterize the optical properties of scattering materials in order either to accurately predict the appearance of products they are made of or to correct measurements for scattering and absorption effects. In the case of strongly diffusing materials, for decades, flux transfer models like the Kubelka-Munk model (2-flux) or 4-flux models have been successfully used to this aim [Duveiller *et al.* (2020), Séroul *et al.* (2016), Van Song *et al.* (2016), Hébert *et al.* (2016), Mazauric *et al.* (2014), Simonot *et al.* (2014), Yoshimura *et al.* (2013), Simonot *et al.* (2011), Latour *et al.* (2009), Yang and Hersch (2008), Durant *et al.* (2007), Pierrat *et al.* (2006), Yang *et al.* (2002), Elias and Elias (2002), Durkin *et al.* (1994), Johnston *et al.* (1986)a]. However, they have well-known limitations when the material is weakly scattering or the optical thickness is small, giving the object a highly translucent appearance. These limitations have been discussed in various papers [Duveiller *et al.* (2020), Happel *et al.* (2014), Thennadil (2008), Fleming *et al.* (2004)]. One source of imprecision is the fact that these models assume that the fluxes are Lambertian (radiance angularly uniform) at any depth within the material. The internal reflectance of the bordering interfaces are computed based on this assumption. But when the layer is weakly scattering, the fluxes are far from being Lambertian, and their angular distribution varies

as a function of the depth within the material. The internal reflectance of the interfaces should therefore be computed in respect to the precise angular distribution of the light that falls on them. This is precisely what we want to investigate in this chapter.

## 7.2 Reminders about the Kubelka-Munk model

In the Kubelka-Munk model, the light is assumed to propagate along two opposite directions, upwards and downwards, inside a slab. The incident light is assumed Lambertian, and all the reflected or transmitted flux is collected. This model assumes that light is either absorbed or scattered isotropically [Vargas and Niklasson (1997)a]. The Fresnel reflections at the interfaces of the slab are accounted for by the Saunderson correction [Saunderson (1942)], which corrects the reflectance and transmittance calculated by the Kubelka-Munk model, taking into account the observation and illumination geometries, and refractive index mismatch. The validity of this correction was discussed by several authors for different applications [Orchard (1977), Johnston *et al.* (1986)b]. One reason for the lack of accuracy of 2-flux models with translucent layers is the poor estimation of the internal reflectance of the interfaces bordering the material layer. Indeed, the Saunderson correction [Saunderson (1942), Hébert *et al.* (2014)] relies on the assumption that the light reaching the interfaces is Lambertian, which may not be the case in thin and weakly scattering layers. More importantly, the exact angular distribution depends on the scattering and absorption properties of each layer, as well as its thickness [Simonot *et al.* (2008)]. Following guidelines from the CIE [Artom *et al.* (1979)], the reflectance or transmittance measurement geometries are the d:8° geometry (where a sample is illuminated with diffuse light in an integrating sphere and the emerging light is captured at an 8° angle) or likewise the 8°:d geometry (where a sample is illuminated with directional light at an 8° angle and the emerging light is collected by an integrating sphere). Thus the incident light (or the captured light) is directional, whereas the 2-flux model assumes measurements based on a bi-hemispherical geometry. This has almost no impact in strongly scattering layers but may raise difficulties in translucent materials. As an example, it has been shown recently that in dental repair biomaterials, using an internal reflectance value of 4% (instead of the expected lambertian value of 60% for a refractive index 1.5) improves a lot the color prediction accuracy for slabs of various thicknesses [Duveiller *et al.* (2020)].

The 4-flux model considers the propagation of upwards and downwards fluxes inside a slab. Compared to the 2-flux model, the 4-flux also considers the propagation of directional light and the fraction of scattered directional light which contributes to the diffuse flux. Therefore, it is in principle more suited to reproduce experiments based on measuring devices with the 8°:d or d:8°geometry as recommended by the CIE [Artom *et al.* (1979)] than the 2-flux model, which assumes a d:d geometry. Let's stress that such a d:d geometry is very difficult to set up experimentally, although it might be equivalent to a d:8° or 8°:d geometry when measuring highly scattering media. The 4-flux model generalized by Maheu *et al.* [Maheu *et al.* (1984)] assumes that light is either absorbed or scattered.

The angular distribution of diffused light is also considered with the forward scattering ratio parameter (denoted  $\zeta$ , it indicates which proportion of the diffused flux is scattered in the forward direction) and the average path length parameter (denoted  $\epsilon$ , it reflects the average increase of distance traveled in the slab by scattered light rays compared to directional light rays) [Vargas and Niklasson (1997)b]. For isotropic scattering, the forward scattering ratio is 0.5 (same amount of light is scattered in the forward and the backward hemispheres) and the average path length parameter is 2.

In principle, these issues could be solved if a more sophisticated solution of the radiative transfer equation (RTE) [Chandrasekhar (1960)b] (either by direct solving or by Monte Carlo methods) is used instead of 2- or 4-flux methods. However, these approaches are more time consuming, making challenging the inverse problem of extraction of optical parameters from a large set of experiments.

The aim of the study is to investigate this point in details using the formalism of the radiative transfer equation, and to compute more accurate values of the internal reflectance at the interfaces to be used in the simplified 2-flux model (such as the Saunderson correction for the Kubelka-Munk model [Saunderson (1942), Hébert *et al.* (2014)]), with respect to the thickness, refractive index, absorption and scattering coefficients of the considered layer.

A short description of the object of study is given first. Then the method described in Chapter 5 is used to compute the angular radiance distribution at their interfaces. The impact of absorption coefficient, layer thickness, scattering anisotropy in both translucent and strongly scattering materials is then carefully investigated. Finally, the accuracy of conventional and improved 2- and 4-flux models is discussed.

### 7.2.1 Description of the object of study

Just a reminder, the radiative transfer, its formalism and its solving have been extensively investigated by many authors. Details about it can be found in the Chapter 5 of this manuscript or in the following reference books [Chandrasekhar (1960)b], [Ishimaru (1978)].

We remind that the direct solving method explained in Chapter 5 and applied in a 1D model enables to obtain the diffused radiance distribution at any depth in the layer, therefore at the two depths of interest here  $z = 0$  and  $z = d$ . These angular distributions, are integrated over the hemisphere to provide the expected internal reflectance. Radiance distributions have been studied for a long time, in particular to highlight the change in shape of the radiance distribution when anisotropic scattering occurs [Graaff *et al.* (1989), Graaff *et al.* (1993)], when light is scattered by a rough interface [Nieto-Vesperinas and Sanchez-Gil (1992)], or during its propagation in a scattering medium [Mudgett and Richards (1971), Da Silva *et al.* (2004), Neuman *et al.* (2011)].

As previously, angles  $|\theta| \leq 90^\circ$  (i.e.,  $\mu \geq 0$ ) correspond to the lower hemisphere  $\Omega'$  where radiance values depict the angular distribution of the light going downwards. The other

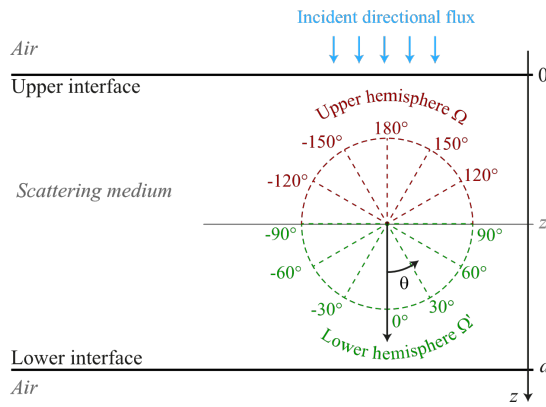


Figure 7.1: Studied configuration where a layer of scattering medium with a refractive index different from the surrounding air (“slab”) is illuminated by directional light at normal incidence. Physical quantities depend on depth  $z$  and angle  $\theta$ .

angles correspond to the upper hemisphere  $\Omega$ , where radiance values depict the angular distribution of the light going towards negative values of  $z$  (therefore upwards).

### 7.3 Semi-infinite layer: Results and discussion

We first consider the case of a semi-infinite scattering medium. To simplify the discussion, the phase function is first assumed isotropic, i.e.,  $g = 0$ . The impact of scattering anisotropy is discussed later, in the case of a slab only. The main mechanisms occurring during light transport in the scattering material are illustrated on Fig. 7.2. First, the incident directional flux can be either reflected by the top interface or transmitted into the medium, where it is progressively scattered or absorbed. Some scattered light propagating upwards may reach the interface, where it can be either transmitted or reflected. Note that all light rays with incident angle higher than the critical angle  $i_c = \arcsin(1/n)$  are necessarily reflected (total internal reflection). It must be noted that in the semi-infinite material, the light that propagates upwards has necessarily undergone one or several scattering events.

Let's us now discuss the collective impact of these mechanisms on the overall angular distribution of the radiance at the top interface. In Fig. 7.3a are plotted, in polar coordinates, cut-views of the relative angular radiance  $L_z(\theta)$  at  $z = 0$  (named  $L_0(\theta)$  hereinafter) as a function of the angle  $\theta$  defined in Fig. 5.4, for a non-absorbing medium (blue curve) or absorbing medium (red curve).

In the case of a non-absorbing semi-infinite material (blue curve), the light that propagates upwards, after backscattering, is lambertian: the radiance is a constant  $L_u$ , the graph draws a hemi-circle. This is expected, and supports the common assumptions made in the literature. In the lower hemisphere, as set by the boundary conditions, the downward radiance  $L_0(\theta)$  is the result of the internal reflection of the radiance propagating upwards, therefore the product of radiance  $L_u$  with the Fresnel reflectance. For a refractive index

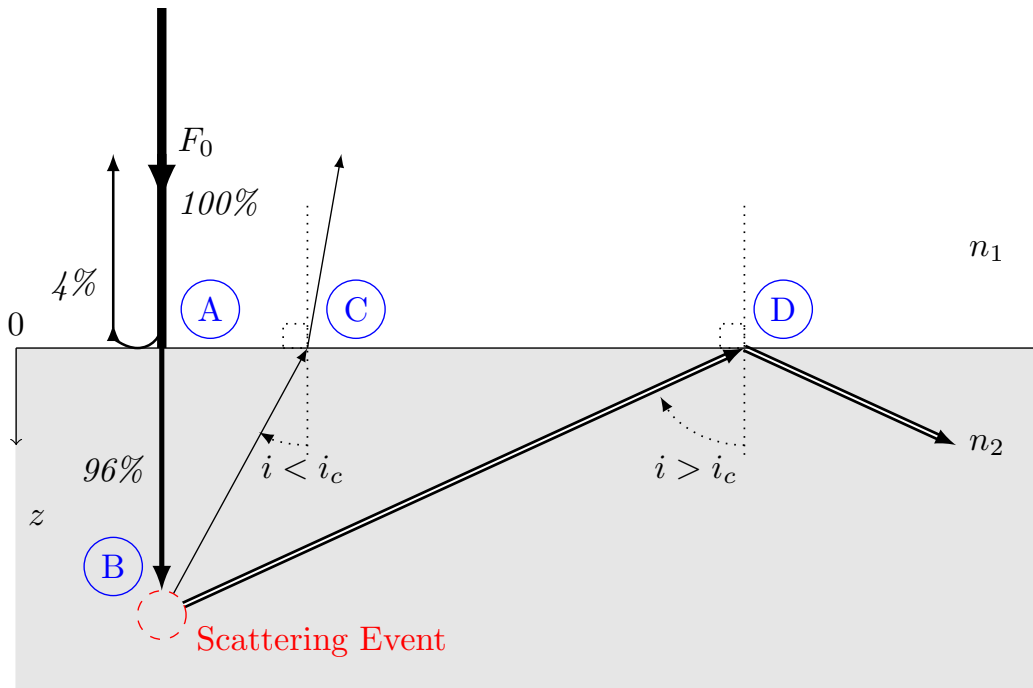


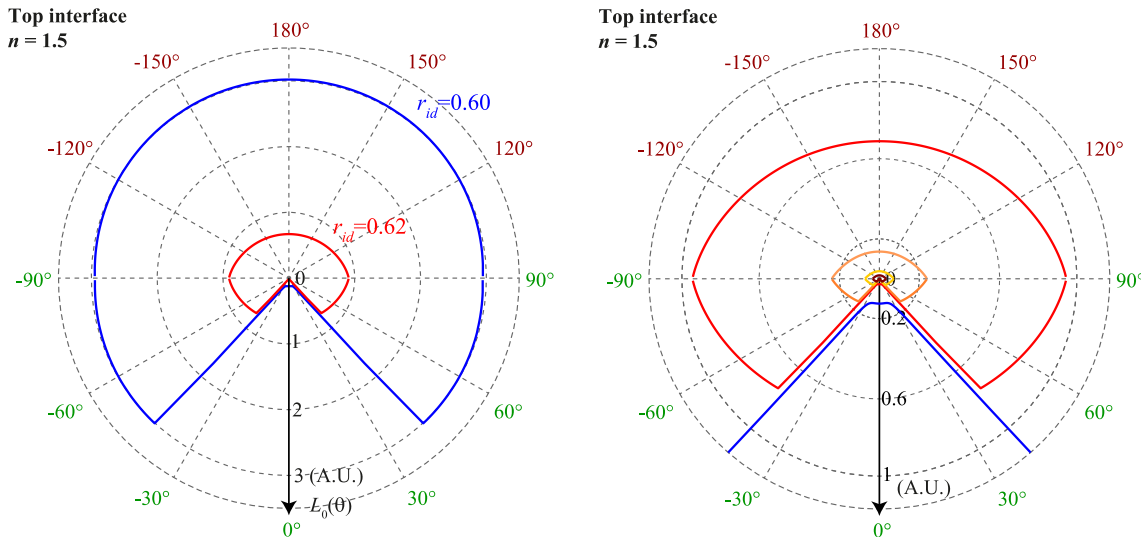
Figure 7.2: Photon trajectory inside a semi-infinite layer of scattering medium under directional incident light (irradiance  $F_0$ ). The incident light can be either reflected at the interface (A) or transmitted into the medium. After a scattering event (B), a photon may propagate until reaching the interface. If the incident angle is below the critical angle  $i_c$ , it can exit the medium or be reflected (C). If it is higher than  $i_c$ , it is totally reflected back to the medium (D). Percentages are given for  $n = n_2/n_1 = 1.5$ .

$n$  of 1.5, this latter is equal to 0.04 at  $\theta = 0^\circ$ , and suddenly reaches 1 beyond the critical angle  $i_c = \arcsin(1/n) \approx 42^\circ$ . Let's examine the corresponding diffused internal reflection coefficient  $r_{id}$ . The latter is defined as:

$$r_{id} = \frac{\int_0^{\pi/2} L_0(\pi - \theta) R_{21}(\theta) \sin(2\theta) d\theta}{\int_0^{\pi/2} L_0(\pi - \theta) \sin(2\theta) d\theta} \quad (7.1)$$

where  $R_{21}(\theta)$  is the Fresnel angular reflectance of the material-air interface when light comes at an angle  $\theta$  from the medium (therefore when the angle is  $180^\circ - |\theta|$  in our radiance diagram, where the light striking the interface propagates with zenithal angles  $|\theta| > 90^\circ$ ). As the upward light is lambertian (the radiance  $L_0(\theta)$  is constant over the hemisphere  $\Omega$ ), we have  $r_i = 0.60$ .

In the case of an absorbing semi-infinite medium (red curve), due to absorption, the overall radiance is of course lower than in the non-absorbing medium (both are plotted with the same scale in Fig. 7.3a). Moreover, we observe that the upward radiance (in the upper hemisphere) is not constant anymore: it takes higher values at  $|\theta| = 90^\circ$  than at  $\theta = 180^\circ$ . The light propagating upwards is therefore no longer lambertian. Let us comment this discrepancy. First, remind that at  $z = 0$ , the upward radiance results from the backscattering of directional light propagating downwards and diffused light propagating



(a) Cut view of the relative angular radiance diagram near the top interface for semi-infinite scattering layers of two media of relative refractive index  $n = 1.5$ , with  $g = 0$ : a non-absorbing medium of scattering coefficient  $\mu_s = 5.0 \text{ mm}^{-1}$  and albedo  $\omega_0 = 1$  (blue curve), and an absorbing medium of extinction coefficient  $(\mu_a + \mu_s) = 5.0 \text{ mm}^{-1}$  and albedo  $\omega_0 = 0.9$  (red curve). The light illuminating the interface from inside the layer propagates with zenithal angles  $|\theta| > 90^\circ$  whereas the reflected light propagates with angles  $|\theta| < 90^\circ$ .

(b) Zoom of the cut view of the relative angular radiance diagram near the top interface for semi-infinite scattering layers of two media of relative refractive index  $n = 1.5$  with  $g = 0$  and the same extinction coefficient  $(\mu_a + \mu_s) = 5.0 \text{ mm}^{-1}$ : a non-absorbing medium of albedo  $\omega_0 = 1$  (blue curve), an absorbing medium of albedo  $\omega_0 = 0.9$ , resp  $\omega_0 = 0.5$ ,  $\omega_0 = 0.2$  and  $\omega_0 = 0.1$  (red curve, resp. orange curve, yellow curve and brown curve).

Figure 7.3

upwards. As previously seen, the downward radiance is not lambertian, because of the angular dependence of the Fresnel angular reflectance of the interface. However, in the non-absorbing medium, the upward radiance results from an infinite number of isotropic scattering events, which allows to get a lambertian distribution. On the contrary, in presence of absorption, the upward radiance results from a limited number of scattering events only. In consequence, although isotropic, scattering fails to distribute light uniformly over the sphere, which explains why the contribution to the upward flux of nearly normal radiances is lower than the one of grazing radiances. According to Fig. 7.3b, the more the absorption increases, the less the upward luminance distribution is lambertian.

Moreover, in Fig. 7.4, normalized radiation for different optical indexes has been computed at the same level of absorption, confirming that the non-lambertian shape of the radiance is indeed a consequence of combined effects of absorption and Fresnel reflection. The anisotropy of  $L_0(\theta)$  modifies the calculation of the diffused internal reflectance  $r_{id}$ . In this case, the numerator of Eq. 7.1 changes less than the denominator which increases, resulting in an increase of  $r_{id}$  to 0.62 (see Fig. 7.3a). In the following, these conclusions are extended to the case of a finite thickness layer, with first isotropic, and then anisotropic scattering.

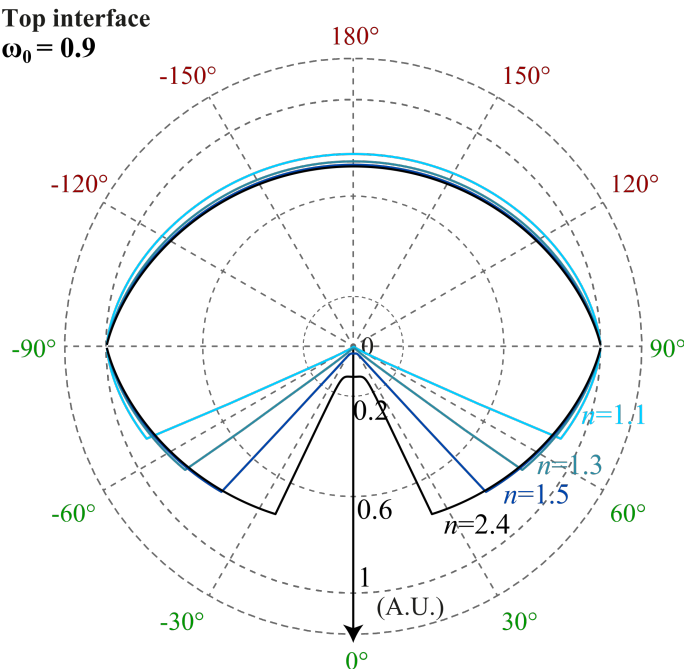


Figure 7.4: Comparison of cut views of the relative angular radiance diagram near the top interface for a semi-infinite scattering layer of albedo  $\omega_0 = 0.9$ , with  $g = 0$  and an extinction coefficient  $(\mu_a + \mu_s) = 5.0 \text{ mm}^{-1}$  for various relative refractive index  $n = 1.1$ , resp 1.3, 1.5, 2.4.

## 7.4 Finite thickness layer (slab): Results and Discussion

We now consider the case of a layer of finite thickness  $d$  with optical thickness  $\tau_d = (\mu_a + \mu_s)d$ . Global internal reflection may occur at both interfaces in a similar way, although the situation of each interface is not symmetrical, as the directional light enters from the top interface only. In this case, not only the top (denoted  $r_{id}$ ) but also the bottom (denoted  $r'_{id}$ ) internal reflectance require attention. It is worth to be noted that  $r_{id}$  and  $r'_{id}$  refer to the internal reflectance of the diffused radiance component  $L_d$  only. For this reason, we introduced two other internal reflectances (named global internal reflectances):  $r_{ig}$  for the front interface, and  $r'_{ig}$  for the back interface, that account for both directional and diffused components, such that

$$r_{ig} = \frac{F_d}{F_d + F_N} r_{id} + \frac{F'_N}{F_d + F_N} r_N \quad (7.2)$$

and

$$r'_{ig} = \frac{F'_d}{F'_d + F'_N} r'_{id} + \frac{F'_N}{F'_d + F'_N} r'_N \quad (7.3)$$

with  $F_d$  and  $F'_d$ , resp.  $F_N$  and  $F'_N$ , the diffused, resp. the directional, fluxes falling on the interface,  $r_N$  and  $r'_N$  the Fresnel reflectance at normal incidence from the medium through air. All quantities without quote mark, resp. with quote mark, refers to the top interface, resp. to the bottom interface.

As the 4-flux model treats the propagation of directional and diffused light separately,  $r_{id}$  and  $r'_{id}$  should be used for the diffused component in the 4-flux model. On the contrary, as the 2-flux model ignores directional light, the reflectance  $r_{ig}$  and  $r'_{ig}$  should be used as correct parameters for this latter approach.

#### 7.4.1 Radiance angular variations and internal reflectances in the case of an isotropic scattering phase function

Fig. 7.5A, resp. Fig. 7.5B, represents diffused radiances  $L_0(\theta)$  and  $L_d(\theta)$  at the top and bottom interfaces as functions of the zenithal angle in isotropic cases in absence of absorption, respectively in presence of absorption, for various optical thicknesses with the sum of the absorption and scattering coefficients remaining constant in our simulations.

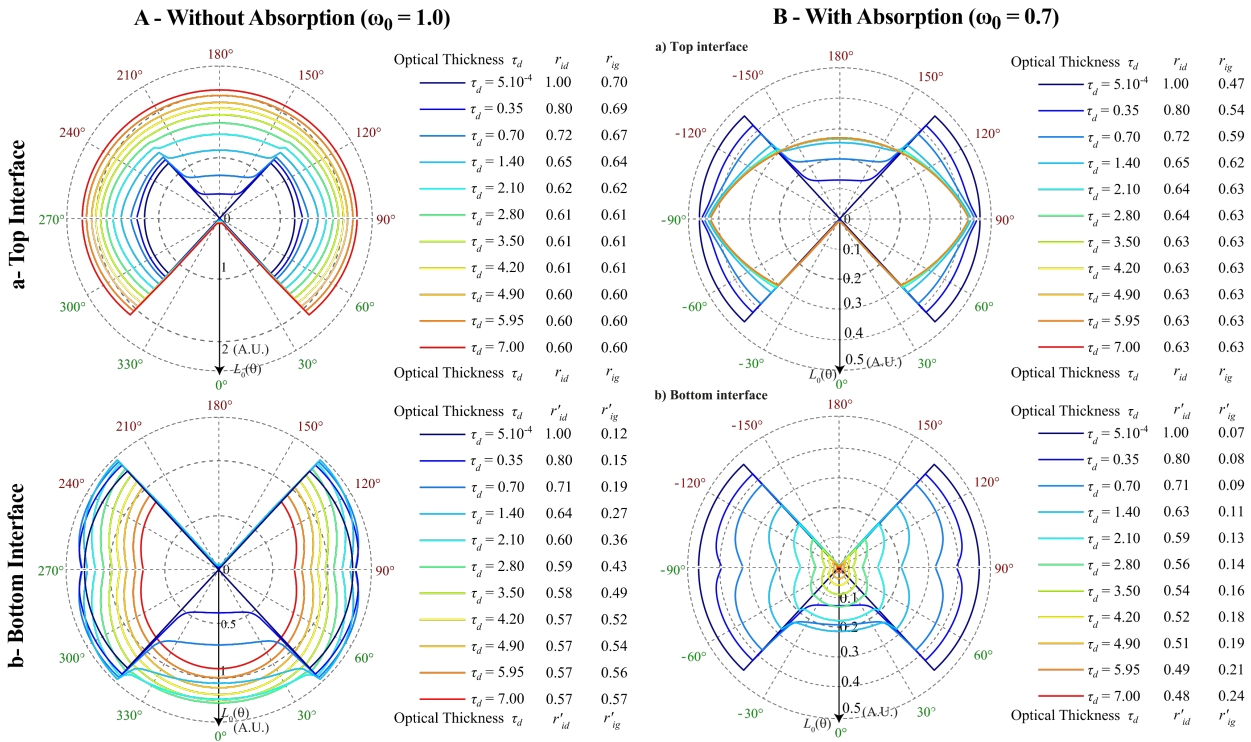


Figure 7.5: Polar plot of the diffuse radiance at the top interface,  $L_0(\theta)$  (Fig. 4Aa), resp. (Fig 4Ba), and the bottom interface,  $L_d(\theta)$  (Fig. 4Ab), resp. (Fig 4Bb), for isotropic layers of different optical thicknesses in absence of absorption (refractive index  $n = 1.5$ , albedo  $\omega_0 = \mu_s/(\mu_a + \mu_s) = 1.0$ ), resp. in presence of absorption (refractive index  $n = 1.5$ , albedo  $\omega_0 = \mu_s/(\mu_a + \mu_s) = 0.7$ ).

For large optical thicknesses, i.e.,  $(\mu_a + \mu_s)d \gg 1$  (red-orange curves), with or without absorption, for an isotropic phase function, the diffused radiance distribution at the top interface tends to the one observed for a semi-infinite medium discussed in the previous section (Fig. 7.3a): the slab simply behaves as a semi-infinite medium. In absence of absorption, the radiance distribution at the bottom interface also tends to be a constant, and thus,  $r_{ig}$  (resp.  $r_{id}$ ) tends to be equal to  $r'_{ig}$  (resp.  $r'_{id}$ ). In presence of absorption,

the diffused radiance distribution at the bottom interface tends to be negligible for large optical thicknesses. Even if it is possible (although difficult) to compute a diffused and global internal reflectance at this bottom interface, as the bottom radiance is negligible, this quantity does not really have any physical meaning. Consequently, this case will not be discussed hereafter.

For small optical distance i.e.,  $(\mu_a + \mu_s)d \ll 1$  (blue curves), however, the impact of scattering becomes negligible. We thus observe a similar radiance pattern at both interfaces, in presence or in absence of absorption: radiances  $L_0(\theta)$  and  $L_d(\theta)$  become almost negligible for incidence angles lower than the critical angle  $i_c$ . Indeed, the radiance at lower incidence angles is mainly transmitted out of the scattering medium at each interface and is no longer compensated by scattering. In consequence, upward and downward radiances become almost identical at each interface. For this reason, the numerator and denominator of equation 7.1 tend to be equal for the diffused internal reflectance at both interfaces, resulting in a diffused internal reflectance close to 1 when  $d$  tends to zero.

Note that the value of  $\tau_d = 5.10^{-4}$  is an extremely low value of the optical thickness, corresponding in this example to the questionable physical thickness of  $d = 100$  nm. Results obtained in this case should be regarded more as a theoretical limit. Depending on the value of  $\mu_a$  and  $\mu_s$ , this limit may be relevant or not for certain applications, with respect to the size of the scattering centers for instance. Moreover, it is likely that wave optics effects, depending on the coherence length, should be included for a more accurate description of scattering at such dimension (which has not been done here).

The diffused internal reflectance of the top and bottom interfaces, respectively  $r_{id}$  and  $r'_{id}$ , are plotted in Fig. 7.6Aa, resp. Fig. 7.6Ab, as functions of the optical thickness for various albedo values. We retrieve the fact that when the optical thickness  $\tau_d$  is very small, the diffused internal reflectance value tends to 1 at both interfaces. As the optical thickness increases, the diffused internal reflectance decreases. It asymptotically approaches 0.60, the value usually considered in the Saunderson correction, for the top interface when the medium is non-absorbing ( $\omega_0 = 1$ ), or a higher value than 0.60 if the medium is absorbing (0.63 when  $\omega_0 = 1$ ).

Let's now examine the case of the global internal reflection  $r_{ig}$  and  $r'_{ig}$  (Fig. 7.6Ba and Fig. 7.6Bb). First of all, it should be noted that the two coefficients may differ, in particular at lower optical thickness: when  $r_{id}$  and  $r'_{id}$  tend to 1, their counterparts  $r_{ig}$  and  $r'_{ig}$  take much lower values. Indeed, at low optical thickness, the contribution of diffused light to the total radiance decreases, explaining the decrease of the global internal reflectance, which tends to 4%; the Fresnel coefficient at normal incidence. This effect is particularly strong for low albedo values, as absorption prevents scattering to randomize the light direction. At high optical thickness however, both  $r_{ig}$  and  $r'_{ig}$  tend to  $r_{id}$  and  $r'_{id}$  as expected, justifying the use of the lambertian value 0.6 in the 2-flux model.

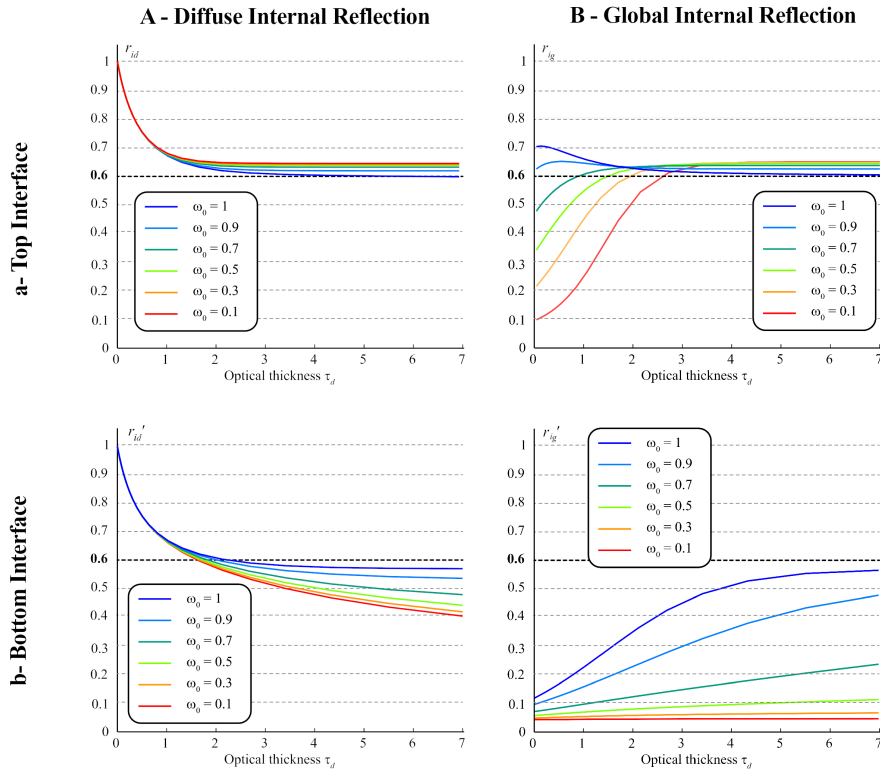


Figure 7.6: Internal reflectances versus optical thickness  $(\mu_a + \mu_s)d$  for isotropic scattering ( $g = 0$ ) and several albedo  $\omega_0 = \mu_s/(\mu_a + \mu_s)$  with  $\mu_a + \mu_s = 5 \text{ cm}^{-1}$ . The bold dashed line at  $r_i = 0.6$  corresponds to the value usually considered in the classical Saunderson correction.

### 7.4.2 RADIANCE ANGULAR VARIATIONS AND INTERNAL REFLECTANCES IN THE CASE OF AN ANISOTROPIC SCATTERING PHASE FUNCTION

It is known that light scattering mechanisms are usually anisotropic, except in the particular case of scattering centers smaller than the wavelength (Rayleigh scattering). Living tissues, such as brain, are well-known examples of turbid media where light is mostly scattered in the forward direction [Jacques (2013)a]. For this reason, we restrict ourselves to an anisotropic scattering phase function with positive values of the anisotropy parameter  $g$ .

Fig. 7.7A, resp. Fig. 7.7B, represents the diffused radiances  $L_0(\theta)$  and  $L_d(\theta)$  at the top and bottom interfaces as functions of the zenithal angle in the anisotropic case ( $g = 0.8$ ) in absence of absorption, respectively in presence of absorption, for various optical thicknesses of the medium. With or without absorption, for large optical thickness, i.e.,  $(\mu_a + \mu_s)d \gg 1$  (red-orange curves), the diffused radiance distribution at the top interface tends to the one observed for a semi-infinite medium as discussed in the previous section (Fig. 7.3a): the high number of scattering events occurring within the slab tends to compensate the effect of anisotropy in this case.

When  $(\mu_a + \mu_s)d \ll 1$  (blue curves), with or without absorption, the impact of

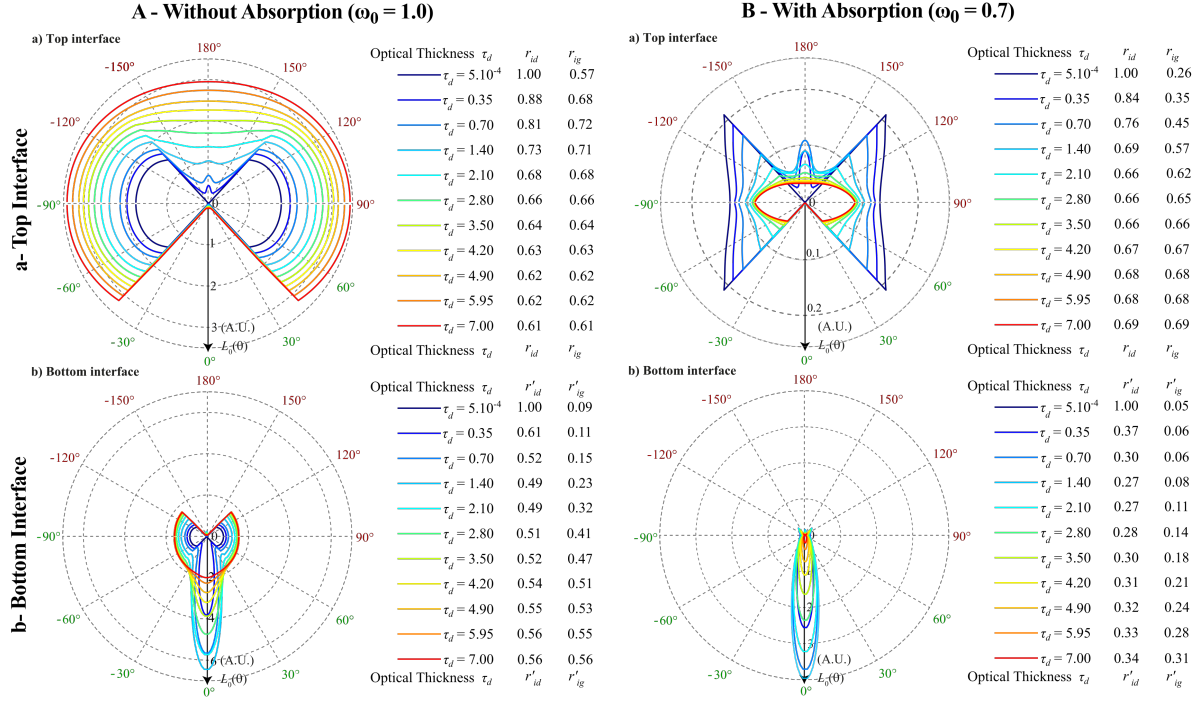


Figure 7.7: Polar plot of the diffuse radiance at the top  $L_0(\theta)$  (Fig. 6Aa), resp (Fig 6Ba), and bottom  $L_d(\theta)$  (Fig. 6Ab), resp. (Fig 6Bb); for layers of different optical thicknesses in presence of absorption (refractive index  $n = 1.5$ , albedo  $\omega_0 = \mu_s/(\mu_a + \mu_s) = 1.0$ , anisotropy factor  $g = 0.8$ ), resp in presence of absorption (refractive index  $n = 1.5$ , albedo  $\omega_0 = \mu_s/(\mu_a + \mu_s) = 0.7$ , anisotropy factor  $g = 0.8$ ).

anisotropy becomes significant, in particular for the radiance at the bottom interface. As the value of the anisotropy factor  $g$  is positive,  $\theta = 0^\circ$  appears to be the privileged direction for scattering light. For this reason, a peak in the  $\theta = 0^\circ$  direction clearly appears in the bottom diffused radiance. Moreover, the radiance overall values are weaker than in the isotropic case, as the scattered light, preferentially directed in the  $\theta = 0^\circ$  direction, can emerge more easily from the back without being affected by any internal reflection. At the front interface, a small peak appears at  $\theta = 180^\circ$ , corresponding to the light reflected back by Fresnel reflection at the bottom interface.

Let's consider the impact of scattering anisotropy on the diffused- and global internal reflectances versus optical thickness (Fig. 7.8). Note that the isotropic case ( $g = 0$ ) is also plotted (solid line) for comparison, together with a medium ( $g = 0.5$ ) and strong ( $g = 0.8$ ) anisotropy. As previously, we will not discuss hereafter the particular case of the bottom interface in presence of absorption, the radiance being negligible at the bottom interface in this case. For all the other cases, anisotropy does not seem to significantly impact the trends previously discussed for both diffused and global internal reflectances.

The most significant differences when comparing isotropic with anisotropic situations are a modest increase of the top internal reflectance  $r_{id}$  which can be observed at high optical thickness (0.7 instead of 0.6 for  $\omega_0 = 0.1$ ), and, due to the light scattered in the

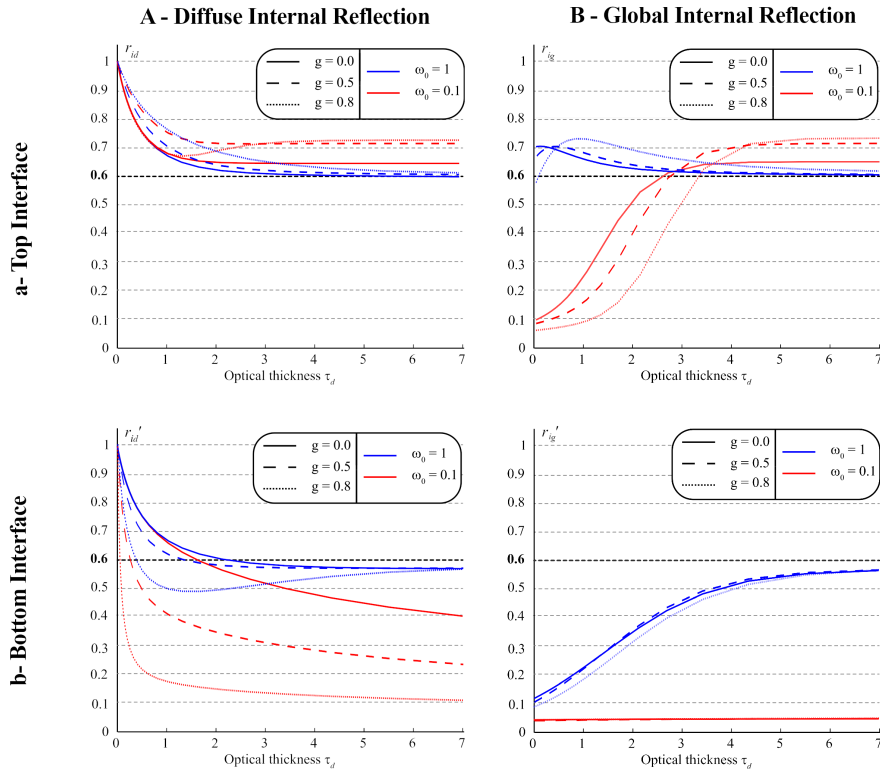


Figure 7.8: Internal reflectances versus optical thickness  $(\mu_a + \mu_s)d$  for several albedo  $\omega_0 = \mu_s/(\mu_a + \mu_s)$  with  $\mu_a + \mu_s = 5 \text{ cm}^{-1}$  and for anisotropic scattering: colored solid lines correspond to  $g = 0$ , colored dashed lines correspond to  $g = 0.5$  and colored dotted lines correspond to  $g = 0.8$ . The bold dashed line at  $r_i = 0.6$  corresponds to the value usually considered in the Saunderson correction.

normal direction, a faster decrease of the top global internal reflectance  $r_{ig}$  as the optical thickness tends to 0 in anisotropic situations.

In conclusion, despite significant changes in term of radiance directivity, scattering anisotropy does not introduce significant changes in term of internal reflectances, especially for large optical thickness.

## 7.5 Validity of the 2- and 4-flux models with and without internal reflectances calculated by the Radiative Transfer Equation

Previous simulations have shown that internal reflectances may differ significantly from the lambertian value in translucent material. In this section, we would like to assess its impact on the prediction accuracy of conventional optical models, and see if it is possible to improve it by simply replacing the lambertian one by the ones calculated by the radiative transfer equation.

For the purpose of this experiment, the propagation of light inside translucent slabs

of variable thickness was simulated with the RTE, and the reflectance and transmittance factors of each slab as well as the internal reflectances  $r_{id}, r'_{id}, r_{ig}, r'_{ig}$  at their interfaces were calculated. The slabs are characterized by a scattering coefficient  $\mu_s = 4.5 \text{ mm}^{-1}$  and an absorption coefficient  $\mu_a = 0.5 \text{ mm}^{-1}$ . Scattering was modelled using the Henyey-Greenstein phase function with  $g = 0$  (isotropic scattering),  $g = 0.5$  and  $g = 0.8$ . Slabs with optical thicknesses ranging from  $5.10^{-4}$  to 7 (thickness ranging from  $10^{-4}$  mm to 1.4 mm) were simulated for each value of  $g$ .

Then, the absorption  $k$  and scattering  $s$  coefficient of the best available model, i.e. the 4-flux model, were extracted using a fitting algorithm to reproduce at best the RTE data (taken as reference) for all thicknesses. Note that here the  $r_{id}$  and  $r'_{id}$  values calculated with the RTE were used to extract the optical parameters of the 4-flux model. The forward scattering ratio  $\zeta$  is calculated according to formula (7.4) as proposed in [Roze *et al.* (2001)] :

$$\begin{cases} \zeta = \frac{1}{2} & \text{if } g = 0 , \\ \zeta = \frac{(1+g)\left[\sqrt{1+g^2}-1+g\right]}{2g\sqrt{1+g^2}} & \text{otherwise.} \end{cases} \quad (7.4)$$

The average path length parameter  $\epsilon$  was set to 2, which corresponds to semi-isotropic scattering, as usually done in 2-flux and 4-flux models. We assume that it is constant with respect to the layer thickness, and that its value is the same at both interfaces of the slab. This is a strong assumption which will necessarily limit the accuracy of all models, but it simplifies the study and allows to draw general conclusions on the models' accuracy. Note that the RTE enables to calculate  $\epsilon$  at any depth within the slab thanks to its integral definition given in [Roze *et al.* (2001)], and use different values for the top and bottom interfaces, as proposed in the 4-flux model from Vargas *et al.* [Vargas *et al.* (2020), Vargas *et al.* (2021)].

The fitting algorithm is based on the GlobalSearch global optimization solver from Matlab, and searches for the parameters that minimize the average root mean square difference between the reflectance and transmittance factors predicted and simulated with the RTE (ground truth).

Finally, the absorption and scattering coefficients of the 2-flux model are deduced from those of the 4-flux model using the well-known equations (12,13) [Gate (1974), Thennadil (2008)]:

$$K = \epsilon k \quad (7.5)$$

and

$$S = \epsilon s(1 - \zeta) \quad (7.6)$$

where  $K$ , resp.  $S$ , denotes the absorption, resp. scattering, coefficient of the 2-flux model and  $k$ , resp.  $s$ , denotes the absorption, resp. scattering, coefficient of the 4-flux model. We take  $k = \mu_a$  and  $s = \mu_s$ . Then, assuming that the absorption and scattering coefficients are not thickness-dependent, diffused reflectance and transmittance of the slab are re-

calculated using the different models, and compared with the true value obtained by RTE simulation. For the 2-flux model, we used the well-known formalism of reference [Kubelka (1931)] combined with the Saunderson correction [Orchard (1977)], and for the 4-flux model, we used the approach of Maheu *et al.* [Maheu *et al.* (1984)] for predicting the reflectance and transmittance of translucent slabs with refractive index  $n = 1.5$ . Let us recall that compared to the 2-flux model which only considers the propagation of diffused flux inside a slab, the 4-flux model describes both the propagation of the diffused and directional incident light, accounting for the fraction of directional flux that is scattered, and the fraction of flux that remains directional inside the layer.

For the 2-flux model, several possible values of global internal reflectance  $r_{ig}$  and  $r'_{ig}$  were considered:

- $r_{ig} = r'_{ig} = 0$ , which represents the case where the Saunderson correction is omitted,
- $r_{ig} = r'_{ig} = 0.04$ , which is the standard value for non-scattering media with  $n = 1.5$ ,
- $r_{ig} = r'_{ig} = 0.60$ , which is the standard value for isotropic scattering with  $n = 1.5$ ,
- $r_{ig}$  and  $r'_{ig}$  calculated with the RTE for each thickness.

For the 4-flux model, only two cases were  $r_{id} = r'_{id} = 0.60$  and the  $r_{id}$  and  $r'_{id}$  values calculated by the RTE were considered. The reflectance and transmittance factor predictions of the 2- and 4-flux models are reported on Fig. 7.9.

The 4-flux model with the  $r_{id}$  and  $r'_{id}$  values calculated by the RTE is found the most accurate for predicting the reflectance and the transmittance, regardless of the  $g$  value. Of course, it is the consequence of the construction of the experiment ( $k$  and  $s$  are extracted from RTE data using this model), but such agreement would not have been possible if the 4-flux model with the  $r_{id}$  and  $r'_{id}$  values calculated by the RTE were not able to reproduce accurately RTE results.

In reflectance, the 4-flux model with  $r_{id}$  and  $r'_{id} = 0.60$  is the most accurate for  $g = 0$ , and for slabs thicker than  $\tau_d = 3.5$  for  $g = 0.5$ . For  $g = 0$ ,  $\epsilon = 2$  and  $\zeta = 0.5$ , the simulation corresponds to the assumptions of the 4-flux model, i.e., lambertian flux within the layer and at the interfaces, which explains why this model fits well with the ground truth. The only error comes from the use of different values of  $r_{id}$  and  $r'_{id}$ . The 2-flux models are less accurate than the 4-flux models, and do not even converge towards the 4-flux model for high optical thickness which is inherent to formulae (12) and (13). For  $g = 0.8$ , the 2-flux model with  $r_{ig}$  and  $r'_{ig}$  values calculated with the RTE is the most accurate model. This tends to show that adapting the value of  $r_{ig}$  and  $r'_{ig}$  is more important for highly asymmetric scattering. 2-flux and 4-flux models with  $r_i = 0.60$  are notably inaccurate for thin slabs, but their accuracy increases for slabs of high optical thickness. The 2-flux model with  $r_{ig} = 0.04$  is inaccurate with  $g = 0$  and  $g = 0.5$ , but is fairly accurate for very thin slabs, i.e.,  $\tau d \leq 1$  when  $g = 0.8$ . The 2-flux model with  $r_{ig}$  and  $r'_{ig} = 0$  is inaccurate in all the tested cases.

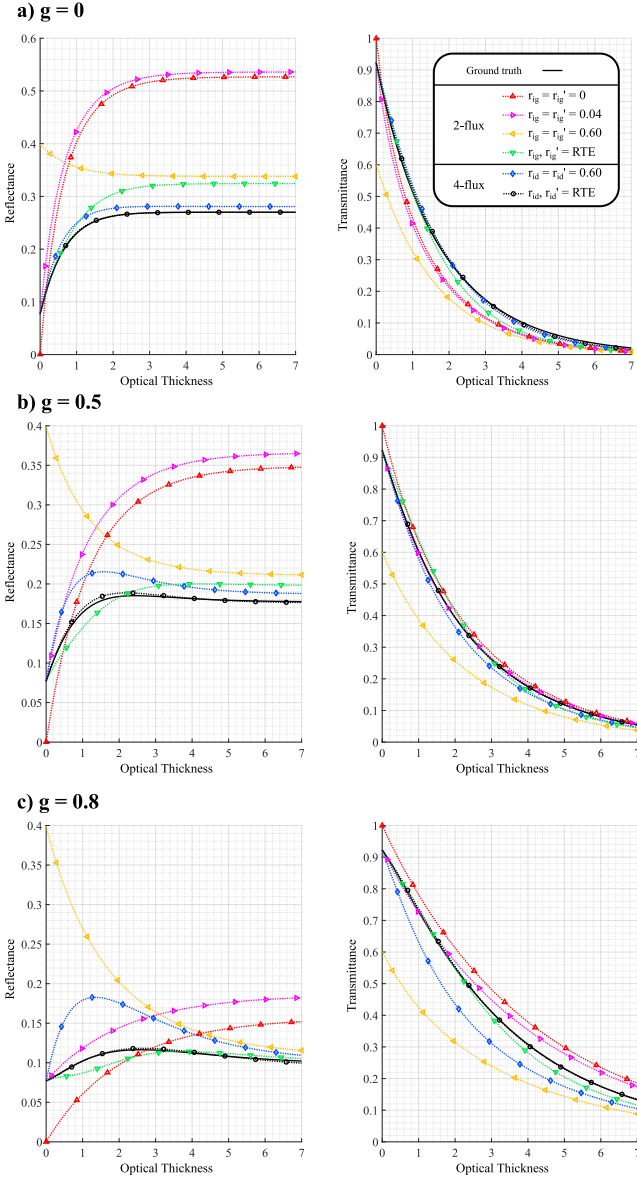


Figure 7.9: Reflectance (left graphs) and transmittance (right graphs) factors predicted by the 2-flux and 4-flux models for different values of the internal reflectance at the interface. The red curve represents the 2-flux model with  $r_{ig} = r'_{ig} = 0$ . The magenta curve represents the 2-flux model with  $r_{ig} = r'_{ig} = 0.04$ . The yellow (resp. blue) curve represents the 2-flux (resp. 4-flux) model with  $r_{ig} = r'_{ig} = 0.60$  (ie. Lambertian flux). The green (resp. black) curve represents the 2-flux (resp. 4-flux) model with  $r_{ig}$  (resp.  $r_{id}$ ) and  $r'_{ig}$  (resp.  $r'_{id}$ ) calculated by the RTE for each slab. The black solid line curve represents the ground truth values simulated with the RTE. a) Simulations of the RTE are performed for  $g = 0$ . b) Simulations of the RTE are performed for  $g = 0.5$ . c) Simulations of the RTE are performed with  $g = 0.8$ .

In transmittance, regardless of the value of  $g$ , the 2-flux model with  $r_{ig}$  and  $r'_{ig} = 0.60$  is inaccurate. For  $g = 0$ , the 4-flux model with  $r_{id}$  and  $r'_{id} = 0.60$  is the most accurate as in reflectance mode. The 2-flux model with  $r_{ig}$  and  $r'_{ig}$  values calculated with the RTE is

more accurate than the other 2-flux models, with the 2-flux model with  $r_{ig}$  and  $r'_{ig} = 0.60$  being the least accurate. For  $g = 0.5$ , the 2-flux model with  $r_{ig}$  and  $r'_{ig} = 0.04$  is the most accurate, but the other models (except the 2-flux model with  $r_{ig}$  and  $r'_{ig} = 0.60$ ) are fairly accurate. For  $g = 0.8$ , the 2-flux model with  $r_{ig}$  and  $r'_{ig}$  values calculated with the RTE is the most accurate, as in reflectance mode. The other models are notably less accurate, except for the 4-flux model with  $r_{id}$  and  $r'_{id} = 0.60$  for very thick slabs and the 2-flux model with  $r_{ig}$  and  $r'_{ig} = 0.04$  for very thin slabs.

It is worth noting that the reflectance and transmittance factors are perfectly predicted when the optical thickness tends towards 0 by the 4-flux models regardless of the value of  $r_{id}$  and the 2-flux model with the  $r_{ig}$  values calculated with the RTE or with  $r_{ig} = 0.04$ . Indeed, for an extremely thin slab (with optical thickness almost 0), scattering and absorption become negligible and light is only reflected by the top and bottom interfaces. Therefore, the slab is equivalent to a layer of clear glass (non-scattering and non-absorbing medium with refractive index  $n = 1.5$ ), and its reflectance and transmittance factors can be calculated easily with Fresnel laws. This trend, which must be accounted for at the interfaces of the layer, is only satisfied by the aforementioned 2-flux and 4-flux models.

Within the limits of this study where the 4-flux model with  $r_{id}$  and  $r'_{id}$  calculated by RTE has been taken as a reference, we conclude that the 4-flux model with  $r_{id} = r'_{id} = 0.60$  is the most accurate model for  $g = 0$  and  $0.5$  in reflectance and transmittance mode. However, for higher values of  $g$ , the model is not accurate enough and specific values of  $r_i$  must be used. This is why the 2-flux model with  $r_{ig}$  and  $r'_{ig}$  values calculated with the RTE is the most accurate model for  $g = 0.8$  in this particular case. The other 2-flux models are generally less accurate than the 4-flux model, although the 2-flux model with  $r_{ig} = r'_{ig} = 0.04$  is more accurate in transmittance mode.

In other words, these preliminary results suggest that in all cases, for an accurate material parameter extraction using 2- or 4-flux models in translucent material, internal reflectance should be modified in agreement with radiative transport theory, especially for highly anisotropic scattering. If conventional values of internal reflectance with  $r_i = r'_i = 0.60$  have to be used for simplicity, it is highly recommended to prefer the 4-flux model rather than the 2-flux model. Indeed, the 4-flux model naturally takes into account the decrease of the diffuse flux compared to the specular flux in translucent materials, whereas the 2-flux models need to account for it by setting appropriate value the global internal reflectances.

## 7.6 Conclusion

Detailed simulations based on the numerical solving of the radiative transfer equation were used to calculate the internal diffused reflectance, a parameter needed in the 2-flux or 4-flux models used for optical parameter extractions and appearance prediction. In this work, both isotropic and anisotropic scattering were considered, even though we found that anisotropy does not significantly impact the overall conclusions.

For large optical thicknesses, the internal diffused reflectances at both interfaces were found in agreement with the expectation of the lambertian approximation when absorption is negligible. In presence of absorption however, these internal reflectances slightly differ, the top one being a bit higher, and the bottom one a bit lower than the lambertian value. For intermediate and low optical thicknesses (translucent material), it turns out that both internal reflectances tends to be approximately equal, and exceed the value for a lambertian distribution. On the opposite, global internal reflectances (including both directional and diffused light), required for 2-flux models, tends to directional values at low optical distances. These results are the consequence of the competition between the directional reflection (Fresnel formulae), which induces anisotropy in the angular distribution of radiance (low incidence angle rays may escape from the slab while high incidence angle rays remain trapped by global internal reflection), and scattering, which tends to distribute light uniformly.

Finally, the impact of the internal reflectances on extraction performed using the 2- and 4-flux models was investigated, using RTE simulations as a reference. It turns out that the commonly used approximation, i.e., keeping constant the internal reflection equal to its lambertian value, can lead to significant errors (up to 100%) for 2-flux models when dealing with translucent materials. Moreover, parameter extraction with the 2- and 4-flux models can be significantly improved using the internal coefficient calculated using the radiative transfer equation, especially in translucent material with highly anisotropic scattering medium.

These results open the way to a better prediction of the spectral reflectance and transmittance, and thus to the estimation of the optical properties of translucent but also strongly scattering materials. As optical properties are a key element of quantification methods, we suggest as future work to investigate the implications of the results of this study on the quantification of fluorophores by simple optical models.



## IV Experimental Setup

---



---

In the state of the art, the experimental systems for fluorescence-guided neurosurgery can be separated into two broad categories. The major part of the state of the art concerns experimental setups which estimate both optical properties and measure the fluorescence at a single excitation wavelength. The rest of the state of the art concerns systems that measure the fluorescence at several excitation wavelengths. To our knowledge, there is no experimental system that combines several excitation wavelengths of fluorescence and estimates the optical properties of biological tissue. It thus seemed necessary to build a new experimental system which will be described in this chapter. In Chapter 8 the hardware part of the system will be described. As mentioned in [Kim *et al.* (2010)b] a calibration of the measured reflectance spectrum to the diffusion theory model is required to correctly retrieve optical properties. This calibration has been done with optical phantoms as described in Chapter 9. Finally, in Chapter 10 we will focus on the software part which is needed to be able to acquire correctly the measurements.



# Chapter 8

---

## A new acquisition system

---

We have seen in Part I the potential of PpIX fluorescence spectroscopy to identify tumor infiltration of gliomas. We also introduced the presence of two PpIX forms with different fluorescence properties. Then, in Part II, we focused on the internal reflectance, one of the parameters of simple optical models. These simple models are generally those used to extract optical properties of a scattering medium from measurements.

In this chapter, we present the development and characterization of an interventional fluorescence spectroscopy system aiming at both identifying the two fluorescence forms of PpIX and extracting optical properties of the probed sample by diffuse reflectance spectroscopy (DRS). This system is equipped with two lasers and one white broadband light source. The white broadband light source allows to get DRS measurements and the lasers sequentially excites the tissues with two distinct wavelengths and collects each emitted fluorescence spectra via a fibered optical probe. We will start by presenting the different components used and their characteristics before proposing the characterization of the complete system.

### 8.1 Specifications of the Experimental System

The developed system aims at measuring fluorescence spectra and diffused reflectance spectra of brain tissues, in the neurosurgery operating room (OR). This imposes strict specifications in the choice of components and their assembly. In order to be used in the OR, the device developed must be safe, transportable and robust (not too bulky or heavy); it must be closed; and its different blocks must be quickly assembled. Moreover, in order to excite the two PpIX forms of interest, we have chosen a multi-wavelength excitation

of the tissues, with wavelengths adapted to the properties of the two desired forms. We decided to use lasers which are more spectrally selective than the LED used by [Alston (2017)]. This distinguishes this prototype from those existing in the litterature, which have either only one fluorescence excitation source in addition of a white light source or only fluorescence excitation systems without white light source.

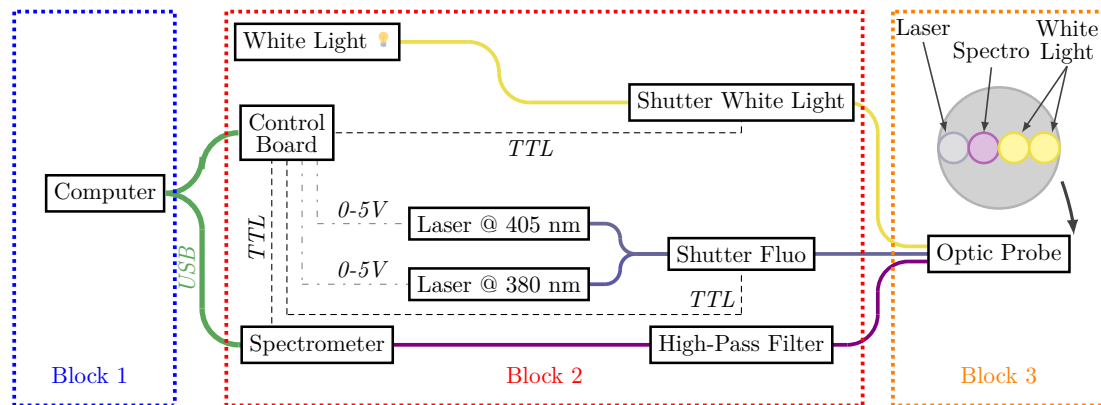


Figure 8.1: Diagram of the acquisition system

Fig. 8.1 describes a schematic of the system. It can be seen that the system is splittable into three blocks: the control interface ,also called software hereafter, the optoelectrical components and finally the probe. More precisely the three blocks are :

Block 1: The computer, the central unit from which the entire system is controlled with a Qt-Python software. This software and its interface are presented in detail in chapter 10.

Block 2: A black box made from compact PVC sheets of different thicknesses (3 mm and 10 mm) containing all the electrical and optical components. The choice of thickness depends on the role of the plate (closure, support...).

Out of this box come a minimal number of connections, two USB connections to the computer (one for the arduino control board, the other for the spectrometer), one standard 220 V electrical outlet for the power supply of the components and four SMA optical connections to the probe. The box measures 49x46x18 cm<sup>3</sup>, weighs 14.3 kg and contains three stages.

All the components are fixed to prevent from moveming during transport and we add handles on the box, for easier transport. The walls are screwed together to ensure a tight seal, but the number of screws is restricted so that any wall can be removed quickly to access system components if necessary.

Block 3: The probe is 1 meter long and is connected to block 2 by four SMA connections. This element is described in detail in section 8.3.

In Sections 8.2 to 8.3, we describe here the components of the blocks 2 and 3. Block 1 will be described in Chapter 10.

## 8.2 Hardware of block 2

Convinced that research should be affordable, accessible to all and as open-source as possible, we chose to use as many non-proprietary components as possible. This required to use other knowledge than optics to be able to realize this hardware part that we will describe in the following sections.

### 8.2.1 Detection system

The fluorescence spectrum emitted by the tissue or the diffuse reflectance spectrum is collected by one of the probe fibers. This light is then transmitted to the spectrometer via a high-pass filter with a cut-off wavelength of 473 nm (BLP01-473R-12.5, *Semrock*), which cuts off all wavelengths below the cut-off wavelength, including the potential excitation signal.

The filtered signal is transmitted to the spectrometer (QEPro, *OceanInsight*) via a fiber bundle of 5 fibers of 200  $\mu\text{m}$  core, "round to linear" (PL200-2-UV-VIS, *OceanInsight*) creating a collimated flow of photons arriving at the spectrometer slit and thus allowing transmittance optimization (refer Fig. 8.2).

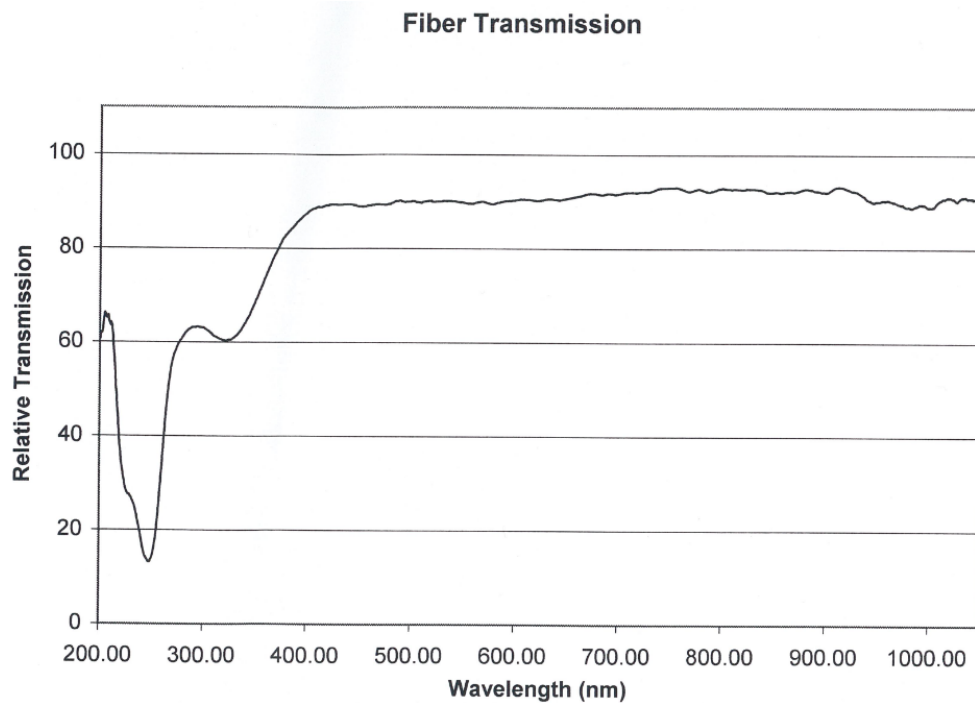


Figure 8.2: Round to Linear Fiber Bunder transfer function

The sensor of the QEPro spectrometer is a 2D back thin CCD sensor (S10420-1106, *Hamamatsu*) cooled by double Peltier stage. It was chosen for its 3.27 nm resolution; its better sensitivity than the MayaPro2000 (a dynamic range of 25000:1 and signal to Noise ratio of 1000:1 for the QEPro against a dynamic range of 10000:1 and a signal to noise ratio of 450:1 for the MayaPro2000); the possibility of a synchronized triggering in near

real time; the very short acquisition times available (8 milliseconds to 1 hour); and for the real-time USB communication with the computer.

The light is collected between 399 nm and 791 nm, on an array with 2064 pixels (4 pixels used for dark noise correction), which leads to an interval of about 0.19 nm per pixel. The diffraction grating (#3 blazed @500 nm) coupled with the 200  $\mu\text{m}$  input slit gives a FWHM resolution of 3.27 nm.

Finally, the technical documentation of the spectrometer indicates that four different external trigger modes exists and for all of them the external trigger input must be a 3 V to 5 V signal. More precisely the four different external trigger modes are:

0. Normal Mode: In this mode, the spectrometer will continuously acquire spectra based on the integration period specified.
1. Software Trigger Mode: In this mode, the spectrometer is continuously scanning and collecting data (just as it is in the Normal mode) and with each trigger, the data collected up to the trigger event is transferred to the software.
2. External Synchronous Trigger Mode: In this Mode, two external triggers are required to complete a data acquisition: The first rising edge starts the integration period and the second rising edge stops the integration while starting the next integration. Thus the integration time is the period between the two external trigger pulses.
3. External Hardware Level Trigger Mode: In this mode, a rising edge detected from the External Trigger input starts the Integration Cycle specified previously through the software interface. After the Integration Cycle completes, the spectrum is retrieved and written to the FIFO stack. As long as the trigger level remains active in a logic one state, continuous acquisitions will occur with the following exception.

### 8.2.2 Electronic Shutters

The diagram in Fig. 8.1 shows two shutters (INLINE-TTL-S, *OceanInsight*): the first between the bundle of optical fibers from the lasers and the probe, the second between the fiber from the white light source and the probe.

The first shutter is used as a safety device, to block any accidental light emission in the block during the handling of the probe. Thus, the opening of this shutter is controlled by the acquisition program which opens it only for fluorescence acquisitions and it closes automatically at the end of the measurement.

The second shutter is also used as a safety device, to block any accidental light emission in the block during the handling of the probe. Its low switching frequency of 5 Hz, i.e. 200 ms, is not a problem for this experimental system because it is currently necessary to change the light injection optical fiber in the probe to be able to measure the diffuse reflectance spectrum of the tissue for two known source-detector distances.

Finally, the technical documentation of this type of shutter indicates that it is remotely controllable via a TTL signal and also reports a maximum optical transmission around 75%.

### 8.2.3 Excitation System

The system we propose performs multi-wavelength excitation with two lasers, which we present here. Moreover, in order to avoid having to manually change the excitation source each time, we use a commercial optic fiber bundle which will also be presented.

#### Fluorescence Excitation Sources

The system excites the tissue with two lasers, centered at 385 nm and 405 nm respectively. Indeed, since we seek to identify two forms of PpIX fluorescence with different absorption properties, we choose to perform a multi-wavelength excitation with sources adapted to both forms. As presented in the Chapter 2, according to the literature and to the absorption spectrum of PpIX634, we choose for the excitation a laser whose emission is centered around 408 nm (LBX-405-900-HPE-PPA, *Oxxius*). Recently PpIX620 having been studied by [Jonin *et al.* (2020)] and according to the absorption spectrum of PpIX620, we choose for the excitation a laser whose emission is centered around 379 nm (LBX-375-200-HPE-PPA, *Oxxius*). We decided to buy all lasers with the fiber coupling option. Thus, each laser is already injected inside a 105  $\mu\text{m}$  core fiber with a N.A. of 0.22. In addition, each laser is sold with a PPA control box for the output power. This box can be controlled manually or remotely via a 0-5 V analog signal. In our case, we will use the remote control to automate the acquisition. Hereafter, these lasers will be noted Laser385 and Laser405. Fig. 8.3 presents the emission spectrum of each of the chosen lasers.

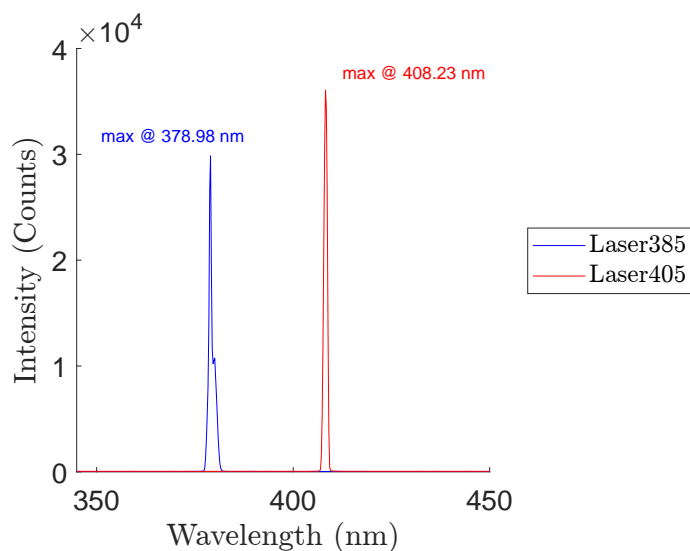


Figure 8.3: Emission spectrum of the lasers used (*Integration time 16 ms*)

Looking at Fig. 8.3, we observe that the spectral bands are relatively thin. Due to the

shoulder on the emission spectrum of Laser385, we decided to compare the spectral width of each laser by comparing their Full Width near the minimal number of counts. We get a width of 3.2 nm, resp. 2.1 nm, for Laser385, resp. Laser405. In addition, we notice that the delivered power is different for each laser. This power difference is consistent with the manufacturing report of the Lasers. Finally, we can notice that the central wavelength of Laser385, resp. Laser405, is  $\approx 379.0$  nm., resp.  $\approx 408.2$  nm.

### Optic Fiber Bundle

Once the fluorescence excitation sources are chosen, a bundle of fibers with SMA terminations is needed so that the tissue can be excited with each of the lasers without having to manually move the probe in front of a new excitation source. Thus, we bought a fiber bundle (SPLIT200-UV-VIS, *OceanInsight*). Each leg has a 100  $\mu\text{m}$  core fiber and the common part has a 200  $\mu\text{m}$  core fiber which is then connected to the probe via the shutter (INLINE-TTL-S, *OceanInsight*).

### DRS Light Source

We want to estimate tissue optical properties using the DRS method as described by [Kim *et al.* (2010)b]. As a tungsten-halogen white light source is mentioned in the paper to do spectrally constrained estimation in the 450-850 nm wavelength range, we decide to use a broadband white light source (KL2500LCD, *Zeiss*), whose spectral irradiance is visible in Fig. 8.4.

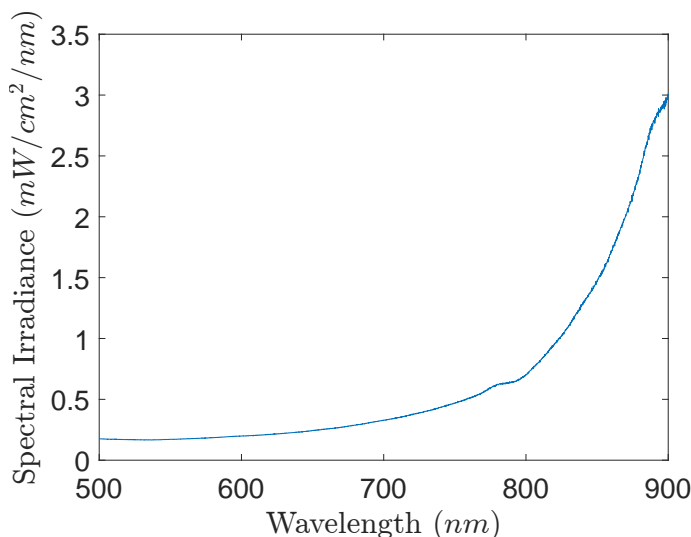


Figure 8.4: Spectral Irradiance of KL2500LCD cropped to the 500 - 900 nm region

### 8.2.4 Microcontroller Board

Instead of using a proprietary NI acquisition Board with the associated Labview software, we decide to use an Arduino Uno <sup>©</sup> board (visible in Fig. 8.5). The three main advantages of using an Arduino board are its ease of programming, its worldwide community gathered around this open-source platform and its small size ( $68.6 \times 53.4 \text{ mm}^2$ ). All theses advantages encourage myself to use one.

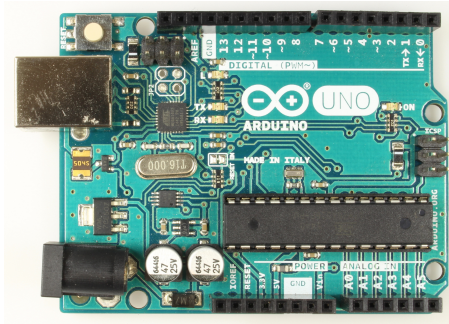


Figure 8.5: Arduino Uno rev3 (Taken from Wikimedia)

In Fig. 8.6, we can see the pinout diagram associated to the Arduino Uno board. In electronics, a pinout diagram describes the cross-reference between the pins of an electronic component and their functions. The Arduino Uno pinout contains 14 digital pins (including 6 with Pulse Width Modulation (PWM) capability), 6 analog inputs, a power jack, a USB connection and an ICSP header. PWM is a modulation technique used to encode a message into a pulsing signal.

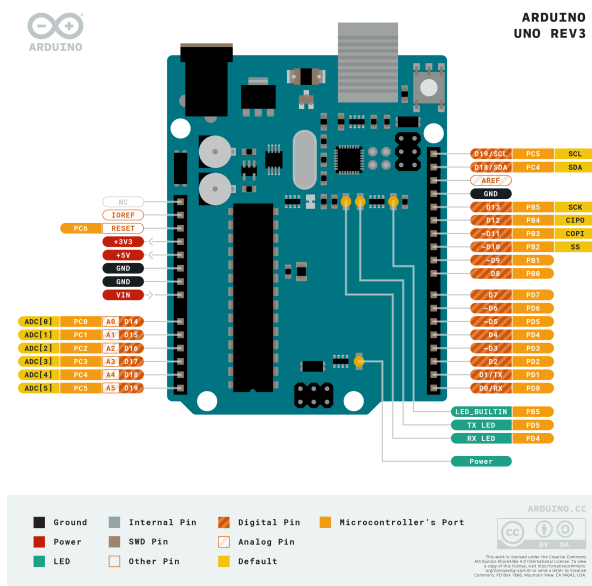


Figure 8.6: Pinout Schematic of Arduino Uno rev3 (Taken from Arduino.cc)

Before going further into the explanation of PWM, it is important to mention that the control of each pin of the card is done by uploading a C program previously written and

compiled. It is also possible to obtain a serial link with the Arduino board, so that you can interact dynamically with its pins. Thus, in our case, the C program on the Arduino Board uses the serial link, and thus sending a specific letter to the Arduino board will put High or Low a digital pin, while sending another specific letter with three numbers will set a PWM pin's duty cycle. Thus, characters (a | b), resp (c | d) or (g | h) or (i | j), refer to digital pin 2, resp 3 or 9 or 10 and character p , resp q or r, refers to PWM pin 5, resp 6 or 11. Each command is separated from the next one by a carriage return + line feed group.

A PWM is described by two key components: a frequency and a duty cycle. The PWM frequency dictates how many cycles are contained inside one second, which is inversely related to duration of a single cycle (called period). In Arduino, the PWM enabled pins produce a constant frequency of 490 Hz for all PWM pins except pins 5 and 6 whose PWM frequency is 980 Hz. According to Fig. 8.7, we can notice that the duty cycle determines the time ratio between the signal stays high over of the total period. Duty cycle is often represented in percentage. In Arduino, the duty cycle changes according to a parameter value (written on one byte) set by the user.

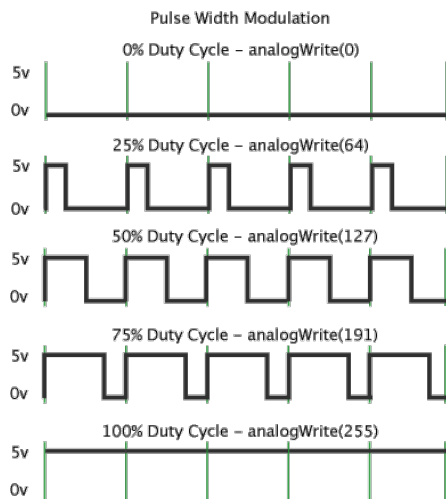


Figure 8.7: Schematic of the PWM technique (Taken from Arduino.cc)

The diversity of the pinout I/O provides many different options. However, it is important to underline that concerning analog I/O, the Arduino Uno board contains only analog inputs. This raises an important problem because lasers can be power-controlled by an analog (0-5 V) signal. There are different possibilities to transform digital signals into analog ones, including filtering and conversion.

Considering the conversion solution, it is then necessary to wire an R-2R DAC whose resolution  $\Delta V$  is given by  $\Delta V = V_{max}/(2^n - 1)$  where n is the number of bits. Because we need to control 2 lasers and we have 14 digital pins available, we could use 7 pin for each at most, which gives a maximum resolution around 0.04 V.

Another possibility is to low filter a PWM signal such that only the averaged signal outputs of the filter. Then, by modulating the duty cycle of the PWM signal, the mean value

of the filtered signal changes (being maximal for a duty cycle equal to 1). As the duty cycle is written on 8 bits, the related resolution  $\Delta V$  is given by  $\Delta V = V_{max}/(2^n - 1)$  equals 0.02 V.

Since we want to have the best resolution available, we will use a PWM signal filtering method to obtain a 0-5 V analog output. Let us now focus on the practical realisation.

### 8.2.5 Home Made Electronic Shield

In the previous section, we identified the Arduino Uno electronic board as the acquisition board to use for our system. However, the outputs of the Arduino board either do not deliver the right type of signals (no analog output) or not enough current. So, we needed to build a home-made shield to pre-process the signals coming from the arduino before sending them to the lasers, shutters or spectrometer.

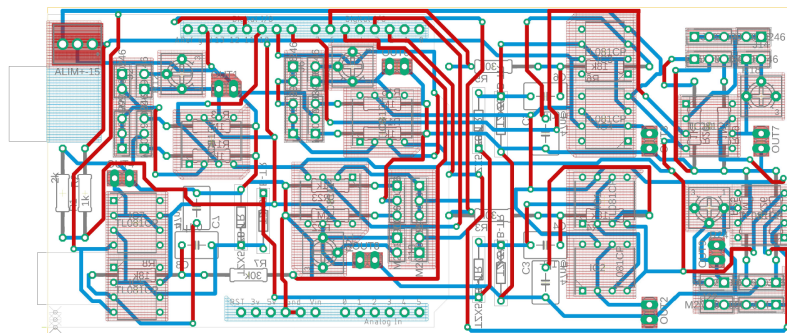


Figure 8.8: PCB Schematic of the Home Made Electronic Shield

In Fig. 8.8, we show the resulting Printed Circuit Board (PCB) scheme. The red and blue colors on it highlights the need of a double-sided engraving of the printed circuit. This was done with the LPKF PromatS63 engraver present on the PiLoT platform. To deeply understand the content of this electronic shield, the following subsections will describe in details the PWM Filtering module and the TTL module which are replicated respectively three and four times on the shield.

#### TTL Output Module

The TTL output module aims at amplifying the digital output signal coming from the arduino pin through an output voltage at 0 or 5 V. In Fig. 8.8, the final PCB contains four times the same analog output module plugged to the Arduino by pins 2, 3, 8 and 9. As visible on Fig. 8.9, it is composed of an operational amplifier which, depending on the jumpers can be used either as a follower or a non-inverting linear amplifier. In our case, since the current delivered by the Arduino board is too low, but the voltage is correct, we have positioned the jumpers to use the TTL module in follower mode.

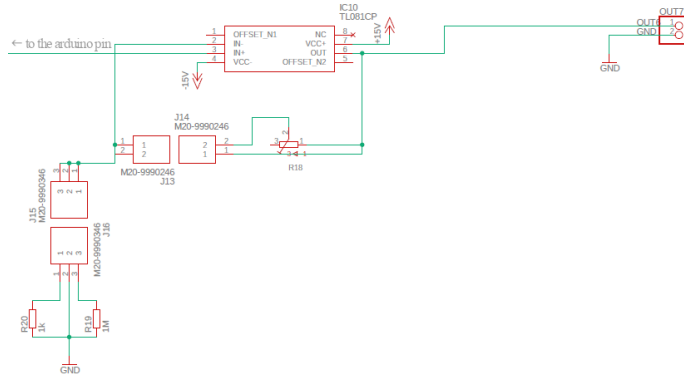


Figure 8.9: Schematic of one TTL pre-processing circuit

## 0-5 V Analog Output Module

The analog output module aims at filtering the PWM signal coming from the arduino pin through an analog output voltage between 0 and 5 V. In Fig. 8.8, the final PCB contains three times the same analog output module plugged to the Arduino by pins 5, 6 and 11. Because we only use two lasers, we connected them to pins 5 and 6, thus the PWM frequency to consider is 980 Hz. We then get either one spare if needed or an analog output if the broadband white light source is changed. In Fig. 8.10, the module is composed of two elements in cascade, a Sallen-Key low-pass filter and an operational amplifier wired as a voltage follower.

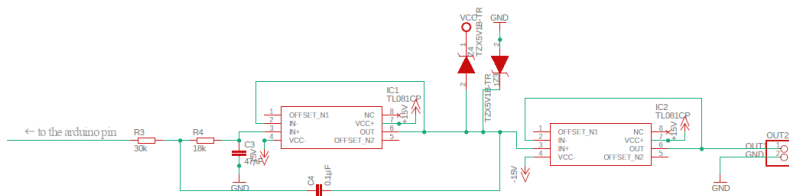
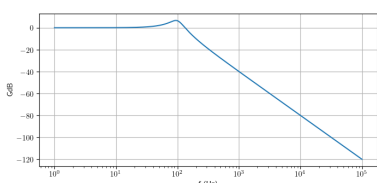
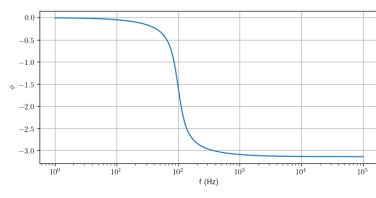


Figure 8.10: Schematic of one PWM Filtering Circuit

Let's first look at the Sallen-Key low-pass filter. The chosen resistors are  $30\text{ k}\Omega$  and  $10\text{ k}\Omega$  and the capacitors are  $47\text{ nF}$  and  $100\text{ nF}$ . On Fig. 8.11a, we see the Bode diagram in amplitude of the said filter; the cutoff frequency  $f_c$  of the filter is 99.90 Hz and its quality factor  $Q$  is 0.33.



(a) Amplitude (dB) versus frequencies



(b) Phase (rad) versus frequencies

Figure 8.11: Bode Diagram of the Sallen-Key 2nd order filter of the PWM Filtering Circuit

The PWM signal  $s(t)$  can be decomposed as a Fourier serie  $s(t) = a_0 + \sum_{k=1}^{\infty} \frac{\sin(2\pi(2k-1)f_0 t)}{2k-1}$  where  $f_0$  is the signal frequency,  $f_0 = 980$  Hz in our case. We notice that  $f_0 > f_c$ , thus all components of  $s$  except the fundamental are attenuated, e.g. the  $f_0$  component is attenuated by 39.6 dB.

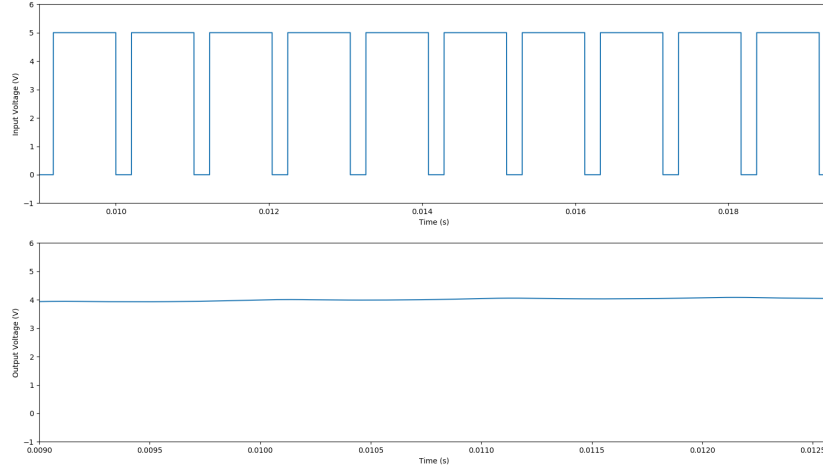


Figure 8.12: Filtering of a PWM Signal: Input PWM signal with 80% Duty Cycle and  $f_0 = 980$  Hz (top) and filtered output signal (bottom)

In Fig. 8.12 are represented, on the top, the input PWM signal which has a duty cycle of 80% and a frequency  $f_0 = 980$  Hz. We can notice that our filter is correctly parameterized because the output signal only contains the fundamental component which corresponds to the average voltage. The small variations around the average voltage (0.022 V for a duty cycle of 99%) are due to the attenuated high frequencies.

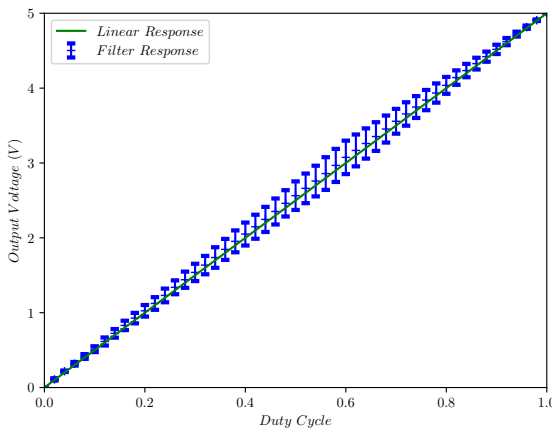


Figure 8.13: Filter, resp. Linear, response (blue crosses, resp. green solid line) versus duty cycle.

To study the overall response of the filter, the Fig. 8.13 plots the mean value and the variance of the filtered signal (blue crosses). By comparison with the linear response (green solid line) we notice that the filter is almost perfect, with a maximum deviation of

0.075 V for a duty cycle of 0.6. The standard deviation for a duty cycle of 0.6 is large compared to the previously calculated resolution. Nevertheless, the fluctuations are not measured at the output of the laser because the 0-5V input of the laser box also contains an additional low pass filter. Thus, we can consider that our filtering module works properly.

### Packaging of the entire Electronic Components



Figure 8.14: Board Packaging

As visible on Fig. 8.14, all the electronic components (Arduino board, Shield and connectors) are packed inside a custom 3D printed box which measures  $17 \times 7.8 \times 9.3 \text{ cm}^3$ . The plastic packaging enables to isolate electrically all the electronics components from the patient, which is mandatory to use the setup *in vivo*.

### 8.3 Optical Probe (block 3)

The optical probe is used to transmit successively the fluorescence excitation light and the white light to the tissue and to collect successively the emitted fluorescence spectra and diffuse reflectance spectra. This probe was made by IDIL, according to optical specifications stated in Table 8.1.

The design of the probe has been studied in [Kim *et al.* (2010)b] and a specific study for our probe will be presented in the next of this section.

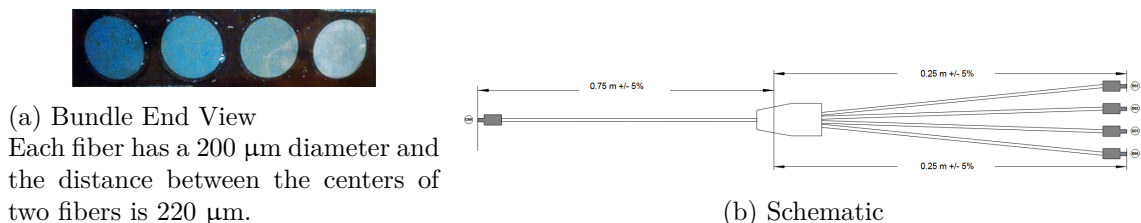


Figure 8.15: Probe Manufacturing Schematic

The optical probe is a  $1 \times 4$  Bundle made of 4 fibers (FG200UEP, *Thorlabs*) tangent to each other, grouped in line and centered in a cylinder of 10 mm diameter and 7 mm length. At the back of the bundle, the four fibers are placed together in a stainless steel sheath

Parameters	Specifications
Length	1 m
Distance between fibers	220 $\mu\text{m}$
Emission Wavelength	300 - 800 nm
Emission Optical Fibers	Multimode Optical Fiber FG200UEP, 0.22 NA, Glass Core Diameter = 200 $\mu\text{m} \pm 4 \mu\text{m}$ , Silica Cladding Diameter = 220 $\mu\text{m} \pm 2 \mu\text{m}$ , High OH fiber
Emission Connectors	SMA 905
Detection Wavelength	450 nm – 800 nm
Detection Optical Fibers	Multimode Optical Fiber FG200UEP, 0.22 NA, Glass Core Diameter = 200 $\mu\text{m} \pm 4 \mu\text{m}$ , Silica Cladding Diameter = 220 $\mu\text{m} \pm 2 \mu\text{m}$ , High OH fiber
Detection Connectors	SMA 905

Table 8.1: Optical specifications for the development of the probe.

covered with black PVC over a length of 75 cm. They are then placed separately in a yellow PVC sheath with a diameter of 2 mm over a length of 25 cm and placed in an SMA connector. The spread is protected by a heat-shrinkable sheath. The positioning scheme of the different fibers is described in the Figures 8.15b and 8.15a.

## 8.4 Study of the validity of the probe for brain samples measurements

According to [Kim *et al.* (2010)b], a probe of this kind can only estimate a restricted range of optical properties  $(\mu_a, \mu'_s)$ . Indeed, for a fixed distance from a source and value of  $\mu_a$ , the curve of the diffuse reflectance versus  $\mu'_s$  describes a bell like the one presented in Fig. 8.16. Thus, to have uniqueness of the solution  $(\mu_a, \mu'_s)$  for a given diffuse reflectance  $R_d$ , it is necessary to restrict the range of  $(\mu_a, \mu'_s)$  in order to have only a portion of the curve.

$\lambda \in [450, 720]\text{(nm)}$	$\mu_a(\text{cm}^{-1})$	$\mu'_s(\text{cm}^{-1})$
White Brain Matter	[0.7,1.4]	[60.15,92.4]
Grey Brain Matter	[0.2,0.7]	[8.4,14.04]

Table 8.2: Brain Tissues Optical Properties (Summarized from [Yaroslavsky *et al.* (2002)])

Therefore, we will check that the optical properties of the brain (Table 8.2) can be estimated with the measurement probe we made. For that, we study the evolution of the value of  $\max(\mu'_s)$  as a function of these parameters for the source-detector distances  $\rho$  given in the probe specifications (Table 8.1).

Based on the optical properties of the brain from the literature (Table 8.2), we notice that

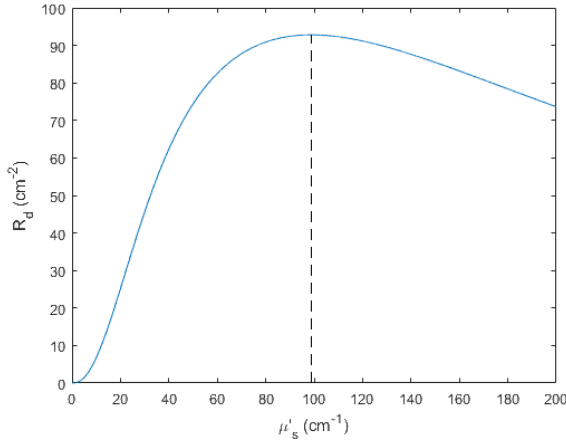


Figure 8.16: Diffuse Reflectance versus Reduced scattering coefficient

	$\rho = 240 \mu m$	$\rho = 480 \mu m$
For $\mu_a = 0.2 \text{ cm}^{-1}$	$\max(\mu'_s) = 96.64 \text{ cm}^{-1}$	$\max(\mu'_s) = 48.04 \text{ cm}^{-1}$
For $\mu_a = 1.4 \text{ cm}^{-1}$	$\max(\mu'_s) = 94.08 \text{ cm}^{-1}$	$\max(\mu'_s) = 46.10 \text{ cm}^{-1}$

Table 8.3: The maximum estimable scattering coefficient with a fixed absorption coefficient as a function of the source-detector distance

the range of  $\mu'_s$  of the brain is always lower than  $\max(\mu'_s)$  (refer to Table 8.3), no matter the value of  $\mu_a$  between  $0.2 \text{ cm}^{-1}$  and  $1.4 \text{ cm}^{-1}$ .

As mentionned in [Kim *et al.* (2010)b] a calibration of the measured reflectance spectrum to the diffusion theory model is required to correctly retrieve optical properties. This calibration has been done with custom liquid optical phantoms and is extensively described in Chapter 9.

## 8.5 Conclusion

In this Chapter, we have described the technical aspects of the new acquisition system we built. At the end, we explain the prerequisites to be able to measure the diffuse reflectance, in particular we mention the need for a calibration step. The next chapter explains this crucial step.

# Chapter 9

---

## Calibration of the experimental setup

---

In order to retrieve the optical properties of a material, here a biological tissue, from the diffuse reflectance measurements, some assumptions must be made, e.g., the shape of the spectral absorbance of components and the analytical expression of the spectral scattering parameters. In addition, a calibration step of the diffuse reflectance measurements in accordance with the diffusion theory model may also be necessary. This chapter proposes to describe the calibration step in our experimental setup.

### 9.1 Theoretical ground

First of all, it is necessary to define the *forward model*  $\mathcal{M}$  which, for a given set of optical properties of a material  $(\mu_a, \mu'_s)$ , returns the associated diffuse reflectance  $R_d$  of a semi-infinite medium, i.e.  $\mathcal{M} : (\mu_a, \mu'_s) \rightarrow R_d$ . Hereinafter, the model relies on the Diffusion Approximation, and the inverse model is defined by  $\mathcal{M}^{-1}$ . By denoting  $\rho$  the source-detector distance,  $n$  relative refractive index between the scattering medium and air,  $\mu_a$  the absorption coefficient and  $\mu'_s$  the reduced scattering coefficient, the diffuse reflectance  $R_d$  associated to  $\mathcal{M}$  is given by :

$$R_d(\mu'_s, \mu_a, \rho, n) = \frac{D}{4\pi} \left[ z_0 \left( \mu_{eff} + \frac{1}{r_1} \right) \frac{e^{-\mu_{eff} r_1}}{r_1} + (z_0 + 2z_b) \left( \mu_{eff} + \frac{1}{r_2} \right) \frac{e^{-\mu_{eff} r_2}}{r_2} \right] \quad (9.1)$$

where  $\mu_{eff} = \sqrt{3\mu_a\mu'_s}$ ,  $D = (3\mu'_s)^{-1}$ ,  $z_0 = 1/\mu'_s$ ,  $r_1^2 = z_0^2 + \rho^2$ ,  $r_2^2 = (z_0 + 2z_b)^2 + \rho^2$  and  $z_b = 2\kappa D$  with the internal reflection parameter  $\kappa = (1 + r_F)/(1 - r_F)$ . An analytical expression for  $r_F$ , which depends on the relative refractive index of the boundary, has been empirically determined using a curve fit by [Egan and Hilgeman (1980)].

The estimation of the optical parameters from the measured diffuse reflectance  $R_d^m$  is schematically described in Figure 9.1. It results from a scaling step  $S$ , which calibrates the projection of the experimental diffuse reflectances  $R_d^m$  onto the output space of the forward model  $\mathcal{M}$ . Then, a second step uses the inverse model  $\mathcal{M}^{-1}$  to extract the optical parameters from the scaled diffuse reflectance measurements  $R_d^{sc}$  with a estimation method.

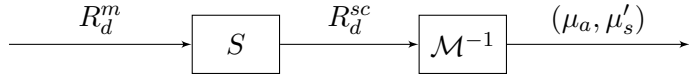


Figure 9.1: Measurement Processing Schematic

Coming back to the scaling step,  $S$  depends only on the setup and thus has to be determined once forever. Its estimation may be splitted into two substeps  $S_{abs}$  and  $S_{ord}$  explicited below. If the experiments  $R_d^m$  directly match the output space of the forward model, then  $S$  is the identity. Otherwise the calibration step consists in determining the function  $S$ , by using the calibration process described below.

The calibration process is based on the exploitation of the characteristic peak of the spectral diffuse reflectance curve which depends on  $\mu'_s$  as shown in Figure 8.16. In practice, the method consists in measuring the radiance scattered by a spectralon, described in Section 9.2.1, and the one scattered by a series of scattering phantoms with known optical properties. The optical properties of the scattering phantoms are selected by fixing a value for  $\mu_a$ , then taking in turn different discrete values of  $\mu'_s$  within a certain range. The borders of the range should coincide with the extreme values of the diffuse reflectance curve; we should also verify that the sampling of  $\mu'_s$  is thin enough in order to have corresponding  $R_d$  values that are close to the peak.

Then, at fixed absorption coefficient, source-detector distance and wavelength, the processing of the measurements to determine the scaling parameters  $S_{abs}$  and  $S_{ord}$  is done in four steps.

- (a) First, the diffuse reflectance parameters are fitted by non-linear least squares estimation so that  $\widetilde{R}_d(\mu'^m_s)$  minimizes the mean square error with the measurement points.
- (b) Then, as in [Kim *et al.* (2010)b], the abscissa  $\mu'^m_{s_{max}}$  corresponding to the maximum of  $\widetilde{R}_d(\mu'^m_s)$  can be determined. The refractive index, the absorption coefficient and the source-detector distance being known, we define  $R_d(\mu'^{sc}_s)$  the diffuse reflectance of the model  $\mathcal{M}$ . We can thus determine the abscissa  $\mu'^{sc}_{s_{max}}$  corresponding to the maximum of  $R_d(\mu'^{sc}_s)$ .
- (c) Then, the scaling parameter  $S_{abs}$  is defined as:

$$S_{abs} = \frac{\mu'^{sc}_{s_{max}}}{\mu'^m_{s_{max}}}. \quad (9.2)$$

- (d) Finally, the parameter  $S_{ord}$  is defined by the following positive nonlinear least squares estimation:

$$S_{ord} = \min_A \left\| A \cdot \widetilde{R}_d(S_{abs} \cdot \mu_s'^m) - R_d(\mu_s'^sc) \right\|^2 \quad (9.3)$$

Let us insist on the fact that the estimation of  $S_{abs}$  is necessary to correctly estimate  $S_{ord}$ . However, outside the calibration process, only  $S_{ord}$  is needed to scale the measured diffuse reflectances  $R_d^m$  to  $R_d^{sc}$ , i.e.,  $S = S_{ord}$ . The rest of this chapter describes how the calibration is performed in our experimental setup.

## 9.2 Experimental Calibration

In our case, the calibration step of function  $S$  is required due to experimental noises and assumptions on which relies the light propagation model  $\mathcal{M}$ .

Hereafter, we first remind the reader the way to perform diffuse reflectance measurements and then describe the composition and the process of realization of the calibration phantoms. In the phantoms, scattering is achieved by titanium dioxide beads (227676, *Sigma Aldrich*) suspended in distilled water and India Ink (N134103, *Sennelier*) is used as the absorber. The absorption coefficient of india ink has been determined previously by absorptance measurement. Then, we present the results of the calibration process performed in the new experimental system.

### 9.2.1 Performing diffuse reflectance measurements

By definition, diffuse reflectance corresponds to the part of incident spectral irradiance that has been scattered back to the interface. Because it is the ratio of back scattered spectral irradiance over the incident spectral irradiance, such a quantity cannot be measured directly and the incident spectral irradiance must be known. To determine the latter, we decided to use one method among many others, which consists in measuring the spectral irradiance  $I_{m,s}(\lambda)$  reflected by a spectralon whose spectral reflectance  $R_s(\lambda)$  is known. Then, the incident spectral irradiance  $I_0(\lambda)$  is simply given by :

$$I_0(\lambda) = \frac{I_{m,s}(\lambda)}{R_s(\lambda)} \quad (9.4)$$

To get as precise measurements as possible, we determine the incident light spectral irradiance before each set of measurements.

Then to determine the diffuse reflectance of a sample, it is necessary to acquire the spectral irradiance at the interface  $I_m(\lambda)$ . Then spectral reflectance  $R_d(\lambda)$  is then :

$$R_d(\lambda) = \frac{I_m(\lambda)}{I_0(\lambda)} \quad (9.5)$$

We emphasize to the reader that it is important to report the spectral irradiances acquired

in the same integration time base of the spectrometer. Otherwise, the obtained diffuse reflectances will be incorrect.

### 9.2.2 Realization of phantoms

Phantom n°	$\mu_a$ (cm <sup>-1</sup> )	$\mu'_s$ (cm <sup>-1</sup> )	TiO <sub>2</sub> (gr)	H <sub>2</sub> O (gr)	India Ink (ml)
C1	0.100	200.012	5.820	80.000	0.051
C2	0.100	180.008	5.238	80.000	0.051
C3	0.100	120.005	3.492	80.000	0.051
C4	0.100	97.017	2.823	80.000	0.051
C5	0.100	80.003	2.328	80.000	0.051
C6	0.100	61.996	1.804	80.000	0.051
C7	0.100	60.003	1.746	80.000	0.051
C8	0.100	54.985	1.600	80.000	0.051
C9	0.100	40.001	1.164	80.000	0.051
C10	0.100	34.984	1.018	80.000	0.051
C11	0.100	30.997	0.902	80.000	0.051
C12	0.100	28.008	0.815	80.000	0.051
C13	0.100	20.001	0.582	80.000	0.051
C14	0.100	10.000	0.291	80.000	0.051
C15	0.100	4.983	0.145	80.000	0.051

Table 9.1: Optical properties and quantities of related components for a set of optical phantoms.

Knowing that the volumic mass of titanium dioxide is 4.23 g/cm<sup>3</sup>, the diameter of titanium dioxide beads is 0.08 μm (equivalent to 325 mesh), the refractive index of titanium dioxide is given by [DeVore (1951)], the volumic mass of distilled water is 0.998 g/cm<sup>3</sup> and the molar extinction coefficient of india ink is given by [Di Ninni *et al.* (2010)], we use the OMLC Mie Scattering Calculator ([https://omlc.org/calc/mie\\_calc.html](https://omlc.org/calc/mie_calc.html)) to compute quantities of titanium dioxide, India Ink and distilled water given in Table 9.1.

To realize phantoms, it is recommended to first add the weight of the titanium dioxide, then the weight of distilled water and finally the volume of india ink. All these steps are performed under magnetic stirring to obtain homogeneous phantoms. We recommend to turn off the magnetic stirrer when performing diffuse reflectance measurements in order to ensure a good quality.

### 9.2.3 Calibration Results

Once, phantoms have been prepared, diffuse reflectances are measured as described in Section 9.2.1. As visible in Figures 9.2a, 9.2b, raw measurements must be scaled to coincide with the direct model  $\mathcal{M}$  values.

The calibration process described previously was used to scale the (relative) reflectance measurements with the probe in order to yield the reflectance in absolute units (i.e., cm<sup>-2</sup>) so that the inverse problem can be solved to extract  $\mu_a$  and  $\mu'_s$ .

In Figures 9.2a, 9.2b, measurements have been fitted with a the diffuse reflectance model defined in Eq. 9.1. Figures 9.2c, 9.2d correspond to the intermediate step where the theoretical and experimental models are scaled according to  $x$  : we observe that the abscissa of the maximum of each model is identical to the other.

Finally, Figures 9.3a, 9.3b represent the end of the scaling step, where experimental measurements and theorical model are comparable.

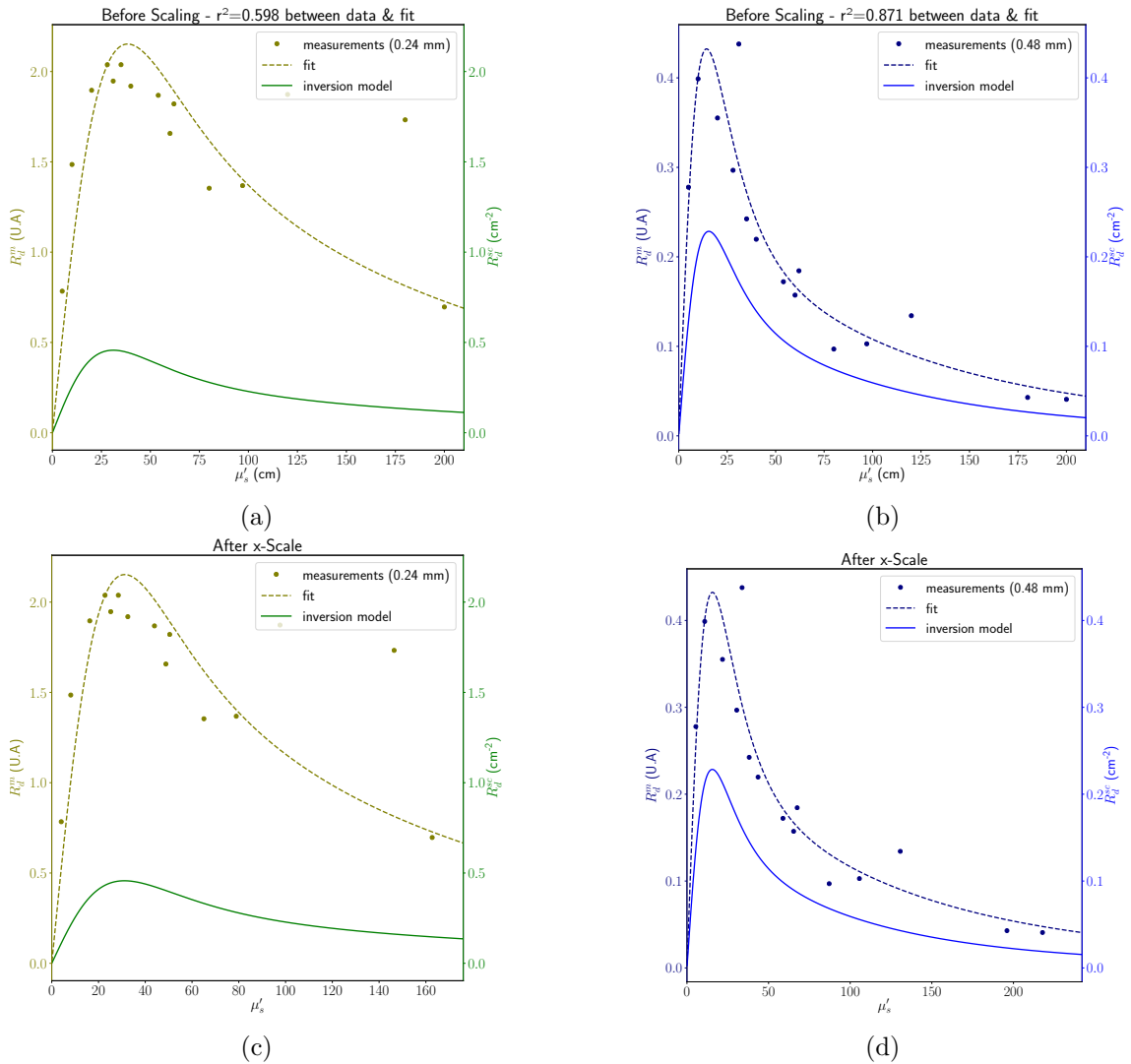


Figure 9.2: Calibration steps for two source-detector distances : Figs. (a) and (c), resp. (b) and (d), correspond to the short source-detector distance (0.24 mm), resp. the long one (0.48 mm). In each figure, the solid line corresponds to the output of  $\mathcal{M}$ , the dashed line to the experimentally fitted model and dots to measurements  $R_d^m$ . Figs. (a), (b) correspond to raw data and Figs. (c), (d) correspond to  $x$ -scaled data. Experimental diffuse reflectance measurements (points) of phantoms measured at 600 nm. Although the data shown are at 600 nm, the calibration was done for all wavelengths.

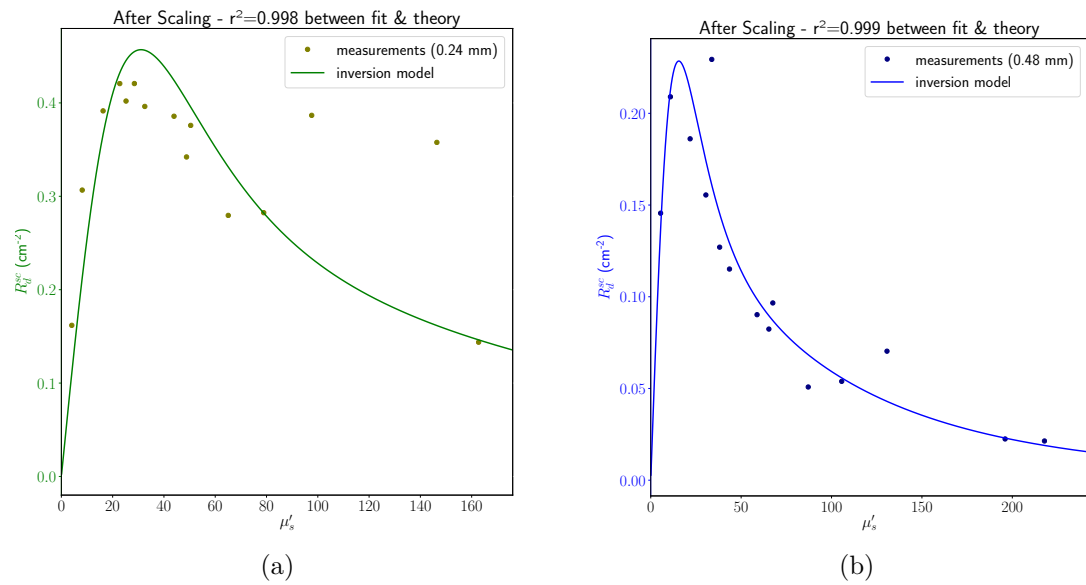


Figure 9.3: Result of the calibration process. Fig. (a), resp. (b), correspond to the short source-detector distance (0.24 mm), resp. the long one (0.48 mm). In each figure, the solid line corresponds to the output of  $\mathcal{M}$ , and dots to the scaled measurements  $R_d^{sc}$ . Experimental diffuse reflectance measurements (points) of phantoms measured at 600 nm. Although the data shown are at 600 nm, the calibration was done for all wavelengths.

### 9.3 Discussion and Conclusions

We have seen in this chapter the calibration method necessary to correctly estimate the optical properties of a material, i.e., a biological tissue in this dissertation. Nevertheless this calibration method has some limitations. First of all, biological tissues are known to be strongly anisotropic (refer to [Jacques (2013)b]), whereas the optical model of the Diffusion Approximation considers only isotropic scattering. This leads to a non-zero lower bound on the estimable  $\mu'_s$  at a fixed  $\mu_a$  as explained in [Kim *et al.* (2010)b]. A solution to this issue could be to use other optical models, by means of a more expensive inversion. Moreover, the diffuse reflectance model in Eq. 9.1 considers an empirically determined formula of the internal reflectance, a parameter whose critical importance has been highlighted in Part II. In addition, even if the calibration can be done once forever, it remains very sensitive to small variations of the experimental system and the measurement conditions, especially the integration time.

Finally, the measurement of diffuse reflectance is very strongly dependent on the measurement of the incident light intensity (performed with the spectralon), and can be the cause of large errors on the estimated optical properties.

# Chapter 10

---

## Acquisition software

---

The experimental system is used in a luminous environment. Thus, to obtain the fluorescence spectrum, it is necessary to acquire two measurements, a first one when the light source of the measurement system is off ("background"), and a second one when the lamp is on. This allows to subtract the portion of ambient light in the room than can access the sensor.

In addition of being easy to use, the main task of the developed software is to manage the mandatory synchronization between spectrometer acquisition and laser excitation to be able to perform correctly the fluorescence measurements.

In this chapter we will first see the graphical user interface before dwelling on the software engineering deployed to realize this acquisition software. The open source software has been fully developed in Python and can be shared upon request.

### 10.1 User Interface Description

The User Interface has been developed using the Python version of Qt 5.12.2.

In the first step, the software (refer to Fig. 10.1) waits for the user to define his private girder key (necessary to save the data on the dedicated laboratory server), to select the COM port corresponding to the Arduino Uno board and to indicate the configuration file of the experimental system (see Section 10.4). Finally, the user validates everything by clicking on the "Load" button.

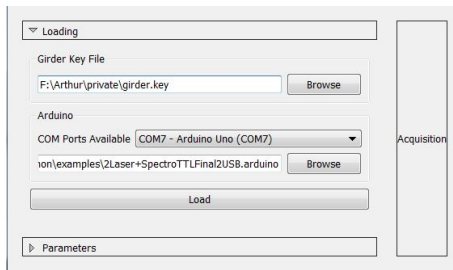


Figure 10.1: User Interface associated with the first step of the Acquisition Software

In the second step, the window has changed its appearance (see Fig. 10.2) and the user can now define the acquisition parameters (the power of each laser, the number of repetitions for each acquisition, the integration time for the white light diffuse reflectance and the fluorescence acquisitions, etc.).

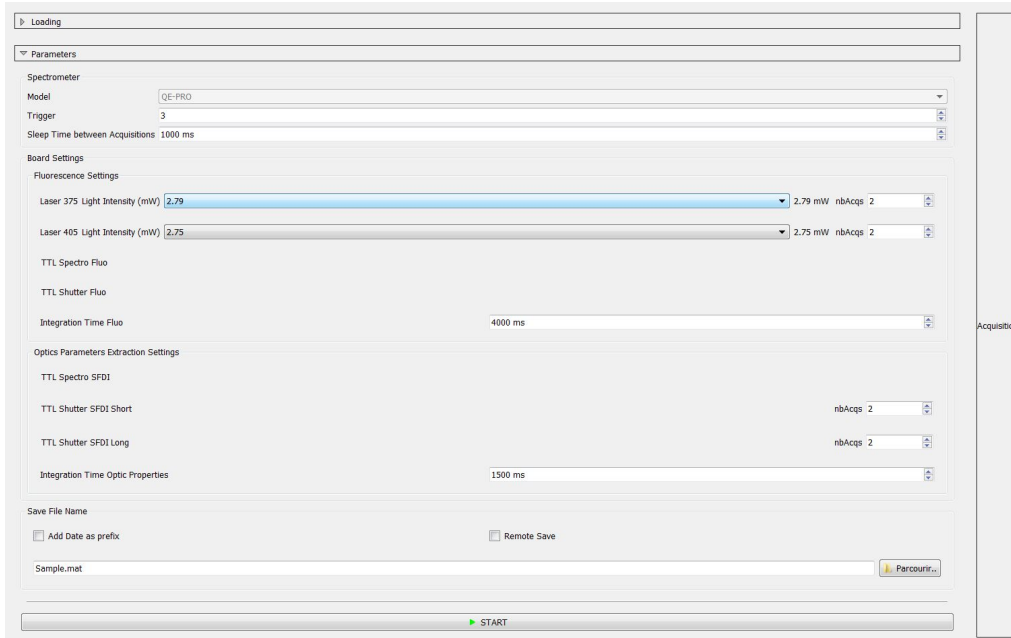


Figure 10.2: User Interface associated with the second step of the Acquisition Software

In the bottom of the window, the user can define the name of the mat file which will contains all acquisition datas. The "Remote Save" checkbox enables to upload the acquisition data to the girder laboratory server. When the user clicks on the "Browse" button, a popup appears to select the file storage location.

When the file storage location is set and the spectrometer is selected, the "Run" button becomes clickable. As soon as it is clicked the acquisition starts. It is possible to follow the acquisition process by watching the acquired spectra on the user interface (see Fig. 10.3).

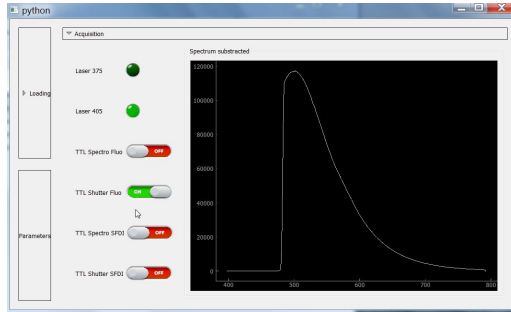


Figure 10.3: User Interface associated with the acquisition step of the Acquisition Software

## 10.2 Software Engineering

The whole software is based on a Model-View-Controller software architecture (refer Fig. 10.4). Indeed, Model-View-Controller or MVC is a software architecture pattern intended for graphical interfaces. Particularly popular for web applications, it consists of three types of modules with three different responsibilities: models, views and controllers.

- A model contains the data to be displayed (in our case it also contains all the optical elements necessary for the acquisition),
- A view contains the presentation of the graphic interface (presented in Section 10.1),
- A controller contains the logic concerning the actions performed by the user : it is the element connecting the models to the views.

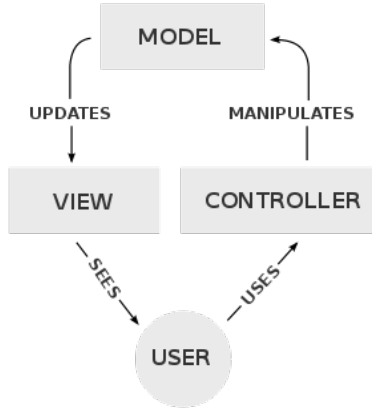


Figure 10.4: Schematic of the MVC software architecture (Taken from Wikimedia)

As mentioned before, the model also contain the classes of each controllable element of the acquisition system (lasers, spectrometer and Arduino board). These classes have been created to interface with the libraries provided by the manufacturers. Because some methods of the constructor libraries are waiting for external events to continue their execution, like an electric trigger signal, I had to use multi-threaded programming.

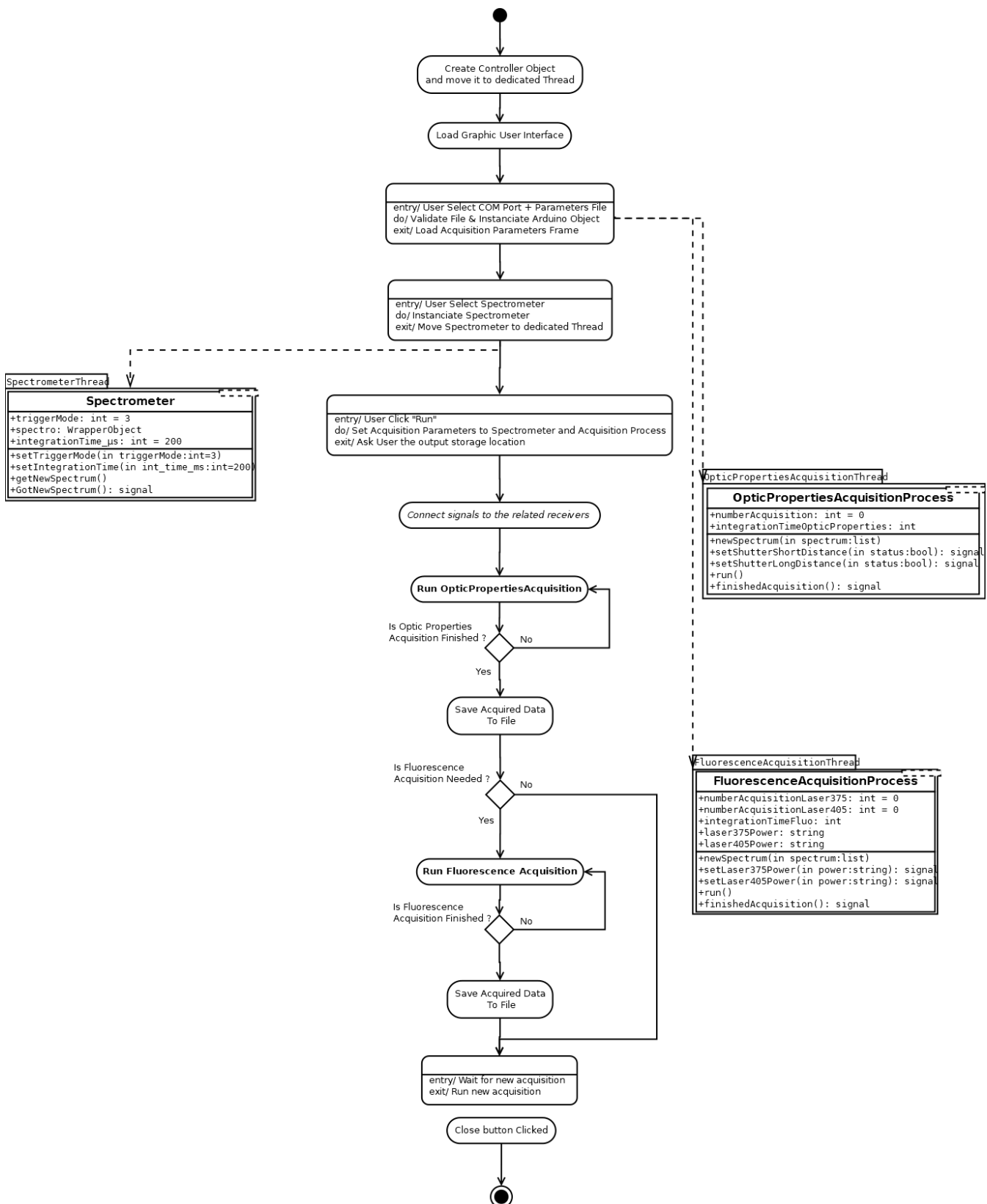


Figure 10.5: Software flowchart

By definition, multithreading extends the idea of multitasking to applications, specific operations within the same application can be subdivided into individual threads. Finally, the operating system divides the processing time not only between different applications, but also between each thread within the same application.

Since each thread can run in parallel, I had to be particularly careful about both the smooth running of the acquisition processes and the data because two threads can't write/read the same data at the same time. In order to synchronize the threads with each others, the only valid element is the *QtSignal* object. When the latter is activated, it launches the execution of the task to which it is connected, regardless of the thread to which the task belongs.

In the figure 10.5 the different threads are represented by tabbed boxes (like SpectrometerThread). I would like to point out to the reader that each acquisition process also has a dedicated thread to allow GUI updates and emergency shutdown without freezing the software. Next section will explain the reader how the acquisition process is performed.

## 10.3 Acquisition Process & Post-Processing

The acquisition protocol consists of two main steps, the measurements for the estimation of the optical properties and then the fluorescence measurements. For the whole acquisition protocol, the trigger mode of the spectrometer is set to 3 (refer to the chapter 8 for the different trigger modes of the spectrometer).

The protocol starts with the measurement of diffuse reflectances of the tissue to extract the optical properties of the latter. The integration time of the spectrometer is set to 7 seconds. To correctly measure the diffuse reflectances, an excitation of the tissue with sequentially white light off/on at short distance "source-detector" then white light off/on at long distance "source-detector". This cycle is repeated four times without break.

For fluorescence measurements, the protocol is essentially identical to the one presented in [Alston (2017)]: tissue excitation with sequentially Laser385 off then on, then Laser405 off/on. This cycle is repeated six times without break. Similarly to the studies presented in the Chapter 2 use a source at 405 nm, we will acquire six more pairs of spectra at this excitation wavelength, in order to increase the signal-to-noise ratio of this excitation wavelength and thus to compare our results more easily with those of the literature. The acquisition time is 200 ms per spectrum. By having respectively 6 and 12 on/off acquisition couples per laser, this gives a duration of 7.2 s during which the probe must held. The 200 ms acquisition time allows a balance between the electronic noise present in the measurement system which requires a long acquisition time, and a possible spurious signal induced by a potential movement of the neurosurgeon, a variation of the ambient light or the movement of the staff, which implies a short acquisition time.

In the case of *ex vivo* measurements, the neurosurgeon cuts the tissue to probe, the biopsy is placed on a compress, then the OR nurse cuts the biopsy in two parts, one is given for measurements with the optical probe and the other one is sent for pathological analysis.

Before analyzing the presence of PpIX in the samples, and thus looking for a marker of tumor cell density, it is necessary to isolate the spectrum emitted by PpIX. Similarly, it is necessary to post-process the measurements performed on the tissue under white light in order to obtain the diffuse reflectances necessary to estimate the optical properties.

The post-processing of the spectra acquired in the operating room starts as follow: for each acquired "on" spectrum, the associated background is removed and then all the spectra obtained under the same excitation wavelength are summed up.

Once the spectra are obtained, for each sample and each laser, all the information is stored in a Matlab structure presenting the patient number, the sample number, its classification by the anatomo-histopathological analysis and the two spectra, one per laser. Each processing step described below will be stored in this same structure in order to have a unique and complete database. The use of a Matlab structure allows to limit the sources of errors like a sample switch for example.

## 10.4 Software Acquisition Parameters File

As explained in Section 10.1, the user has to load an hardware acquisition parameters file which will be described in this section. I decided to use an external parameters file instead of writing them in hard copy in the software code. Even if this allows a greater adaptability of the software, there are still some constraints in the file architecture for everything to work properly.

First, the file must be in JSON Format, which is readable from any basic word processing software and allows to represent structured information. Second, as the json format is based on a set of "key": "value" or "key": "object", keys must be one of the followings:

- `Laser 375,`
- `Laser 405,`
- `TTL Spectro Fluo,`
- `TTL Shutter Fluo,`
- `TTL Spectro WL,`
- `TTL Shutter WL,`
- `TTL Shutter WLShort,`
- `TTL Shutter WLLong.`

Since some keys refer to hardware objects waiting for digital signals (TTL) and others to hardware objects waiting for analog signals (0-5V), it seems relevant to me to explain both cases through simple examples.

As described in chapter 8 Section 8.2.4, a serial link is deployed between the computer and the Arduino board through the USB port. Each pin mentioned in this manuscript can be remotely controlled by sending a specific character to change its status.

First, let see how to declare a digital pin control dedicated to the White Light Shutter in the acquisition parameters file.

```

1 {"TTL Shutter SFDI": [
2     "0": "c",
3     "1": "d"
4 ]
5 }
```

In the statement below and in general, the key corresponds to the command provided by the software. In the case of a boolean, the value corresponds to the numerical representation of the boolean (1 for true and 0 for false).

Now, let see how to declare a PWM pin control dedicated to the Laser385 in the acquisition parameters file. As it is possible to control the laser with an analog signal or through USB, I will first describe how to control a laser with an analog signal and the next part of code will be dedicated to the USB control.

```

6 {"Laser 375": [
7     "0.0": "p0",
8     "0.22": "p10",
9     "0.88": "p30",
10    "1.89": "p65",
11    "2.59": "p88",
12    "2.95": "p90",
13    "3.29": "p100",
14    "3.97": "p120",
15    "4.32": "p132",
16    "7.32": "p220",
17    "8.22": "p255"
18 ]
19 }
```

As previously, the key corresponds to the command provided by the software. In the case of a PWM, the character to select the PWM pin is followed by a integer value between 0 and 255 which corresponds to the duty cycle value to set. The commands list presented in the pieces of code just above and below are not exhaustive. As the lasers are sold with a library to control them through USB, we decided also to implement this way of controlling lasers. Thus, it is relevant to know how to declare USB control parameters in this file.

```

6 {"Laser 375": [
7     "0.00": "0",
```

```
8             "0.13": "10",
9             "0.39": "30",
10            "0.64": "50",
11            "1.68": "130",
12            "2.16": "170",
13            "2.40": "190",
14            "2.53": "200",
15            "2.66": "210",
16            "2.79": "220"
17        }]
18 }
```

---

One can notice that the special character has disappeared because with the USB mode, the command sent to the laser is directly the desired optical power.

## 10.5 Conclusion

In this chapter, we have described how the acquisition software has been built. We also gave some screenshots of the graphical user interface related to the acquisition software. Since the writing of this Part, the acquisition system has been updated to increase the optical power sent to the tissues though the probe. These updates are briefly described inside the perspectives.

## V Perspectives and Conclusion

---



# Chapter 11

---

## Perspectives initiated during the PhD

---

In this chapter, we present the perspectives of the work detailed in the previous chapters and results from the research conducted in parallel. First, the direct continuation of the PhD is briefly described. Then, an extension of the work on gliomas to another neural pathology is suggested. Finally, we detail our contribution to the European project Scan'n'Treat which were done aside of the main theme of this dissertation.

### 11.1 Direct continuation of the PhD

The contributions of the parts II and III are presented as independent in this manuscript. They will be combinable after the completion of the steps described below.

On the optical models side, part III, it is first important to extend the characterization of the reduction of the prediction error already performed on 2-flux and 4-flux models to the scattering approximation. In a second step, it will be necessary to study the impact of this reduction of prediction error on the quantification of a fluorophore.

On the side of the multispectral excitation estimation method, part II, it is necessary to propose a solution to the hot spot problem in order to make our method more robust.

Finally, the two approaches can be combined to quantify the two forms of PpIX in a relative and absolute way under multispectral excitation.

### 11.2 Application to Focal Cortical Dysplasia

The work done on glioma may in fact have broader application to neurosurgery in general. Following discussions with Dr. Joseph Toulouse, it seems that focal cortical dysplasia

is a good example.

Focal cortical dysplasias (FCD) are cerebral malformations that appear during brain development. They are characterized by morphological changes of the cells (large cells called balloon cells) and their organization in the cerebral cortex [Guerrini and Dobyns (2014)]. These dysplasias can be associated with a so-called focal epilepsy [Bautista *et al.* (2003)], i.e. affecting only a limited area of the brain. Focal epilepsies are the most common type of epilepsy, affecting about 2 epileptic patients out of 3.

Patients with severe focal epilepsy, which is resistant to drug treatment, can have surgery to remove the epileptogenic focus, i.e. the area of the brain responsible for the seizures. The comparative study [Hamiwka *et al.* (2005)] includes a cohort of 40 children operated on from 1980 to 1992 and aged from 6 months to 18 years at the time of their surgery. After a follow-up during ten years, 40% were seizure-free, 26% had a major reduction in seizures (reduction rate over 90%) and 34% were unchanged. The study noted that complete resection was statistically significant for a favorable outcome, and no patient with incomplete resection was seizure-free. However, successful neurosurgical resection depends on the ability to remove dysplastic tissue with minimal damage to normal perilesional tissue; and the fluorescence technique has been implemented using fiberoptic probes and used to characterize neoplastic tissue [Ramanujam (2000)].

Recent studies [Kleen *et al.* (2011), Anand *et al.* (2017), Roberts *et al.* (2019)] have attempted to determine whether ALA-induced PpIX fluorescence can consistently discriminate epileptogenic areas from healthy tissue. However, the study [Roberts *et al.* (2019)] reports few visible fluorescence under 405 nm excitation. The [Kleen *et al.* (2011)] study uses 633 nm PpIX excitation, whereas [Anand *et al.* (2017)] suggests a multispectral excitation of PpIX at 378 nm and 445 nm.

Thus, to our knowledge, there is no study that seeks to separate neoplastic tissue from healthy tissue using a method of multispectral fluorescence excitation at 380 nm and 405 nm. This study could directly derive from the work explained in this dissertation.

### **11.3 Contribution to the Scan'n'Treat european project : Characterization of the fluorescence dose-effect response of X-PDT nanoparticles**

The study of fluorescence carried out on glioma can be applied to a wider scope in the cancerology sector. We had the opportunity to observe this by participating in the European project Scan'n'Treat whose theme is outside the main one of the PhD.

While Europe represents only 9% of the world population, it accounts for 23% of the global amount of cancer, which is thus the second leading cause of death in Europe. Many treatment strategies exist: surgery, chemotherapy, radiotherapy or targeted therapy, but the results are not always convincing. And while in some cases, five-year survival after treatment can be encouraging, patients' living conditions deteriorate due to the side effects

of the therapies.

A significant increase in the five-year survival of patients while having a significant positive impact on the patient's quality of life therefore seems to be necessary. To achieve this, a new technology is needed to ensure effective treatment of cancer, even radioresistant cancer, with low side effects, allowing accurate diagnosis and providing access to in situ treatment monitoring. The other innovative aspect of this technology is the fact that everything takes place at the same time, with the same machine, which will be much less stressful and disturbing for the patients compared to other treatments.

Scan'n'Treat is the first building block of this ambition, by combining two cutting-edge technologies: the Spectral Photon Counting Scanner (SPCCT), which is a revolutionary imaging modality, and a new X-ray-based treatment called X-ray Activated Photodynamic Therapy (X-PDT). The perfect match between these two technologies will be ensured by specially designed probes that serve as both contrast and therapeutic agents.

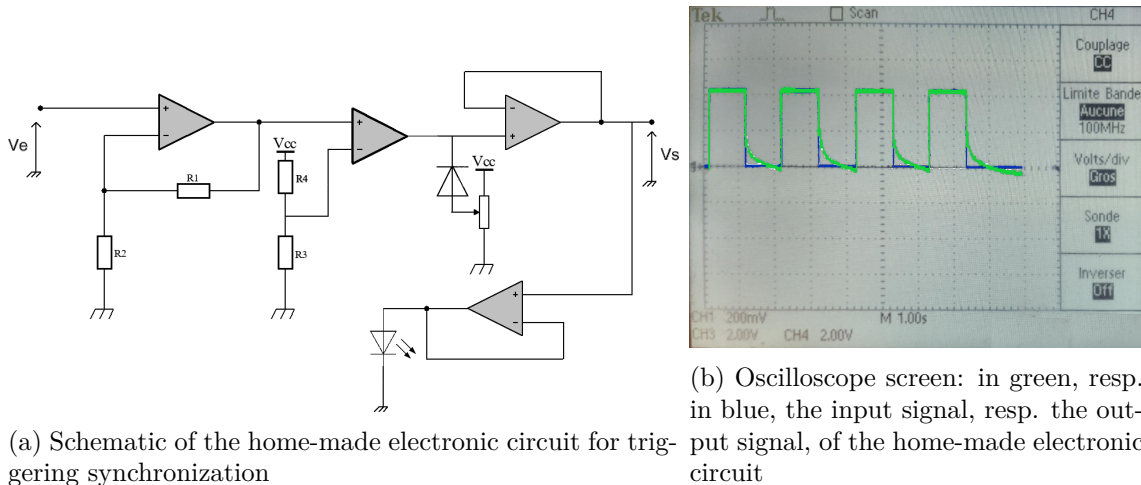
The first step of the Scan'n'Treat project was to realize fluorescent nanoparticles as well as to add surface modifications to ensure their biocompatibility and in vitro evaluation of their internalization and toxicity. Thus, we used different nanoparticles : "naked" nanoparticles (LC174) at 1 mol.L<sup>-1</sup>, PEG functionalized nanoparticles (LC205) at 1 mol.L<sup>-1</sup>, Terbium chloride molecules at 1 mol.L<sup>-1</sup>, PAA functionalized nanoparticles (LC230), silica dioxide + PEG functionalized nanoparticles (LC237) and Terbium Fluoride molecules.

Then, the project team contacted us because of our knowledge of fluorescence and of acquisition systems allowing a quantifiable measurement of fluorescence. Indeed, they need to quantify the fluorescence emitted by new nanoparticles made in the framework of the project. This element is crucial to study the dose-response effect. Briefly, fluorescent nanoparticles result from a combination of Gadolinium (Gd) and Terbium III (Tb). Basically, the gadolinium absorbs the energy given by X-rays and gives it to Terbium III which goes back to a stable state by emitting fluorescence. In the final nanoparticles, Rosebengal is also added inside the nanoparticles, which will absorbe photons resulting from fluorescence and generates singulet oxygens. On a practical aspect, the nanoparticles are stored inside an eppendorf.

## Fluorescence Measurement Experimental Setup

To dermine the fluorescence, the experimental system is composed of an FG550UEC optical fiber from Thorlabs Inc. whose cleaved end is immersed in the nanoparticle solution and whose SMA connector end is connected to an Round to Linear bundle of fiber (PL200-2-VIS-NIR, Ocean Insight). The bundle maximizes the light signal entering the spectrometer and thus is connected to the Ocean Insight MayaPro2000 spectrometer. The spectrometer has previously been calibrated in order to give absolute spectral irradiance measurements.

In addition, since the fluorescence excitation signal is emitted from the SPCCT, we needed a trigger signal indicating whether the X-rays are on or off. After contacting Philips, it appears that attempts to obtain a direct signal from the gantry were met with obstacles. A simple alternative was to use a stand-alone scintillation detector, i.e. a basic scintillation detector attached to a photodiode. Philips provided us with a stand-alone detector measuring approximately 1x1x20 mm, with the entire assembly encapsulated in epoxy to protect the assembly.



(a) Schematic of the home-made electronic circuit for triggering synchronization  
(b) Oscilloscope screen: in green, resp. in blue, the input signal, resp. the output signal, of the home-made electronic circuit

Figure 11.1

Nevertheless, an home-made electronic circuit was still needed because both a background and a fluorescent signal are required to measure a fluorescence spectrum. In Fig. 11.1a, one can notice 4 electronic "stages" in cascade. The first one allows to amplify the signal of the detector (represented by the voltage  $V_e$ ), the second one compares the voltage resulting from the amplification stage with a reference voltage. If the voltage from the amplification stage is higher than the reference voltage, then the output voltage of this second stage is +5V, otherwise it is -5V. Because the output voltage must be between 0 and 5V, we can note the presence of a diode whose voltage at the anode is adjusted by a potentiometer in order to cut the negative voltage and assign it to 0V. Finally, the third stage allows the separation of the electronic processing stages from the output via a so-called "follower" assembly. One also note the presence of a last tracking stage just before the LED which lights up when the trigger signal is at 5V and switches off when the trigger is at 0V.

On Fig. 11.1b, one observe the input and output signals of the electronic system. Attention, the input signal (of which one notices the exponential decreases) is displayed with a scale of 200mV/DIV whereas the output signal (square signal) is displayed with a scale of 2.00V/DIV. We note that the electronic system transforms the signal of the detector into a digital signal (0 or 5V).

To get the background measurement, an Arduino Nano board has been added at the

end of the electronic circuit. This board enables to send the 5V signal when the trigger is on, and also to generate a 5V short square pulse when there is no trigger. This additionnal 5V short square trigger pulse enables to measure the background. The electronic system has been encapsulated into a small box.

The processing of raw measurements is done in two steps : the first one is to substract the background measurement from the fluorescent signal one, and the second is a sliding average filtering with a window of 3 pixels to reduce detector noise. As example, spectra for LC205 at 0.5 mol.L<sup>-1</sup> are given in Fig. 11.2.

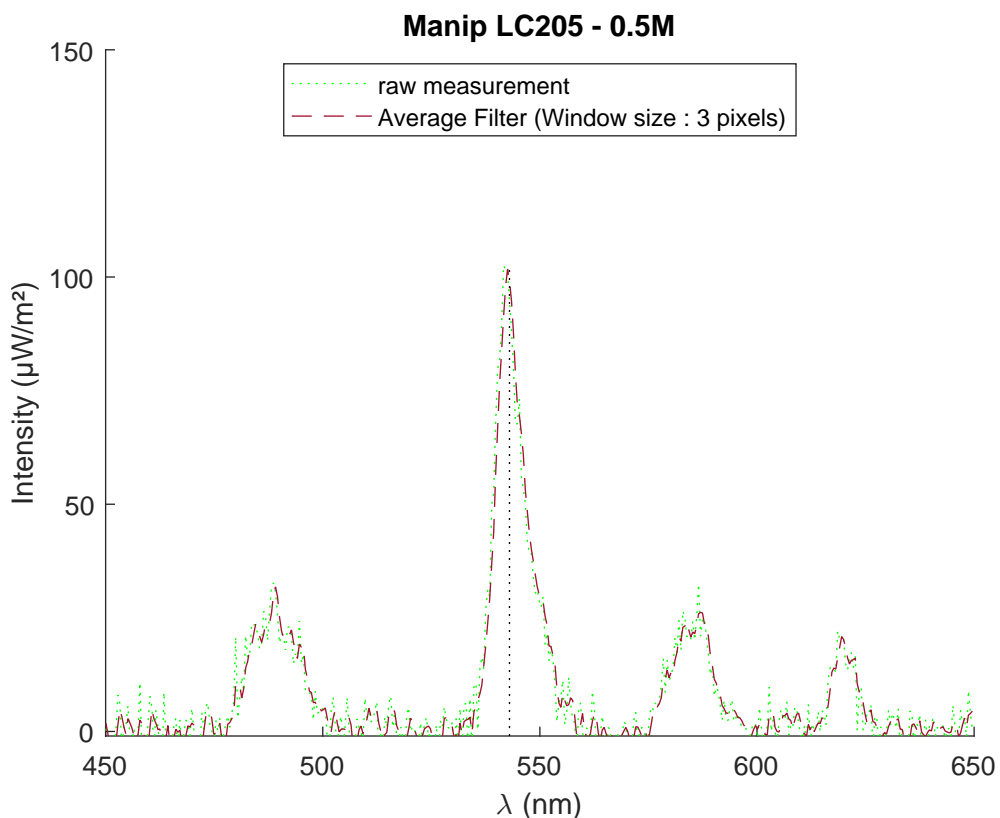


Figure 11.2: Fluorescence spectrum obtained for PEG functionalized nanoparticles concentrated at 0.5M under 120 keV, 300 mAs excitation.

The four pics at 490 nm, 543 nm, 585 nm and 622 nm are typical from the fluorescence of Terbium III. This first result is reassuring and confirms the good functioning of our experimental system and processing of raw measurements. Then, the aim of this experimental setup is to study the dose-response effect. The study of the dose-response effect corresponds to the analysis of the fluorescent response according to different parameters such as the type of nanoparticles (functionalized or not), the concentration of nanoparticles, the number of mAs or the X-ray energy. Thus, we decided to define the fluorescent

response related to a measurement  $m$  as :

$$I_{response} = \int_{\lambda=481 \text{ nm}}^{496 \text{ nm}} m(\lambda) d\lambda + \int_{\lambda=535 \text{ nm}}^{553 \text{ nm}} m(\lambda) d\lambda + \int_{\lambda=577 \text{ nm}}^{591 \text{ nm}} m(\lambda) d\lambda + \int_{\lambda=615 \text{ nm}}^{624 \text{ nm}} m(\lambda) d\lambda . \quad (11.1)$$

## Results

Let now focus on the analysis of the dose-response effect. First, we study the evolution of the response as a function of mAs and keV for "naked" nanoparticles (LC174) at  $1 \text{ mol.L}^{-1}$ , PEG functionalized nanoparticles (LC205) at  $1 \text{ mol.L}^{-1}$  as well as Terbium chloride molecules at  $1 \text{ mol.L}^{-1}$ . Then, we will look at the evolution of the response as a function of the concentration for LC174 and LC205 nanoparticles, but also for PAA functionalized nanoparticles (LC230), silica dioxide + PEG functionalized nanoparticles (LC237) as well as Terbium Fluoride molecules.

To get more quantitative results, we made the assumption that each set of points of Fig. 11.3 corresponds to a linear model

$$I_{response}(mAs, keV) = a(keV) * mAs + b(keV) .$$

Resulting values of parameters  $a(keV)$  and  $b(keV)$  are given in table 11.1. According to Fig. 11.3, at the same concentration level, the response increases with an increase of mAs for both LC205 and LC174, which is confirmed by the positive value of  $a$  for each row of table 11.1. In addition, we notice that mAs has no effect on terbium chloride molecules. This is relevant because the fluorescent effect of nanoparticles is resulting from the energy transfer between gadolinium and terbium. Thus, there is no fluorescence because there is no gadolinium in terbium chloride molecules.

Nanoparticle	$a(keV)$ $\mu W/m^2/mAs$	$b(keV)$ $\mu W/m^2$	$R^2$
LC205 - 80keV	0.0025	1.8224	0.1072
LC205 - 100keV	0.1929	0.6695	0.999
LC205 - 120keV	0.3032	1.1606	0.999
LC205 - 140keV	0.4685	7.0200	0.961
LC174 - 80keV	0.1193	0.3592	0.991
LC174 - 100keV	0.2222	0.7920	0.979
LC174 - 120keV	0.3652	0.0850	0.994
LC174 - 140keV	0.9450	1.0719	0.999
TbCl <sub>3</sub> - 140keV	-0.0026	0.978	0.0137

Table 11.1: Linear model parameters of the fluorescent response as a function of mAs for different nanoparticles.

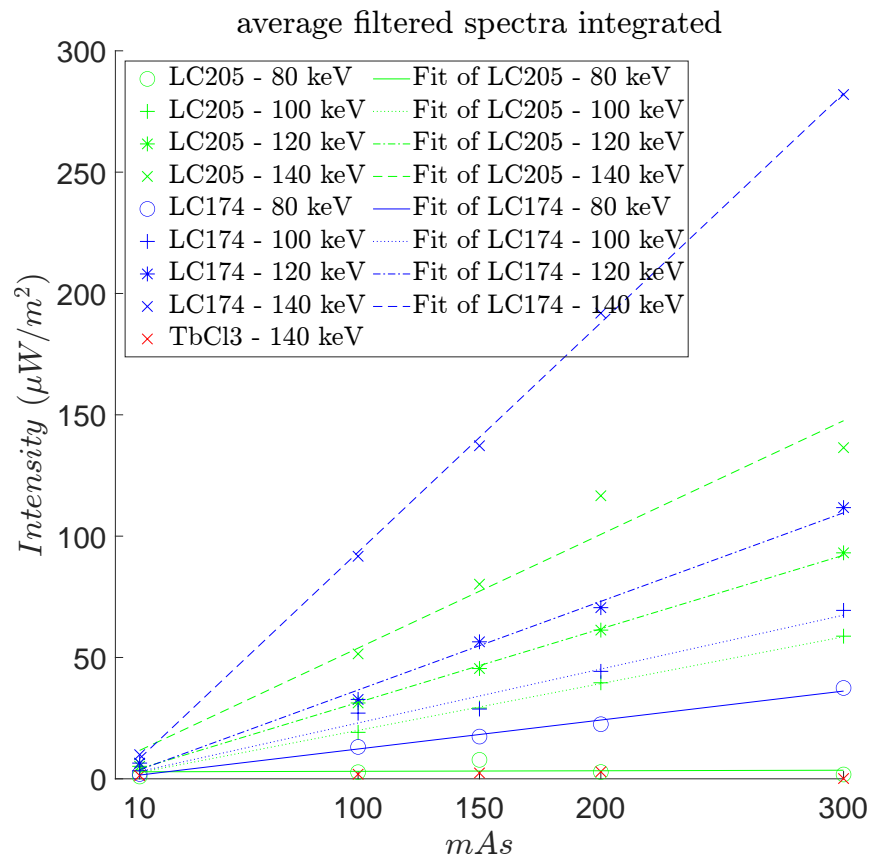


Figure 11.3: Fluorescent response for two different types of nanoparticles, PEG functionalized LC205 (green lines) and not functionalized LC174 (blue lines) as well as the witness sample of terbium chloride (red lines) depending on mAs (horizontal axis) and keV (Marker type). Cross marker  $\times$ , resp. star marker  $*$ , corresponds to 140 keV, resp. 120 keV and tick marker  $+$ , resp. circle marker  $\circ$ , corresponds to 100 keV, resp. 80 keV. All chemical component are  $1 \text{ mol.L}^{-1}$  concentrated.

As visible on Fig. 11.4, we also note that the functionalization of nanoparticles by PEG impacts the fluorescent response which is on average 35.6% less intense than that of non-functionalized nanoparticles. Moreover, except for the fluorescence efficiency at 80 keV, the ratio of fluorescence efficiency of LC205 over LC174 is 73,14% in average, which confirms that the functionalization reduces the fluorescent response.

Because, these first results are given at fixed concentration in nanoparticles and for a single functionalization method, we will now study the fluorescent response according to the functionalization method of the nanoparticle as well as the nanoparticle concentration. For this study, the X rays parameters are fixed to 300 mAs and 120 keV.

According to Fig. 11.5, one can notice that the fluorescent response increases with

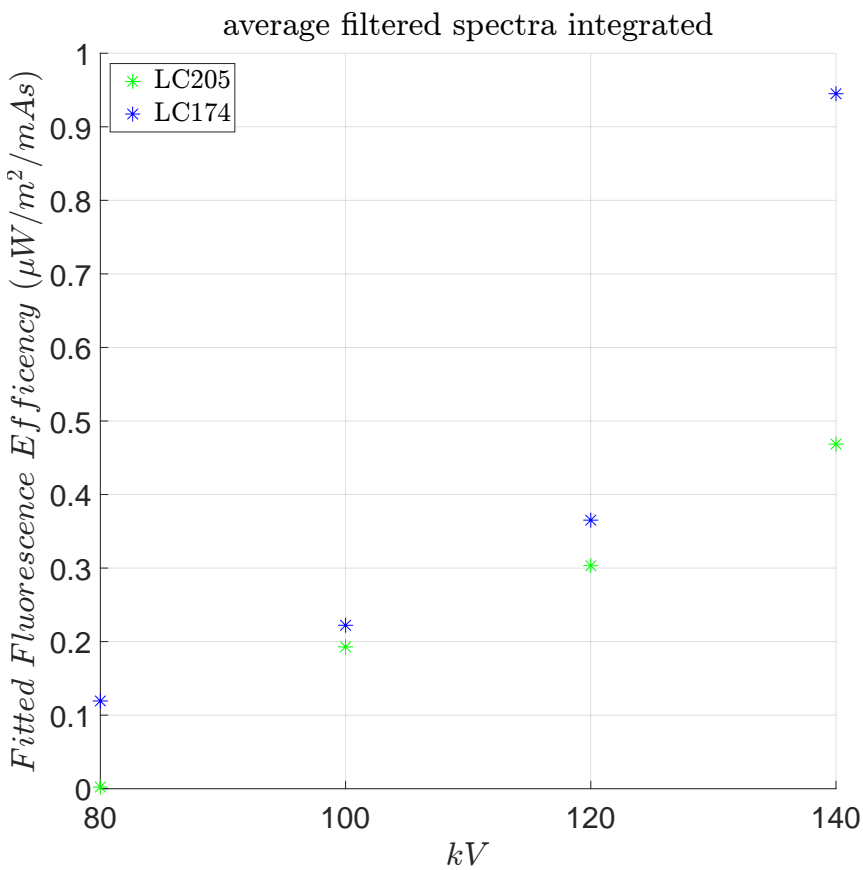


Figure 11.4: mAs dependent fitted fluorescent efficency for two different types of nanoparticles, PEG functionalized LC205 (green stars) and not functionnalized LC174 (blue circles) depending on keV. All chemical component are  $1 \text{ mol.L}^{-1}$  concentrated.

increasing nanoparticle concentration. This response can be modeled by

$$I_{response}(C) = \alpha C^2 + \beta C + \gamma$$

where C is the nanoparticles concentration in  $\text{mol.L}^{-1}$  and the coefficients  $\alpha$ ,  $\beta$ ,  $\gamma$  for LC230 and LC237 are given in the table 11.2 just below.

Nanoparticle	$\alpha$ $\mu W/m^2/(mol/L)^2$	$\beta$ $\mu W/m^2/(mol/L)$	$\gamma \mu W/m^2$	$R^2$
LC237	426.979	277.331	1.523	0.998
LC230	734.104	324.112	-7.4382	0.999

Table 11.2: Polynomial model parameters of the fluorescent response as a function of concentration for different nanoparticles.

Depending on the functionalization method, the increase in fluorescent response is more or less with the concentration. Thus, functionalization with PAA offers the best fluorescent response among all the proposed functionalization methods. The PEG functionalization gives a response almost identical to that of PAA. Only the SiO<sub>2</sub>+PEG functionalization

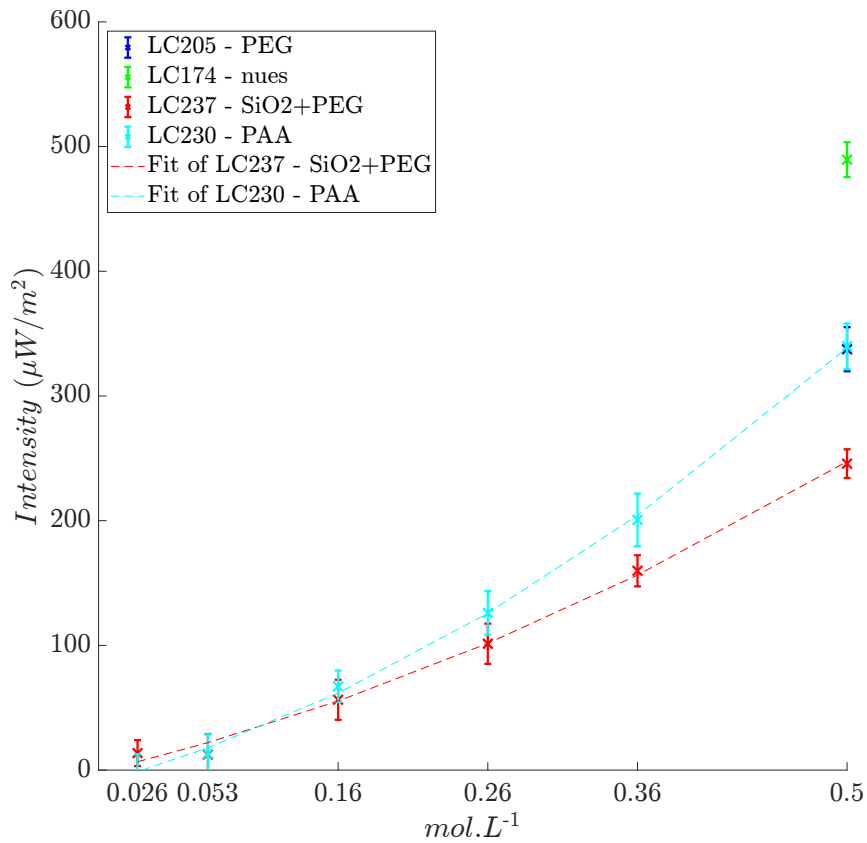


Figure 11.5: Fluorescent response for two different functionalization methods of the nanoparticle. Acquisitions are done at 120 keV and 300 mAs.

gives a lower fluorescent response than the other functionalization methods. The concentration effect observed in Fig. 11.5 is also confirmed by Fig. 11.6, whose analysis can only be qualitative, but we can notice a decrease in the fluorescent response when the nanoparticles are half as concentrated.

## Conclusions and Outlook

The first results of the Scan'n'Treat project show that the dose-response effect is non-linear as a function of concentration and keV, but linear as a function of mAs.

However, in the final nanoparticles, rosebengal is also added. It will absorb the photons resulting from the fluorescence and generate singlet oxygens. Some methods exist today to quantify the number of singlet oxygens by fluorescence [Ahmad *et al.* (2019)], so it seems relevant to use this method to quantify the final dose-response effect of the nanoparticle that is intended to be used in X-PDT.

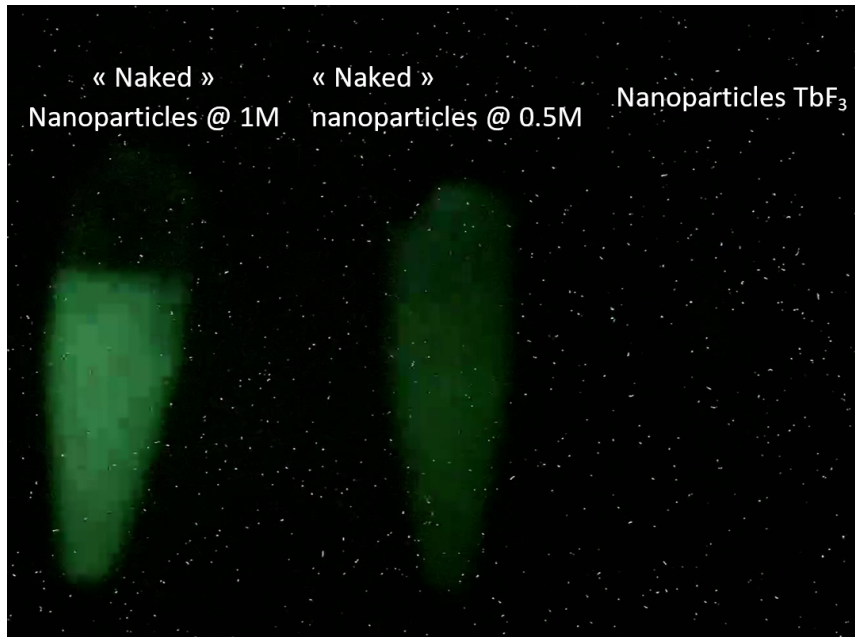


Figure 11.6: Image of various nanoparticles scintillation at different concentrations (from left to right  $1.0 \text{ mol.L}^{-1}$ ,  $0.5 \text{ mol.L}^{-1}$  and witness  $0.5 \text{ mol.L}^{-1}$ ) under X Ray excitation at 120 keV and 300 mAs.

# Chapter 12

---

## Conclusion

---

The work presented in this manuscript is in the clinical context of glioma resection. As gliomas are infiltrating tumors of the central nervous system, the clinical problem is to remove a maximum of tumor infiltrations.

The aim of this thesis work was to improve the distinction between tumor margin and healthy tissue. Thus, two complementary investigations took place: one concerning the so-called semi-quantitative approaches, the other on the quantitative approaches.

For the semi-quantitative approach, we started from previous works which showed the interest of PpIX fluorescence to visualize tumor infiltrations and the variability of its emission spectrum according to its microenvironment. This variability of the emission spectrum of PpIX with its microenvironment allowed the demonstration of the presence of two states of PpIX in tumor tissues, where the current techniques were looking for only one state. The proposed states are configurations where PpIX emits different fluorescence spectra, showing a maximum either around 622 nm (620 state) or around 634 nm (634 state). These two states, whose properties have been studied at an earlier stage, are still misestimated by the literature models in some cases because of crosstalks with other endogenous fluorophores present in the acquired fluorescence signals. Thus, in Section II, we propose a method to estimate the two forms of PpIX without any *a priori* on the components of the signal other than PpIX. For this purpose, our method relies on several fluorescence excitation wavelengths and the *a priori* knowledge of the quantum yield of each of the PpIX forms. This method has been compared to the state of the art on a set of cases, including synthetic clinical images of glioma. It was shown to be equivalent to the state of the art methods in the already solved cases, but significantly better than the existing methods in the presence of crosstalk. Our method keeps a specificity almost

equal to that of the ground truth while that of the existing methods is null. Further work should focus on the application of this method to phantoms or clinical data and on the solving the problem of hot spots where our method is still not accurate.

For the quantitative approach, all the tools for solving the radiative transfer equation have been presented in the introduction. Nevertheless, the diffusion approximation model is widely used in the bibliography of PpIX quantification. After describing the discrete ordinates method used to solve the radiative transfer equation, we focused on the validation of its implementation. It highlighted the effect on convergence of the Fresnel angular reflectance and a discussion about the impact of the discretization method on the relative convergence speed. By studying precisely the internal reflectance value of the air-tissue interface and its dependence on several relevant parameters such as albedo, optical thickness, anisotropy factor or relative optical index, we demonstrated that the commonly used value, i.e. 0.6 for a relative refractive index of 1.5, is valid only for the specific case of non absorbing and optically thick media. Furthermore, we have shown that the use of the correct internal reflectance value significantly reduces the error of the prediction of reflectance and transmittance below 1.0% with the Kubelka-Munk or 4-flux model for translucent media as biological tissues in the optical window. Further work should first characterize the reduction in prediction error with the diffusion approximation and then extend the study to fluorophore quantification. A final step will connect the two approaches presented in this manuscript by allowing quantification of both forms of PpIX in a relative and absolute manner.

The experimental part presents the system that we designed during the PhD. It allows to perform fluorescence measurements at two excitation wavelengths as well as diffuse reflectance measurements. A calibration of the system is however necessary to be able to extract the optical properties of the studied medium by post-processing the diffuse reflectance measurements. The calibration process is described in detail in the chapter "Calibration". Due to the COVID-19 crisis, it has not yet been possible to perform measurements in the operating room. A future work will therefore be to acquire a set of *ex vivo* measurements with annotation of the gold standard.

# Appendix



# Appendix A

---

## Résumé en français

---

### A.1 Introduction

Le cancer tue 13% de la population mondiale et ce pourcentage est en constante augmentation [[WHO \(2022\)](#)]. Les tumeurs cérébrales ne représentent qu'une faible proportion des cancers (1% en France) mais un tiers d'entre elles sont malignes. Les gliomes représentent la moitié de la totalité des tumeurs cérébrales et constituent un problème de santé publique majeur, avec 308 102 nouveaux cas en 2020 selon [[Sung et al. \(2021\)](#)]. Ce sont des tumeurs infiltrantes, ce qui les rend difficiles à traiter. La majorité des gliomes sont des glioblastomes (GBM), une tumeur pour laquelle l'espérance de vie des patients ne dépasse guère un an [[Yu et al. \(2022\)](#)]. Outre la nature maligne de certains gliomes, leur présence peut entraîner divers symptômes tels que des maux de tête, des nausées, mais aussi des convulsions, des changements de personnalité, une faiblesse musculaire, voire une hémi-paralysie ou une paralysie complète du patient. Dans la mesure du possible, les patients atteints de gliome subissent une intervention chirurgicale visant à retirer le plus grand nombre possible de cellules tumorales afin de réduire les effets secondaires de la tumeur et d'empêcher sa progression. Cependant, dans plus de 85 % des cas de glioblastome, les patients opérés présentent une récidive à l'emplacement de la cavité de l'opération précédente [[Petrecca et al. \(2013\)](#)]. Ce risque élevé de récidive s'explique par la nature infiltrante des gliomes et la difficulté à séparer les infiltrats tumoraux des tissus sains en temps réel lors de l'opération. De plus, ces tumeurs apparaissent dans le tissu glial, qui est le tissu de soutien des neurones. Les gliomes peuvent donc être situés à côté ou même dans une zone fonctionnelle du cerveau, ce qui complique l'exérèse en raison des déficits postopératoires sévères que la résection de ces zones peut entraîner.

Ainsi, en présence d'un gliome, le neurochirurgien est confronté à un double défi: d'une part, il doit identifier les infiltrations tumorales afin d'enlever un maximum de tumeur et ainsi augmenter l'espérance de vie, et d'autre part, il doit identifier la fonctionnalité cérébrale afin de limiter les dommages postopératoires et ainsi préserver la qualité de vie du patient. Cette double identification doit se faire en temps réel, une fois le cerveau exposé, car les techniques d'imagerie préopératoire non invasive ne permettent pas de

détecter fidèlement les infiltration et ne fournissent pas de cartes suffisamment fidèles à ce que le chirurgien observe pendant l'opération. En effet, l'ouverture du crâne implique une modification de la pression et un affaissement du cerveau, un phénomène appelé "brain shift", qui génère un décalage de position pouvant aller jusqu'à 3 cm entre la disposition du tissu cérébral sur l'image pré-craniectomique et celle dans le champ opératoire [Nabavi *et al.* (2009)].

Différentes techniques peropératoires existent déjà pour guider le neurochirurgien lors de la chirurgie et ont permis d'augmenter l'espérance de vie moyenne des patients de quelques mois tout en améliorant leur qualité de vie. Cependant, ces techniques présentent un certain nombre de limites qu'il s'agit aujourd'hui de dépasser. L'émergence des techniques optiques présente un grand potentiel car elles sont non invasives, non ionisantes, compatibles avec une analyse en temps réel, et économiques [Valdés *et al.* (2016)]. Afin d'identifier l'infiltration tumorale en temps réel, l'exploitation des propriétés de fluorescence des tissus a notamment fait ses preuves ces 20 dernières années et la microscopie de fluorescence de la protoporphyrine IX (PpIX) est désormais utilisée en routine clinique [Stummer *et al.* (2000)]. De nombreux travaux continuent d'exploiter ce potentiel pour tenter d'identifier les marges tumorales. C'est dans ce contexte que s'inscrit l'objectif principal de cette thèse. En effet, la microscopie à fluorescence seule ne permet pas une délimitation correcte du gliome, notamment parce qu'il s'agit d'une tumeur infiltrante. Ainsi, la méthode et les outils permettant au neurochirurgien de réaliser une résection complète du gliome tout en se restreignant au strict périmètre tumoral afin de ne pas affecter de tissus sains potentiellement fonctionnels restent un problème ouvert.

Une multitude de possibilités sont explorées par la communauté scientifique pour résoudre cette question, notamment la spectroscopie de fluorescence. Cette dernière utilise l'information spectrale de biomarqueurs optiques fluorescents, également appelés fluorophores, et elle a démontré un réel intérêt pour l'extension de la résection des gliomes [Stummer *et al.* (1998), Sanai *et al.* (2011)b, Lacroix and Toms (2014), Corns *et al.* (2015)]. Depuis, une véritable émulation scientifique est apparue afin de lever ce verrou qui stimule la communauté de l'optique biomédicale : améliorer la sensibilité de la chirurgie guidée par la fluorescence (FGS) pour permettre une résection complète. Cela implique de pouvoir distinguer directement les tissus sains des tissus infiltrés environnants qui se ressemblent souvent. Deux des principales approches de la communauté scientifique sont la quantification de biomarqueurs [Valdés *et al.* (2011), Saager *et al.* (2011), Valdés *et al.* (2012), Valdés *et al.* (2014), Valdés *et al.* (2015), Valdés *et al.* (2016), Sibai *et al.* (2017), Angelo *et al.* (2019)] et l'analyse de la forme spectrale de la fluorescence émise [Haidar *et al.* (2015), Montcel *et al.* (2013)b, Montcel *et al.* (2013)a, Alston *et al.* (2018), Alston *et al.* (2019), Black *et al.* (2021)]. Chaque approche nécessite une sonde d'acquisition spécifique ainsi que des modèles spécifiques, pour quantifier correctement les fluorophores, ou alors pour estimer les concentrations relatives des fluorophores par recherche de leur forme spectrale propre dans le spectre acquis.

Le travail rapporté dans ce manuscrit de thèse s'inscrit dans la continuité cette démarche, en suivant les deux approches distinctes décrites ci-dessus. La première approche tente de mieux estimer les concentrations relatives des fluorophores utiles à la délimitation de la zone d'infiltration tumorale par une analyse des spectres de fluorescence. L'autre, plus exploratoire, vise à modéliser la propagation de la lumière dans les tissus, de la source au détecteur, afin d'obtenir des méthodes robustes de quantification des fluorophores.

Ce manuscrit de thèse est structuré de manière à rappeler tout d'abord les problèmes scientifiques et cliniques généraux de l'imagerie peropératoire en neurochirurgie pour la résection totale de gliomes (Chapitre 2). Puis, il présente les principales contributions de

cette thèse dans ce domaine à travers des modèles originaux d'estimation des concentrations relatives des fluorophores par analyse multispectrale de la fluorescence (Partie II), et des avancées sur les méthodes quantitatives (Partie III) notamment à travers la mise en œuvre d'un modèle de transfert radiatif où la réflectance interne de l'interface tissu-air est analysée de manière plus rigoureuse que dans de nombreuses études précédentes. La partie IV est consacrée à la description du dispositif expérimental conçu afin de pouvoir effectuer des mesures combinant des méthodes quantitatives et semi-quantitatives. Les perspectives de recherche envisagées pour les prochaines années et notre contribution au projet européen Scan'n'treat sont décrites dans la partie V, avant de proposer une conclusion plus générale. Enfin, les communications scientifiques sont rapportées dans l'annexe B.

## A.2 Méthode d'estimation des concentrations relatives de PpIX par analyse spectrale sous excitation multispectrale sans *a priori* sur les autres composantes

Dans cette section, nous proposons une méthode pour estimer les biomarqueurs liés à la fluorescence de la PpIX. Comme mentionné dans l'introduction de ce manuscrit, les approches existantes pour l'estimation des concentrations relatives de PpIX sont limitées par des erreurs, appelées *interférences*, dues à l'omission ou à la prise en compte de la mauvaise forme spectrale de certains fluorophores endogènes présents dans le signal de fluorescence mesuré. Elles se produisent lorsque le spectre des fluorophores endogènes omis est spectralement proche de celui d'émission de PpIX. Cela conduit à une surestimation de la quantité de PpIX et donc à une classification erronée des tissus sains dans une catégorie tumorale. Ainsi, ces interférences nuisent largement à la spécificité de la classification des tissus en fonction de leur statut pathologique.

Le problème vient du fait que les produits endogènes capables d'émettre un signal de fluorescence sont nombreux et varient fortement d'un individu à l'autre. Habituellement, la forme spectrale de leur signal de fluorescence est modélisée approximativement avec de fortes hypothèses *a priori*. Pour la suite, les fluorophores d'intérêt sont les deux formes différentes de PpIX décrites dans [Montcel *et al.* (2013)b]. En plus de l'émission de fluorescence bien connue de la PpIX apparaissant avec un maximum à 634 nm sous excitation à 405 nm, une autre bande de fluorescence peut être observée avec un maximum à 620 nm dans des conditions spécifiques. Ces deux bandes, appelées ci-après PpIX620 et PpIX634, peuvent être interprétées comme des bandes correspondant à deux formes différentes de PpIX, toutes deux présentant un intérêt particulier. Ici, nous proposons une méthode qui ne nécessite aucun *a priori* sur ces produits endogènes présents et leur forme spectrale respective. Pour cela, plusieurs longueurs d'onde d'excitation de fluorescence sont nécessaires pour ajouter des *a priori* dans le rendement quantique de fluorescence de PpIX620 et PpIX634 et pour estimer la partie du signal liée aux fluorophores endogènes. La *ligne de base* est donc définie comme la fluorescence non induite par le 5-ALA, c'est-à-dire la fluorescence qui serait émise dans le même tissu sans administration préalable de 5-ALA au patient.

La nouvelle méthode fait néanmoins l'hypothèse que la forme spectrale de la ligne de base est inchangée entre les signaux de différentes longueurs d'onde d'excitation. Cette hypothèse semble logique car nous nous intéressons uniquement aux fluorophores dont l'émission est spectralement proche de celle de la PpIX.

Dans le chapitre 3, nous décrivons le modèle permettant d'estimer les concentrations relatives de PpIX620 et PpIX634, appelées ci-après *contributions de PpIX*, dans le signal de fluorescence. Ce modèle est basé sur l'analyse des spectres d'émission de fluorescence obtenus sous de multiples longueurs d'onde d'excitation. Ainsi, la méthode que nous proposons utilise plusieurs longueurs d'onde d'excitation pour estimer les contributions des biomarqueurs liés à la fluorescence de la PpIX, ce qui rend notre méthode libre de tout *a priori* sur le spectre d'émission de fluorescence de la ligne de base. L'obtention des expressions analytiques pour l'estimateur des moindres carrés du modèle proposé permet à notre méthode d'être efficace sur le plan informatique et de ne pas utiliser de procédure d'estimation non linéaire itérative.

Dans le chapitre 4, nous considérons le cas pratique de l'estimation des contributions de la PpIX dans un signal de fluorescence adapté à partir de données cliniques réelles. Les paramètres du chapitre avec l'indice 1 indiquent les quantités liées à PpIX620 et les paramètres avec l'indice 2 indiquent les quantités liées à PpIX634. Tout d'abord, l'accent est mis sur le fantôme de fluorescence numérique avant d'examiner les différents ensembles de paramètres de ligne de base utilisés et la méthode de classification bayésienne. Ensuite, on s'intéressera aux erreurs d'estimation des paramètres avant de terminer par leur impact sur la classification du tissu simulé.

Nous comparons aussi notre méthode avec des modèles d'excitation multiple extrapolés à partir de ceux de la littérature. Nous définissons un fantôme numérique calibré sur des données réelles de gliomes de haut grade (HGG) et de gliomes de bas grade (LGG) pour obtenir un environnement de simulation réaliste. Nous tenons à souligner que les cinq catégories données dans [Alston *et al.* (2019)] ne peuvent pas apparaître simultanément dans le même échantillon. Nous distinguons maintenant les LGG avec deux statuts pathologiques, LGG et Sain, des HGG avec quatre statuts pathologiques : Partie solide, Marges denses, Marges de densité éparses, et Sain.

Tout d'abord, nous étudions l'erreur d'estimation des paramètres d'intérêt pour tous les ensembles de paramètres de la ligne de base. Ensuite, nous étudions les conséquences de l'erreur d'estimation des paramètres d'intérêt sur l'objectif final de classification. Une attention particulière est mise sur la spécificité qui fait défaut dans les méthodes d'estimation existantes. La performance du modèle EB est estimée pour différentes conditions de fluorophores de base dont le spectre d'émission recouvre celui de PpIX. Les mesures de performance que nous considérons sont l'erreur d'estimation des contributions de PpIX et la précision, la sensibilité et la spécificité de la classification dans le statut pathologique. Enfin, la performance du diagnostic clinique est évaluée à l'aide d'images de gliome synthétisées par un fantôme numérique calibré expérimentalement.

Les résultats montrent que notre méthode (EB<sub>2</sub>) permet de mieux estimer l'état pathologique du tissu mesuré lorsque l'amplitude de la ligne de base augmente : elle conserve une spécificité presque égale à celle de la vérité terrain lorsque celle des modèles existants tombe à 0. En outre, notre modèle est aussi précis que les modèles existants dans les cas défavorables, appelés points chauds, par exemple lorsque le rendement quantique de la ligne de base est proche de celui de PpIX. Notre modèle révèle le potentiel d'utilisation de plusieurs longueurs d'onde d'excitation pour augmenter la sensibilité de classification des mesures de fluorescence. Des travaux futurs pourraient porter sur la gestion des points chauds, l'extension de cette étude à plus de deux longueurs d'onde d'excitation et la comparaison de EB<sub>2</sub> avec les méthodes de pointe sur des données cliniques acquises par [Alston (2017)].

### A.3 Avancées dans les méthodes quantitatives

Cette seconde partie vise à aller un peu plus loin que la simple identification de fluorophores en essayant de quantifier la concentration de chacune de ces substances. Les méthodes à utiliser ne sont plus les mêmes : si, pour déterminer la proportion respective de chacune, une analyse de la forme des spectres mesurés est suffisante, dans cette autre approche il est nécessaire d'exploiter le signal de manière absolue, c'est-à-dire en considérant les effets du milieu de propagation sur le signal en plus de son amplitude et de sa forme spectrale. Il faut donc être capable d'estimer les effets du milieu pour ensuite déterminer la quantité de fluorophores ayant généré le signal. En bref, il faut pouvoir modéliser rigoureusement les trajectoires de la lumière tout au long du processus de propagation, de la source lumineuse au capteur optique.

Comme évoqué au chapitre 2, certains modèles optiques tels que le modèle de Kubelka-Munk ou celui de l'approximation de diffusion (aussi appelée approximation P1) sont le résultat d'hypothèses simplificatrices dans la résolution de l'équation de transfert radiatif (ETR). Les hypothèses associées à ces modèles permettent de fixer la valeur de certains de leurs paramètres.

Pour cela, le chapitre 5 décrit dans un premier temps comment l'équation de transfert radiatif (ETR) est établie de manière générale. En effet, la théorie du transport de la diffusion de la lumière (également appelée formalisme du transfert radiatif) est une méthode puissante pour modéliser la diffusion de la lumière à travers un milieu turbide. L'approche par transfert radiatif a été largement étudiée depuis les années 50, suite aux travaux pionniers de Chandrasekhar (Prix Nobel en 1983 pour ses études théoriques des processus physiques importants pour la structure et l'évolution des étoiles). Elle prend en compte l'absorption et la diffusion multiple (éventuellement anisotrope), mais néglige tout type d'effet ondulatoire (diffraction et effets d'interférence) à l'exception de la polarisation. L'intensité spécifique (dans le vocabulaire de la théorie du transfert radiatif) ou la luminance spectrale (dans le vocabulaire de la radiométrie) peut être calculée avec cette approche, [ce qui permet d'étudier en détail les effets angulairement dépendants](#). Elle a de nombreuses applications dans le domaine de l'optique tissulaire, de la biologie marine, de l'optique du papier, de la réalité virtuelle (modélisation BRDF) et de la propagation de l'énergie radiante dans l'atmosphère des planètes, des étoiles et des galaxies. Ce chapitre est largement inspiré du livre [[Ishimaru \(1978\)](#)]. Les détails concernant les conditions aux limites ont été plus clairement spécifiés dans ce chapitre, en particulier la réflexion de Fresnel aux interfaces entre milieux d'indices optiques différents qui est négligée dans les milieux diffusants comme les gaz ou l'atmosphère, mais qui est cruciale dans les matériaux diffusants comme les tissus biologiques. Enfin, le cas de la fluorescence est également décrit mathématiquement.

Le chapitre 6 a pour but d'expliquer comment nous avons validé l'implémentation de notre solveur d'équation de transfert radiatif, basé sur la méthode des ordonnées discrètes expliquée dans le chapitre 5. Pour cela, nous avons décidé de comparer nos résultats avec ceux issus de simulations de Monte-Carlo dans différentes configurations. Ainsi, après avoir expliqué comment une configuration de simulation est construite, nous décrivons les résultats de la validation dans différentes configurations, y compris des configurations comparables à celles trouvées dans la littérature [[Giovanelli \(1955\)](#), [Van de Hulst \(1980\)](#), [Prahl et al. \(1989\)](#), [Leh \(2011\)](#)].

La validité de la simulation dans une configuration donnée est définie par deux mesures

différentes : la convergence relative de la solution de notre solveur ETR et l'erreur relative entre la réflectance diffuse de Monte-Carlo et celle du solveur analytique. La convergence relative est définie comme suit :

$$\forall n \in \{2k \leq N_n, k \in \mathbb{N}^*\}, CV(n) = \sqrt{\sum_i^N \frac{(U_n(z_i) - U_{n-2}(z_i))^2}{N}} \quad (\text{A.1})$$

où  $n$  est l'ordre du polynôme de Legendre,  $U_n$  l'éclairement énergétique moyen à un  $n$  donné,  $N$  la dernière profondeur pour laquelle l'éclairement énergétique moyen est calculé, et  $N_n$  l'ordre maximal du polynôme de Legendre. On rappelle que l'ordre du polynôme de Legendre est directement lié au nombre de points de discréétisation angulaire.

Cette validation par comparaison avec des simulations de Monte-Carlo a mis en évidence tout d'abord que l'anisotropie a un effet sur la convergence relative : pour des valeurs élevées du facteur d'anisotropie, la convergence relative est plus lente qu'avec un facteur d'anisotropie fixé à 0. Ensuite, il a été montré que la réflectance angulaire de Fresnel a un impact important sur la convergence relative, en particulier dans les milieux dont l'indice optique est supérieur à celui du milieu environnant (effet en dents de scie sur la courbe de convergence relative). De plus, nous soulignons que la précision de la convergence relative a un faible impact sur la valeur de la réflectance diffuse.

La validation du cas de la fluorescence doit aussi être réalisée, mais le simulateur de Monte-Carlo que nous avons utilisé pour les validations précédentes ne prend pas en compte les matières fluorescentes. Malgré une littérature abondante sur les modèles optiques de fluorescence, trop peu d'articles fournissent des données tabulées utiles pour valider l'implémentation de notre solveur ETR. Nous nous appuyons donc sur le chapitre I-2 de [Mycek and Pogue (2003)], qui est à notre connaissance le seul élément de la littérature fournissant des données cohérentes avec notre géométrie et nos hypothèses. Cependant, le seul moyen de validation en notre possession est de comparer la Fig. 6.9a du chapitre I-2 de [Mycek and Pogue (2003)] avec la Fig. 6.9b réalisée par nos soins. Nous comparons donc l'exitance de notre solveur ETR en fonction de la profondeur avec celle des modèles de diffusion présentés dans le manuel. Il est important de souligner que le manuel fournit la description de deux modèles de diffusion distincts. Le premier considère que le flux d'excitation est décrit par une loi de Beer-Lambert (milieux non diffusant ou diffusant et fortement absorbant). Le second considère que la diffusion est importante (milieux plus diffusant qu'absorbant), le flux d'excitation est donc une solution de l'équation de diffusion.

Dans la suite du chapitre, nous nous proposons d'étudier l'impact de la méthode de discréétisation sur la convergence relative. Comme nous l'avons remarqué précédemment, la discréétisation de la réflectance angulaire de Fresnel a un impact sur la vitesse de convergence de la méthode des ordonnées discrètes utilisant les racines des polynomes de Legendre. Nous souhaitons ici comparer la convergence relative de la méthode de discréétisation utilisant les racines des polynomes de Legendre avec la méthode de discréétisation utilisant un pas régulier. Nous considérons uniquement un milieu semi-infini. Les paramètres pour l'indice optique et le facteur d'anisotropie sont les mêmes que ceux donnés dans les tableaux 6.2 à 6.5. Les résultats de cette étude comparative sont résumés dans le tableau 6.10 qui suggère un nombre correct de pas de discréétisation pour les différentes configurations étudiées. Nous concluons que la discréétisation de Legendre est très efficace selon le critère de convergence relative pour un milieu de diffusion isotrope ou anisotrope sans interface, i.e. lorsque l'indice optique du milieu d'étude est égal à celui du milieu environ-

nant. En particulier, nous avons vu que l'anisotropie de diffusion augmente la vitesse de convergence relative car la discréétisation de Legendre n'est pas régulière sur l'intervalle, ce qui est finalement un grand avantage. Néanmoins, la discréétisation de la réflectance angulaire de Fresnel est si compliquée que la méthode de discréétisation à pas constant semble être plus efficace que celle de Legendre lorsque le milieu environnant n'a pas le même indice optique que le milieu étudié. Malgré cela, nous conserverons la méthode de discréétisation de Legendre pour les autres chapitres de la partie, en considérant volontairement un ordre élevé pour éviter les erreurs dues à une discréétisation angulaire trop grossière de la réflectance angulaire de Fresnel : par exemple 160 points de discréétisation pour un milieu d'indice optique 1,5 entouré d'air dont l'indice optique est 1.

Le chapitre 7 se concentre sur l'étude de la réflectance interne uniquement et son application directe sur un cas lié au sujet de cette thèse. En effet, pour la quantification de la fluorescence comme dans de nombreux domaines de l'ingénierie tels que l'infographie, les restaurations dentaires ou les technologies d'impression 3D, il est nécessaire de caractériser les propriétés optiques des matériaux diffusants afin de prédire avec précision l'apparence des produits qui les composent. Dans le cas des matériaux très diffusants, des modèles de transfert de flux comme le modèle de Kubelka-Munk (2-flux) ou le modèle à 4 flux sont utilisés avec succès depuis des décennies à cette fin [Duveiller *et al.* (2020), Séroul *et al.* (2016), Van Song *et al.* (2016), Yoshimura *et al.* (2013), Yang *et al.* (2002), Durkin *et al.* (1994), Johnston *et al.* (1986)a]. Cependant, ils présentent des limites bien connues lorsque le matériau est faiblement diffusant ou que l'épaisseur optique est faible, ce qui donne à l'objet étudié un aspect très translucide. Ces limitations ont été discutées dans divers articles [Duveiller *et al.* (2020), Happel *et al.* (2014), Thennadil (2008), Fleming *et al.* (2004)]. Une source d'imprécision est le fait que ces modèles supposent que les flux sont lambertiens (luminance angulairement uniforme) à toute profondeur dans le matériau. La réflectance interne des interfaces est calculée sur la base de cette hypothèse. Mais lorsque la couche est faiblement diffusante, les flux ne sont plus lambertiens, et leur distribution angulaire varie en fonction de la profondeur dans le matériau. La réflectance interne des interfaces doit donc être calculée en fonction de la distribution angulaire précise de la lumière qui tombe sur elles. C'est précisément ce que nous voulons étudier dans ce chapitre. Des simulations détaillées basées sur la résolution numérique de l'équation de transfert radiatif ont été utilisées pour calculer la réflectance diffuse interne, un paramètre nécessaire dans les modèles 2-flux ou 4-flux utilisés pour l'extraction des paramètres optiques et la prédition de l'apparence. Dans ce travail, la diffusion isotrope et anisotrope a été considérée, même si nous avons constaté que l'anisotropie n'a pas d'impact significatif sur les conclusions générales.

Pour de grandes épaisseurs optiques, les réflectances diffusées internes aux deux interfaces ont été trouvées en accord avec l'approximation lambertienne lorsque l'absorption est négligeable. En présence d'absorption cependant, ces réflectances internes diffèrent légèrement, celle de l'interface du haut étant un peu plus élevée, et celle de l'interface du bas un peu plus basse que la valeur lambertienne. Pour les épaisseurs optiques intermédiaires et faibles (matériau translucide), il s'avère que les deux réflectances internes tendent à être approximativement égales, et dépassent la valeur pour une distribution lambertienne. A l'inverse, les réflectances internes globales (incluant à la fois la lumière directionnelle et la lumière diffuse), requises pour les modèles à 2 flux, tendent vers des valeurs directionnelles aux faibles distances optiques. Ces résultats sont la conséquence de la compétition entre la diffusion, qui tend à distribuer la lumière uniformément, et la réflexion directionnelle (formules de Fresnel), qui induit une anisotropie dans la distribution angulaire de la luminance (les rayons à faible angle d'incidence peuvent s'échapper du milieu alors que les

rayons à fort angle d'incidence restent piégés par la réflexion interne globale).

Enfin, l'impact des réflectances internes sur l'extraction réalisée à l'aide des modèles à 2 et 4 flux a été étudié, en utilisant les simulations ETR comme référence. Il s'avère que l'approximation couramment utilisée, c'est-à-dire le maintien constant de la réflexion interne égale à sa valeur lambertienne, peut conduire à des erreurs importantes (jusqu'à 100 %) pour les modèles à 2 flux lorsqu'il s'agit de matériaux translucides. De plus, l'extraction des paramètres avec les modèles à 2 et 4 flux peut être améliorée de manière significative en utilisant le coefficient interne calculé à l'aide de l'équation de transfert radiatif, en particulier dans les matériaux translucides avec un milieu de diffusion fortement anisotrope.

Ces résultats ouvrent la voie à une meilleure prédition de la réflectance et de la transmittance spectrale, et donc à l'estimation des propriétés optiques des matériaux translucides mais aussi fortement diffusants. Les propriétés optiques étant un élément clé des méthodes de quantification, nous suggérons comme travail futur d'étudier les implications des résultats de cette étude sur la quantification des fluorophores par des modèles optiques simples.

## A.4 Système expérimental

Les systèmes expérimentaux de l'état de l'art peuvent être séparés en deux grandes catégories. La majeure partie concerne ceux qui estiment à la fois les propriétés optiques et la fluorescence à une seule longueur d'onde d'excitation. Le reste concerne ceux qui mesurent la fluorescence à plusieurs longueurs d'onde d'excitation. A notre connaissance, il n'existe actuellement pas de système expérimental permettant de combiner plusieurs longueurs d'onde d'excitation de la fluorescence et permettant d'estimer les propriétés optiques d'un tissu biologique. Il est donc apparu nécessaire de construire un nouveau système expérimental qui est décrit dans cette partie.

La partie I avait souligné le potentiel de la spectroscopie de fluorescence PpIX pour identifier l'infiltration tumorale des gliomes, notamment par la présence de deux formes de PpIX ayant des propriétés de fluorescence différentes. Dans le chapitre 8, nous présentons le développement et la caractérisation d'un système de spectroscopie de fluorescence interventionnelle visant à la fois à identifier les deux formes de fluorescence de PpIX et à extraire les propriétés optiques de l'échantillon sondé par spectroscopie de réflectance diffuse (DRS). Ce système est équipé de deux lasers et d'une source de lumière blanche. La source de lumière blanche permet d'obtenir des mesures de DRS et les lasers excitent séquentiellement les tissus avec deux longueurs d'onde. La collection du spectre de fluorescence émis est réalisé par un spectromètre. L'ensemble des composants d'excitation et de collection sont connectés à une sonde optique fibrée. Nous commençons par présenter les différents composants utilisés et leurs caractéristiques avant de proposer la description du système complet.

Le système développé vise à mesurer les spectres de fluorescence et les spectres de réflectance diffuse de tissus cérébraux, dans le bloc opératoire de neurochirurgie. Ceci impose des spécifications strictes dans le choix des composants et leur assemblage. En effet, pour être utilisé au bloc opératoire, le dispositif développé doit être sûr, transportable et robuste (pas trop encombrant ni lourd), il doit être fermé et ses différents blocs doivent pouvoir être assemblés rapidement. De plus, afin d'exciter les deux formes PpIX d'intérêt, nous avons choisi une excitation multi-longueurs d'onde des tissus, avec des longueurs d'onde adaptées aux propriétés des deux formes de fluorescence recherchées. Nous avons

décidé d'utiliser des lasers plus sélectifs spectralement que la LED utilisée par [Alston (2017)]. Ceci distingue ce prototype de ceux existant dans la littérature, qui ont soit une seule source d'excitation de fluorescence en plus d'une source de lumière blanche, soit uniquement des systèmes d'excitation de fluorescence sans source de lumière blanche. La figure 8.1 décrit un schéma du système. On peut voir que le système peut être divisé en 3 blocs : l'interface homme-machine (également appelé logiciel ci-après), le système opto-électronique et enfin la sonde. Plus précisément, les trois blocs sont :

**Bloc 1:** L'ordinateur, l'unité centrale à partir de laquelle l'ensemble du système est contrôlé depuis une interface Qt-Python. Cette interface est présentée en détail dans le chapitre 10.

**Bloc 2:** Une boîte noire constituée de feuilles de PVC compact de différentes épaisseurs (3 mm et 10 mm) contenant tous les composants électriques et optiques. Le choix de l'épaisseur dépend du rôle de la plaque (fermeture, support...).

De cette boîte sortent un nombre minimal de connexions, 2 connexions USB à l'ordinateur (une pour la carte de contrôle Arduino, une autre pour le spectromètre), 1 prise électrique standard de 220 V pour l'alimentation des composants et 4 connexions optiques SMA à la sonde. La boîte mesure 49x46x18 cm<sup>3</sup>, pèse 14,3 kg et contient trois étages.

Tous les éléments sont fixés pour éviter qu'ils ne bougent pendant le transport et nous ajoutons des poignées sur la boîte, pour faciliter le transport. Les parois sont vissées les unes aux autres pour assurer l'étanchéité, mais le nombre de vis est limité afin de pouvoir retirer rapidement n'importe quelle paroi pour accéder aux composants du système si nécessaire.

**Block 3:** La sonde mesure 1 mètre de long et est reliée au bloc 2 par quatre connexions SMA. Cet élément est décrit en détail dans la section 8.3 du chapitre 8.

Comme mentionné dans l'article [Kim *et al.* (2010)b], une calibration de la réflectance spectrale mesurée par rapport au modèle de la théorie de la diffusion est nécessaire. Pour retrouver correctement les propriétés optiques spectrales ( $\mu_a(\lambda)$  et  $\mu'_s(\lambda)$ ), certaines hypothèses doivent être faites, par exemple, la forme spectrale des composantes d'absorption et l'expression littérale de la diffusion spectrale, mais une étape de calibration du spectre de réflectance mesuré par rapport au modèle de la théorie de la diffusion est également nécessaire. Le chapitre 9 a pour but de décrire la théorie et la réalisation de l'étape de calibration sur notre installation expérimentale avec des fantômes optiques.

Enfin, dans le chapitre 10, nous nous concentrerons sur la partie logicielle nécessaire pour pouvoir acquérir correctement les mesures. En effet, le système expérimental est utilisé dans un environnement lumineux. Ainsi, pour obtenir le spectre de fluorescence, il est nécessaire d'acquérir deux mesures, une première lorsque la source lumineuse du système est éteinte ("fond lumineux") et une seconde, lorsque la source lumineuse du système est allumée. Cela permet de soustraire le signal du fond lumineux de la pièce à la mesure effectuée avec la lampe allumée.

En plus d'être facile à utiliser, la tâche principale du logiciel est d'assurer la synchronisation obligatoire entre l'acquisition des mesures par le spectromètre et l'excitation du laser pour pouvoir effectuer correctement les mesures de fluorescence. L'utilisateur du logiciel définit les paramètres d'acquisition en deux étapes, puis sélectionne le lieu d'enregistrement des données avant de lancer l'acquisition. Une fois l'acquisition terminée, on peut ajuster

certains paramètres avant de commencer une nouvelle acquisition. Dans ce chapitre, une première section décrit l'interface utilisateur graphique, puis une seconde section présente l'ingénierie logicielle déployée pour réaliser ce logiciel d'acquisition. Le logiciel open source a été entièrement développé en Python et peut être partagé sur demande.

## A.5 Perspectives

Dans cette section, nous présentons les perspectives des travaux détaillés dans les chapitres précédents et les résultats des recherches menées en parallèle. Tout d'abord, la suite directe du doctorat est brièvement décrite. Ensuite, une extension des travaux sur les gliomes à une autre pathologie neuronale est proposée. Enfin, nous détaillons notre contribution au projet européen Scan'n'Treat qui ont été réalisés en marge du thème principal de cette thèse.

### A.5.1 Poursuite directe

Les contributions des parties II et III sont présentées comme indépendantes dans ce manuscrit. Elles seront combinables après l'achèvement des étapes décrites ci-dessous.

Du côté des modèles optiques, partie III, il est d'abord important d'étendre la caractérisation de la réduction de l'erreur de prédiction déjà réalisée sur les modèles à 2 et 4 flux à l'approximation de diffusion. Dans un second temps, il sera nécessaire d'étudier l'impact de cette réduction de l'erreur de prédiction sur la quantification d'un fluorophore.

Du côté de la méthode d'estimation de l'excitation multispectrale, partie II, il est nécessaire de proposer une solution au problème des points chauds afin de rendre notre méthode plus robuste.

Enfin, les deux approches peuvent être combinées pour quantifier les deux formes de PpIX de manière relative et absolue sous excitation multispectrale.

### A.5.2 Application à la dysplasie corticale focale

Les travaux réalisés sur le gliome peuvent en fait trouver une portée plus large dans le secteur de la neurochirurgie. Suite à des discussions avec le Dr. Joseph Toulouse, il semble que la dysplasie corticale focale en soit un bon exemple.

Les dysplasies corticales focales (DCF) sont des malformations cérébrales qui apparaissent pendant le développement du cerveau. Elles sont caractérisées par des modifications morphologiques des cellules (grandes cellules appelées cellules cytomégaliques) et de leur organisation dans le cortex cérébral [[Guerrini and Dobyns \(2014\)](#)]. Ces dysplasies peuvent être associées à une épilepsie dite focale [[Bautista et al. \(2003\)](#)], c'est-à-dire n'affectant qu'une zone limitée du cerveau. Les épilepsies focales sont le type d'épilepsie le plus fréquent, touchant environ 2 patients épileptiques sur 3.

Les patients souffrant d'épilepsie focale sévère, résistante au traitement médicamenteux, peuvent subir une intervention chirurgicale visant à retirer le foyer épileptogène, c'est-à-dire la zone du cerveau responsable des crises. L'étude comparative [[Hamiwka et al. \(2005\)](#)] comprend une cohorte de 40 enfants opérés entre 1980 et 1992 et âgés de 6 mois à 18 ans au moment de leur chirurgie. Après un suivi de dix ans, 40 % étaient exempts de crises, 26 % présentaient une réduction importante des crises (taux de réduction supérieur à 90 %) et 34 % étaient inchangés. L'étude a noté qu'une résection complète était statistiquement significative pour un résultat favorable, et qu'aucun patient ayant subi une

résection incomplète n'était exempt de crises. Cependant, la réussite d'une résection neurochirurgicale dépend de la capacité à retirer le tissu dysplasique en endommageant le moins possible le tissu périlésionnel normal. La technique de fluorescence a été mise en œuvre à l'aide de sondes à fibres optiques et utilisée pour caractériser le tissu néoplasique : [Ramanujam (2000)].

Des études récentes [Kleen *et al.* (2011), Anand *et al.* (2017), Roberts *et al.* (2019)] ont tenté de déterminer si la fluorescence PpIX induite par l'ALA peut discriminer de manière cohérente les zones épileptogènes des tissus sains. Cependant, l'étude [Roberts *et al.* (2019)] rapporte peu de fluorescence visible sous excitation à 405 nm. L'étude [Kleen *et al.* (2011)] utilise une excitation de PpIX à 633 nm, tandis que l'étude [Anand *et al.* (2017)] suggère une excitation multispectrale de PpIX à 378 nm et 445 nm.

Ainsi, à notre connaissance, aucune étude ne cherche à séparer le tissu néoplasique du tissu sain en utilisant une méthode d'excitation multispectrale de la fluorescence à 380 nm et 405 nm. Cette étude pourrait directement découler du travail exposé dans ce mémoire.

## A.6 Contribution au projet européen Scan'n'Treat : Caractérisation de la réponse dose-effet de fluorescence des nanoparticules X-PDT

L'étude de la fluorescence réalisée sur le gliome peut être appliquée à un champ plus large dans le secteur de la cancérologie. Nous avons eu l'occasion de le constater en participant au projet européen Scan'n'Treat dont le thème est extérieur au thème principal de la thèse.

Alors que l'Europe ne représente que 9 % de la population mondiale, elle concentre 23 % de la quantité globale de cancers, qui constituent ainsi la deuxième cause de mortalité en Europe. De nombreuses stratégies de traitement existent : chirurgie, chimiothérapie, radiothérapie ou thérapie ciblée, mais les résultats ne sont pas toujours convaincants. Et si dans certains cas, la survie à cinq ans après traitement peut être encourageante, les conditions de vie des patients se dégradent en raison des effets secondaires des thérapies. Une augmentation significative de la survie à cinq ans des patients tout en ayant un impact positif important sur la qualité de vie du patient semble donc nécessaire. Pour y parvenir, une nouvelle technologie est nécessaire pour assurer un traitement efficace du cancer, même radiorésistant, avec de faibles effets secondaires, permettant un diagnostic précis et donnant accès à un suivi *in situ* du traitement. L'autre aspect innovant de cette technologie est le fait que tout se déroule en même temps, avec la même machine, ce qui sera beaucoup moins stressant et perturbant pour les patients par rapport aux autres traitements.

Scan'n'Treat est la première pierre de cette ambition, en combinant deux technologies de pointe : le Spectral Photon Counting Scanner (SPCCT), qui est une modalité d'imagerie révolutionnaire, et un nouveau traitement à base de rayons X appelé X-PDT (X-ray Activated Photodynamic Therapy). L'adéquation parfaite entre ces deux technologies sera assurée par des sondes spécialement conçues qui servent à la fois d'agents de contraste et d'agents thérapeutiques.

La première étape du projet Scan'n'Treat a été de réaliser des nanoparticules fluorescentes ainsi que d'ajouter des modifications de surface pour assurer leur biocompatibilité et l'évaluation *in vitro* de leur internalisation et de leur toxicité. Ainsi, nous avons utilisé différentes nanoparticules : des nanoparticules "nues" (LC174) à 1 mol.L<sup>-1</sup>, des nanoparticules fonctionnalisées au PEG (LC205) à 1 mol.L<sup>-1</sup>, des molécules de chlorure de Terbium à

1 mol.L<sup>-1</sup>, des nanoparticules fonctionnalisées au PAA (LC230), des nanoparticules fonctionnalisées au dioxyde de silice + PEG (LC237) et des molécules de Fluorure de Terbium.

Ensuite, l'équipe du projet a pris contact avec notre équipe du laboratoire CREATIS en raison de notre expertise concernant la fluorescence et des systèmes d'acquisition permettant une mesure quantifiable de la fluorescence. En effet, ils ont besoin de quantifier la fluorescence émise par les nouvelles nanoparticules fabriquées dans le cadre du projet. Cet élément est crucial pour étudier l'effet dose-réponse. En bref, les nanoparticules fluorescentes résultent d'une combinaison de gadolinium (Gd) et de terbium III (Tb). Fondamentalement, le gadolinium absorbe l'énergie donnée par les rayons X et la transmet au terbium III qui retourne à un état stable en émettant de la fluorescence. Dans les nanoparticules finales, on ajoute également du rosebengal à l'intérieur des nanoparticules, qui吸orbe les photons résultant de la fluorescence et génère des oxygènes singulet. D'un point de vue pratique, les nanoparticules sont stockées dans un eppendorf.

Pour mesurer la fluorescence, le système expérimental est composé d'une fibre optique FG550UEC de Thorlabs Inc. dont l'extrémité clivée est immergée dans la solution de nanoparticules et dont l'extrémité du connecteur SMA est connectée à un faisceau de fibres Round to Linear (PL200-2-VIS-NIR, Ocean Insight). Le faisceau maximise le signal lumineux entrant dans le spectromètre et est donc connecté au spectromètre MayaPro2000 d'Ocean Insight. Le spectromètre a été préalablement calibré afin de donner des mesures d'irradiance spectrale absolue.

De plus, comme le signal d'excitation de la fluorescence est émis par le SPCCT, nous avions besoin d'un signal de déclenchement indiquant si les rayons X sont activés ou non. Après avoir contacté Philips, il apparaît que les tentatives d'obtenir un signal direct à partir du portique se sont heurtées à des obstacles. Une alternative simple consistait à utiliser un détecteur de scintillation autonome, c'est-à-dire un détecteur de scintillation de base relié à une photodiode. Philips nous a fourni un détecteur autonome mesurant environ 1x1x20 mm, l'ensemble étant encapsulé dans de l'époxy pour le protéger.

Dans un premier temps, nous étudions l'évolution de la réponse en fonction de mAs et keV pour des nanoparticules "nues" (LC174) à 1 mol.L<sup>-1</sup>, des nanoparticules fonctionnalisées au PEG (LC205) à 1 mol.L<sup>-1</sup> ainsi que des molécules de chlorure de Terbium à 1 mol.L<sup>-1</sup>. Nous verrons ensuite l'évolution de la réponse en fonction de la concentration pour les nanoparticules LC174 et LC205, mais aussi pour les nanoparticules fonctionnalisées PAA (LC230), les nanoparticules fonctionnalisées dioxyde de silice + PEG (LC237) ainsi que les molécules de Fluorure de Terbium.

Selon la Figure 11.3, à un même niveau de concentration, la réponse augmente avec une augmentation de mAs pour les deux LC205 et LC174, ce qui est confirmé par la valeur positive de  $a$  pour chaque ligne du tableau 11.1. En outre, nous remarquons que le paramètre mAs n'a aucun effet sur les molécules de chlorure de terbium. Ceci est pertinent car l'effet fluorescent des nanoparticules résulte du transfert d'énergie entre le gadolinium et le terbium. Ainsi, il n'y a pas de fluorescence parce qu'il n'y a pas de gadolinium dans les molécules de chlorure de terbium.

Les résultats précédents étant donnés à une concentration fixe en nanoparticules et pour une seule méthode de fonctionnalisation, nous allons maintenant étudier la réponse fluorescente en fonction de la méthode de fonctionnalisation de la nanoparticule ainsi que de la concentration en nanoparticules. Pour cette étude, les paramètres des rayons X sont fixés à 300 mAs et 120 keV.

Selon la méthode de fonctionnalisation, l'augmentation de la réponse fluorescente est plus ou moins importante avec la concentration. Ainsi, la fonctionnalisation avec le PAA offre la

meilleure réponse fluorescente parmi toutes les méthodes de fonctionnalisation proposées. La fonctionnalisation par le PEG donne une réponse presque identique à celle du PAA. Seule la fonctionnalisation SiO<sub>2</sub>+PEG donne une réponse fluorescente plus faible que les autres méthodes de fonctionnalisation. L'effet de concentration observé sur la figure 11.5 est également confirmé par la figure 11.6, dont l'analyse ne peut être que qualitative, mais on peut noter une diminution de la réponse fluorescente lorsque les nanoparticules sont deux fois moins concentrées.

Les premiers résultats du projet Scan'n'Treat montrent que l'effet dose-réponse est non linéaire en fonction de la concentration et du keV, mais linéaire en fonction du mAs. Cependant, dans les nanoparticules finales, du rosebengal est également ajouté. Il va absorber les photons issus de la fluorescence et générer des oxygènes singlets. Certaines méthodes existent aujourd'hui pour quantifier le nombre d'oxygènes singlets par fluorescence [Ahmad *et al.* (2019)], il semble donc pertinent d'utiliser cette méthode pour quantifier l'effet dose-réponse final de la nanoparticule destinée à être utilisée en X-PDT.

## A.7 Conclusion

Le travail présenté dans ce manuscrit s'inscrit dans le contexte clinique de la résection des gliomes. Les gliomes étant des tumeurs infiltrantes du système nerveux central, le problème clinique est de retirer un maximum d'infiltrations tumorales.

L'objectif de ce travail de thèse était d'améliorer la distinction entre la marge tumorale et le tissu sain. Ainsi, deux investigations complémentaires ont eu lieu : l'une concernant les approches dites semi-quantitatives, l'autre sur les approches quantitatives.

Pour l'approche semi-quantitative, nous sommes partis de travaux antérieurs qui ont montré l'intérêt de la fluorescence PpIX pour visualiser les infiltrations tumorales et la variabilité de son spectre d'émission en fonction de son microenvironnement. Cette variabilité du spectre d'émission de PpIX avec son microenvironnement a permis de démontrer la présence de deux états de PpIX dans les tissus tumoraux, là où les techniques actuelles ne recherchaient qu'un seul état. Les états proposés sont des configurations où la PpIX émet des spectres de fluorescence différents, présentant un maximum soit autour de 622 nm (état 620), soit autour de 634 nm (état 634). Ces deux états, dont les propriétés ont été étudiées à un stade antérieur, sont encore sous-estimés par les modèles de la littérature dans certains cas, en raison des interférences avec d'autres fluorophores endogènes présents dans les signaux de fluorescence acquis. Ainsi, dans la section II, nous proposons une nouvelle méthode pour estimer les deux formes de PpIX sans aucun *a priori* sur les composantes du signal autres que PpIX. Pour cela, cette nouvelle méthode s'appuie sur plusieurs longueurs d'onde d'excitation de fluorescence et la connaissance *a priori* du rendement quantique de chacune des formes de PpIX. Cette nouvelle méthode a été comparée à l'état de l'art sur un ensemble de cas, dont des images cliniques synthétiques de gliome. Elle s'est révélée équivalente aux méthodes de l'état de l'art dans les cas déjà résolus, mais significativement meilleure que les méthodes existantes en présence d'interférences.

Pour l'approche quantitative, tous les outils pour résoudre l'équation de transfert radiatif ont été présentés dans l'introduction. Néanmoins, le modèle d'approximation de la diffusion est largement utilisé dans la bibliographie de la quantification de PpIX. Après avoir décrit la méthode des ordonnées discrètes utilisée pour résoudre l'équation de transfert radiatif, nous nous concentrerons sur la validation de sa mise en œuvre. Celle-ci a mis en évidence l'effet sur la convergence de la réflectance angulaire de Fresnel. En étudiant précisément la valeur de la réflectance interne et sa dépendance à plusieurs paramètres pertinents tels que l'albédo, l'épaisseur optique, le facteur d'anisotropie ou l'indice optique

relatif, nous avons démontré que la valeur couramment utilisée n'est valable que pour un cas spécifique. De plus, nous avons montré que l'utilisation de la valeur correcte de la réflectance interne améliore significativement la précision de la prédiction.

## Appendix B

---

### Publications and communications

---

#### International peer-reviewed journals

A. Gautheron, R. Clerc, V. Duveiller, L. Simonot, B. Montcel, M. Hébert "On the validity of two-flux and four-flux models for light scattering in translucent layers: angular distribution of internally reflected light at the interfaces", Optic Express (submitted)

A. Gautheron, M. Sdika, M. Hébert , B. Montcel "An explicit Estimated Baseline Model for Robust Estimation of Fluorophores using Multiple-Wavelength Excitation Fluorescence Spectroscopy ", IEEE Transactions on Biomedical Engineering (submitted)

#### International peer-reviewed conferences and publication of proceedings

V. Duveiller, E. Kim, M. Locquet, A. Gautheron, R. Clerc, J.P. Salomon, M. Hébert *Two-flux transfer model predicting the reflectance factor of translucent layered dental resin composites*, Colour and Visual Computing Symposium, Gjøvik, Norway, 2022. **Oral Presentation**

A. Gautheron, M. Sdika, M. Hébert , B. Montcel "Robust Estimation of 5-ALA Induced PpIX Multiple-Wavelength Excitation Fluorescence Spectroscopy for Improving Glioma Classification", SPIE Photonics Europe, Strasbourg, France, 2022. **Oral presentation**

A. Gautheron, R. Clerc, V. Duveiller, L. Simonot, B. Montcel, M. Hébert "Light scattering in translucent layers: angular distribution and internal reflections at flat interfaces.", Electronic Imaging, San Francisco, États-Unis, 2022. **Oral presentation**

A. Gautheron, M. Hébert, L. Mahieu-Williame, J. Guyotat, B. Montcel "Multiple wavelength excitation 5-ALA induced PpIX fluorescence spectroscopy in guided neurosurgery

*for improving glioma classification", European Conferences on Biomedical Optics, Online Only, 2021. Oral presentation*

## National peer-reviewed conferences

C. Caredda, L. Alston, A. Gautheron, L. Mahieu-Willame, B. Montcel, R. Sablong, M. Sdika, R. Clerc, M. Hébert, P.F. Brevet, C. Jonin, P. Leclerc, C. Ray, E. Salmon, X. Armoiry, J. Guyotat, P. Kantapareddy, J. Koelher, D. Meyronet, F. Schneider, D. Rousseau *"Intraoperative optical imaging for neurosurgery guidance"*, Recherche en imagerie et technologies pour la santé, Brest, France, 2022. **Oral presentation - Invited**

A. Gautheron, M. Sdika, M. Hébert , B. Montcel *"Estimation of Fluorescence Contributions using Multiple-Wavelength Excitation: the example of PpIX for improving Glioma Classification"*, Journées Imagerie Optique Non Conventionnelle (JIONC), Paris, France, 2022. **Oral presentation**

A. Gautheron, M. Hébert, M. Sdika , V. Duveiller, L. Simonot, R. Clerc, B. Montcel *"Towards quantitative multispectral excitation fluorescence spectroscopy for intraoperative assistance in glioma resection in neurosurgery"*, Journée Labex PRIMES, Lyon, France, 2022. **Poster**

A. Gautheron, R. Clerc, V. Duveiller, L. Simonot, B. Montcel, M. Hébert *"How much light is internally reflected at the boundaries of translucent layers ?"*, Sleight Science Event #8 - Photonics for health, Saint-Etienne, France, 2022. **Poster**

# List of Figures

2.1	.....	8
2.2	Protective envelopes of the brain (image from the <a href="#">SEER Development Team</a> of National Institute of Health) . . . . .	8
2.3	Number of publications related to GBM depending on the year from 2000 to 2021. (data taken from PubMed) . . . . .	11
2.4	Schematic of the operating room. In orange, the sterile area, in blue the people present and in grey the areas occupied by tools (operating microscope, screens, neuronavigation system, stocks...) The space dedicated to the prototype is in the disinfected area. (adapted from [ <a href="#">Alston (2017)</a> ]) . . . . .	11
2.5	Modeling infiltrations of high-grade gliomas (translated from [ <a href="#">Alston (2017)</a> ]) . . . . .	12
2.6	Pre-operative MRI showing a high-grade glioma located in associative areas and ventricular crossroad. On the right, early post-operative control (<72h) with no more contrast enhancing tumor (taken from [ <a href="#">Dupont et al. (2016)</a> ]). . . . .	13
2.7	Absorption spectra of the main components of biological tissues: water, melanin, protein, hemoglobin (Hb), oxyhemoglobin (HbO <sub>2</sub> ). The quantity given as a function of wavelength is the absorption coefficient $\mu_a$ . Extracted and translated from [ <a href="#">Ogien (2017)</a> ] . . . . .	15
2.8	Henyey-Greenstein phase function [ <a href="#">Henyey and Greenstein (1941)</a> ] for various values of the anisotropy parameter $g$ . The incident radiation arrives from the left. (Wikimedia) . . . . .	17
2.9	Jablonski diagram illustrating the phenomena of fluorescence and phosphorescence . . . . .	18
2.10	Cycle of heme biosynthesis in a human cell from 5-ALA. Enzymes are written in red and products are black. Circled in green, the two molecules of interest in the thesis. (adapted from [ <a href="#">Olivo et al. (2011)</a> ]) . . . . .	19
2.11	Chemical structure of PpIX . . . . .	19
2.12	Absorption (top) and emission (bottom) spectra of different endogenous fluorophores. Adapted from [ <a href="#">Leh (2011)</a> ]. . . . .	20
2.13	Cerebral cortex with a tumor, under excitation at 405 nm. (image taken from Zeiss' website) . . . . .	24
2.14	Absorption (a) and emission (b) spectra of PpIX according to the microenvironment. 1) pH 7; 2) pH 7 and addition of protenoids; 3) pH 7 and addition of human albumin; 4) dissolution of PpIX in methanol. Taken from [ <a href="#">Lozovaya et al. (1990)</a> ] . . . . .	27
2.15	Emission spectra of <i>P. intermedia</i> suspensions (bacteria containing mainly PpIX) under excitation at 398 nm and 410 nm. In red, acidic pH. In green, neutral pH and in blue, basic pH. From [ <a href="#">Hope and Higham (2016)</a> ] . . . . .	29
2.16	. . . . .	30

2.17 (a) Point spread function (PSF), which can be measured using DRS, and (b) modulation transfer function (MTF), which can be measured using SFDI. (Taken from [Gevaux (2019)]) . . . . .	36
2.18 Optical probe measuring both fluorescence and scattering reflectance to correct the fluorescence measurement from effects of absorption and scattering induced by the tissue. (Taken from [Kim <i>et al.</i> (2010)b]) . . . . .	37
4.1 Measurement signal (in blue) and PpIX signal (in orange) for each baseline dataset in row and for each excitation wavelength in column. The green area corresponds to the signal addition due to the baseline. . . . .	54
4.2 Probability Maps with categories identified. . . . .	54
4.3 Map of $(\alpha_1, \alpha_2)$ absolute estimation Error for each estimation method in row : Baseline Free (BF), Gaussian Baseline (GB), and Estimated Baseline (EB). Each column represent the same baseline dataset defined in Table 4.1. Each map has been computed by 100000 drawings equally split in 100x100 bins. The more red is the color, the greater the absolute error of estimation and the greener the color, the lower the absolute error of estimation. . . . .	57
4.4 Mean and standard error of Absolute estimation Error of $\alpha$ . Each color bar corresponds to an estimation method, and each group corresponds to a set of baseline parameters (refer Table 4.1). BF <sub>1</sub> , GB <sub>1</sub> , BF <sub>2</sub> , GB <sub>1</sub> refer to state-of-the-art methods and EB is our proposed method. . . . .	58
4.5 Mean Accuracy of the ROI ( $0 \leq \alpha_1 \leq 0.25$ , $0 \leq \alpha_2 \leq 0.75$ ). Each color corresponds to the same model and each group to a specific set of baseline parameters. GT refers to Ground Truth, BF <sub>1</sub> , GB <sub>1</sub> , BF <sub>2</sub> , GB <sub>1</sub> refer to state of the art methods and EB <sub>2</sub> is our proposed method. . . . .	59
4.6 Accuracy Map for each estimation method in column : BF <sub>1</sub> , GB <sub>1</sub> , BF <sub>2</sub> , GB <sub>1</sub> refer to state-of-the-art methods and EB is our proposed method. We classify on one side Low Grade Glioma (a) and on the other side High Grade Glioma (b). Rows give the set name defined in Table 4.1. . . . . .	60
4.7 Confusion matrices of healthy/tumoral classification on images of simulated glioma accounting for the spatial point spread function of the probe. In the case of LGG and HGG, each row corresponds to a specific baseline dataset referring to Table 4.1 and each column to an estimation model. Each confusion matrix is row normalized. Inside each confusion matrix, each row corresponds to the true class while each column to the predicted class. . . . .	61
4.8 Results on a 300x300 clinical synthetic images of Low Grade Glioma (a) and High Grade Glioma (b). Row name corresponds to an estimation models : GT refers to Ground Truth, BF <sub>1</sub> , GB <sub>1</sub> , BF <sub>2</sub> , GB <sub>1</sub> refer to state of the art methods and EB <sub>2</sub> . Columns gives the set name defined in Table 4.1 : the baseline's amplitude increased when going from General to Amplitude dataset. Red color refers to tumor area while green color refers to healthy area. In HGG Case (b), orange color refers to sparse tumor margins. . . . .	62
5.1 Definition of angles $\theta$ and $\phi$ in a system of spherical coordinates . . . . .	70
5.2 Geometrical extent $d^3G$ describing a large pencil of light based on a infinitesimal area $dS$ on a surface and a solid angle $d^2\Omega$ in the spatial direction $\vec{\Omega}$ . .	70

5.3 Radiance $I(A, \theta, \phi)$ emitted by a small area $dS$ around point $A$ on a curved surface. Angles are defined in the hemisphere based on the plane containing $dS$ . ( <i>adapted from [Hébert (2022)]</i> ) . . . . .	71
5.4 The plane parallel geometry. The axis $z$ and angle $\theta$ are defined. . . . .	73
5.5 Energy balance in an elementary volume designed around the light direction $\vec{\Omega}$ . . . . .	74
5.6 Boundaries of an index-matching slab medium . . . . .	83
5.7 Boundary of an index-matching semi-infinite medium . . . . .	84
5.8 Boundaries of a non index-matching slab medium . . . . .	85
5.9 Boundaries of a non index-matching semi-infinite medium . . . . .	87
 6.1 Monte Carlo randomization process (taken from [Jacques (1998)]) . . . . .	94
6.2 Studied configuration where a semi-infinite scattering medium with a refractive index different from the surrounding air is illuminated by directional light at normal incidence. Physical quantities depend on depth $z$ and angle $\theta$ . . . . .	95
6.3 Plots of Validity Metrics versus the Legendre polynomial order . . . . .	96
6.4 Plots of Validity Metrics versus the Legendre polynomial order . . . . .	97
6.5 Plots of Validity Metrics versus the Legendre polynomial order . . . . .	98
6.6 Fresnel angular reflectance function (dashed black line) and its piecewise constant discretisation for various Legendre polynomial order (color diamonds). . . . .	99
6.7 Plots of Validity Metrics versus the Legendre polynomial order . . . . .	100
6.8 . . . . .	102
6.9 . . . . .	103
6.10 Log <sub>10</sub> of the Relative Convergence of the Legendre Discretization- (solid line) and Regular Discretization- (dashed line) solver solution for the study case. . . . .	105
6.11 Log <sub>10</sub> of the Relative Convergence of the Legendre Discretization- (solid line) and Regular Discretization- (dashed line) solver solution for the study case. . . . .	105
6.12 Log <sub>10</sub> of the Relative Convergence of the Legendre Discretization- (solid line) and Regular Discretization- (dashed line) solver solution for the study case. . . . .	106
6.13 Log <sub>10</sub> of the Relative Convergence of the Legendre Discretization- (solid line) and Regular Discretization- (dashed line) solver solution for the study case. . . . .	107
 7.1 Studied configuration where a layer of scattering medium with a refractive index different from the surrounding air ("slab") is illuminated by directional light at normal incidence. Physical quantities depend on depth $z$ and angle $\theta$ . . . . .	112
7.2 Photon trajectory inside a semi-infinite layer of scattering medium under directional incident light (irradiance $F_0$ ). The incident light can be either reflected at the interface (A) or transmitted into the medium. After a scattering event (B), a photon may propagate until reaching the interface. If the incident angle is below the critical angle $i_c$ , it can exit the medium or be reflected (C). If it is higher than $i_c$ , it is totally reflected back to the medium (D). Percentages are given for $n = n_2/n_1 = 1.5$ . . . . .	113
7.3 . . . . .	114

7.4 Comparison of cut views of the relative angular radiance diagram near the top interface for a semi-infinite scattering layer of albedo $\omega_0 = 0.9$ , with $g = 0$ and an extinction coefficient $(\mu_a + \mu_s) = 5.0 \text{ mm}^{-1}$ for various relative refractive index $n = 1.1$ , resp $1.3, 1.5, 2.4$ . . . . .	115
7.5 Polar plot of the diffuse radiance at the top interface, $L_0(\theta)$ (Fig. 4Aa), resp. (Fig 4Ba), and the bottom interface, $L_d(\theta)$ (Fig. 4Ab), resp. (Fig 4Bb), for isotropic layers of different optical thicknesses in absence of absorption (refractive index $n = 1.5$ , albedo $\omega_0 = \mu_s/(\mu_a + \mu_s) = 1.0$ ), resp. in presence of absorption (refractive index $n = 1.5$ , albedo $\omega_0 = \mu_s/(\mu_a + \mu_s) = 0.7$ ). . . . .	116
7.6 Internal reflectances versus optical thickness $(\mu_a + \mu_s)d$ for isotropic scattering ( $g = 0$ ) and several albedo $\omega_0 = \mu_s/(\mu_a + \mu_s)$ with $\mu_a + \mu_s = 5 \text{ cm}^{-1}$ . The bold dashed line at $r_i = 0.6$ corresponds to the value usually considered in the classical Saunderson correction. . . . .	118
7.7 Polar plot of the diffuse radiance at the top $L_0(\theta)$ (Fig. 6Aa), resp (Fig 6Ba), and bottom $L_d(\theta)$ (Fig. 6Ab), resp. (Fig 6Bb); for layers of different optical thicknesses in presence of absorption (refractive index $n = 1.5$ , albedo $\omega_0 = \mu_s/(\mu_a + \mu_s) = 1.0$ , anisotropy factor $g = 0.8$ ), resp in presence of absorption (refractive index $n = 1.5$ , albedo $\omega_0 = \mu_s/(\mu_a + \mu_s) = 0.7$ , anisotropy factor $g = 0.8$ ). . . . .	119
7.8 Internal reflectances versus optical thickness $(\mu_a + \mu_s)d$ for several albedo $\omega_0 = \mu_s/(\mu_a + \mu_s)$ with $\mu_a + \mu_s = 5 \text{ cm}^{-1}$ and for anisotropic scattering: colored solid lines correspond to $g = 0$ , colored dashed lines correspond to $g = 0.5$ and colored dotted lines correspond to $g = 0.8$ . The bold dashed line at $r_i = 0.6$ corresponds to the value usually considered in the Saunderson correction. . . . .	120
7.9 Reflectance (left graphs) and transmittance (right graphs) factors predicted by the 2-flux and 4-flux models for different values of the internal reflectance at the interface. The red curve represents the 2-flux model with $\text{rig} = \text{rig}' = 0$ . The magenta curve represents the 2-flux model with $\text{rig} = \text{rig}' = 0.04$ . The yellow (resp. blue) curve represents the 2-flux (resp. 4-flux) model with $\text{rig} = \text{rig}' = 0.60$ (ie. Lambertian flux). The green (resp. black) curve represents the 2-flux (resp. 4-flux) model with $\text{rig}$ (resp. $\text{rid}$ ) and $\text{rig}'$ (resp. $\text{rid}'$ ) calculated by the RTE for each slab. The black solid line curve represents the ground truth values simulated with the RTE. a) Simulations of the RTE are performed for $g = 0$ . b) Simulations of the RTE are performed for $g = 0.5$ . c) Simulations of the RTE are performed with $g = 0.8$ . . . . .	123
8.1 Diagram of the acquisition system . . . . .	132
8.2 Round to Linear Fiber Bunder transfer function . . . . .	133
8.3 Emission spectrum of the lasers used ( <i>Integration time 16 ms</i> ) . . . . .	135
8.4 Spectral Irradiance of KL2500LCD cropped to the 500 - 900 nm region . . . . .	136
8.5 Arduino Uno rev3 (Taken from Wikimedia) . . . . .	137
8.6 Pinout Schematic of Arduino Uno rev3 (Taken from Arduino.cc) . . . . .	137
8.7 Schematic of the PWM technique (Taken from Arduino.cc) . . . . .	138
8.8 PCB Schematic of the Home Made Electronic Shield . . . . .	139
8.9 Schematic of one TTL pre-processing circuit . . . . .	140
8.10 Schematic of one PWM Filtering Circuit . . . . .	140
8.11 Bode Diagram of the Sallen-Key 2nd order filter of the PWM Filtering Circuit	140

8.12 Filtering of a PWM Signal: Input PWM signal with 80% Duty Cycle and $f_0 = 980$ Hz (top) and filtered output signal (bottom) . . . . .	141
8.13 Filter, resp. Linear, response (blue crosses, resp. green solid line) versus duty cycle. . . . .	141
8.14 Board Packaging . . . . .	142
8.15 Probe Manufacturing Schematic . . . . .	142
8.16 Diffuse Reflectance versus Reduced scattering coefficient . . . . .	144
 9.1 Measurement Processing Schematic . . . . .	146
9.2 Calibration steps for two source-detector distances : Figs. (a) and (c), resp. (b) and (d), correspond to the short source-detector distance (0.24 mm), resp. the long one (0.48 mm). In each figure, the solid line corresponds to the output of $\mathcal{M}$ , the dashed line to the experimentally fitted model and dots to measurements $R_d^m$ . Figs. (a), (b) correspond to raw data and Figs. (c), (d) correspond to $x$ -scaled data. Experimental diffuse reflectance measurements (points) of phantoms measured at 600 nm. Although the data shown are at 600 nm, the calibration was done for all wavelengths. . . . .	149
9.3 Result of the calibration process. Fig. (a) , resp. (b), correspond to the short source-detector distance (0.24 mm), resp. the long one (0.48 mm). In each figure, the solid line corresponds to the output of $\mathcal{M}$ , and dots to the scaled measurements $R_d^{sc}$ . Experimental diffuse reflectance measurements (points) of phantoms measured at 600 nm. Although the data shown are at 600 nm, the calibration was done for all wavelengths. . . . .	150
 10.1 User Interface associated with the first step of the Acquisition Software . . . . .	152
10.2 User Interface associated with the second step of the Acquisition Software . . . . .	152
10.3 User Interface associated with the acquisition step of the Acquisition Software	153
10.4 Schematic of the MVC software architecture (Taken from Wikimedia) . . . . .	153
10.5 Software flowchart . . . . .	154
 11.1 . . . . .	164
11.2 Fluorescence spectrum obtained for PEG functionalized nanoparticles concentrated at 0.5M under 120 keV, 300 mAs excitation. . . . .	165
11.3 Fluorescent response for two different types of nanoparticles, PEG functionalized LC205 (green lines) and not functionnalized LC174 (blue lines) as well as the witness sample of terbium chloride (red lines) depending on mAs (horizontal axis) and keV (Marker type). Cross marker $\times$ , resp. star marker $*$ , corresponds to 140 keV, resp. 120 keV and tick marker $+$ , resp. circle marker $\circ$ , corresponds to 100 keV, resp. 80 keV. All chemical component are 1 mol.L <sup>-1</sup> concentrated. . . . .	167
11.4 mAs dependent fitted fluorescent efficency for two different types of nanoparticles, PEG functionalized LC205 (green stars) and not functionnalized LC174 (blue circles) depending on keV. All chemical component are 1 mol.L <sup>-1</sup> concentrated. . . . .	168
11.5 Fluorescent response for two different functionalization methods of the nanoparticle. Acquisitions are done at 120 keV and 300 mAs. . . . .	169
11.6 Image of various nanoparticles scintillation at different concentrations (from left to right 1.0 mol.L <sup>-1</sup> , 0.5 mol.L <sup>-1</sup> and witness 0.5 mol.L <sup>-1</sup> ) under X Ray excitation at 120 keV and 300 mAs. . . . .	170



# List of Tables

2.1	Comparison of methods for solving the radiative transfer equation with other light propagation models. . . . .	35
4.1	Parameters used for the simulation of the seven baseline datasets. Only differences from "General" are specified for the following six datasets. **: In this Table, endogenous fluorophore corresponds to non 5-ALA-induced fluorophore. . . . .	55
4.2	Sensitivity (TPR) and Specificity (TNR) values. For all clinical synthetic images (CSI) datasets, each model's sensitivity is equal to 1. . . . .	63
6.1	Optical Parameters for isotropic index matching case of a semi-infinite medium	96
6.2	Optical Parameters for isotropic index matching case of a semi-infinite medium	97
6.3	Optical Parameters for the isotropic medium and air . . . . .	98
6.4	RMS Error of Fresnel Reflectance Function Discretization with roots of various Legendre polynomial order. . . . .	99
6.5	Optical Parameters for anisotropic semi-infinite medium with an interface with the air . . . . .	99
6.6	Optical Parameters extracted from article [Prahl <i>et al.</i> (1989)] . . . . .	100
6.7	Results comparison between various methods . . . . .	101
6.8	Optical Parameters extracted from article [Prahl <i>et al.</i> (1989)] . . . . .	101
6.9	Results comparison between various methods . . . . .	101
6.10	Recommended number of discretization steps for the different configurations studied in this section . . . . .	108
8.1	Optical specifications for the development of the probe. . . . .	143
8.2	Brain Tissues Optical Properties (Summarized from [Yaroslavsky <i>et al.</i> (2002)]) . . . . .	143
8.3	The maximum estimable scattering coefficient with a fixed absorption coefficient as a function of the source-detector distance . . . . .	144
9.1	Optical properties and quantities of related components for a set of optical phantoms. . . . .	148
11.1	Linear model parameters of the fluorescent response as a function of mAs for different nanoparticles. . . . .	166
11.2	Polynomial model parameters of the fluorescent response as a function of concentration for different nanoparticles. . . . .	168



# Bibliography

- [Acerbi *et al.* (2013)] Acerbi, F., Broggi, M., Eoli, M., Anghileri, E., Cappini, L., Pollo, B., Schiariti, M., Visintini, S., Orsi, C., Franzini, A., Broggi, G., and Ferroli, P. (2013). Fluorescein-guided surgery for grade IV gliomas with a dedicated filter on the surgical microscope: preliminary results in 12 cases. *Acta Neurochir (Wien)*, 155(7):1277–1286.
- [Acerbi *et al.* (2014)] Acerbi, F., Broggi, M., Eoli, M., Anghileri, E., Cavallo, C., Boffano, C., Cordella, R., Cappini, L., Pollo, B., Schiariti, M., Visintini, S., Orsi, C., La Corte, E., Broggi, G., and Ferroli, P. (2014). Is fluorescein-guided technique able to help in resection of high-grade gliomas? *Neurosurg. Focus*, 36(2):E5.
- [Aguénounon *et al.* (2020)] Aguénounon, E., Smith, J. T., Al-Taher, M., Diana, M., Intes, X., and Gioux, S. (2020). Real-time, wide-field and high-quality single snapshot imaging of optical properties with profile correction using deep learning. *Biomed Opt Express*, 11(10):5701–5716.
- [Ahmad *et al.* (2019)] Ahmad, F., Wang, X., Jiang, Z., Yu, X., Liu, X., Mao, R., Chen, X., and Li, W. (2019). Codoping Enhanced Radioluminescence of Nanoscintillators for X-ray-Activated Synergistic Cancer Therapy and Prognosis Using Metabolomics. *ACS Nano*, 13(9):10419–10433.
- [Alston (2017)] Alston, L. (2017). *Spectroscopie de fluorescence et imagerie optique pour l’assistance à la résection de gliomes : conception et caractérisation de systèmes de mesure et modèles de traitement des données associées, sur fantômes et au bloc opératoire*. PhD thesis. 2017LYSE1295.
- [Alston *et al.* (2018)] Alston, L., Rousseau, D., Hébert, M., Mahieu-Williame, L., and Montcel, B. (2018). Nonlinear relation between concentration and fluorescence emission of protoporphyrin IX in calibrated phantoms. *J. Biomed. Opt.*, 23(9):097002.
- [Alston *et al.* (2019)] Alston, L., Mahieu-Williame, L., Hebert, M., Kantapareddy, P., Meyronet, D., Rousseau, D., Guyotat, J., and Montcel, B. (2019). Spectral complexity of 5-ALA induced PpIX fluorescence in guided surgery: a clinical study towards the discrimination of healthy tissue and margin boundaries in high and low grade gliomas. *Biomed. Opt. Express*, 10(5):2478–2492.
- [Anand *et al.* (2017)] Anand, S., Cicchi, R., Giordano, F., Conti, V., Buccoliero, A. M., Guerrini, R., and Pavone, F. S. (2017). Multimodal fiber-probe spectroscopy allows detecting epileptogenic focal cortical dysplasia in children. *Journal of Biophotonics*, 10(6-7):896–904.
- [Ando *et al.* (2011)] Ando, T., Kobayashi, E., Liao, H., Maruyama, T., Muragaki, Y., Iseki, H., Kubo, O., and Sakuma, I. (2011). Precise comparison of protoporphyrin IX

- fluorescence spectra with pathological results for brain tumor tissue identification. *Brain Tumor Pathol.*, 28(1):43–51.
- [Angelo *et al.* (2019)] Angelo, J. P., Chen, S.-J., Ochoa, M., Sunar, U., Gioux, S., and Intes, X. (2019). Review of structured light in diffuse optical imaging. *J Biomed Opt*, 24(7):071602.
- [Artom *et al.* (1979)] Artom, M., Billmeyer, F., Budde, W., Clarke, F., Erb, W., Fillinger, L., Hammond, H., Hemmendinger, H., Krochmann, J., Lozano, R., Morren, L., Mishima, Y., Nonaka, N., Nündel, S., Ooba, N., H. Reiter, H., Reule, A., Robertson, A., Sanders, C., J. Schanda, J., R. Sève, R., W. Stanioch, W., A. Stenius, A., Terstiege, H., and Venable, W. (1979). *Absolute methods for reflection measurements / CIE*.
- [Azevedo *et al.* (2009)] Azevedo, F. A. C., Carvalho, L. R. B., Grinberg, L. T., Farfel, J. M., Ferretti, R. E. L., Leite, R. E. P., Filho, W. J., Lent, R., and Herculano-Houzel, S. (2009). Equal numbers of neuronal and nonneuronal cells make the human brain an isometrically scaled-up primate brain. *J. Comp. Neurol.*, 513(5):532–541.
- [Barron *et al.* (2013)] Barron, G. A., Valentine, R., Moseley, H., Brancaleon, L., Hill, C., and Woods, J. A. (2013). Porphyrin profile in four human cell lines after supplementation with 5-aminolaevulinic acid and its methyl ester. *Photodiagn. Photodyn. Ther.*, 10(4):654–663.
- [Bautista *et al.* (2003)] Bautista, J. F., Foldvary-Schaefer, N., Bingaman, W. E., and Lüders, H. O. (2003). Focal cortical dysplasia and intractable epilepsy in adults: clinical, EEG, imaging, and surgical features. *Epilepsy Research*, 55(1-2):131–136.
- [Beck *et al.* (2007)] Beck, T. J., Kreth, F. W., Beyer, W., Mehrkens, J. H., Obermeier, A., Stepp, H., Stummer, W., and Baumgartner, R. (2007). Interstitial photodynamic therapy of nonresectable malignant glioma recurrences using 5-aminolevulinic acid induced protoporphyrin IX. *Lasers Surg Med*, 39(5):386–393.
- [Beer (1852)] Beer, A. (1852). Bestimmung der Absorption des rothen Lichts in farbigen Flüssigkeiten. *Annalen der Physik*, 162(5):78–88.
- [Behbahaninia *et al.* (2013)] Behbahaninia, M., Martirosyan, N. L., Georges, J., Udovich, J. A., Kalani, M. Y. S., Feuerstein, B. G., Nakaji, P., Spetzler, R. F., and Preul, M. C. (2013). Intraoperative fluorescent imaging of intracranial tumors: a review. *Clin Neurol Neurosurg*, 115(5):517–528.
- [Belykh *et al.* (2016)] Belykh, E., Martirosyan, N. L., Yagmurlu, K., Miller, E. J., Eschbacher, J. M., Izadyyazdanabadi, M., Bardanova, L. A., Byvaltsev, V. A., Nakaji, P., and Preul, M. C. (2016). Intraoperative Fluorescence Imaging for Personalized Brain Tumor Resection: Current State and Future Directions. *Front Surg*, 3:55.
- [Black *et al.* (2021)] Black *et al.* (2021). Characterization of autofluorescence and quantitative protoporphyrin IX biomarkers for optical spectroscopy-guided glioma surgery - Scientific Reports. *Sci. Rep.*, 11(20009):1–12.
- [Boas *et al.* (1997)] Boas, D. A., O’Leary, M. A., Chance, B., and Yodh, A. G. (1997). Detection and characterization of optical inhomogeneities with diffuse photon density waves: a signal-to-noise analysis. *Applied Optics*, 36(1):75–92. Publisher: Optica Publishing Group.

- [Boas *et al.* (2016)] Boas, D. A., Pitrish, C., and Ramanujam, N. (2016). *Handbook of biomedical optics*. CRC press.
- [Bohren and Huffman (1983)] Bohren, C. F. and Huffman, D. R. (1983). *Absorption and scattering of light by small particles*. John Wiley & Sons.
- [Bongetta *et al.* (2016)] Bongetta, D., Zoia, C., Pugliese, R., Adinolfi, D., Silvani, V., and Gaetani, P. (2016). Low-Cost Fluorescein Detection System for High-Grade Glioma Surgery. *World Neurosurg.*, 88:54–58.
- [Born *et al.* (1999)] Born, M. *et al.* (1999). *Principles of Optics: Electromagnetic Theory of Propagation, Interference and Diffraction of Light*. Cambridge University Press, Cambridge, England, UK.
- [Bradley and Thorniley (2006)] Bradley, R. S. and Thorniley, M. S. (2006). A review of attenuation correction techniques for tissue fluorescence. *J R Soc Interface*, 3(6):1–13.
- [Bravo *et al.* (2017)] Bravo, J. J., Olson, J. D., Davis, S. C., Roberts, D. W., Paulsen, K. D., and Kanick, S. C. (2017). Hyperspectral data processing improves PpIX contrast during fluorescence guided surgery of human brain tumors. *Sci. Rep.*, 7(9455):1–13.
- [Butte *et al.* (2011)] Butte, P. V., Mamelak, A. N., Nuno, M., Bannykh, S. I., Black, K. L., and Marcu, L. (2011). Fluorescence lifetime spectroscopy for guided therapy of brain tumors. *Neuroimage*, 54(Suppl):1.
- [Caredda (2020)] Caredda, C. (2020). *Imagerie optique spectrale : applications cliniques et précliniques*. Theses, Université de Lyon.
- [Chaichana *et al.* (2014)] Chaichana, K. L., Jusue-Torres, I., Navarro-Ramirez, R., Raza, S. M., Pascual-Gallego, M., Ibrahim, A., Hernandez-Hermann, M., Gomez, L., Ye, X., Weingart, J. D., Olivi, A., Blakeley, J., Gallia, G. L., Lim, M., Brem, H., and Quinones-Hinojosa, A. (2014). Establishing percent resection and residual volume thresholds affecting survival and recurrence for patients with newly diagnosed intracranial glioblastoma. *Neuro-oncol.*, 16(1):113–122.
- [Chan *et al.* (2021)] Chan, H. W., Uff, C., Chakraborty, A., Dorward, N., and Bamber, J. C. (2021). Clinical Application of Shear Wave Elastography for Assisting Brain Tumor Resection. *Front. Oncol.*, 11:619286.
- [Chance *et al.* (1998)] Chance, B., Anday, E., Nioka, S., Zhou, S., Hong, L., Worden, K., Li, C., Murray, T., Ovetsky, Y., Pidikiti, D., and Thomas, R. (1998). A novel method for fast imaging of brain function, non-invasively, with light. *Optics Express*, 2(10):411–423.
- [Chandrasekhar (1960)a] Chandrasekhar, S. (1960a). *Radiative Transfer*. Dover Publications, Mineola, NY, USA.
- [Chandrasekhar (1960)b] Chandrasekhar, S. (1960b). *Radiative Transfer*. Dover Books on Intermediate and Advanced Mathematics. Dover Publications.
- [Cheeseman *et al.* (1988)] Cheeseman, P., Kelly, J., Self, M., Stutz, J., Taylor, W., and Freeman, D. (1988). Autoclass: A bayesian classification system. In *Machine learning proceedings 1988*, pages 54–64. Elsevier.

- [Chen *et al.* (1998)] Chen, B., Stamnes, J. J., and Stamnes, K. (1998). Reconstruction algorithm for diffraction tomography of diffuse photon density waves in a random medium. *Pure Applied Optics*, 7:1161–1180. ADS Bibcode: 1998PAPOp...7.1161C.
- [Chen *et al.* (2020)] Chen, L., Xu, T., Jia, Q., Wang, X., Li, M., and Liang, G. (2020). RSK4: a new prognostic factor in glioma. *Pathology - Research and Practice*, 216(8):153020.
- [Cheong *et al.* (1990)] Cheong, W., Prahl, S., and Welch, A. (1990). A review of the optical properties of biological tissues. *IEEE J. Quantum Electron.*, 26(12):2166–2185.
- [Coburger *et al.* (2014)] Coburger, J., Engelke, J., Scheuerle, A., Thal, D. R., Hlavac, M., Wirtz, C. R., and König, R. (2014). Tumor detection with 5-aminolevulinic acid fluorescence and Gd-DTPA-enhanced intraoperative MRI at the border of contrast-enhancing lesions: a prospective study based on histopathological assessment. *Neurosurg. Focus*, 36(2):E3.
- [Coburger *et al.* (2015)] Coburger, J., Hagel, V., Wirtz, C. R., and König, R. (2015). Surgery for Glioblastoma: Impact of the Combined Use of 5-Aminolevulinic Acid and Intraoperative MRI on Extent of Resection and Survival. *PLoS One*, 10(6):e0131872.
- [Collaud *et al.* (2004)] Collaud, S., Juzeniene, A., Moan, J., and Lange, N. (2004). On the Selectivity of 5-Aminolevulinic Acid-Induced Protoporphyrin IX Formation. *Curr. Med. Chem.: Anti-Cancer Agents*, 4(3):301–316.
- [Cornette and Shanks (1992)] Cornette, W. M. and Shanks, J. G. (1992). Physically reasonable analytic expression for the single-scattering phase function. *Applied Optics*, 31(16):3152–3160.
- [Corns *et al.* (2015)] Corns, R., Mukherjee, S., Johansen, A., and Sivakumar, G. (2015). 5-aminolevulinic acid guidance during awake craniotomy to maximise extent of safe resection of glioblastoma multiforme. *BMJ case reports*, 2015:bcr2014208575.
- [Corwin *et al.* (1968)] Corwin, A. H., Chivvis, A. B., Poor, R. W., Whitten, D. G., and Baker, E. W. (1968). Porphyrin studies. XXXVII. The interpretation of porphyrin and metalloporphyrin spectra. *J. Am. Chem. Soc.*, 90(24):6577–6583.
- [Croce *et al.* (2003)] Croce, A. C., Fiorani, S., Locatelli, D., Nano, R., Ceroni, M., Tancioni, F., Giombelli, E., Benericetti, E., and Bottiroli, G. (2003). Diagnostic potential of autofluorescence for an assisted intraoperative delineation of glioblastoma resection margins. *Photochem. Photobiol.*, 77(3):309–318.
- [Croce *et al.* (2017)] Croce, A. C., Ferrigno, A., Bertone, V., Piccolini, V. M., Berardo, C., Di Pasqua, L. G., Rizzo, V., Bottiroli, G., and Vairetti, M. (2017). Fatty liver oxidative events monitored by autofluorescence optical diagnosis: Comparison between subnormothermic machine perfusion and conventional cold storage preservation. *Hepatology Research: The Official Journal of the Japan Society of Hepatology*, 47(7):668–682.
- [Cuccia *et al.* (2005)] Cuccia, D. J., Bevilacqua, F., Durkin, A. J., and Tromberg, B. J. (2005). Modulated imaging: quantitative analysis and tomography of turbid media in the spatial-frequency domain. *Opt. Lett.*, 30(11):1354–1356.

- [Cuccia *et al.* (2009)] Cuccia, D. J., Bevilacqua, F. P., Durkin, A. J., Ayers, F. R., and Tromberg, B. J. (2009). Quantitation and mapping of tissue optical properties using modulated imaging. *JBO*, 14(2):024012.
- [Dailey and Smith (1984)] Dailey, H. A. and Smith, A. (1984). Differential interaction of porphyrins used in photoradiation therapy with ferrochelatase. *Biochem. J.*, 223(2):441.
- [Dasgupta *et al.* (2016)] Dasgupta, A., Liu, M., Ojha, T., Storm, G., Kiessling, F., and Lammers, T. (2016). Ultrasound-mediated drug delivery to the brain: principles, progress and prospects. *Drug Discovery Today: Technologies*, 20:41–48.
- [Da Silva (2013)] Da Silva, A. (2013). *Méthodes optiques pour le diagnostic et l'imagerie biomédicale*. Habilitation à diriger des recherches, Aix-Marseille Université.
- [Da Silva *et al.* (2004)] Da Silva, A., Andraud, C., Lafait, J., Robin, T., and Barrera, R. (2004). A model of the angular distribution of light scattered by multilayered media. *Journal of modern optics*, 51(3):313–332. Publisher: Taylor & Francis.
- [DeVore (1951)] DeVore, J. R. (1951). Refractive Indices of Rutile and Sphalerite. *J. Opt. Soc. Am.*, 41(6):416–419. Publisher: Optica Publishing Group.
- [Delpy *et al.* (1988)] Delpy, D. T., Cope, M., van der Zee, P., Arridge, S., Wray, S., and Wyatt, J. (1988). Estimation of optical pathlength through tissue from direct time of flight measurement. *Physics in Medicine & Biology*, 33(12):1433. Publisher: IOP Publishing.
- [De Coene *et al.* (1992)] De Coene, B., Hajnal, J. V., Gatehouse, P., Longmore, D. B., White, S. J., Oatridge, A., Pennock, J., Young, I., and Bydder, G. (1992). Mr of the brain using fluid-attenuated inversion recovery (flair) pulse sequences. *American journal of neuroradiology*, 13(6):1555–1564.
- [Diaz *et al.* (2015)] Diaz, R. J., Dios, R. R., Hattab, E. M., Burrell, K., Rakopoulos, P., Sabha, N., Hawkins, C., Zadeh, G., Rutka, J. T., and Cohen-Gadol, A. A. (2015). Study of the biodistribution of fluorescein in glioma-infiltrated mouse brain and histopathological correlation of intraoperative findings in high-grade gliomas resected under fluorescein fluorescence guidance. *J. Neurosurg.*, 122(6):1360–1369.
- [Dietel *et al.* (1997)] Dietel, W., Fritsch, C., Pottier, R. H., and Wendenburg, R. (1997). 5-aminolaevulinic-acid-induced formation of different porphyrins and their photomodifications. *Lasers Med. Sci.*, 12(3):226–236.
- [Dietel *et al.* (2007)] Dietel, W., Pottier, R., Pfister, W., Schleier, P., and Zinner, K. (2007). 5-Aminolaevulinic acid (ALA) induced formation of different fluorescent porphyrins: a study of the biosynthesis of porphyrins by bacteria of the human digestive tract. *J. Photochem. Photobiol., B*, 86(1):77–86.
- [Di Ninni *et al.* (2010)] Di Ninni, P., Martelli, F., and Zaccanti, G. (2010). The use of India ink in tissue-simulating phantoms. *Optics Express*, 18(26):26854–26865.
- [Dolman *et al.* (1981)] Dolman, C. *et al.* (1981). Lipofuscin and its relation to aging. In Fedoroff, S. and Hertz, L., editors, *Advances in Cellular Neurobiology*, volume 2 of *Advances in Cellular Neurobiology*, pages 205–247. Elsevier.

- [Drezek *et al.* (2001)] Drezek, R. A., Sokolov, K. V., Utzinger, U., Boiko, I., Malpica, A., Follen, M., and Richards-Kortum, R. R. (2001). Understanding the contributions of nadh and collagen to cervical tissue fluorescence spectra: modeling, measurements, and implications. *Journal of biomedical optics*, 6(4):385–396.
- [Duffau (2018)] Duffau, H. (2018). The error of Broca: From the traditional localizationist concept to a connectomal anatomy of human brain. *J Chem Neuroanat*, 89:73–81.
- [Duffau (2022)] Duffau, H. (2022). Awake mapping with transopercular approach in right insular-centered low-grade gliomas improves neurological outcomes and return to work. *Neurosurgery*, 91(1):182–190.
- [Duncan (1940)] Duncan, D. R. (1940). The colour of pigment mixtures. *Proceedings of the Physical Society*, 52(3):390–401. Publisher: IOP Publishing.
- [Dupont *et al.* (2016)] Dupont, C., Betrouni, N., Reyns, N., and Vermandel, M. (2016). On Image Segmentation Methods Applied to Glioblastoma: State of Art and New Trends. *IRBM*, 37(3):131–143.
- [Durant *et al.* (2007)] Durant, S., Calvo-Perez, O., Vukadinovic, N., and Greffet, J.-J. (2007). Light scattering by a random distribution of particles embedded in absorbing media: full-wave monte carlo solutions of the extinction coefficient. *JOSA A*, 24(9):2953–2962.
- [Durkin *et al.* (1994)] Durkin, A., Jaikumar, S., Ramanujam, N., and Richards-Kortum, R. (1994). Relation between fluorescence spectra of dilute and turbid samples. *Applied Optics*, 33(3):414–423.
- [Duveiller *et al.* (2020)] Duveiller, V., Gevaux, L., Clerc, R., Salomon, J.-P., and Hebert, M. (2020). Reflectance and transmittance of flowable dental resin composite predicted by the two-flux model: on the importance of analyzing the effective measurement geometry. *Color and Imaging Conference*, 2020(28):313–320.
- [Dysart and Patterson (2006)] Dysart, J. S. and Patterson, M. S. (2006). Photobleaching kinetics, photoproduct formation, and dose estimation during ALA induced PpIX PDT of MLL cells under well oxygenated and hypoxic conditions. *Photochem. Photobiol. Sci.*, 5(1):73–81.
- [Dögnitz and Wagnières (1998)] Dögnitz, N. and Wagnières, G. (1998). Determination of tissue optical properties by steady-state spatial frequency-domain reflectometry. *Lasers Med. Sci.*, 13(1):55–65.
- [Egan and Hilgeman (1980)] Egan, W. G. and Hilgeman, T. W. (1980). Optical Properties of Inhomogeneous Materials: Applications to Geology, Astronomy, Chemistry, and Engineering. *J. Opt. Soc. Am*, 70(11).
- [Elias and Elias (2002)] Elias, M. and Elias, G. (2002). New and fast calculation for incoherent multiple scattering. *JOSA A*, 19(5):894–901.
- [Estrella *et al.* (2013)] Estrella, V., Chen, T., Lloyd, M., Wojtkowiak, J., Cornnell, H. H., Ibrahim-Hashim, A., Bailey, K., Balagurunathan, Y., Rothberg, J. M., Sloane, B. F., Johnson, J., Gatenby, R. A., and Gillies, R. J. (2013). Acidity Generated by the Tumor Microenvironment Drives Local Invasion Acid-Mediated Invasion. *Cancer Res.*, 73(5):1524–1535.

- [Ewelt *et al.* (2015)] Ewelt, C., Nemes, A., Senner, V., Wölfer, J., Brokinkel, B., Stummer, W., and Holling, M. (2015). Fluorescence in neurosurgery: Its diagnostic and therapeutic use. Review of the literature. *J. Photochem. Photobiol., B*, 148:302–309.
- [Fang *et al.* (2009)] Fang, Q. *et al.* (2009). Monte carlo simulation of photon migration in 3d turbid media accelerated by graphics processing units. *Opt. Express*, 17(22):20178–20190.
- [Farrell *et al.* (1992)] Farrell, T. J., Patterson, M. S., and Wilson, B. (1992). A diffusion theory model of spatially resolved, steady-state diffuse reflectance for the noninvasive determination of tissue optical properties in vivo. *Medical Physics*, 19(4):879–888.
- [Ferroli *et al.* (2011)] Ferroli, P., Acerbi, F., Albanese, E., Tringali, G., Broggi, M., Franzini, A., and Broggi, G. (2011). Application of intraoperative indocyanine green angiography for CNS tumors: results on the first 100 cases. *Acta Neurochir. Suppl.*, 109(251-7.):;.
- [Fleming *et al.* (2004)] Fleming, R. W., Jensen, H. W., and Bülthoff, H. H. (2004). Perceiving translucent materials. In *Proceedings of the 1st Symposium on Applied perception in graphics and visualization*, APGV '04, pages 127–134, New York, NY, USA. Association for Computing Machinery.
- [Fouke *et al.* (2015)] Fouke, S. J., Benzinger, T., Gibson, D., Ryken, T. C., Kalkanis, S. N., and Olson, J. J. (2015). The role of imaging in the management of adults with diffuse low grade glioma: A systematic review and evidence-based clinical practice guideline. *J Neurooncol*, 125(3):457–479. Place: United States.
- [Frka-Petescic *et al.* (2015)] Frka-Petescic, B., Sugiyama, J., Kimura, S., Chanzy, H., and Maret, G. (2015). Negative Diamagnetic Anisotropy and Birefringence of Cellulose Nanocrystals. *Macromolecules*, 48(24):8844–8857.
- [Fuchs *et al.* (1997)] Fuchs, C., Riesenber, R., Siegert, J., and Baumgartner, R. (1997). H-dependent formation of 5-aminolaevulinic acid-induced protoporphyrin IX in fibrosarcoma cells. *J. Photochem. Photobiol., B*, 40(1):49–54.
- [Gate (1974)] Gate, L. F. (1974). Comparison of the Photon Diffusion Model and Kubelka-Munk Equation with the Exact Solution of the Radiative Transport Equation. *Appl. Opt., AO*, 13(2):236–238. Publisher: Optica Publishing Group.
- [Gevaux (2019)] Gevaux, L. (2019). *3D-hyperspectral imaging and optical analysis of skin for the human face*. PhD thesis. Thèse de doctorat dirigée par Hébert, Mathieu Optique Lyon 2019.
- [Giessen *et al.* (2015)] Giessen, M. v. d., Angelo, J. P., and Gioux, S. (2015). Real-time, profile-corrected single snapshot imaging of optical properties. *Biomed. Opt. Express, BOE*, 6(10):4051–4062. Publisher: Optica Publishing Group.
- [Gilbert and Lang (2007)] Gilbert, M. R. and Lang, F. F. (2007). Management of patients with low-grade gliomas. *Neurol. Clin.*, 25(4):1073–1088.
- [Gioux *et al.* (2019)] Gioux, S., Mazhar, A., and Cuccia, D. J. (2019). Spatial frequency domain imaging in 2019: principles, applications, and perspectives. *Journal of Biomedical Optics*, 24(7):1–18.

- [Giovanelli (1955)] Giovanelli, R. (1955). Reflection by semi-infinite diffusers. *Optica Acta: International Journal of Optics*, 2(4):153–162. Publisher: Taylor & Francis.
- [Graaff *et al.* (1989)] Graaff, R., Aarnoudse, J. G., Mul, F. F. M. d., and Jentink, H. W. (1989). Improved Expressions For Anisotropic Scattering In Absorbing Media. In Ferwerda, H. A., editor, *Scattering and Diffraction*, volume 1029, pages 103 – 110. SPIE. Backup Publisher: International Society for Optics and Photonics.
- [Graaff *et al.* (1993)] Graaff, R., Aarnoudse, J. G., de Mul, F. F., and Jentink, H. W. (1993). Similarity relations for anisotropic scattering in absorbing media. *Optical engineering*, 32(2):244–252. Publisher: SPIE.
- [Gray (1878)] Gray, H. (1878). *Anatomy of the human body*, volume 8. Lea & Febiger.
- [Guerrini and Dobyns (2014)] Guerrini, R. and Dobyns, W. B. (2014). Malformations of cortical development: clinical features and genetic causes. *The Lancet Neurology*, 13(7):710–726.
- [Hadjipanayis *et al.* (2015)] Hadjipanayis, C., Widhalm, G., and Stummer, W. (2015). What is the Surgical Benefit of Utilizing 5-Aminolevulinic Acid for Fluorescence-Guided Surgery of Malignant Gliomas? *Neurosurgery*, 77(5):663–673.
- [Haidar *et al.* (2015)] Haidar, D. A., Leh, B., Zanello, M., and Siebert, R. (2015). Spectral and lifetime domain measurements of rat brain tumors. *Biomed. Opt. Express*, 6(4):1219–1233.
- [Haj-Hosseini *et al.* (2010)] Haj-Hosseini, N., Richter, J., Andersson-Engels, S., and Wårdell, K. (2010). Optical touch pointer for fluorescence guided glioblastoma resection using 5-aminolevulinic acid. *Lasers Surg. Med.*, 42(1):9–14.
- [Hamamcioğlu *et al.* (2016)] Hamamcioğlu, M. K., Akçakaya, M. O., Göker, B., Kasımcıan, M. Ö., and Kiriş, T. (2016). The use of the YELLOW 560 nm surgical microscope filter for sodium fluorescein-guided resection of brain tumors: Our preliminary results in a series of 28 patients. *Clin. Neurol. Neurosurg.*, 143:39–45.
- [Hamiwka *et al.* (2005)] Hamiwka, L., Jayakar, P., Resnick, T., Morrison, G., Ragheb, J., Dean, P., Dunoyer, C., and Duchowny, M. (2005). Surgery for epilepsy due to cortical malformations: ten-year follow-up. *Epilepsia*, 46(4):556–560.
- [Happel *et al.* (2014)] Happel, K., Dörsam, E., and Urban, P. (2014). Measuring isotropic subsurface light transport. *Optics Express*, 22(8):9048–9062. Publisher: Optica Publishing Group.
- [Hefti (2013)] Hefti, M. (2013). Fluorescence-guided surgery for brain tumors. *CNS Oncol.*, 2(1):67.
- [Henyey and Greenstein (1941)] Henyey, L. G. and Greenstein, J. L. (1941). Diffuse radiation in the Galaxy. *The Astrophysical Journal*, 93:70–83.
- [Hoffmann *et al.* (1998)] Hoffmann, J., Lübbbers, D., and Heise, H. (1998). Applicability of the Kubelka-Munk theory for the evaluation of reflectance spectra demonstrated for haemoglobin-free perfused heart tissue. *Physics in Medicine & Biology*, 43(12):3571. Publisher: IOP Publishing.

- [Hope and Higham (2016)] Hope, C. K. and Higham, S. M. (2016). Evaluating the effect of local pH on fluorescence emissions from oral bacteria of the genus Prevotella. *J. Biomed. Opt.*, 21(8):84003.
- [Hébert *et al.* (2016)] Hébert, M., Mazauric, S., and Simonot, L. (2016). Assessing the capacity of two-flux models to predict the spectral properties of layered materials. In *Electronic Imaging*, San Francisco, United States.
- [Hébert (2022)] Hébert, M. (2022). *Optical models for material appearance*. EDP Sciences & Science Press.
- [Hébert *et al.* (2014)] Hébert, M., Hersch, R. D., and Emmel, P. (2014). Fundamentals of Optics and Radiometry for Color Reproduction. In *Handbook of Digital Imaging*, pages 1–57. John Wiley & Sons, Ltd.
- [Irvine (1965)] Irvine, W. M. (1965). Multiple scattering by large particles. Technical report.
- [Ishihara *et al.* (2007)] Ishihara, R., Katayama, Y., Watanabe, T., Yoshino, A., Fukushima, T., and Sakatani, K. (2007). Quantitative spectroscopic analysis of 5-aminolevulinic acid-induced protoporphyrin IX fluorescence intensity in diffusely infiltrating astrocytomas. *Neurologia Medico-Chirurgica*, 47(2):53–57; discussion 57.
- [Ishimaru (1978)] Ishimaru, A. (1978). *Wave propagation and scattering in random media*, volume 2. Academic press New York.
- [Jacques (1998)] Jacques, S. L. (1998). Light distributions from point, line and plane sources for photochemical reactions and fluorescence in turbid biological tissues. *Photochem. Photobiol.*, 67(1):23–32.
- [Jacques (2013)a] Jacques, S. L. (2013a). Corrigendum: Optical properties of biological tissues: a review. *Phys. Med. Biol.*, 58(14):5007–5008. Publisher: IOP Publishing.
- [Jacques (2013)b] Jacques, S. L. (2013b). Optical properties of biological tissues: a review. *Phys. Med. Biol.*, 58(11):R37–R61. Publisher: IOP Publishing.
- [Jacques *et al.* (1987)] Jacques, S. L., Alter, C. A., and Prahl, S. A. (1987). Angular Dependence of HeNe Laser Light Scattering by Human Dermis. *Lasers Life Sci.*, 1:309–333.
- [Janzer (1993)] Janzer, R. C. (1993). The blood-brain barrier: Cellular basis. *J. Inherit. Metab. Dis.*, 16(4):639–647.
- [Johansson *et al.* (2010)] Johansson, A., Palte, G., Schnell, O., J. C., T., Herms, J., and Stepp, H. (2010). 5-Aminolevulinic acid-induced protoporphyrin IX levels in tissue of human malignant brain tumors. *Photochem. Photobiol.*, 86(6):1373–1378.
- [Johnston *et al.* (1986)a] Johnston, W. M., O'Brien, W. J., and Tien, T.-Y. (1986a). Concentration additivity of kubelka-munk optical coefficients of porcelain mixtures. *Color Research & Application*, 11(2):131–137.
- [Johnston *et al.* (1986)b] Johnston, W. M., O'Brien, W. J., and Tien, T.-Y. (1986b). The determination of optical absorption and scattering in translucent porcelain. *Color Research & Application*, 11(2):125–130. Publisher: Wiley Online Library.

- [Jolly *et al.* (2002)] Jolly, R. D., Palmer, D. N., and Dalefield, R. R. (2002). The analytical approach to the nature of lipofuscin (age pigment). *Archives of Gerontology and Geriatrics*, 34(3):205–217.
- [Jonin *et al.* (2020)] Jonin, C., Ray, C., Salmon, E., Leclerc, P., Montcel, B., Mahieu-Willame, L., and Brevet, P.-F. (2020). Two photon excited fluorescence and hyper-rayleigh scattering of protoporphyrin ix. *Journal of Photochemistry and Photobiology A: Chemistry*, 402:112812.
- [Khalfaoui-Bendriss (2010)] Khalfaoui-Bendriss, G. (2010). *Rôle de l'adrénomédulline dans la néoangiogénèse tumorale des glioblastomes*. PhD Thesis.
- [Kienle *et al.* (1998)] Kienle, A., Patterson, M. S., Dögnitz, N., Bays, R., Wagnières, G., and van Den Bergh, H. (1998). Noninvasive determination of the optical properties of two-layered turbid media. *Applied optics*, 37(4):779–791.
- [Kim (2011)] Kim, A. D. (2011). Correcting the diffusion approximation at the boundary. *JOSA A*, 28(6):1007–1015.
- [Kim *et al.* (2010)a] Kim, A., Khurana, M., Moriyama, Y., and Wilson, B. C. (2010a). Quantification of in vivo fluorescence decoupled from the effects of tissue optical properties using fiber-optic spectroscopy measurements. *J. Biomed. Opt.*, 15(6):067006.
- [Kim *et al.* (2010)b] Kim, A., Roy, M., Dadani, F., and Wilson, B. C. (2010b). A fiberoptic reflectance probe with multiple source-collector separations to increase the dynamic range of derived tissue optical absorption and scattering coefficients. *Opt Express*, 18(6):5580–5594.
- [Kleen *et al.* (2011)] Kleen, J. K., Valdes, P. A., Harris, B. T., Holmes, G. L., Paulsen, K. D., and Roberts, D. W. (2011). ALA-induced PpIX fluorescence in epileptogenic tissue. In *Proceedings Volume 7883, Photonic Therapeutics and Diagnostics VII*, volume 7883, pages 468–474. SPIE.
- [Klose (2009)] Klose, A. (2009). *Radiative transfer of luminescence light in biological tissue*, volume 4, pages 293–345. Springer.
- [Klose (2010)] Klose, A. D. (2010). The forward and inverse problem in tissue optics based on the radiative transfer equation: a brief review. *Journal of quantitative spectroscopy & radiative transfer*, 111(11):1852–1853.
- [Klose *et al.* (2002)] Klose, A. D., Netz, U., Beuthan, J., and Hielscher, A. H. (2002). Optical tomography using the time-independent equation of radiative transfer—Part 1: forward model. *Journal of Quantitative Spectroscopy and Radiative Transfer*, 72(5):691–713.
- [Klose and Hielscher (2002)] Klose, A. D. and Hielscher, A. H. (2002). Optical tomography using the time-independent equation of radiative transfer—Part 2: inverse model. *Journal of Quantitative Spectroscopy and Radiative Transfer*, 72(5):715–732.
- [Klose and Larsen (2006)] Klose, A. D. and Larsen, E. W. (2006). Light transport in biological tissue based on the simplified spherical harmonics equations. *Journal of Computational Physics*, 220(1):441–470.

- [Koc *et al.* (2008)] Koc, K., Anik, I., Cabuk, B., and Ceylan, S. (2008). Fluorescein sodium-guided surgery in glioblastoma multiforme: a prospective evaluation. *Br J Neurosurg*, 22(1):99–103.
- [Koenig *et al.* (2015)] Koenig, A., Roig, B., Digabel, J. L., Josse, G., and Dinten, J.-M. (2015). Accessing deep optical properties of skin using diffuse reflectance spectroscopy. In *Clinical and Biomedical Spectroscopy and Imaging IV*, page 95370E. Optica Publishing Group.
- [Kokhanovsky (2009)] Kokhanovsky, A. A. (2009). *Light Scattering Reviews 4: Single Light Scattering and Radiative Transfer*. Springer Science & Business Media. Google-Books-ID: tMPgQ91cmDwC.
- [Krammer and Plaetzer (2008)] Krammer, B. and Plaetzer, K. (2008). ALA and its clinical impact, from bench to bedside. *Photochem Photobiol Sci*, 7(3):283–289.
- [Kreth *et al.* (1999)] Kreth, F. W., Berlis, A., Spiropoulou, V., Faist, M., Scheremet, R., Rossner, R., Volk, B., and Ostertag, C. B. (1999). The role of tumor resection in the treatment of glioblastoma multiforme in adults. *Cancer*, 86(10):2117–2123.
- [Krivosheya *et al.* (2016)] Krivosheya, D., Prabhu, S. S., Weinberg, J. S., and Sawaya, R. (2016). Technical principles in glioma surgery and preoperative considerations. *J Neurooncol.*, 130(2):243–252.
- [Kröger *et al.* (2018)] Kröger, S., Niehoff, A.-C., Jeibmann, A., Sperling, M., Paulus, W., Stummer, W., and Karst, U. (2018). Complementary Molecular and Elemental Mass-Spectrometric Imaging of Human Brain Tumors Resected by Fluorescence-Guided Surgery. *Anal. Chem.*, 90(20):12253–12260.
- [Kubben *et al.* (2011)] Kubben, P. L., ter Meulen, K. J., Schijns, O. E., ter Laak-Poort, M. P., van Overbeeke, J. J., and Santbrink, H. v. (2011). Intraoperative MRI-guided resection of glioblastoma multiforme: a systematic review. *The Lancet Oncology*, 12(11):1062–1070.
- [Kubelka (1931)] Kubelka, P. (1931). Ein Beitrag zur Optik der Farbanstriche (Contribution to the optic of paint). *Zeitschrift fur technische Physik*, 12:593–601.
- [Kuroiwa *et al.* (1998)] Kuroiwa, T., Kajimoto, Y., and Ohta, T. (1998). Development of a fluorescein operative microscope for use during malignant glioma surgery: a technical note and preliminary report. *Surg Neurol*, 50(1):41–48; discussion 48–49.
- [Lacroix *et al.* (2001)] Lacroix, M., Abi-Said, D., Journey, D. R., Gokaslan, Z. L., Shi, W., DeMonte, F., Lang, F. F., McCutcheon, I. E., Hassenbusch, S. J., Holland, E., Hess, K., Michael, C., Miller, D., and Sawaya, R. (2001). A multivariate analysis of 416 patients with glioblastoma multiforme: prognosis, extent of resection, and survival. *J Neurosurg.*, 95(2):190–198.
- [Lacroix and Toms (2014)] Lacroix, M. and Toms, S. A. (2014). Maximum safe resection of glioblastoma multiforme. *J. Clin. Oncol.*, 32(8):727–728.
- [Lang *et al.* (2015)] Lang, A., Stepp, H., Homann, C., Hennig, G., Brittenham, G. M., and Vogeser, M. (2015). Rapid screening test for porphyria diagnosis using fluorescence spectroscopy. In *Clinical and Biomedical Spectroscopy and Imaging IV*, page 953706. Optica Publishing Group. Journal Abbreviation: Clinical and Biomedical Spectroscopy and Imaging IV.

- [Latour *et al.* (2009)] Latour, G., Elias, M., and Frigerio, J.-M. (2009). Determination of the absorption and scattering coefficients of pigments: application to the identification of the components of pigment mixtures. *Applied Spectroscopy*, 63(6):604–610. Publisher: Society for Applied Spectroscopy.
- [Leclerc *et al.* (2020)] Leclerc, P., Ray, C., Mahieu-Willame, L., Alston, L., Frindel, C., Brevet, P., Meyronet, D., Guyotat, J., Montcel, B., and Rousseau, D. (2020). Machine learning-based prediction of glioma margin from 5-ALA induced PpIX fluorescence spectroscopy - Scientific Reports. *Sci. Rep.*, 10(1462):1–9.
- [Leh (2011)] Leh, B. (2011). *Caractérisation par autofluorescence de tissus cérébraux tumoraux : mesures sur fantômes et modèle animal*. Theses, Université Paris Sud - Paris XI. Issue: 2011PA112166.
- [Leroy *et al.* (2015)] Leroy, H.-A., Vermandel, M., Lejeune, J.-P., Mordon, S., and Reynolds, N. (2015). Fluorescence guided resection and glioblastoma in 2015: A review. *Lasers Surg. Med.*, 47(5):441–451.
- [Li *et al.* (2014)] Li, Y., Rey-Dios, R., Roberts, D. W., Valdés, P. A., and Cohen-Gadol, A. A. (2014). Intraoperative fluorescence-guided resection of high-grade gliomas: a comparison of the present techniques and evolution of future strategies. *World Neurosurg.*, 82(1-2):175–185.
- [Li *et al.* (2016)] Li, Y. M., Suki, D., Hess, K., and Sawaya, R. (2016). The influence of maximum safe resection of glioblastoma on survival in 1229 patients: Can we do better than gross-total resection? *J. Neurosurg.*, 124(4):977–988.
- [Liu *et al.* (2014)] Liu, J. T. C., Meza, D., and Sanai, N. (2014). Trends in Fluorescence Image-Guided Surgery for Gliomas. *Neurosurgery*, 75(1):61–71.
- [Louis *et al.* (2007)] Louis, D. N., Ohgaki, H., Wiestler, O. D., Cavenee, W. K., Burger, P. C., Jouvet, A., Scheithauer, B. W., and Kleihues, P. (2007). The 2007 WHO Classification of Tumours of the Central Nervous System. *Acta Neuropathol.*, 114(2):97–109.
- [Louis *et al.* (2016)] Louis, D. N., Perry, A., Reifenberger, G., von Deimling, A., Figarella-Branger, D., Cavenee, W. K., Ohgaki, H., Wiestler, O. D., Kleihues, P., and Ellison, D. W. (2016). The 2016 World Health Organization Classification of Tumors of the Central Nervous System: a summary. *Acta Neuropathol.*, 131(6):803–820.
- [Lozovaya *et al.* (1990)] Lozovaya, G. I., Masinovsky, Z., and Sivash, A. A. (1990). Protoporphyrin ix as a possible ancient photosensitizer: Spectral and photochemical studies. *Origins Life Evol. Biosphere*, 20(3):321–330.
- [Lu *et al.* (2020)] Lu, H., Floris, F., Rensing, M., and Andersson-Engels, S. (2020). Fluorescence spectroscopy study of protoporphyrin ix in optical tissue simulating liquid phantoms. *Materials*, 13(9):2105.
- [Lu and Shiou (2002)] Lu, T.-T. and Shiou, S.-H. (2002). Inverses of  $2 \times 2$  block matrices. *Computers & Mathematics with Applications*, 43(1-2):119–129.
- [Mahboob *et al.* (2016)] Mahboob, S., McPhillips, R., Qiu, Z., Jiang, Y., Meggs, C., Schiavone, G., Button, T., Desmulliez, M., Demore, C., Cochran, S., and Eljamal, S. (2016). Intraoperative Ultrasound-Guided Resection of Gliomas: A Meta-Analysis and Review of the Literature. *World Neurosurg.*, 92:255–263.

- [Maheu *et al.* (1984)] Maheu, B., Letoulouzan, J., and Gouesbet, G. (1984). Four-flux models to solve the scattering transfer equation in terms of lorenz-mie parameters. *Applied optics*, 23(19):3353–3362. Publisher: Optical Society of America.
- [Marois *et al.* (2016)] Marois, M., Bravo, J. J., Davis, S. C., and Kanick, S. C. (2016). Characterization and standardization of tissue-simulating protoporphyrin ix optical phantoms. *Journal of biomedical optics*, 21(3):035003.
- [Marumoto and Saya (2012)] Marumoto, T. and Saya, H. (2012). Molecular Biology of Glioma. In *Glioma*, pages 2–11. Springer, New York, NY, USA.
- [Mazauric *et al.* (2014)] Mazauric, S., Hébert, M., Simonot, L., and Fournel, T. (2014). Two-flux transfer matrix model for predicting the reflectance and transmittance of duplex halftone prints. *JOSA A*, 31(12):2775–2788.
- [Melø and Reisaeter (1986)] Melø, T. B. and Reisaeter, G. (1986). The physicochemical state of protoporphyrin IX in aqueous solution investigated by fluorescence and light scattering. *Biophys. Chem.*, 25(1):99–104.
- [Menei *et al.* (2005)] Menei, P., Capelle, L., Guyotat, J., Fuentes, S., Assaker, R., Bataille, B., François, P., Dorwling-Carter, D., Paquis, P., Bauchet, L., Parker, F., Sabatier, J., Faisant, N., and Benoit, J.-P. (2005). Local and sustained delivery of 5-fluorouracil from biodegradable microspheres for the radiosensitization of malignant glioma: a randomized phase II trial. *Neurosurgery*, 56(2):242–248.
- [Mercadante and Tadi (2022)] Mercadante, A. A. and Tadi, P. (2022). Neuroanatomy, Gray Matter. In *StatPearls*. StatPearls Publishing, Treasure Island (FL).
- [Montcel *et al.* (2013)a] Montcel, B., Mahieu-Williame, L., Armoiry, X., Meyronet, D., and Guyotat, J. (2013a). 5-ALA-induced PpIX fluorescence in gliomas resection: spectral complexity of the emission spectrum in the infiltrative compound. In *Neurophotonics*, volume 8804, page 880409. International Society for Optics and Photonics.
- [Montcel *et al.* (2013)b] Montcel, B., Mahieu-Williame, L., Armoiry, X., Meyronet, D., and Guyotat, J. (2013b). Two-peaked 5-ALA-induced PpIX fluorescence emission spectrum distinguishes glioblastomas from low grade gliomas and infiltrative component of glioblastomas. *Biomed. Opt. Express*, 4(4):548–558.
- [Moore *et al.* (1948)] Moore, G. E., Peyton, W. T., French, L. A., and Walker, W. W. (1948). The Clinical Use of Fluorescein in Neurosurgery: The localization of brain tumors. *J. Neurosurg.*, 5(4):392–398.
- [Mourant *et al.* (1998)] Mourant, J. R., Freyer, J. P., Hielscher, A. H., Eick, A. A., Shen, D., and Johnson, T. M. (1998). Mechanisms of light scattering from biological cells relevant to noninvasive optical-tissue diagnostics. *Applied Optics*, 37(16):3586–3593.
- [Mudgett and Richards (1971)] Mudgett, P. and Richards, L. (1971). Multiple scattering calculations for technology. *Applied Optics*, 10(7):1485–1502. Publisher: Optica Publishing Group.
- [Murray (1982)] Murray, K. J. (1982). Improved surgical resection of human brain tumors: Part 1. A preliminary study. *Surgical Neurology*, 17(5):316–319.

- [Mursch *et al.* (2017)] Mursch, K., Scholz, M., Brück, W., and Behnke-Mursch, J. (2017). The value of intraoperative ultrasonography during the resection of relapsed irradiated malignant gliomas in the brain. *Ultrasonography*, 36(1):60–65.
- [Mycek and Pogue (2003)] Mycek, M.-A. and Pogue, B. W. (2003). *Handbook of biomedical fluorescence*. CRC Press.
- [Nabavi *et al.* (2001)] Nabavi, A., Black, P. M., Gering, D. T., Westin, C. F., Mehta, V., Pergolizzi, Jr., R. S., Ferrant, M., Warfield, S. K., Hata, N., Schwartz, R. B., Rd, W. M. W., Kikinis, R., and Jolesz, F. A. (2001). Serial intraoperative magnetic resonance imaging of brain shift. *Neurosurgery*, 48(4):787–797.
- [Nabavi *et al.* (2009)] Nabavi, A., Thurm, H., Zountsas, B., Pietsch, T., Lanfermann, H., Pichlmeier, U., Mehdorn, M., -ALA Recurrent Glioma Study Group, Oppel, F., Brune, A., Langenbach, U., Weber, F., and Komboss, T. (2009). Five-aminolevulinic acid for fluorescence-guided resection of recurrent malignant gliomas: a phase II study. *Neurosurgery*, 65(6):1070–1076.
- [Neuman *et al.* (2011)] Neuman, M., Coppel, L. G., and Edström, P. (2011). Angle resolved color of bulk scattering media. *Applied Optics*, 50(36):6555–6563. Publisher: Optica Publishing Group.
- [Neuman and Logan (1950)] Neuman, R. E. and Logan, M. A. (1950). The determination of collagen and elastin in tissues. *J. Biol. Chem.*, 186(2):549–556.
- [Nieto-Vesperinas and Sanchez-Gil (1992)] Nieto-Vesperinas, M. and Sanchez-Gil, J. (1992). Light scattering from a random rough interface with total internal reflection. *JOSA A*, 9(3):424–436. Publisher: Optica Publishing Group.
- [Nitta and Sato (1995)] Nitta, T. and Sato, K. (1995). Prognostic implications of the extent of surgical resection in patients with intracranial malignant gliomas. *Cancer*, 75(11):2727–2731.
- [Novotny and Stummer (2003)] Novotny, A. and Stummer, W. (2003). 5-Aminolevulinic Acid and the Blood-Brain Barrier – A Review. *Medical Laser Application*, 18(1):36–40.
- [Ogien (2017)] Ogien, J. (2017). *Développement de systèmes de microscopie par cohérence optique pour l'imagerie de la peau*. PhD Thesis.
- [Olivo *et al.* (2011)] Olivo, M., Bhuvaneswari, R., and Keogh, I. (2011). Advances in bio-optical imaging for the diagnosis of early oral cancer. *Pharmaceutics*, 3(3):354–378.
- [Orchard (1977)] Orchard, S. E. (1977). The missing variable: internal surface reflection. *Color Res. Appl.*, 2:26–31.
- [Palmer and Ramanujam (2006)] Palmer, G. M. and Ramanujam, N. (2006). Monte carlo-based inverse model for calculating tissue optical properties. part i: Theory and validation on synthetic phantoms. *Appl. Opt.*, 45(5):1062–1071.
- [Palmer and Ramanujam (2008)] Palmer, G. M. and Ramanujam, N. (2008). Monte-carlo-based model for the extraction of intrinsic fluorescence from turbid media. *Journal of biomedical optics*, 13(2):024017.

- [Pascu *et al.* (2009)] Pascu, A., Romanitan, M. O., Delgado, J.-M., Danaila, L., and Pascu, M.-L. (2009). Laser-induced autofluorescence measurements on brain tissues. *Anat. Rec. (Hoboken)*, 292(12):2013–2022.
- [Patterson *et al.* (1989)] Patterson, M. S., Chance, B., and Wilson, B. C. (1989). Time resolved reflectance and transmittance for the noninvasive measurement of tissue optical properties. *Applied Optics*, 28(12):2331–2336.
- [Patterson and Pogue (1994)] Patterson, M. S. and Pogue, B. W. (1994). Mathematical model for time-resolved and frequency-domain fluorescence spectroscopy in biological tissues. *Appl Opt*, 33(10):1963–1974.
- [Pavlova *et al.* (2008)] Pavlova, I., Weber, C. E. R., Schwarz, R. A., Williams, M. D., El-Naggar, A. K., Gillenwater, A. M., and Richards-Kortum, R. R. (2008). Monte carlo model to describe depth selective fluorescence spectra of epithelial tissue: applications for diagnosis of oral precancer. *Journal of biomedical optics*, 13(6):064012.
- [Petrecca *et al.* (2013)] Petrecca, K., Guiot, M.-C., Panet-Raymond, V., and Souhami, L. (2013). Failure pattern following complete resection plus radiotherapy and temozolomide is at the resection margin in patients with glioblastoma. *J. Neurooncol.*, 111(1):19–23.
- [Pierrat *et al.* (2006)] Pierrat, R., Greffet, J.-J., and Carminati, R. (2006). Photon diffusion coefficient in scattering and absorbing media. *JOSA A*, 23(5):1106–1110. Publisher: Optica Publishing Group.
- [Porta (2002)] Porta, E. A. (2002). Pigments in Aging: An Overview. *Annals of the New York Academy of Sciences*, 959(1):57–65.
- [Pouratian and Schiff (2010)] Pouratian, N. and Schiff, D. (2010). Management of Low-Grade Glioma. *Curr. Neurol. Neurosci. Rep.*, 10(3):224–231.
- [Prabhu *et al.* (2010)] Prabhu, V. C., Khaldi, A., Barton, K. P., Melian, E., Schneck, M. J., Primeau, M. J., and Lee, J. M. (2010). Management of Diffuse Low-Grade Cerebral Gliomas. *Neurol. Clin.*, 28(4):1037–1059.
- [Prahl *et al.* (1989)] Prahl, S. A., Keijzer, M., Jacques, S. L., and Welch, A. J. (1989). A Monte Carlo model of light propagation in tissue. In Müller, G. J. and Sliney, D. H., editors, *SPIE Proceedings of Dosimetry of Laser Radiation in Medicine and Biology*, volume IS 5, pages 102–111.
- [Quigley and Maroon (1991)] Quigley, M. R. and Maroon, J. C. (1991). The relationship between survival and the extent of the resection in patients with supratentorial malignant gliomas. *Neurosurgery*, 29(3):385–388; discussion 388–389.
- [Ramanujam (2000)] Ramanujam, N. (2000). Fluorescence Spectroscopy of Neoplastic and Non-Neoplastic Tissues. *Neoplasia*, 2(1):89–117.
- [Richards-Kortum and Sevick-Muraca (1996)] Richards-Kortum, R. and Sevick-Muraca, E. (1996). Quantitative optical spectroscopy for tissue diagnosis. *Annu Rev Phys Chem*, 47:555–606.
- [Richter *et al.* (2011)] Richter, J. C., Haj-Hosseini, N., Andersson-Engel, S., and Wårdell, K. (2011). Fluorescence spectroscopy measurements in ultrasonic navigated resection of malignant brain tumors. *Lasers in Surgery and Medicine*, 43(1):8–14.

- [Richter and Rienits (1980)] Richter, M. L. and Rienits, K. G. (1980). The synthesis of magnesium and zinc protoporphyrin IX and their monomethyl esters in etioplast preparations studied by high pressure liquid chromatography. *FEBS Letters*, 116(2):211–216.
- [Roberts *et al.* (2019)] Roberts, D. W., Bravo, J. J., Olson, J. D., Hickey, W. F., Harris, B. T., Nguyen, L. N., Hong, J., Evans, L. T., Fan, X., Wirth, D., Wilson, B. C., and Paulsen, K. D. (2019). 5-Aminolevulinic Acid-Induced Fluorescence in Focal Cortical Dysplasia: Report of 3 Cases. *Operative Neurosurgery*, 16(4):403–414.
- [Rogers (1998)] Rogers, G. L. (1998). Halftone Color: Diffusion of Light within Paper. *Color and Imaging Conference*, 6:185–188.
- [Roze *et al.* (2001)] Roze, C., Girasole, T., Gréhan, G., Gouesbet, G., and Maheu, B. (2001). Average crossing parameter and forward scattering ratio values in four-flux model for multiple scattering media. *Optics Communications*, 194(4-6):251–263.
- [Saager *et al.* (2011)] Saager, R. B., Cuccia, D. J., Saggese, S., Kelly, K. M., and Durkin, A. J. (2011). Quantitative fluorescence imaging of protoporphyrin IX through determination of tissue optical properties in the spatial frequency domain. *J Biomed Opt*, 16(12):126013.
- [Saban (2002)] Saban, R. (2002). Conception de la physiologie cerebrale de Francois-Joseph Gall a Paul Broca: Les localisations des fonctions cerebrales. *Biometrie Humaine et Anthropologie*, 20(3-4):195–203.
- [Sanai *et al.* (2011)a] Sanai, N., Chang, S., and Berger, M. S. (2011a). Low-grade gliomas in adults: A review. *J. Neurosurg.*, 115(5):948–965.
- [Sanai *et al.* (2011)b] Sanai, N., Polley, M.-Y., McDermott, M. W., Parsa, A. T., and Berger, M. S. (2011b). An extent of resection threshold for newly diagnosed glioblastomas. *J. Neurosurg.*, 115(1):3–8.
- [Sanai and Berger (2008)] Sanai, N. and Berger, M. S. (2008). Glioma extent of resection and its impact on patient outcome. *Neurosurgery*, 62(4):753–764.
- [Saunderson (1942)] Saunderson, J. L. (1942). Calculation of the Color of Pigmented Plastics\*. *J. Opt. Soc. Am., JOSA*, 32(12):727–736. Publisher: Optical Society of America.
- [Schebesch *et al.* (2013)] Schebesch, K.-M., Proescholdt, M., Höhne, J., Hohenberger, C., Hansen, E., Riemschneider, M. J., Ullrich, W., Doenitz, C., Schlaier, J., Lange, M., and Brawanski, A. (2013). Sodium fluorescein-guided resection under the YELLOW 560 nm surgical microscope filter in malignant brain tumor surgery—a feasibility study. *Acta Neurochir (Wien)*, 155(4):693–699.
- [Scholkmann *et al.* (2014)] Scholkmann, F., Kleiser, S., Metz, A. J., Zimmermann, R., Pavia, J. M., Wolf, U., and Wolf, M. (2014). A review on continuous wave functional near-infrared spectroscopy and imaging instrumentation and methodology. *NeuroImage*, 85:6–27.
- [Senders *et al.* (2017)] Senders, J. T., Muskens, I. S., Schnoor, R., Karhade, A. V., Cote, D. J., Smith, T. R., and Broekman, M. L. D. (2017). Agents for fluorescence-guided glioma surgery: a systematic review of preclinical and clinical results. *Acta Neurochir.*, 159(1):151.

- [Senft *et al.* (2011)] Senft, C., Bink, A., Franz, K., Vatter, H., Gasser, T., and Seifert, V. (2011). Intraoperative MRI guidance and extent of resection in glioma surgery: a randomised, controlled trial. *Lancet Oncol.*, 12(11):997–1003.
- [Sibai *et al.* (2017)] Sibai, M., Fisher, C., Veilleux, I., Elliott, J. T., Leblond, F., Roberts, D. W., and Wilson, B. C. (2017). Preclinical evaluation of spatial frequency domain-enabled wide-field quantitative imaging for enhanced glioma resection. *J Biomed Opt*, 22(7):076007.
- [Simonot *et al.* (2008)] Simonot, L., Hébert, M., Hersch, R. D., and Garay, H. (2008). Ray scattering model for spherical transparent particles. *JOSA A*, 25(7):1521–1534. Publisher: Optica Publishing Group.
- [Simonot *et al.* (2011)] Simonot, L., Thoury, M., and Delaney, J. (2011). Extension of the kubelka–munk theory for fluorescent turbid media to a nonopaque layer on a background. *JOSA A*, 28(7):1349–1357.
- [Simonot *et al.* (2014)] Simonot, L., Signac, L., Meneveaux, D., and Hébert, M. (2014). Modélisation de la diffusion multiple de la lumière dans un réseau cubique selon une approche discrète. Research report, université de Poitiers ; université Jean Monnet - Saint-Etienne.
- [Simonot and Boulenguez (2019)] Simonot, L. and Boulenguez, P. (2019). *Quand la matière diffuse la lumière*. Sciences de la matière. Presse des Mines, presses des mines edition.
- [Skardelly *et al.* (2021)] Skardelly, M., Kaltenstadler, M., Behling, F., Mäurer, I., Schittenhelm, J., Bender, B., Paulsen, F., Hedderich, J., Renovanz, M., Gempt, J., Barz, M., Meyer, B., Tabatabai, G., and Tatagiba, M. S. (2021). A continuous correlation between residual tumor volume and survival recommends maximal safe resection in glioblastoma patients: A nomogram for clinical decision making and reference for non-randomized trials. *Frontiers in Oncology*, 11:748691.
- [Star *et al.* (1988)] Star, W., Marijnissen, J., and Van Gemert, M. (1988). Light dosimetry in optical phantoms and in tissues: I. multiple flux and transport theory. *Physics in Medicine & Biology*, 33(4):437.
- [Stummer *et al.* (1998)] Stummer, W., Stepp, H., Möller, G., Ehrhardt, A., Leonhard, M., and Reulen, H. J. (1998). Technical principles for protoporphyrin-IX-fluorescence guided microsurgical resection of malignant glioma tissue. *Acta Neurochir.*, 140(10):995–1000.
- [Stummer *et al.* (2000)] Stummer, W., Stocker, S., Stepp, H. G., Bise, K., Reulen, H.-J., and Baumgartner, R. (2000). Clinical experiences with fluorescence guided resection of malignant glioma. In *Laser Florence'99: A Window on the Laser Medicine World*, volume 4166, pages 130–133. International Society for Optics and Photonics.
- [Stummer *et al.* (2006)] Stummer, W., Pichlmeier, U., Meinel, T., Wiestler, O. D., Zanella, F., Reulen, H.-J., and ALA-Glioma Study Group (2006). Fluorescence-guided surgery with 5-aminolevulinic acid for resection of malignant glioma: a randomised controlled multicentre phase III trial. *Lancet Oncol.*, 7(5):392–401.
- [Stummer *et al.* (2008)] Stummer, W., Reulen, H.-J., Meinel, T., Pichlmeier, U., Schumacher, W., Tonn, J.-C., Rohde, V., Oppel, F., Turowski, B., Woiciechowsky, C.,

- Franz, K., Pietsch, T., ALA-Glioma Study Group, Oppel, F., Brune, A., Lanksch, W., Woiciechowsky, C., Brock, M., Vesper, J., Tonn, J.-C., Goetz, C., Gilsbach, J. M., Mayfrank, L., Oertel, M. F., Seifert, V., Franz, K., Bink, A., Schackert, G., Pinzer, T., Hassler, W., Bani, A., Meisel, H.-J., Kern, B. C., Mehdorn, H. M., Nabavi, A., Brawanski, A., Ullrich, O. W., Böker, D. K., Winking, M., Weber, F., Langenbach, U., Westphal, M., Kähler, U., Arnold, H., Knopp, U., Grumme, T., Stretz, T., Stolke, D., Wiedemayer, H., Turowski, B., Pietsch, T., Wiestler, O. D., Reulen, H.-J., and Stummer, W. (2008). Extent of resection and survival in glioblastoma multiforme: identification of and adjustment for bias. *Neurosurgery*, 62(3):564–576.
- [Stummer *et al.* (2014)] Stummer, W., Tonn, J.-C., Goetz, C., Ullrich, W., Stepp, H., Bink, A., Pietsch, T., and Pichlmeier, U. (2014). 5-Aminolevulinic Acid-derived Tumor Fluorescence: The Diagnostic Accuracy of Visible Fluorescence Qualities as Corroborated by Spectrometry and Histology and Postoperative Imaging. *Neurosurgery*, 74(3):310.
- [Stupp *et al.* (2005)] Stupp, R., Mason, W. P., van den Bent, M. J., Weller, M., Fisher, B., Taphoorn, M. J. B., Belanger, K., Brandes, A. A., Marosi, C., Bogdahn, U., Curschmann, J., Janzer, R. C., Ludwin, S. K., Gorlia, T., Allgeier, A., Lacombe, D., Cairncross, J. G., Eisenhauer, E., and Mirimanoff, R. O. (2005). Radiotherapy plus Concomitant and Adjuvant Temozolomide for Glioblastoma. *N. Engl. J. Med.*, 352(10):987–996.
- [Su *et al.* (2014)] Su, X., Huang, Q.-F., Chen, H.-L., and Chen, J. (2014). Fluorescence-guided resection of high-grade gliomas: A systematic review and meta-analysis. *Photodiagnosis and Photodynamic Therapy*, 11(4):451–458.
- [Sung *et al.* (2021)] Sung, H., Ferlay, J., Siegel, R. L., Laversanne, M., Soerjomataram, I., Jemal, A., and Bray, F. (2021). Global cancer statistics 2020: Globocan estimates of incidence and mortality worldwide for 36 cancers in 185 countries. *CA: A Cancer Journal for Clinicians*, 71(3):209–249.
- [Séroul *et al.* (2016)] Séroul, P., Hébert, M., Cherel, M., Vernet, R., Clerc, R., and Jomier, M. (2016). Model-based skin pigment cartography by high-resolution hyperspectral imaging. *electronic imaging*, 2017:108–114.
- [Thennadil (2008)] Thennadil, S. N. (2008). Relationship between the Kubelka-Munk scattering and radiative transfer coefficients. *J Opt Soc Am A Opt Image Sci Vis*, 25(7):1480–1485.
- [Thomas and Stamnes (2002)] Thomas, G. E. and Stamnes, K. (2002). *Radiative transfer in the atmosphere and ocean*. Cambridge University Press.
- [Tian *et al.* (2006)] Tian, F., Johnson, K., Lesar, A. E., Moseley, H., Ferguson, J., Samuel, I. D. W., Mazzini, A., and Brancaleon, L. (2006). The pH-dependent conformational transition of  $\beta$ -lactoglobulin modulates the binding of protoporphyrin IX. *Biochimica et Biophysica Acta (BBA) - General Subjects*, 1760(1):38–46.
- [Toms *et al.* (2005)] Toms, S. A., Lin, W.-C., Weil, R. J., Johnson, M. D., Jansen, E. D., and Mahadevan-Jansen, A. (2005). Intraoperative optical spectroscopy identifies infiltrating glioma margins with high sensitivity. *Neurosurgery*, 57(4):Suppl.

- [Toms *et al.* (2006)] Toms, S. A., Konrad, P. E., Lin, W.-C., and Weil, R. J. (2006). Neuro-oncological applications of optical spectroscopy. *Technol. Cancer Res. Treat.*, 5(3):231–238.
- [Tuchin (2015)] Tuchin, V. V. (2015). *Tissue Optics: Light Scattering Methods and Instruments for Medical Diagnostics, Third Edition*. SPIE.
- [Unsgaard *et al.* (2002)] Unsgaard, G., Ommedal, S., Muller, T., Gronningsaeter, A., and Hernes, T. A. N. (2002). Neuronavigation by intraoperative three-dimensional ultrasound: initial experience during brain tumor resection. *Neurosurgery*, 50(4):804–812.
- [Utsuki *et al.* (2006)] Utsuki, S., Oka, H., Sato, S., Suzuki, S., Shimizu, S., Tanaka, S., and Fujii, K. (2006). Possibility of using laser spectroscopy for the intraoperative detection of nonfluorescing brain tumors and the boundaries of brain tumor infiltrates. *Journal of neurosurgery*, 104(4):618–620.
- [Utsuki *et al.* (2007a)] Utsuki, S., Miyoshi, N., Oka, H., Miyajima, Y., Shimizu, S., Suzuki, S., and Fujii, K. (2007a). Fluorescence-guided resection of metastatic brain tumors using a 5-aminolevulinic acid-induced protoporphyrin ix: pathological study. *Brain tumor pathology*, 24(2):53–55.
- [Utsuki *et al.* (2007b)] Utsuki, S., Oka, H., Sato, S., Shimizu, S., Suzuki, S., Tanizaki, Y., Kondo, K., Miyajima, Y., and Fujii, K. (2007b). Histological examination of false positive tissue resection using 5-aminolevulinic acid-induced fluorescence guidance. *Neurologia medico-chirurgica*, 47(5):210–214.
- [Utsuki *et al.* (2008)] Utsuki, S., Oka, H., Miyajima, Y., Shimizu, S., Suzuki, S., and Fujii, K. (2008). Auditory alert system for fluorescence-guided resection of gliomas—technical note—. *Neurologia medico-chirurgica*, 48(2):95–98.
- [Valdes *et al.* (2017)] Valdes, P. A., Angelo, J. P., Choi, H. S., and Gioux, S. (2017). qF-SSOP: real-time optical property corrected fluorescence imaging. *Biomed. Opt. Express, BOE*, 8(8):3597–3605. Publisher: Optica Publishing Group.
- [Valdes *et al.* (2019)] Valdes, P. A., Juvekar, P., Agar, N. Y. R., Gioux, S., and Golby, A. J. (2019). Quantitative Wide-Field Imaging Techniques for Fluorescence Guided Neurosurgery. *Frontiers in Surgery*, 6.
- [Valdés *et al.* (2011)] Valdés, P. A., Leblond, F., Kim, A., Harris, B. T., Wilson, B. C., Fan, X., Tosteson, T. D., Hartov, A., Ji, S., Erkmen, K., Simmons, N. E., Paulsen, K. D., and Roberts, D. W. (2011). Quantitative fluorescence in intracranial tumor: implications for ALA-induced PpIX as an intraoperative biomarker. *J. Neurosurg.*, 115(1):11–17.
- [Valdés *et al.* (2012)] Valdés, P. A., Leblond, F., Jacobs, V. L., Wilson, B. C., Paulsen, K. D., and Roberts, D. W. (2012). Quantitative, spectrally-resolved intraoperative fluorescence imaging - Scientific Reports. *Sci. Rep.*, 2(798):1–7.
- [Valdés *et al.* (2014)] Valdés, P. A., Jacobs, V. L., Leblond, F., Wilson, B. C., Paulsen, K. D., and Roberts, D. W. (2014). Quantitative spectrally resolved intraoperative fluorescence imaging for neurosurgical guidance in brain tumor surgery: pre-clinical and clinical results. In *Optical Techniques in Neurosurgery, Neurophotonics, and Optogenetics*, volume 8928, page 892809. International Society for Optics and Photonics.

- [Valdés *et al.* (2015)] Valdés, P. A., Jacobs, V., Harris, B. T., Wilson, B. C., Leblond, F., Paulsen, K. D., and Roberts, D. W. (2015). Quantitative fluorescence using 5-aminolevulinic acid-induced protoporphyrin IX biomarker as a surgical adjunct in low-grade glioma surgery. *J. Neurosurg.*, 123(3):771–780.
- [Valdés *et al.* (2016)] Valdés, P. A., Roberts, D. W., Lu, F.-K., and Golby, A. (2016). Optical technologies for intraoperative neurosurgical guidance. *Neurosurg. Focus*, 40(3):E8.
- [Valdés *et al.* (2011a)] Valdés, P., Kim, A., Brantsch, M., Niu, C., Moses, Z., Tosteson, T., Wilson, B., Paulsen, K., Roberts, D., and Harris, B. (2011a).  $\delta$ -aminolevulinic acid-induced protoporphyrin IX concentration correlates with histopathologic markers of malignancy in human gliomas: the need for quantitative fluorescence-guided resection to identify regions of increasing malignancy. *Neuro Oncol*, 13(8):846–856.
- [Valdés *et al.* (2011b)] Valdés, P. A., Leblond, F., Paulsen, K. D., Kim, A., Wilson, B. C., Conde, O., Harris, B., and Roberts, D. W. (2011b). Combined fluorescence and reflectance spectroscopy for in vivo quantification of cancer biomarkers in low- and high-grade glioma surgery. *Journal of Biomedical Optics*, 16(11):1–15.
- [Van Song *et al.* (2016)] Van Song, T. P., Andraud, C., and Ortiz-Segovia, M. V. (2016). Towards spectral prediction of 2.5D prints for soft-proofing applications. In *2016 Sixth International Conference on Image Processing Theory, Tools and Applications (IPTA)*, pages 1–6, Oulu, Finland. IEEE.
- [Van Velthoven and Auer (1990)] Van Velthoven, V. and Auer, L. M. (1990). Practical application of intraoperative ultrasound imaging. *Acta Neurochir.*, 105(1-2):5–13.
- [Van de Hulst (1980)] Van de Hulst, H. C. (1980). Multiple light scattering.
- [Vargas *et al.* (2020)] Vargas, W. E., Wang, J., and Niklasson, G. A. (2020). Scattering and absorption cross sections of light diffusing materials retrieved from reflectance and transmittance spectra of collimated radiation. *Journal of Modern Optics*, 67(11):974–991.
- [Vargas *et al.* (2021)] Vargas, W. E., Wang, J., and Niklasson, G. A. (2021). Effective backscattering and absorption coefficients of light diffusing materials retrieved from reflectance and transmittance spectra of diffuse radiation. *Journal of Modern Optics*, 68(12):605–623.
- [Vargas and Niklasson (1997a)] Vargas, W. E. and Niklasson, G. A. (1997a). Applicability conditions of the Kubelka–Munk theory. *Applied optics*, 36(22):5580–5586. Publisher: Optica Publishing Group.
- [Vargas and Niklasson (1997b)] Vargas, W. E. and Niklasson, G. A. (1997b). Forward-scattering ratios and average pathlength parameter in radiative transfer models. *Journal of Physics: Condensed Matter*, 9(42):9083.
- [Vasefi *et al.* (2017)] Vasefi, F., MacKinnon, N., Farkas, D. L., and Kateb, B. (2017). Review of the potential of optical technologies for cancer diagnosis in neurosurgery: a step toward intraoperative neurophotonics. *Neurophotonics*, 4(1):011010.
- [Vervandier and Gioux (2013)] Vervandier, J. and Gioux, S. (2013). Single snapshot imaging of optical properties. *Biomed. Opt. Express*, 4(12):2938.

- [Vuorinen *et al.* (2003)] Vuorinen, V., Hinkka, S., Färkkilä, M., and Jääskeläinen, J. (2003). Debulking or biopsy of malignant glioma in elderly people - a randomised study. *Acta Neurochir.*, 145(1):5–10.
- [WHO (2022)] WHO (2022). Cancer. *World Health Organization: WHO*.
- [Weller *et al.* (2014)] Weller, M., van den Bent, M., Hopkins, K., Tonn, J. C., Stupp, R., Falini, A., Cohen-Jonathan-Moyal, E., Frappaz, D., Henriksson, R., Balana, C., Chinot, O., Ram, Z., Reifenberger, G., Soffietti, R., Wick, W., and European Association for Neuro-Oncology (EANO) Task Force on Malignant Glioma (2014). EANO guideline for the diagnosis and treatment of anaplastic gliomas and glioblastoma. *Lancet Oncol.*, 15(9):395–403.
- [Widhalm *et al.* (2019)] Widhalm, G., Olson, J., Weller, J., Bravo, J., Han, S. J., Phillips, J., Hervey-Jumper, S. L., Chang, S. M., Roberts, D. W., and Berger, M. S. (2019). The value of visible 5-ALA fluorescence and quantitative protoporphyrin IX analysis for improved surgery of suspected low-grade gliomas. *Journal of Neurosurgery*, 133(1):79–88. Publisher: American Association of Neurological Surgeons Section: Journal of Neurosurgery.
- [Wilson and Adam (1983)] Wilson, B. C. and Adam, G. (1983). A monte carlo model for the absorption and flux distributions of light in tissue. *Medical physics*, 10(6):824–830.
- [Wilson and Mycek (2011)] Wilson, R. H. and Mycek, M.-A. (2011). Models of light propagation in human tissue applied to cancer diagnostics. *Technology in Cancer Research & Treatment*, 10(2):121–134. Publisher: SAGE Publications Inc.
- [Wu *et al.* (1993)] Wu, J., Feld, M. S., and Rava, R. P. (1993). Analytical model for extracting intrinsic fluorescence in turbid media. *Appl. Opt., AO*, 32(19):3585–3595. Publisher: Optica Publishing Group.
- [Wu *et al.* (2006)] Wu, G. N., Ford, J. M., and Alger, J. R. (2006). MRI measurement of the uptake and retention of motexafin gadolinium in glioblastoma multiforme and uninvolved normal human brain. *J. Neurooncol.*, 77(1):95–103.
- [Yang *et al.* (2002)] Yang, Y., Celmer, E. J., Koutcher, J. A., and Alfano, R. R. (2002). DNA and protein changes caused by disease in human breast tissues probed by the Kubelka-Munk spectral functional. *Photochemistry and Photobiology*, 75(6):627–632.
- [Yang and Hersch (2008)] Yang, L. and Hersch, R. D. (2008). Kubelka-munk model for imperfectly diffuse light distribution in paper. *Journal of Imaging Science and Technology*, 52(3):30201–30500.
- [Yaroslavsky *et al.* (2002)] Yaroslavsky, A. N., Schulze, P. C., Yaroslavsky, I. V., Schober, R., Ulrich, F., and Schwarzmaier, H.-J. (2002). Optical properties of selected native and coagulated human brain tissues in vitro in the visible and near infrared spectral range. *Physics in Medicine and Biology*, 47(12):2059–2073.
- [Yoneda *et al.* (2018)] Yoneda, T., Nonoguchi, N., Ikeda, N., Yagi, R., Kawabata, S., Furuse, M., Hirose, Y., Kuwabara, H., Tamura, Y., Kajimoto, Y., and Kuroiwa, T. (2018). Spectral Radiance of Protoporphyrin IX Fluorescence and Its Histopathological Implications in 5-Aminolevulinic Acid-Guided Surgery for Glioblastoma. *Photomed. Laser Surg.*, 36(5):266–272.

- [Yong *et al.* (2006)] Yong, W. H., Butte, P. V., Pikul, B. K., Jo, J. A., Fang, Q., Papaioannou, T., Black, K., and Marcu, L. (2006). Distinction of brain tissue, low grade and high grade glioma with time-resolved fluorescence spectroscopy. *Front Biosci*, 11:1255–1263.
- [Yoshimura *et al.* (2013)] Yoshimura, H. N., Pinto, M. M., de Lima, E., and Cesar, P. F. (2013). Optical Properties of Dental Bioceramics Evaluated by Kubelka-Munk Model. In Bose, S., Bandyopadhyay, A., and Narayan, R., editors, *Ceramic Transactions Series*, pages 71–79. John Wiley & Sons, Inc., Hoboken, NJ, USA.
- [Yu *et al.* (2022)] Yu, J., Ghiaseddin, A., and Ahluwalia, M. (2022). Glioblastoma (GBM) - American Brain Tumor Association.
- [Zanello *et al.* (2017)] Zanello, M., Poulon, F., Pallud, J., Varlet, P., Hamzeh, H., Abi La-houd, G., Andreiuolo, F., Ibrahim, A., Pages, M., Chretien, F., Di Rocco, F., Dezamis, E., Nataf, F., Turak, B., Devaux, B., and Abi Haidar, D. (2017). Multimodal optical analysis discriminates freshly extracted human sample of gliomas, metastases and meningiomas from their appropriate controls. *Sci. Rep.*, 7:41724.
- [Zhadin and Alfano (1998)] Zhadin, N. N. and Alfano, R. R. (1998). Correction of the internal absorption effect in fluorescence emission and excitation spectra from absorbing and highly scattering media: theory and experiment. *J Biomed Opt*, 3(2):171–186.
- [Zhang *et al.* (2017)] Zhang, N., Tian, H., Huang, D., Meng, X., Guo, W., Wang, C., Yin, X., Zhang, H., Jiang, B., He, Z., and Wang, Z. (2017). Sodium Fluorescein-Guided Resection under the YELLOW 560 nm Surgical Microscope Filter in Malignant Gliomas: Our First 38 Cases Experience. *Biomed Res Int*, 2017:7865747.
- [Zhang *et al.* (2018)] Zhang, N., Tian, H., Huang, D., Meng, X., Guo, W., Wang, C., Yin, X., Zhang, H., Jiang, B., He, Z., and Wang, Z. (2018). Corrigendum to "Sodium Fluorescein-Guided Resection under the YELLOW 560 nm Surgical Microscope Filter in Malignant Gliomas: Our First 38 Cases Experience". *Biomed Res Int*, 2018:6348625.
- [Zhu *et al.* (2008)] Zhu, C., Breslin, T. M., Harter, J., and Ramanujam, N. (2008). Model based and empirical spectral analysis for the diagnosis of breast cancer. *Optics express*, 16(19):14961–14978.